UNIVERSITY OF SOUTHAMPTON

Faculty of Social and Human Sciences

Geography and Environment

Patterns and trends of cloud cover and photosynthetically active solar irradiation in southern England: implications for vegetation productivity

by

Prasan Pankaew

Thesis for the degree of Doctor of Philosophy

November, 2013

UNIVERSITY OF SOUTHAMPTON

ABSTRACT

FACULTY OF SOCIAL AND HUMAN SCIENCES

GEOGRAPHY AND ENVIRONMENT

Thesis for the degree of Doctor of Philosophy

Prasan Pankaew

The aim of the research described in this thesis was to investigate the spatial and temporal variability of photosynthetically active radiation (PAR) over the UK, in particular, to estimate both global PAR and the fraction of diffuse PAR at spatial and temporal scales appropriate for use with plant productivity models. In the UK, the spatial and temporal variation of PAR is primarily controlled by the fractional cloud cover and the solar geometry. Diffuse flux (skylight) penetrates further into the canopy than direct flux, so knowing the diffuse PAR fraction (K_{dQ}) will improve the accuracy of plant productivity models, especially for canopies with significant 3D structure, such as forest.

The first part of the research investigated a novel sunshine sensor, the Delta-T Devices BF3, to test whether this simple low-cost instrument was an adequate substitute for the instruments normally used to measure the components of PAR. This was the first independent test of this instrument and it concluded that the BF3 was highly suitable for this purpose.

The main study developed and tested a method to map the amount of incident PAR (Q_t) and the diffuse fraction (K_{dQ}), based on satellite sensor data. The main systems used were the Meteosat Visible and Infrared Imager (MVIRI) on board the Meteosat First Generation (MFG) satellite and the Spinning Enhance Visible and Infrared Imager (SEVIRI) on board the Meteosat Second Generation (MSG) satellite.

The resulting maps of global and diffuse PAR over the whole of the UK were validated using ground data from meteorological stations and instruments at eight FLUXNET sites around the country. It is estimated that global hourly PAR was accurate to < 50 $\mu\mathrm{mol\,m^{-2}\,s^{-1}}$ (RMSE) and diffuse PAR fraction to <10 % (RMSE). This is the first time these variables have been mapped at moderate spatial resolution (1km) over the whole of the UK.

The Forest LIGHT (FLIGHT) model (North, 1996) was used to study the influence of $\mathrm{Q_t}$ and $\mathrm{K_{dQ}}$ on forest canopy photosynthesis. The effect of diffuse PAR fraction on gross primary productivity was clear. With the same overall level of PAR, a forest canopy under ‘direct and diffuse’ illumination had an increase in GPP around 12 % compared to one under direct illumination only.

One of the major issues faced in this research was the lack of adequate ground data for validation. The research has shown that both the amount of PAR and the diffuse fraction are important factors in forest productivity, and that the Delta-T Devices BF3 instrument is well-suited as a source of validation data for a national network to monitor the gross primary productivity of forests in the UK.

DECLARATION OF AUTHORSHIP

I, Mr. Prasan Pankaew

declare that the thesis entitled

Patterns and trends of cloud cover and photosynthetically active solar irradiation in southern England: implication on vegetation productivity

and the work presented in the thesis are both my own, and have been generated by me as the result of my own original research. I confirm that:

- this work was done wholly or mainly while in candidature for a research degree at this University;
- where any part of this thesis has previously been submitted for a degree or any other qualification at this University or any other institution, this has been clearly stated;
- where I have consulted the published work of others, this is always clearly attributed;
- where I have quoted from the work of others, the source is always given. With the exception of such quotations, this thesis is entirely my own work;
- I have acknowledged all main sources of help;
- where the thesis is based on work done by myself jointly with others, I have made clear exactly what was done by others and what I have contributed myself;
- parts of this work have been published as:
    - Pankaew, P., Milton, E. J., & Dawson, T. P. (2011). *Estimating the proportion of diffuse photosynthetically active radiation from satellite measured cloud fraction: a test under humid temperate conditions.* Proceeding of the Annual Conference of the Remote Sensing and Photogrammetry Society: Earth Observation in a Changing World (RSPSoc 2011), Bournemouth, GB, 13 - 15 September 2011.
    - Pankaew, P., Dash, J., Milton, E. J., & Dawson, T. P. (2013). *Estimating gross primary productivity (GPP) of forests across southern England at high spatial and temporal resolution using the FLIGHT model.* Proceeding of the European Geosciences Union: General Assembly (EGU2013), Vienna, Austria, 7-12 April 2013.
    - Pankaew, P., Milton, E. J., & Dash, J. (2013). *Estimating hourly variation in photosynthetically active radiation across the UK using MSG SEVIRI data.* Proceeding of the 35th International Symposium on Remote Sensing of Environment (ISRSE35), Beijing, China, 22-26 April 2013.

Signed: ....

Date: ....

ACKNOWLEDGEMENT

First and foremost, I would like to thank Professor Edward J. Milton and Dr. Jadu Dash for their continuous supervision, support, advice, guidance and encouragement during the time I was studying here. Thanks to my first supervisor who introduced me in the first year before he moved to the University of Dundee, Professor Terry P. Dawson.

I also thank those UK organisations which support the data and study sites: (i) British Atmospheric Data Centre (BADC), (ii) Centre for Ecology and Hydrology (CEH), (iii) Science and Technology Facilities Council (STFC) Chilbolton Facility for Atmospheric and Radio Research (CFARR). Thanks to the laboratory of my original affiliation for additional data and a study site, the Solar Energy Research Laboratory in Department of Physics at Silpakorn University, Thailand.

Personal thanks to those people who have supplied me useful information and help: Mal Clarke and Jan Lass of CFARR, Charles George and Matthew Wilkinson of CEH, and Sara-Jane Harris of the UK Met Office.

I am grateful for the support and fulltime scholarship from the Ministry of Science and Technology of the Royal Thai government and for supervision from the Office of Educational Affairs in the Royal Thai Embassy. I am also grateful to the Department of Physics at Silpakorn University in Thailand for allowing me study leave.

Finally, I would like to thank my family especially my mother who always blesses me since the first day I am away for my study. Thanks to all my friends and colleagues who supported me and helped me get through difficulties.

Table of Contents

CHAPTER 5 ESTIMATION OF PAR AMOUNT OVER THE UK AND EXTENSION TO SEVIRI DATA 111

List of Figures

List of Tables

Nomenclature and abbreviations

AOT = aerosol optical thickness [unitless]

c = light velocity [3.00×10^{8} m·s^{-1}]

CO_2 = carbon dioxide

DN = digital number of a pixel [0-255, unitless]

DN_{max} = maximum of DN [0-255, unitless]

DN_{min} = minimum of DN [0-255, unitless]

E_0 = eccentricity correction factor (unit less),

ECC = estimated cloud cover [0-1, unitless]

fDIF = diffuse PAR fraction, Q_d/Q_t [0-1, unitless]

FLIGHT = forest light vegetation model

GCP = ground control point

GEP = gross ecosystem productivity [μmol C m^{-2} s^{-1}]

GPP = gross primary productivity [μmol C m^{-2} s^{-1}]

h = Planck's constant [6.63×10^{-34} J·s]

$\dot{I}_{0n}(\lambda)$ = extraterrestrial spectral irradiance at the mean Sun-Earth distance [W m^{-2} nm^{-1}]

$I_{ex}(\lambda)$ = extraterrestrial spectral irradiance on horizontal surface at TOA [W m^{-2} nm^{-1}]

I_{sc} = solar constant [1,367 W m^{-2}]]

ISCCP = International Satellite Cloud Climatology Project

K_{dQ} = diffuse PAR fraction, Q_d/Q_t [0-1, unitless]

K_{dS} = diffuse broadband fraction, S_d/S_t [0-1, unitless]

K_T = clearness index, S_t/S_0 [0-1, unitless]

K_{TQ} = clearness PAR index, Q_t/Q_0 [0-1, unitless]

$k_{\lambda,r}$ = spectral attenuation coefficient due to Rayleigh attenuation [0-1, unitless]

$k_{\lambda,oz}$ = spectral attenuation coefficient due to ozone [0-1, unitless]

ℓ = ozone column [cm]

LTS = least trimmed square

LUE = light use efficiency [0-1, unitless]

m_a = local airmass [1-∞, unitless]

MBE = means bias error [unit depends on variable, % of reference]

m_r = relative airmass [1-∞, unitless]

MVIRI = Meteosat Visible and Infrared Imager

NPP = net primary productivity [$\mu\text{mol C m}^{-2}\text{ s}^{-1}$]

NEE = net ecosystem exchange [$\mu\text{mol C m}^{-2}\text{ s}^{-1}$]

O_2 = oxygen

PAR = photosynthetically active radiation [$\mu\text{mol m}^{-2}\text{ s}^{-1}$]

P_{local} = local pressure [millibars]

PPFD = photosynthetic photon flux density [$\mu\text{mol m}^{-2}\text{ s}^{-1}$]

$P_{standard}$ = standard pressure at average sea level [1013.25 millibars]

Q_0 = extraterrestrial PAR on the horizontal surface at the TOA [$\mu\text{mol m}^{-2}\text{ s}^{-1}$]

Q_d = diffuse PAR [$\mu\text{mol m}^{-2}\text{ s}^{-1}$]

Q_t = global PAR [$\mu\text{mol m}^{-2}\text{ s}^{-1}$]

RMSE = root mean square error [unit depends on variable, % of reference]

$R_{Q,c}$ = reflection of cloud in PAR wavelength band [0-1, unitless]

$R_{sat,c}$ = reflection of cloud in satellite visible (400-1100 nm) wavelength band [0-1, unitless]

S_0 = extraterrestrial solar irradiance on the horizontal surface at the TOA [W m^{-2}]

S_d = diffuse broadband, 305-2800 nm, solar irradiance [W m^{-2}]

SEVIRI = Spinning Enhanced Visible and Infrared Imager

S_t = global broadband, 305-2800 nm, solar irradiance [W m^{-2}]

T_Q = PAR transmittance due to atmospheric component [0-1, unitless]

$T_{Q,c}$ = PAR transmittance due to cloud [0-1, unitless]

$T_{Q,oz}$ = PAR transmittance due to ozone attenuation [0-1, unitless]

$T_{Q,r}$ = PAR transmittance due to Rayleigh attenuation [0-1, unitless]

$T_{\lambda,oz}$ = solar spectral transmittance due to ozone attenuation [0-1, unitless]

$T_{\lambda,r}$ = solar spectral transmittance due to Rayleigh attenuation [0-1, unitless]

TOA = top of atmosphere

UTC = coordinated universal time

α = wavelength exponent in Ångström’s turbidity formula [unitless]

β = Ångström’s turbidity parameter [unitless]

θ_z = Sun zenith angle [°, radian]

δ = declination angle [°, radian]

λ = wavelength [μm, nm]

ϕ = azimuth angle, latitude angle [°, radian]

ω = hour angle [°, radian]

Chapter 1 Introduction

1.1 Introduction

The research described in this thesis concerns the measurement of incident photosynthetically active radiation (PAR) based on data from a satellite sensor. The amount of PAR integrated over different time periods (daily, monthly, seasonal) is a key factor controlling the growth of plants, and therefore vitally important in controlling the accumulation of carbon over large areas of the Earth's surface.

The conceptual basis for the research is the 'Image Chain' idea proposed by Schott (1997). This considers Earth observation (EO) as a system of linked observations and models, all of which have associated assumptions, errors and uncertainties. The extent to which a user can have confidence in the output from such a system depends on the accuracy and reliability of the individual parts. The chain is only as strong as its weakest link. The corollary of this is that effort expended in improving one part of the system is wasted unless all the other parts are equally good. There is no point in having perfect atmospheric correction if the relationship between the remotely sensed variable (e.g. radiance) and the biophysical variable of interest (e.g. biomass) is poor.

The starting point for all quantitative applications of passive remote sensing in the optical region (0.4 - 2.4 μm) is the Sun, as this is the source of energy which interacts with matter, whether in the atmosphere or in a vegetation canopy. The spectrum at the mean Sun-Earth distance, 1 astronomical unit (AU), is used to calculate the extra-terrestrial spectrum at the top of the Earth’s atmosphere. It was measured by the World Radiation Center (WRC), as shown in Figure 1.1.1 (Iqbal, 1983; Liou, 2002).

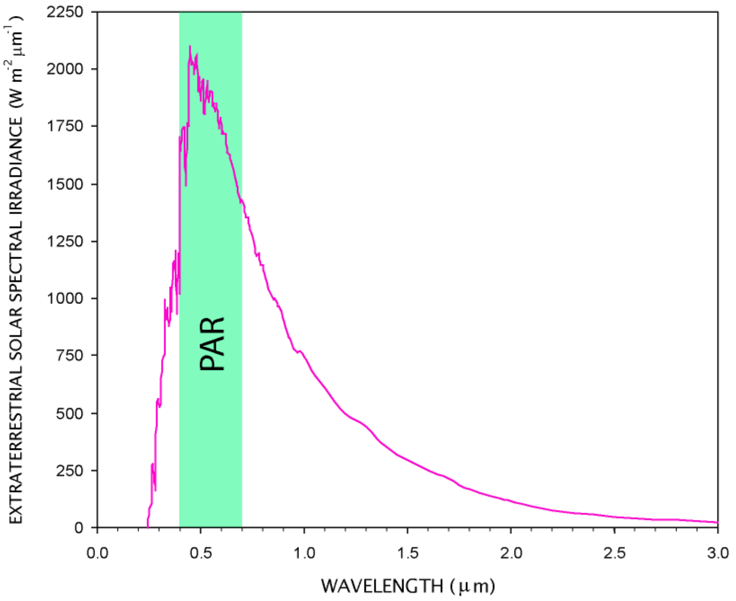

Figure 1.1.1 Spectrum of the extra-terrestrial solar radiation at 1 AU (modified from data in Iqbal, 1983)

Between the top of atmosphere (TOA) and the Earth's surface there are factors in the atmosphere that modify the solar irradiance. All of them have differing transmittance with wavelength, and with the density of the components themselves (Fig 1.1.2).

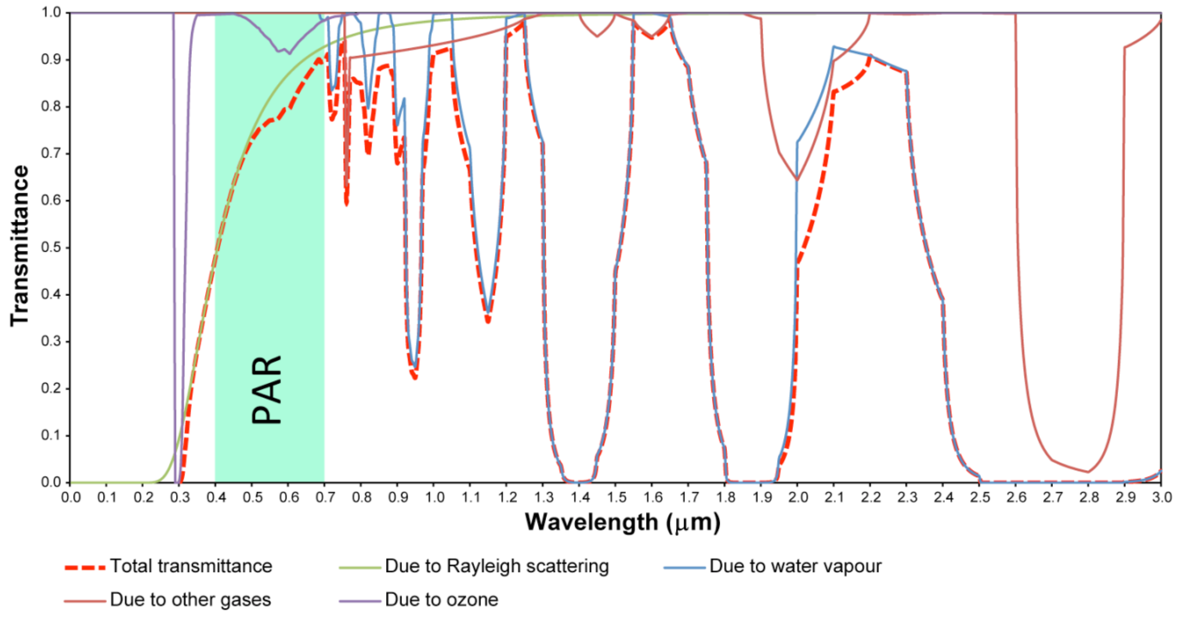

Figure 1.1.2 Spectrum transmittance of the solar irradiance due to atmospheric components (modified from data in Iqbal, 1983)

Furthermore, the geometry of solar illumination has a very strong influence on the variation of the atmospheric transmittance. Even the densities of the atmospheric components remain constant, the Sun position can result in great variation in solar irradiance at the Earth's surface. Due to the Sun position has strong influence on solar irradiance at the Earth's surface.

The PAR spectrum includes the peak energy curve of the solar spectrum. PAR has a spectrum band of 400-700 nm, while the solar energy spectrum has the highest peak at ~ 550 nm.

The spectrum of PAR under a cloudless sky (e.g. in Lacis and Hansen, 1974; Iqbal, 1983; Liou, 2002) is influenced mainly by the Rayleigh scattering effect. Other minor factors affecting the PAR spectrum are gases, such as O_3 (ozone), O_2 (oxygen), aerosols and H_2O (water vapour). There are many physical and statistical models that can accurately estimate the PAR at the Earth's surface under a clear sky (e.g. 6S: Vermote et al., 1995; Vermote et al., 1997a; Vermote et al., 1997b). The solar spectrum within the PAR wavelength band is shown in Figure 1.2.1.

Although the real atmosphere is turbulent, modern radiative transfer models can estimate the solar radiation at the Earth's surface very accurately (e.g., Hay and Hanson, 1978; Tarpley, 1979; Gautier et al., 1980; Möser and Rachke, 1984; Pinker and Ewing, 1985; Dedieu et al., 1987; King et al., 1990; Pinker and Laszlo, 1992; Vermote et al., 1995, 1997b; Janjai et al., 2005; Vignola et al., 2007; Badescu, 2008; Meyer et al., 2008; Janjai et al., 2009; Janjai et al., 2011), especially under a cloudless sky (e.g., 6S: Vermote et al., 1995; Vermote et al., 1997a; Vermote et al., 1997b). One of the advantages of such models is that they represent physically the light transmittance in the atmosphere. Furthermore, radiative transfer modelling is a time-dependent method. Therefore, it is very useful for the estimation of the real solar radiation which is always varying with time.

1.2 Influence of the atmosphere on PAR

The main causes of spectral modification in the PAR wavelength band are Rayleigh scattering and ozone absorption (Figure 1.2.1).

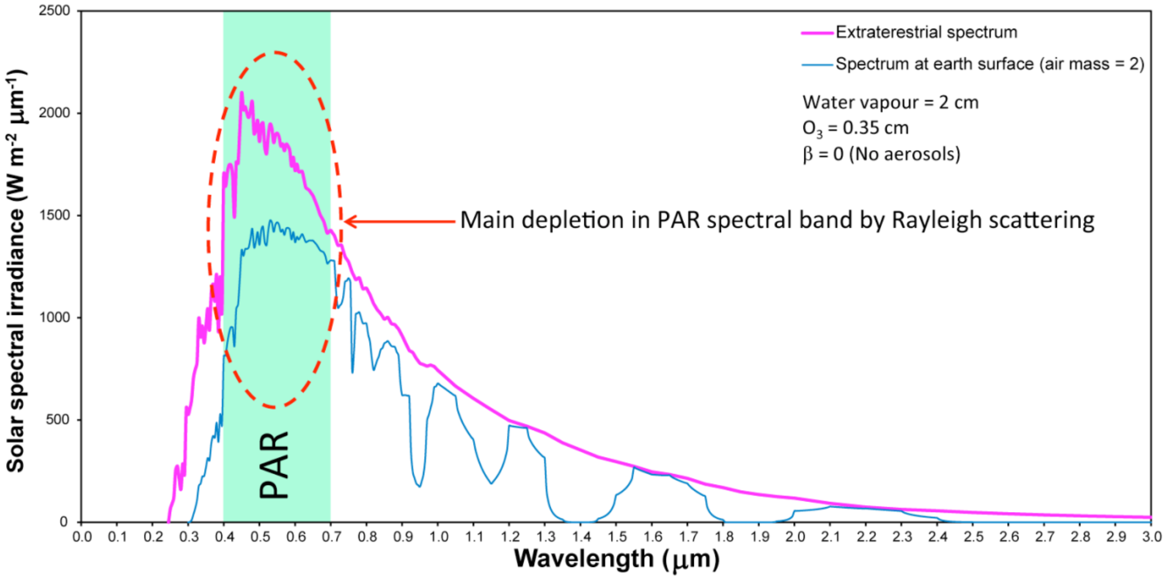

Figure 1.2.1 Spectrum solar irradiance on the Earth surface (modified from data in Iqbal, 1983)

1.2.1 The Rayleigh scattering effect

Rayleigh scattering is scattering of solar irradiance by air molecules (Iqbal, 1983, pp. 111-116). The Rayleigh scattering effect is not a phenomenon from a specific atmospheric component. It is a phenomenon from the entire atmosphere. The Rayleigh scattering phenomenon in the atmosphere makes the sky look blue and can be noticed by the naked eye.

The Rayleigh scattering effect plays an importance role on the transmitted PAR spectra onto the Earth's surface. The Rayleigh scattering phenomenon affects every wavelength within the PAR band. The lowest transmittance (highest depletion) due to the Rayleigh scattering effect within the PAR wavelength band is at 0.4 µm. The trend of transmittance, due to the Rayleigh scattering effect, increases depending on the increasing wavelength. The highest transmittance is at 0.7 µm. By approximation, 20% of the PAR from TOA is depleted during the path through the atmosphere to the Earth's surface, at a 60 degree zenith angle, air mass = 2 (Figure 1.2.2).

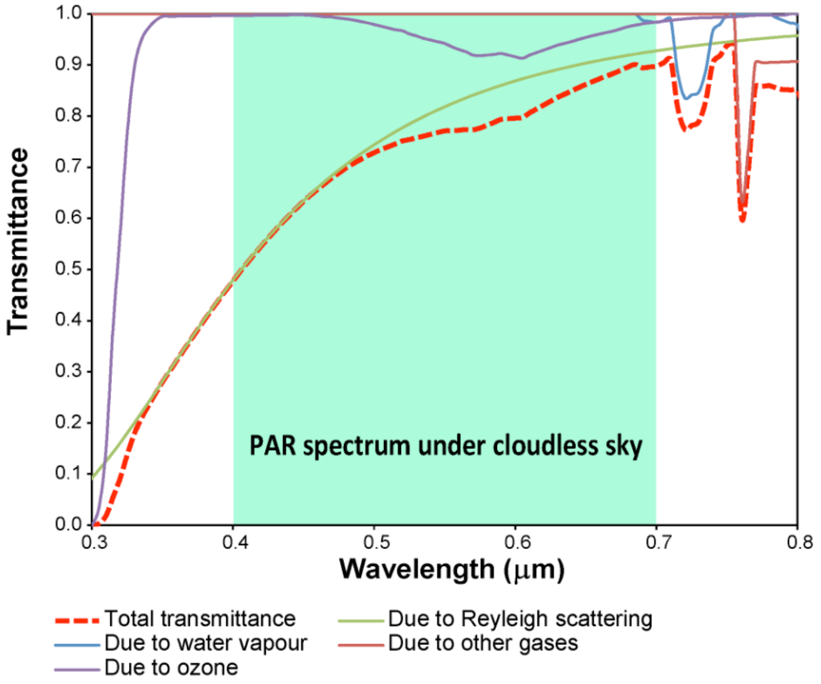

Figure 1.2.2 Transmittance spectra of the atmospheric components within the PAR wavelength band under a cloudless sky (modified from data in Iqbal, 1983)

1.2.2 Ozone

Ozone is the second atmospheric component that plays a main role on the depletion in the PAR spectral band. Ozone affects the spectral transmittance of the spectral band between 375-650 nm, Chappuis band (e.g. Lahoz and Peuch, 2012). The PAR band has the highest depletion at approximately 600 nm. The highest transmittance due to the ozone in the PAR band is at 400 nm and has another transmittance peak at 700 nm. By approximation the average amount of ozone at a 60 degree zenith angle (air mass = 2) depletes 4-5% in the PAR spectral band (Figure 1.2.2).

1.2.3 Water vapour effects

Water vapour (H_2O) is water in a gas state that is invisible, floating in the atmosphere. The quantity of water vapour varies across the Earth surface. The water vapour in the Tropics is higher than in areas in the higher and lower latitudes.

The majority of effects from water vapour are on the broadband solar irradiance spectrum, especially in infrared bands and longer wavelengths. Water vapour has little effect in the PAR spectral band (Figure 1.2.2), causing less than 1% of transmittance depletion by water vapour in the PAR band.

1.2.4 Other gases effects

Other gases in the solar irradiation contexts are the mixed gases which include CO_2, O_2 and other minor absorbers, but exclude ozone (O_3) and water vapour. Above 0.7 μm, the other gases have effects on the broadband spectral irradiance. There is no depletion due to the other gases within the PAR spectral band. Therefore, PAR modelling has no need to consider the depletion of the other gases, while it is needed in the broadband irradiance.

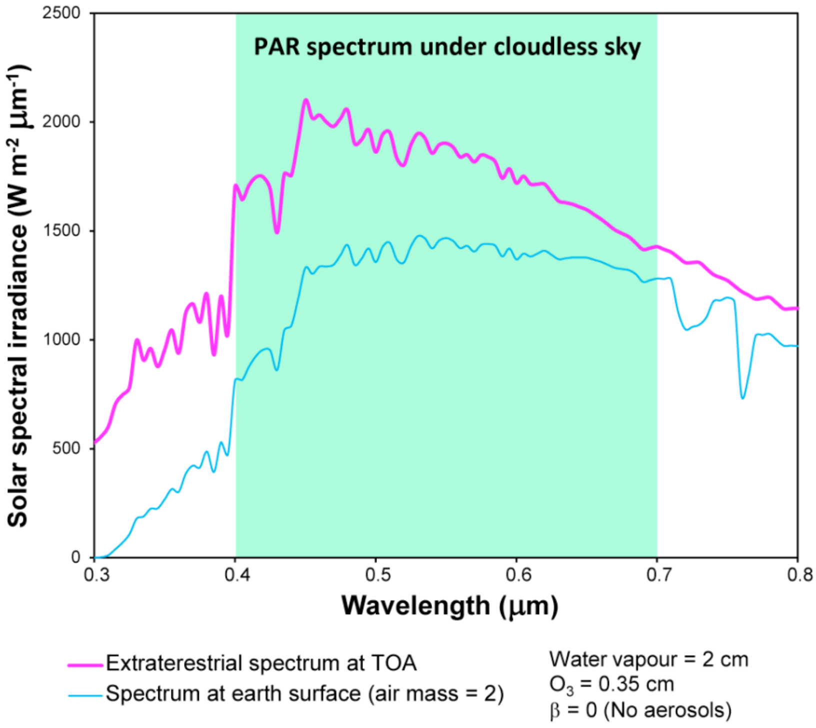

Figure 1.2.3 PAR spectrum at the TOA and on the Earth's surface under cloudless conditions (modified from data in Iqbal, 1983)

1.2.5 Aerosol effects

Aerosols are the solid particles (smoke, soot, soil dust, spray etc.) suspended in the atmosphere. The main sources of aerosols are the smoke from burning, incomplete vehicle combustion, factories, human activity, wind-blown marine and dust etc.. Aerosols deplete the amount of solar irradiance by affecting the transmission across the entire PAR region (Figure 1.2.4). In some countries, especially the UK, the government has policies to control air pollution, so the very large aerosol loads found in the tropics and in countries with unregulated industries are not present.

Aerosols are not the main factors causing spectral attenuation of PAR in the UK. Weather in the UK is dominated by the passage of fronts, so dense cloud controls PAR much more than aerosol amount. Also, the country has little biomass burning, the factories and vehicles have strict CO_2 emission controls, there is no desert, and the UK is an island, so absolute levels of aerosols are generally low (www1).

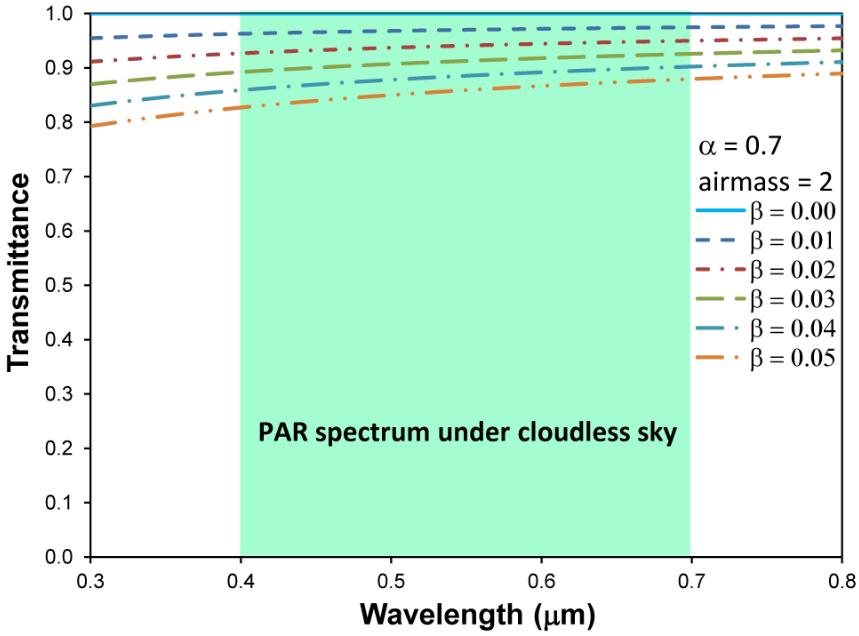

Figure 1.2.4 Transmittance spectra of aerosols within the PAR wavelength band under a cloudless sky (modified from equations in Iqbal, 1983)

1.3 Other influences on quantity of PAR at the Earth's surface

1.3.1 Solar zenith angle effects

The angle of the Sun’s irradiance and how it interacts with the Earth’s surface is one of the main things to consider in every solar radiation work. In a polar co-ordinate system, the Sun direction in the hemispherical sky is composed of two angles; the zenith angle and the azimuth angle.

The zenith angle is the angle from the Sun’s direction to the nadir. It has a value of 0-90 degrees from nadir to the horizontal. The zenith angle is the main angle that is usually referred to. This is because the path length of the irradiance in the atmosphere varies mostly due to the zenith angle, but does not vary on the azimuth.

The zenith angle can deplete the entire solar irradiance spectrum so that it almost disappears. The solar irradiance has the highest spectral irradiance at the zenith angle being 0 degrees (at nadir, air mass = 1). At the largest zenith angle, 90 degrees, the spectral irradiance is very low, it almost vanishes, but does not completely disappear. At the largest zenith angle there are two reasons why the small amount of solar radiation still exists. The first is the multiple reflections in the atmosphere, and the second is the reflection of the light in the atmosphere.

The zenith angle variable can be found in almost all of the equations calculating the solar irradiance. The PAR spectrum also varies on the zenith angle (Figure 1.3.1). Therefore, consideration of the zenith angle is also necessary for the PAR estimation using satellite data.

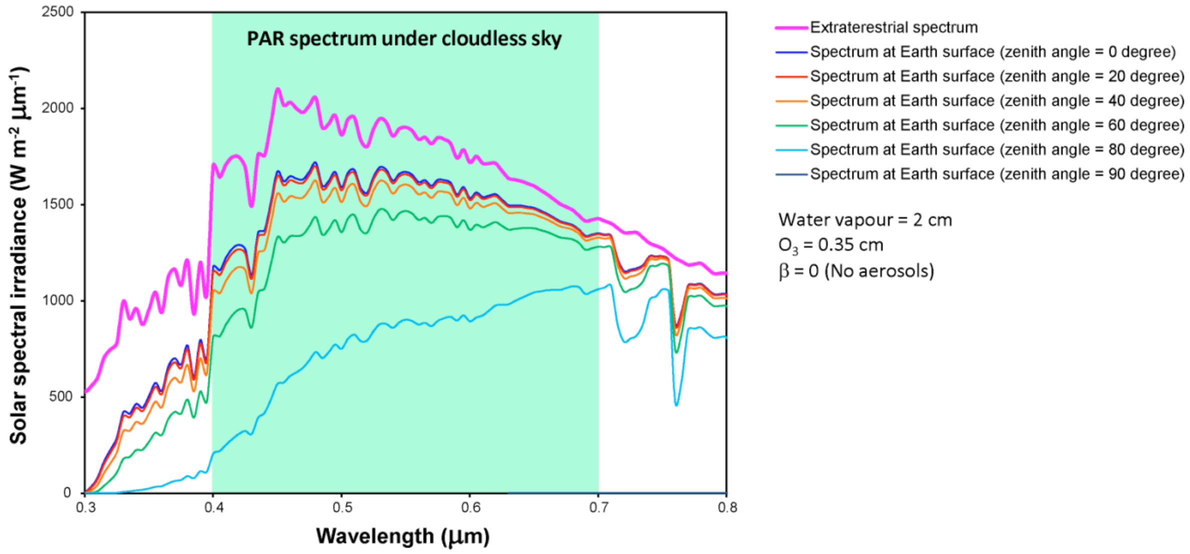

Figure 1.3.1 Variation of the spectrum transmittance on the different zenith angle (modified from data in Iqbal, 1983)

The zenith angle effects cause the greatest problem in the PAR estimation in the cloudless sky. Its effects are the next in importance to cloud effects in a cloudy sky.

1.3.2 Cloud effects

In a cloudy area nothing can affect the solar irradiance on the ground more than clouds. Generally, clouds can decrease the solar flux by up to 70% of the solar irradiance that transmits through the atmosphere to the surface (e.g. Iqbal, 1983, p. 218; Pankaew et al., 2011). Although clouds do not absorb significantly at the PAR wavelength (Frouin and Pinker, 1995), clouds can deplete the transmittance by reflection and scattering. Furthermore, the variation of cloud has a high fluctuation within a very short period of time.

The spectrum of PAR under cloudy skies does not only have the same influence from the Rayleigh scattering, aerosols and gases as under a cloudless sky, but also has the influence from the light interception of clouds. There are many physical models and statistical models that can explain the PAR spectrum under a cloudless sky. The models for a cloudless sky are more accurate than for the cloudy sky because they do not include the problems of cloud. However, in the real situation, clouds exist. To estimate the solar irradiance in the real situation, it is necessary to include cloud effects.

1.4 The components of PAR

Firstly, according to the wavelength band, type of sensors and definitions of irradiance, there are many points of confusion of the physical meaning of the global, direct and diffuse. To clarify their definitions and measurements, an explanation and example will be described first, then the effects on the global, direct and diffuse PAR will be explained.

One of the important things necessary for clarification before using the words global, diffuse and direct is that, all of them are irradiance on the horizontal surface. These terms are often confused, especially the ‘direct’ irradiance. If this word is written alone in the solar irradiance context it means direct irradiance on the horizontal surface. If it is written ‘direct normal’ it has another meaning, which is the direct irradiance that is perpendicular to the receiver.

1.4.1 Measurements based on the directional component of solar irradiation

In solar radiation measurement, the irradiance is not only separated based on wavelength band (to be UV, PAR, broadband irradiance, etc.), but also based on the directional properties. In this instance, they are global, direct and diffuse PAR. Measuring each type of directional irradiance requires equipment to manage the direction of the irradiance before it reaches the light sensors. In order to study PAR irradiation in the ecosystem it is necessary to know the PAR equipment for the measurement of global direct and diffuse.

The methods for measurement of the global, direct and diffuse PAR were derived from those used to measure global, direct and diffuse broadband irradiance. The main difference is in the spectral responses of the sensors.

1.4.2 Global PAR

Global PAR is the global irradiance in the PAR wavelength band that reaches the horizontal plane from every direction of the hemispherical sky. The equipment for the global PAR is a general PAR sensor. One of the most widely known and used is the LI-COR Quantum Sensor of LI-COR Biosciences Ltd.

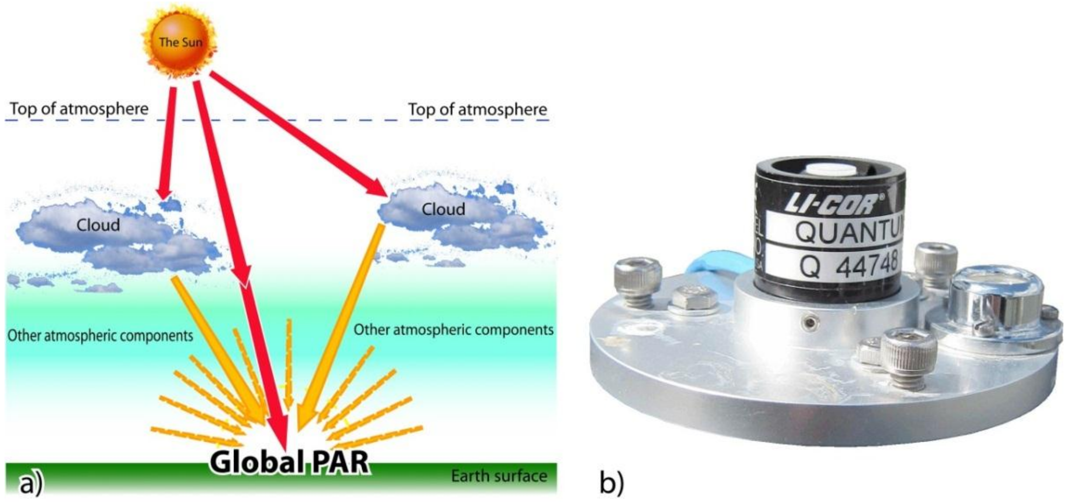

Figure 1.4.1 Diagram of global PAR and b) the PAR sensor, global PAR measurement

1.4.3 Diffuse PAR

Diffuse PAR is the solar irradiance in the PAR wavelength band from every direction which does not include the irradiance from a small solid angle directly from the Sun. The equipment for the diffuse PAR is the combination of the global PAR sensor and a shade object. The shade object might be a ball, a dish or a diffuse ring. In the case of the diffuse ring it is necessary to use correction factors for changing the measured value to the real value of diffuse irradiance (Figure 1.4.2).

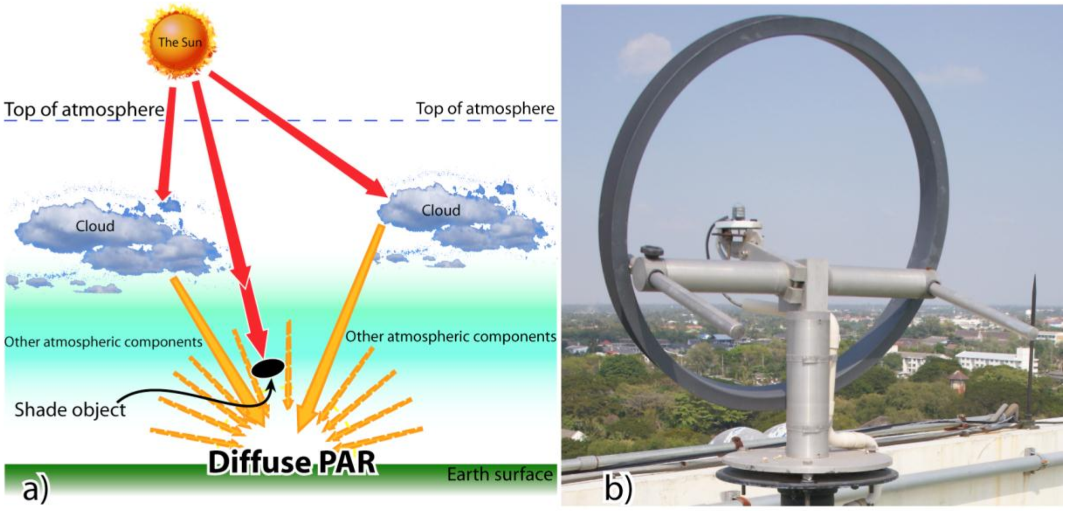

Figure 1.4.2 a) diagram of diffuse PAR and b) the diffuse PAR measurement using diffuse ring (an example from Silpakorn University in Thailand), the ring needs the correction factors to calculate the real diffuse PAR

1.4.4 Direct PAR

In the solar radiation context, the ‘direct normal’ irradiance is defined as the solar irradiance that reaches the plane that is perpendicular to the direction of the irradiance, within a small solid angle.

Therefore, direct normal PAR is the solar irradiance in the PAR wavelength band which reaches the plane that is perpendicular to the direction of irradiance, directly in the direction pointing to the Sun, in a small solid angle. Generally, the direct PAR on the horizontal surface can be estimated using the measured global PAR data, minus the evaluated diffuse PAR.

Another method to measure the direct PAR on the horizontal surface is by measure the direct normal PAR, and then converts to be the direct PAR on the horizontal surface. The equipment for the direct normal PAR is called a Phytoactinometer (Figure 1.4.3). The direct normal PAR from the Phytoactinometer can then be changed to be the direct PAR on the horizontal surface using the cosine of the zenith angle correction.

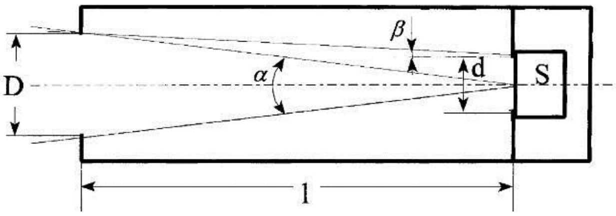

Figure 1.4.3 Schematic diagram of the applied Phytoactinometer, D is diameter of the front aperture, d is the diameter of the receiver's aperture, l is the distance between the diaphragms, α is the view angle, 10°, β is the slope angle, 2.5° and S is the PAR measurement (Mõttus et al., 2001)

However, an alternative way for measuring direct PAR on the horizontal surface is by using the BF3 Sunshine Sensor (Figure 1.4.4b) from Delta-T Instruments (Delta-T Devices Ltd., 2002a, b). The BF3 Sunshine Sensor can indirectly measure the global and diffuse PAR using a complicated shade pattern. The BF3 is composed of the computer generated shade pattern and a set of seven small PAR sensors inside. The BF3 can calculate the global and diffuse PAR using inside microprocessors. Alternatively, there is an option to set the BF3 Sunshine Sensor to calculate direct PAR as one of its outputs.

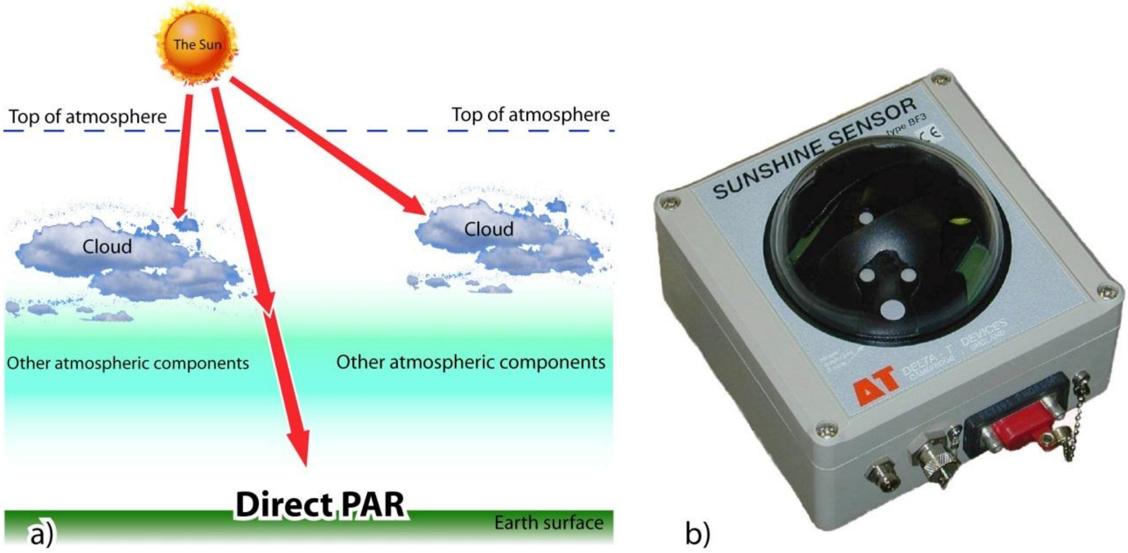

Figure 1.4.4 Diagram of direct PAR and b) the BF3 Sunshine Sensor that can be indirectly used to evaluate the direct PAR

1.5 Factors affecting the directional properties of Global, direct and diffuse PAR

1.5.1 Atmospheric components

The major effect on the global, direct and diffuse of PAR is the Earth's atmosphere. If the Earth had no atmosphere, there will be no diffuse PAR. In that case, the global irradiance will only be composed of the direct irradiance. Also, if the Earth had no atmosphere, the global PAR on the Earth's surface will be equal to the direct PAR at the mean Sun-Earth distance (the PAR at TOA).

In the real world, the Earth's atmosphere exists. The atmosphere causes the diffuse irradiance during the path of the irradiance through the atmosphere, from the TOA to the Earth's surface. In the Section 1.1 page 2, it is mentioned that the atmospheric components affect the spectral transmittance. The atmospheric component does not only affect the spectral transmittance, but is also the cause of the diffuse irradiance.

1.5.2 Solar zenith angle

Under a cloudless sky, the zenith angle plays the most important role on the diffuse irradiance. The zenith angle does not change the quantity of the atmospheric components, but changes the path length of the irradiance that is needed to transmit through the atmosphere. Longer path lengths have more diffuse and reflection. The bigger zenith angle causes the longer path length. Therefore, the bigger zenith angle causes more diffuse irradiance than direct irradiance. This means that the fraction between the diffuse per global PAR will be increased, if the zenith angle is bigger.

The bigger zenith angle is the cause of a lowering of the PAR on the surface. As the bigger zenith angle causes the longer the atmospheric path length, the longer path length has more atmospheric reflection. The higher atmospheric reflection reflects higher irradiance in outer space. In the case of the bigger zenith angle, the transmitted irradiance is reduced. Therefore, increasing the zenith angle does not only increase the diffuse fraction, but also reduces the transmittance of the atmosphere. The irradiance is lower at larger zenith angles. This means that with low PAR the diffuse PAR is higher than the direct PAR. To sum up, under cloudless conditions, the bigger zenith angle reduces the global PAR, but the fraction of the diffuse per global PAR increases.

In radiative transfer models, the zenith angle is concealed in the transmittance coefficient in terms of the relative air mass. The zenith angle varies the relative air mass from 1 to ~∞. The relative airmass is 1 for the Sun position at the nadir. The relative air mass at another zenith angle is approximately $1/\cos\theta_z$, where the θ_z is the Sun zenith angle. Practically, the relative air mass is not ∞ at the 90° Sun zenith angle, because of the distortion of the irradiance in the atmosphere. However, the difference is very small and it can be assumed that the relative air mass is $1/\cos\theta_z$. The more complicated equations for the relative air mass can be found in more detail in Iqbal (1983).

Jacovides et al. (1997) found the zenith angle variation in term of airmass has effect to the diffuse component of PAR. The large airmass increases the diffuse component (Jacovides et al., 1997).

1.5.3 Clouds

In the real situation, the atmosphere varies between cloudless, cloudy and partly cloudy. Under cloudy conditions, not only do other atmospheric components influence the quantity of the diffuse irradiance, but the clouds become the main source of the diffuse irradiance. Clouds have not only reduced the global irradiance, but they also scatter the irradiance to be the diffuse. Once there is greater cloud cover the irradiance is much reduced and most of the transmittance is the diffuse (other cloud effects are explained in other sections).

This chapter has described the nature of PAR and its importance to life on Earth. The next chapter will review the use of satellite sensors to estimate the components of PAR, and the use of these data in plant productivity models.

Chapter 2 Literature review

2.1 Measurement of solar irradiation at the Earth's surface

PAR is a wavelength band of the solar irradiance and many definitions from the broadband solar irradiance are applied to use in PAR. Solar irradiance has complicated definitions. To understand PAR, understanding the solar irradiance is an essential.

2.1.1 Global irradiance

The measurement of solar radiation at the Earth's surface has a long history, but the main focus of interest has been broadband radiation, not PAR. The first PAR sensors were modified thermopile devices, but these lacked sensitivity and did not have the necessary speed of response for many biological applications (Szeicz et al., 1964; McCree, 1972a, b). Selenium cells with gelatin or glass filters were also used in the 20th century (Federer and Tanner, 1966; McPherson, 1969; Szeicz, 1974), but by the end of the century silicon photodiodes had become the dominant PAR sensing device, combined with one or more filters to modify their spectral response (Norman et al., 1969; Woodward, 1983). Silicon photodiodes are highly linear when operated in short-circuit mode, respond quickly to changes in illumination and are relatively stable over time, making them very suitable sensors for the PAR region.

The measurement of PAR requires the evaluation of the intensity of photons in PAR wavelengths. The result of this is called Photosynthetic Photon Flux Density (PPFD). Generally, the unit of PPFD is $\mu\mathrm{mol\,m^{-2}\,s^{-1}}$. The unit of $\mu\mathrm{E\,m^{-2}\,s^{-1}}$ is the same as the unit of $\mu\mathrm{mol\,m^{-2}\,s^{-1}}$. In the study of PAR, the photon is treated as both particle and wave. A mole of the photon is the photon particle of the amount equal to the Avogadro number, N_A= 6.02214179 x10^{23} photon particles. Photons of PAR are limited by the wave property of photons. The ideal for PAR measurement is for the photons that have a wavelength between 400 nm – 700 nm. PAR normally can be measured by a photodiode sensor which has a spectral response according to the definition of PAR.

The spectral response of PAR sensors is one of the important factors for the accuracy and precision of PAR measuring at the Earth's surface. The relative response for the amount of the photon density of the ideal PAR sensors is unity between 400 nm – 700 nm. The relative response before 400 nm and after 700 nm is zero for the ideal PAR sensor. The spectral response of relative photon density for the ideal PAR sensor is shown in the Figure 2.1.1.

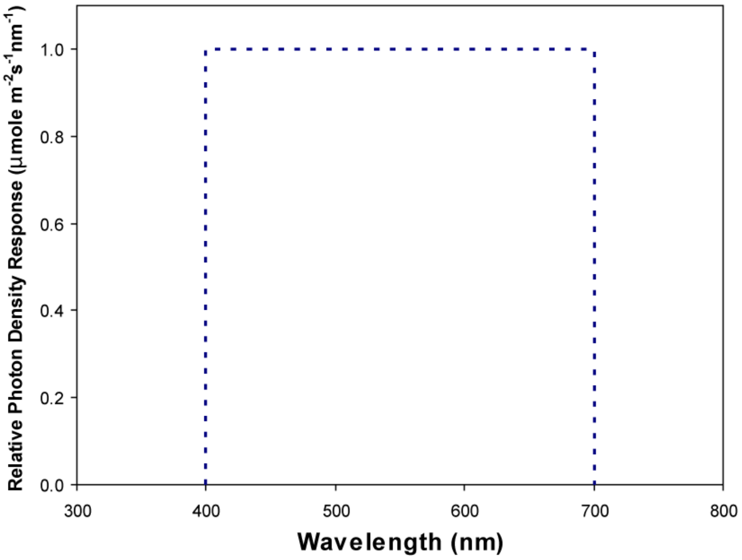

Figure 2.1.1 Relative photon flux density spectral response for the ideal PAR sensor

Due to the physical property of the photon, its energy can be calculated from its wave property. The energy of a photon can be calculated from the equation;

$$E = h\nu \qquad (2.1.1)$$

by $\nu = C/\lambda$,where h is Planck's constant ($6.626\,068\,96 \times 10^{-34}$ J·s), ν is Photon frequency [Hertz], C is Light velocity (299,792,458 m·s^{-1}), λ is Photon wavelength (m).

This means that the energy of a photon at wavelength 400 nm is higher than the energy of a photon at 700 nm. Therefore, the relative energy response of a PAR detector to a photon that has a shorter wavelength is lower than the of relative energy response to a photon that has a longer wavelength. This is because the ideal

PAR sensor has the spectrum relative photon density response at the same value for the whole band between 400 nm -700 nm. To measure the same amount of energy for each spectrum, the shorter one will receive the lower amount of photons, while the longer one will give the higher results for the output of the measuring. The spectrum relative energy response of the ideal PAR sensor is shown in Figure 2.1.2.

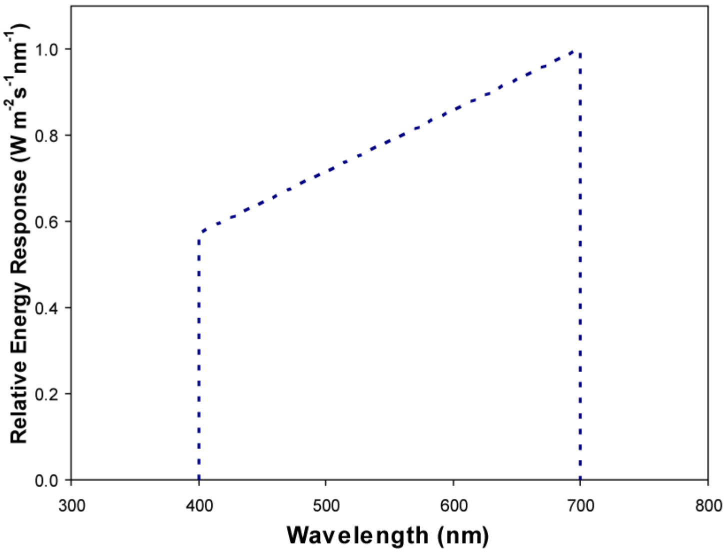

Figure 2.1.2 Relative energy spectral response for the ideal PAR sensor

Most of the PAR sensors that have been installed on the Earth's surface are made of semiconductor photodiode sensors which have a high sensitivity over the region 400 – 1100 nm. A diffusing material (e.g. milky quartz or Polytetrafluoroethylene) is used to achieve the cosine response correction of PAR sensors. Glass filters are used to block unwanted wavelengths (Figure 2.1.3). Relative energy spectral responses of typical photodiode PAR sensors are shown in Figure 2.1.4 (Biggs et al., 1971; Campbell Scientific (Canada) Crop., 2001; Delta-T Devices Ltd., 2002b; EKO, 2010; Kipp & Zonen, 2010; LI-COR Inc., 2010).

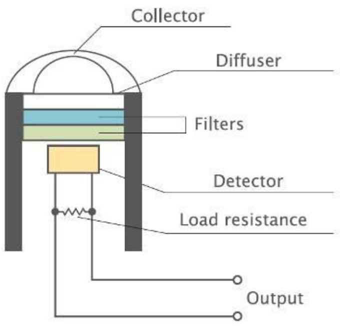

Figure 2.1.3 Schematic diagram of PAR sensor (EKO, 2010)

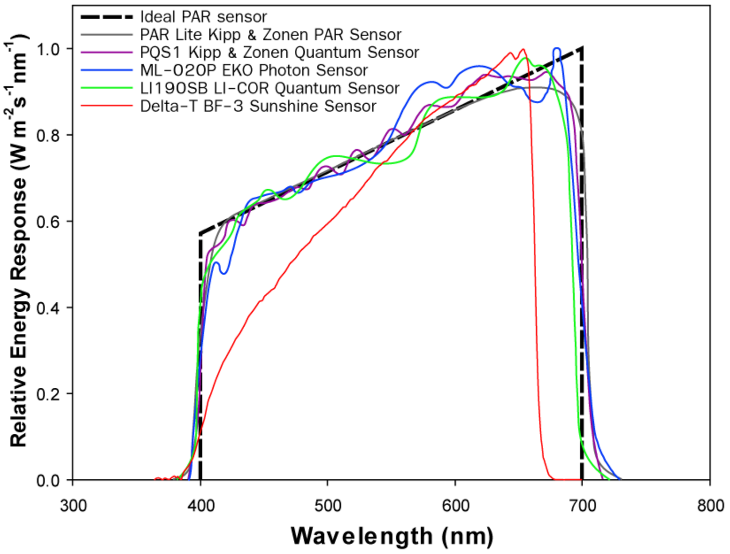

Figure 2.1.4 Spectral response of PAR sensor

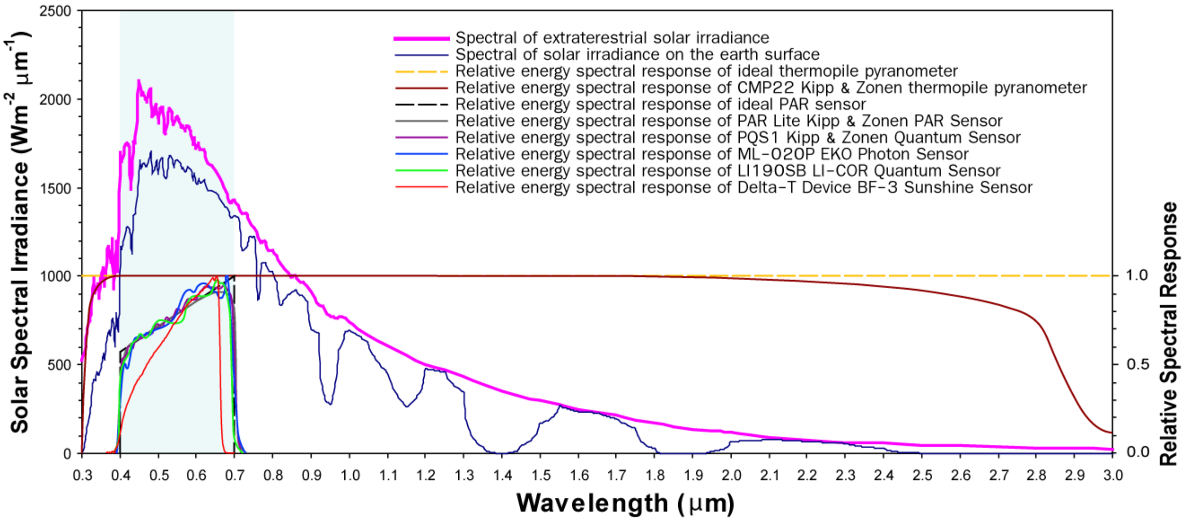

Figure 2.1.5 Spectral response of PAR sensor compared with that of a thermopile pyranometer

The sensitivity of the photodiode can easily decline, especially for all day measuring in an area of strong solar radiation. The effect of this is to make the estimation of PAR lower. Therefore, regular calibration is an important factor for the accuracy and precision of PAR measuring.

There is no world standard of PAR measurement. Normally, the calibration source is a bulb that has been certified by a national standards organisation (e.g. National Physical Laboratory in the UK). The spectral output of these bulbs is measured with a highly accurate spectroradiometer and the energy in the PAR spectrum determined. The bulbs are made by the companies such as Bentham Instruments Ltd., USA and Optronics Laboratories Inc., USA (Optronic Laboratories, 2009; Bentham, 2010). The LI190SB Licor Quantum sensor uses a certified bulb traceable to the National Institute of Standards and Technology (National Aeronautics and Space Administration) of the United States of America (USA) (LI-COR Inc., 2010). Kipp & Zonen PAR sensors use the reference PQS 1 PAR quantum sensor for the calibration. The reference PQS 1 has been calibrated against the standard 1000 W tungsten halogen standard lamp, supplied by Optronics Laboratories Inc. The standard lamp for the PQS 1 has been calibrated against a filter radiometer at the Metrology Research Institute of the Helsinki University of Technology (HUT) (Kipp & Zonen, 2010b).

2.1.2 Diffuse irradiation

Currently, there is no established direct way to measure both the intensity and angular distribution of diffuse flux, whether broadband or PAR, although instruments are being developed to achieve this (Choi and Milton, 2011; Dunagan et al., 2013). Steven and Unsworth (1980a) studied angular distribution of diffuse solar radiation using Actinometer under cloudy sky. In the absence of such an instrument in present day, diffuse flux can be estimated in three ways:

- From the difference between global flux measured with a pyranometer and direct flux measured with a pyrheliometer (e.g. Drummond, 1956; Batlles et al., 1995).

- By shading a pyranometer with a device to obscure the solar disc. In this case, the shade may be adjusted using an automated Sun tracker or a manually adjusted shade ring may be used with a correction factor (e.g. Blackwell, 1954; Drummond, 1956).

- From the clarity of the atmosphere, as estimated by a meteorological index or from a sky radiance model.

A number of indices of sky clarity have been developed over the last 50 years but for the purpose of this thesis the most useful is one of the most enduring and simplest formulations, first described by Liu and Jordan (1960). This states that the fraction of diffuse flux at the ground is related to $\mathrm{K_T}$, the ratio of the global flux measured at the ground with a horizontal sensor to that measured (or estimated) at a horizontal plane at the top of the atmosphere. Therefore, the diffuse fraction can be used to calculate the diffuse flux using the equation: $\mathrm{diffuse} = \mathrm{diffuse\ fraction} \times \mathrm{global}$. Some representative studies which have used this method to estimate diffuse broadband flux are shown in Table 2.1.1. No studies were found which have used $\mathrm{K_T}$ to estimate diffuse PAR (400 – 700 nm).

Table 2.1.1 Publication on diffuse fraction

Publication	Application	Location
Liu and Jordan (1960)	$S_d/S_t = K_{dS} = 0.2710 - 0.2939\,K_D$; $K_D = (S_t - S_d)/S_0$	United States of America and Canada
Orgill and Hollands (1977)	$S_d/S_t = K_{dS} = 1 - 0.249\,K_T$	Canada
Erbs et al. (1982)	$\frac{S_d}{S_t} = K_{dS} = f(K_T)$; depend on period of K_T	United States of America
Spitters et al. (1986)	$\frac{S_d}{S_t} = K_{dS} = f(K_T)$; derived from a sinusoid with a correction depending on solar angle	Netherland
Skartveit et al. (1998)	$\frac{S_d}{S_t} = K_{dS} = f(K_T)$; based on different sky conditions, solar elevation and group of K_T	Norway
Gonzalez and Calbo (1999)	$\frac{S_d}{S_t} = K_{dS} = f(K_T)$; groups of K_T	Spain
Roderick (1999)	$\frac{S_d}{S_t} = K_{dS} = A_0 + A_1 K_T$	Australia and Antarctica
Boland et al. (2001)	$\frac{S_d}{S_t} = K_{dS} = f(K_T)$; groups of K_T	Australia
Oliveira et al. (2002)	$\frac{S_d}{S_t} = K_{dS} = \sum_{n=0}^{N} A_n (K_T)^n$; 4th degree polynomial	Brazil
Jacovides et al. (2006)	$\frac{S_d}{S_t} = K_{dS} = f(K_T)$; Compared against 10 models.	Cyprus
Muneer (2006)	Effect of cloud cover and sunshine fraction on $K_{dS} - K_T$ relationship	India, Japan, Spain, UK
Jacovides et al. (2007)	$\frac{Q_d}{Q_t} = K_{dQ} = f(K_{TQ})$; 3rd degree polynomial	Greece
Boland et al. (2008)	$\frac{S_d}{S_t} = K_{dS} = \frac{1}{1 + e^{-5.00 + 8.60 K_T}}$	Australia
Jacovides et al. (2010)	$\frac{Q_d}{Q_t} = K_{dQ} = f(K_{TQ})$; empirical model	Greece
Ridley et al. (2010)	$\frac{S_d}{S_t} = K_{dS} = f(K_T)$; multiple predictor model	Australia, Belgium, China, Mozambique, Portugal, UK

2.2 Measurement of solar irradiation at the Earth's surface from a satellite sensor

The only practical way to measure incident solar flux over the whole globe is to use data from satellites. A sensor on three of geostationary satellites or one in low Earth orbit can provide measurements of reflected radiance from all parts of the globe, and can also detect cloud cover which is the main factor affecting the receipt of solar radiation at the ground.

Early attempts to measure incident solar energy from space proved the concept, but the lack of calibration meant that the data were not very accurate (e.g. Fritz et al., 1964). However, by the 1970s, satellite sensors had improved and much better results were reported by Van der Haar and Ellis (1975) and Hanson (1976). In 1977 the US National Environmental Satellite Service (NESS) and the Great Plains Agricultural Council (GPC) organised a large experiment as part of the AgRISTARS programme to test whether incident solar flux could be measured from satellite data for agricultural applications. This experiment led to an important publication by Tarpley (1979) in which he showed that daily insolation could be estimated to within 10% of the mean, which was sufficiently accurate for agricultural applications.

Data from the NESS/GPC experiment have been used by other authors to improve the basic method, for example, Justus et al (1986) introduced a cloud modifier and showed how mean monthly insolation could be estimated to better than 5% of the mean.

Many of the early methods were empirical and could not be easily extended to other areas. An important step forward came with the development of physically-based approaches, which at least in principle could be applied in other areas. Gautier et al (1980) describes one of the earliest physically-based methods, and this model was extended in later papers to include absorption due to ozone (Diak and Gautier, 1983) and the effect of aerosols (Gautier and Frouin, 1984).

Many of these important papers from the 1970s and 1980s were reviewed by Hay (1993), who categorised them into four broad approaches (Table 2.2.1). Raphael and Hay (1984) provided a further insight into the strengths and weaknesses of the empirical and physically-based approaches, by comparing the results from three models: the Hay and Hanson model, the Tarpley model and the Gautier model.

Table 2.2.1 Classification of satellite approaches for solar irradiance estimation (Hay 1993)

Empirical		Theoretical	
Statistical	Physically-based	Broadband	Spectral
Hanson (1976) Nimira (1980) Shaltout and Hassen (1990)	Hanson (1971) Tarpley (1979) Hay and Hanson (1978) Sorapipatana and Exell (1988)	Gautier et al. (1980) Nimira (1980)	Halpern (1984) Justus (1984)

2.2.1 Estimation of global PAR at the Earth's surface from space

Near the end of the 1980s, a decade after the beginning of using satellite data for estimation of incoming solar flux, studies began to involve PAR estimation (e.g. Gueymard, 1989; Pinker and Laszlo, 1992). Gueymard (1989) suggested the idea of using satellite data and known atmospheric data for estimating PAR under clear sky conditions on an hourly and daily basis without simultaneous ground measurements. After Gueymard (1989), the estimation of PAR using data from satellite sensors has been widely applied in many areas and countries.

Frouin and Pinker (1995) reviewed the status of PAR estimation from space, and highlighted the benefits gained from allied research on satellite-based estimates of broadband irradiance. They noted that while the accuracies achieved for daily (10%) and monthly (6%) estimates of PAR were acceptable, there remained a problem with estimating PAR over shorter timescales, mainly due to variable cloud cover.

2.2.2 Estimates based on relationships between spectral bands

There are relationships between PAR and solar radiation in other spectral regions. For example, the relationship between PAR and broadband described in Section 5.4.1 Chapter 5. The relationships were used to convert the existing measured solar irradiance maps from other bands to PAR in the early days of using satellite data to estimate PAR (e.g. Frouin and Gautier, 1990; Eck and Dye, 1991). Frouin and Gautier was also based on Gautier's model, not just relationship between bands. Frouin and Gautier (1990) showed that large-scale broadband irradiance from satellite sensors can be converted to PAR with a standard error or around 6.5%. Eck and Dye (1991) developed a method to use UV reflectance from remote sensing to estimate PAR over ocean and land surfaces, which has the advantage that the contrast between clouds and bright land surfaces is much greater in the UV region than the visible.

2.2.3 Estimates based on radiative transfer models

Radiative transfer models can be used to estimate the transmittance of PAR through the atmosphere (e.g. Pinker and Laszlo, 1992; Zheng et al., 2008; Nasahara, 2009; Janjai and Wattan, 2011). It is one of the most suitable methods for estimation of the transmitted PAR, especially when applied to satellite data. Using radiative transfer, the data from satellites can be used to estimate the density of the atmospheric components. Then, their components from satellite estimation can be used to estimate the transmittance of PAR. Finally, the transmittance is used to calculate the quantity of PAR that can transmit the atmosphere to the ground.

Chen et al. (2008) described the use of a simple radiative transfer model to estimate PAR over 54 days cloud-free conditions at a station in China. The model they used was SPCTRAL2 (Bird, 1984; Bird and Riordan, 1986), a simplified radiative transfer model designed for solar energy applications.

Van Laake and Sanches-Azofeifa (2004, 2005) developed a more elaborate model called PARcalc to estimate PAR from MODIS data. In PARcalc, the atmospheric components are modelled in a few layers based on the transmittance of the atmosphere due to the clouds and aerosol load.

Van Laake and Sanchez-Azofeifa (2004) demonstrated a method to estimate instantaneous PAR using MODIS data. Their method simplified the general radiative transfer equation. The atmospheric transmittance was calculated using the equations in Iqbal (1983). The transmittance of the broadband irradiance was calculated by considering Rayleigh scattering, ozone absorption, water vapour absorption, and aerosol absorption. The broadband irradiance was estimated on the surface first, then converted to PAR on ground using conversion of radiant power ($\mathrm{W\,m^{-2}}$) to photon flux density ($\mathrm{\mu mol\,m^{-2}\,s^{-1}}$).

Van Laake and Sanchez-Azofeifa (2005) demonstrated a method to map daily integrated PAR ($\mathrm{mol\,m^{-2}\,day^{-1}}$) using MODIS data. Van Laake and Sanchez-Azofeifa (2005) applied the PARcalc model to daily pairs of MODIS Terra and Aqua images to produce a daily integrated map. However, the 8-day sampling window of MODIS meant that this was not a true daily map.

2.2.4 Estimates based on a physical model and neural net

Schiller (2006) used two different models, a physical model and a neural net for the estimation of PAR from Meteosat data in the German bight.

The physical model used in Schiller (2006) estimated the broadband solar irradiance on the surface using the clear sky index (k_t^*) for characterizing the atmospheric transmittance. The clear sky index for the physical model in Schiller (2006) was calculated from: $k_t^* = E_{gl}/E_{gl}^{cl}$, where the E_{gl} is the global irradiance and the E_{gl}^{cl} is the global irradiance under clear sky conditions. The global PAR was then calculated from the global irradiance using a constant conversion.

The neural net used by Schiller (2006) was composed of layers: input layer, hidden layer and output layer. Each layer had equations with weights of links between layers. The neural net was trained by feeding sampled inputs to layers, then tested by adjusting the weights of links. The results showed that the neural net was better than a physical model.

2.2.5 Estimates based on a look-up table

Although the methods to estimate global PAR based on radiative transfer models met with much success, a simpler method would have considerable advantages for generating routine PAR products in an operational environment. Several approaches have been investigated to achieve this, and reduce the requirement for simultaneous ground data.

A look-up table (LUT) approach was first applied to the problem of PAR estimation from MODIS data by Liang et al. (2006). Later on, there were several studies which applied the LUT method for estimating PAR over other areas (e.g. Liu et al., 2008; Wang et al., 2010).

Liang et al. (2006) avoids complexity by using LUT approach, as is widely used in various scientific investigations. The LUT was created based on the reflected irradiance at the TOA toward the sensor by assuming that the Earth’s atmosphere is Lambertian. Instead of calculating parameters using complicated equations, the parameters were tabulated for every pixel for each Sun-viewing angle. The Sun-viewing angle was computed for only nine zenith angles, five viewing angle and seven relative azimuth angles (Liang et al., 2006, p. 4). This use of a LUT greatly simplified the radiation environment, and the complexity of the calculations needed. A limitation of this method is that an enormous amount of data is required to fill in the LUT, however, advances in computing power are addressing this issue.

In term of mapping, the daily mapping using MODIS data and the idea proposed by Liang et al. (2006) in Liu et al. (2008) is based on the assumption of ‘atmospheric conditions remaining unchanged for half day period’ (Liu et al., 2008, p. 1008), which is hardly ever going to be true, especially in areas like the UK. However, the LUT method proposed by Liang et al. (2006) has been used to map instantaneous PAR over Washington, D.C. in USA, and has been later applied to map the instantaneous PAR, and daily integrated PAR over China using MODIS data in Liu et al. (2008).

2.3 Measurement of diffuse irradiation at the Earth’s surface from a satellite sensor

To map the diffuse flux over a wide area using traditional measurements without satellite data, the only method is to use ground measurement sites and use interpolation, extrapolation and contouring techniques (e.g. Lavagnini and Jibril, 1991). This provides a generalised map but is unsuitable for high spatial resolution applications such as plant productivity mapping. There are many reports of diffuse flux measurements using the traditional method, without using satellite data.

However, there are very few publications using satellite data to estimate diffuse flux before the 1990s.

The first diffuse flux model for measurement of the diffuse flux using satellite data was developed from a model for calculating global flux. The Institut für Geophysik Meteorogie Universität zu Köln (IGMK; Möser and Raschke, 1983) is the first global flux model that has been applied for the estimation of diffuse flux. From the complicated IGMK model, Stuhlmann et al. (1990) increased the multiple reflection parts of the irradiance in the atmosphere which can be used to estimate the diffuse flux. The satellite data was indirectly used to estimate the diffuse flux in Stuhlmann et al. (1990). The satellite data was used to estimate the cloud transmittance, and then to estimate the atmospheric transmittance. After this, the atmospheric transmittance was used to estimate the diffuse proportion before it could be used to calculate the diffuse flux.

Most diffuse flux estimation using satellite data in the past was based on ISCCP data, the same as that used by Stuhlmann et al. (1990). However, the ISCCP data set has not been available since June 2008. In the present day, the estimation of diffuse flux using higher temporal resolution and spatial resolution needs to be implemented using other alternative satellites.

The difficulty of using satellite data to estimate the diffuse flux is the accuracy of the models, especially at higher latitudes. The highest accuracy on the hourly basis of diffuse flux estimation from satellite data up to now is $R^2 \sim 0.7$ (e.g. Prathumsit and Janjai, 2012). Examples of some publications on diffuse flux using satellite data are in the Table 2.1.1.

Table 2.3.1 Publications of diffuse flux estimation from satellite data

Publications	Model	Flux wavelength bands	Satellites data	Areas of study	Resolution (temporal; spatial)
Stuhlmann et al. (1990)	IGMG	Broadband (0.2-4.0 μm)	ISCCP B2 (Meteosat 2)	Europe and Africa	Annual, contour of 30-50 km pixel size
Pinker and Laszlo (1992)	Radiative transfer	Broadband (0.2-4.0 μm)	ISCCP C1	Global map	Monthly, contour of 250 km pixel size
Martins et al. (2008)	Radiative transfer (BRAZIL-SR)	Broadband (0.0-4.0 μm)	GOES	Brazil	Annual, 10 km pixel size
Butt et al. (2010)	Diffuse fraction	Broadband (~0.3-3.0 μm)	ISCCP-DX	Amazonia	3-hourly; 2 sites of 30-50 km pixel size
Prathumsit and Janjai (2012)	Diffuse fraction	Illuminance	MTSAT-1R	Thailand	hourly; 4 sites testing of 2.5 km pixel size

As the table above demonstrates, Prathumsit and Janjai (2012) did the highest resolution, in both temporal and spatial resolution for the diffuse flux of the Illuminance. However, Illuminance irradiance is not the same as PAR. Even though, the Illuminance has the same wavelength band with PAR, the spectral response of the Illuminance is totally different. The concept of the Illuminance is the irradiance sensed by the human eyes. It has a peak of the spectral response at 550 nm, but the response at the 400 nm and 700 nm are zero. The PAR has the peak of the spectral response at 700 and the lowest spectral response at 400 nm. The method described by Prathumsit and Janjai (2012) used the diffuse fraction and the data from a geostationary satellite. The sensors used for the modelling and validation on the surface were Illuminance sensors (Prathumsit and Janjai, 2012).

Knowledge of the diffuse fraction is advantageous for the estimation of diffuse irradiance, using satellite data. The diffuse fraction is defined as the fraction between the diffuse irradiance per unit global irradiance. However, the diffuse fraction for each wavelength band is different. The diffuse fraction for the calculation of the diffuse PAR, in this instance is the diffuse PAR fraction ($\mathrm{K_{dQ}}$).

The diffuse fraction of solar irradiance on the Earth's surface varies according to the atmospheric composition such as aerosols, cloud etc. (e.g. Gu et al., 2002; Alton et al., 2005), therefore it should be possible to determine $\mathrm{K_{dQ}}$ remotely, from space. No publications using satellite data to establish the relationship between atmospheric properties and $\mathrm{K_{dQ}}$ were found, however, there are some studies estimating diffuse irradiance in other wavelength bands (e.g. Stuhlmann et al., 1990), more detail is available in the Table 2.3.1 (Pinker and Laszlo, 1992; Martins et al., 2008; Butt et al., 2010; Prathumsit and Janjai, 2012). The most recent work is that of Butt et al. (2010) who demonstrated the estimation of the diffuse fraction of broadband solar irradiance from the ISCCP data. Also, Prathumsit and Janjai (2012) tested the method of predicting diffuse illuminance using geostationary satellite data.

2.3.1 Zenith angle effects

This not only influences the incoming horizontal solar flux from the Sun to the top of the Earth's atmosphere, it also has an influence on the PAR that reaches the Earth's surface (e.g. Iqbal, 1983; Liou, 2002). Even though the zenith angle can be calculated using equations, the difficulties are the light interactions as the function of the zenith angle in the Earth's atmosphere.

2.3.2 Multiple scattering effects

One of the greatest difficulties of using models composed of satellite data for evaluating the PAR on the Earth's surface is the complication of the multiple scattering. The multiple scattering or multiple reflections, in this place, is the light interaction in the atmosphere that is reflecting many times between the atmospheric components (e.g. Iqbal, 1983; Liou, 2002). It is considered to be one of the causes of the diffuse irradiance, atmospheric absorption and atmospheric light attenuation. However, there are many studies that do not consider the multiple scattering, but can predict the solar irradiance correctly (e.g. Möser and Rachke, 1984).

2.4 Errors in the ground validation data

PAR measurements with a ground-based sensor are subject to errors from various sources. The most influence of the Sun's elevation on the accuracy of measuring PAR is in the few hours after sunrise and the few hours before sunset, as the Sun's elevation is low in both situations. It is the problem regarding the imperfect cosine response of the PAR sensors, which makes it difficult to use them for accurate ground reference during those hours (e.g. Iqbal, 1983; Wood et al., 2003; Grifoni et al., 2008, p. 359).

2.4.1 The satellite wavelength band

The spectral band of the reflected irradiance that satellite sensors can detect is not the same as the PAR spectral band. This is because most satellite sensors were not specifically made to monitor PAR. Therefore, PAR estimation using satellite data must also be manipulated to match with the PAR wavelength band. The estimation of PAR, using satellite data, uses the advantage of the overlap between the satellite band and the PAR band to predict PAR (e.g. Liang et al., 2006; Liu et al., 2008; Zheng et al., 2008; Wang et al., 2010; Janjai and Wattan, 2011).

2.4.2 The difference between the time scale of the satellite data and the needed data on the surface

Satellite data is instantaneous at a specific time, but the data needed for application is specific, for example every hour. The eight-day PAR product from MODIS (Liang et al., 2006) is not enough to study GPP in detail. In reality, the actual GPP varies every hour because PAR varies every hour. The eight-day MODIS product cannot give any information on an hourly basis. Therefore, to study and map the vegetation productivity on an hourly basis, hourly PAR mapping is essential.

2.4.3 Acceptable accuracy

It is very difficult to accurately model PAR using satellite data. Over a monthly time scale, accuracies better than 10% are feasible (Frouin and Pinker, 1995). The accuracies for the hourly time scales are lower than the accuracies in the monthly scale, therefore, it is likely that the hourly accuracy is lower than 10%.

2.4.4 There is no world organisation or international organisation that controls the PAR measurements, on the Earth's surface

The absence of such an organisation makes it difficult to make a judgment on the accuracy of PAR measurement on the ground. There are many different materials used to make PAR sensors, which alter the spectral response. Also, there are different units used in PAR measurement, and it is very difficult to convert correctly. Many studies use the conversion between the units of the sensors based on the assumption that it would be correct. Therefore, it would be better to have an international organisation to judge or make agreements on the material for PAR sensors and on the conversion between the units.

2.4.5 Validation sites

To validate PAR estimation using satellite data, the measured PAR data on the surface is needed. However, there are not many sites of PAR sensors to validate the methods using satellite data. Although, PAR on the surface can be converted from the measured data of the solar irradiance on the other bands, there are errors among the conversions.

2.4.6 Use of solar radiation data in vegetation productivity models

So far, this literature review has considered the development of ground-based and space-based methods to measure global and diffuse solar radiation at the Earth's surface. This is useful information in its own right, but such measurements are also important input data for use in a wide range of scientific applications, from the design of buildings to plant science and agriculture.

Plant productivity has a strong relationship with global PAR, however, the relationship between plant productivity and diffuse PAR is not clear. Modelling is needed to study the relationships between global PAR, diffuse PAR and plant productivity. Many vegetation productivity models have been published since the beginning of the 1970s, and the most important of these are listed in Table 2.6.1

(p39). One of the main issues which emerges from a study of these models is that there is no clear agreement on the rules of productivity modelling. For example, regarding solar radiation, there are many wavelengths and bands, units, equipment and physical properties. This is still a subject developing rapidly, and standardisation of methods and approaches has not been achieved.

Variability of the atmospheric parameters is one of the difficulties for PAR prediction using these models. Also, the validation methods are different. Furthermore, scientists have not yet made any agreement to standardise calibration. So far most validation for GPP/NPP estimated remotely is by comparing it with eddy covariance data from FLUXNET stations.

2.5 Specific plant productivity models

Most vegetation productivity models have solar irradiance as an input parameter, but very few take diffuse irradiance into account. The solar irradiance that has been used as an input of the model is mostly in the PAR wavelength band. Some models, in the early stages of the development of vegetation productivity modelling, did not include parameters of the solar irradiance.

The models listed in Table 2.6.1 represent the development of the subject over 40 years, since the 1970s. It remains unclear how diffuse PAR physically influences vegetation productivity, however, there is a clear trend over time for the models to include more information about the radiation environment, and diffuse flux is one parameter that has become more commonly incorporated into plant productivity models. One question needing to be asked, therefore, is whether the diffuse irradiance (or diffuse fraction) can be expected to have any influence on vegetation productivity. However, it is important to note that even if diffuse flux has no effect on productivity, its omission from a model will mean that the model cannot explain the physical light trajectory, which is a weakness.

The following models incorporate solar radiation as an input variable:

- **BIOME-BGC**:

BIOME-BGC includes both global irradiance and global PAR parameters. However, the wavelength band of global broadband (~ 300 - 3000 nm) overlaps with the PAR irradiance (400-700 nm) and the model fails to focus separately on the solar irradiance in individual bands.

- **CASA**:

The Carnegie-Ames-Stanford approach (CASA) uses both global broadband and global PAR but does not include the diffuse parameter of the solar irradiance (Potter et al., 1993). The focus of the CASA model is on the many possible ecosystem parameters affecting vegetation productivity.

- **GLO-PEM**:

The GLObal Production Efficiency Model (GLO-PEM) includes solar irradiance as one of its parameters (Prince and Goward, 1995). The estimated PAR from satellite data is used as an input of the model. However, PAR varies significantly over a monthly period, therefore, Prince and Goward (1995) interpolated the monthly PAR to a 10-day time period PAR for the model. However, the model still failed to interpret the significant variation of PAR on a diurnal and hourly basis.

- **TEM**:

The Terrestrial Ecosystem Model (TEM version 4.0) takes into account global PAR in the model, but not diffuse PAR or the directional properties of light (McGuire et al., 1995). The input data for TEM are vegetation type, soil texture, elevation, PAR, precipitation and air temperature. McGuire et al. (1995) examined the influence of soil organic carbon (SOC) on the atmosphere carbon cycle using TEM 4.0, and this is the type of application that this model is best suited to.

- **TURC**:

The Terrestrial Uptake and Release of Carbon (TURC) model focuses on plant respiration (Ruimy et al., 1996). The TURC considers the solar irradiance in the PAR wavelength band as an input parameter. However, the global PAR data used in the model is the derived PAR from the global broadband using a conversion factor of 0.48. The global broadband data used in TURC by Ruimy et al. (1996) were taken from ISCCP data. However, they did not take into account the variation of the conversion factor, which varies with location and time.

- **BIOME3**:

BIOME3 has global PAR as a solar irradiance parameter in the model (Haxeltine and Prentice, 1996). The global PAR used in the BIOME3 was calculated from the global broadband irradiance, using a correction factor 0.5 (Haxeltine and Prentice, 1996). However, this conversion factor is different from the conversion factor in other models, for example 0.48 in the TURC model (Ruimy et al., 1996). The global broadband in Haxeltine and Prentice (1996) for the BIOME3 model was derived from the daily sunshine hour. The main weakness of the solar irradiance in this model is the calculation of the solar irradiance from the sunshine hour. In practice the sunshine hour is based on those hours in the day when the global broadband is stronger than 120 Wm^{-2}. The conversion using this method fails to interpret the actual value of the solar irradiance which can vary more than 1000 Wm^{-2}.

- **MOD17**:

MODIS vegetation production and net primary production (MOD17) considers the global PAR to be an input parameter (Parkinson and Greenstone, 2000). However, from the perspective of the atmospheric sciences, this model fails to explain the significant temporal variation of the solar irradiance. In practice, the variation of the solar irradiance can change significantly in an hour, but the temporal variation of MOD17 is eight days.

- **C-Fix**:

The C-Fix is the model for carbon fixation estimation (Veroustraete et al., 2002). This model represents solar irradiance in terms of the global broadband irradiance. The model uses satellite derived fAPAR from the relationship fAPAR/NDVI. However, this model as described by Veroustraete et al. (2002) did not indicate how to convert the broadband global irradiance into global PAR. Furthermore, the C-Fix fails to take into account the effects of the diffuse PAR.

- **LPJ-DGVM:**

The Lund-Potsdam-Jena Dynamic Global Vegetation Model (LPJ-DGVM) has a parameter to deal with the global PAR (Sitch et al., 2003). The model uses global PAR and the fraction of the PAR intercepted to deal with the incident light on vegetation leaves. However, the model has no dimension (0D), and fails to interpret the physical properties of light in 3D. This model is a global model, but tends to focus on other ecosystem parameters rather than solar irradiance.

- **FLIGHT:**

FLIGHT is a model specifically designed for forest canopies, and takes into account three parameters to account for solar irradiance: (i) global PAR, (ii) diffuse PAR and (iii) global IR. This model is a 3D model, while the other models described above are dimensionless (0D). FLIGHT represents the physical light trajectories in the forest, rather than using only statistical relationships, but also includes many parameters represented in the ecosystem.

Another distinction of FLIGHT is that it has an option to deal with diffuse PAR. The diffuse PAR in the model can be inputted in terms of the diffuse fraction of PAR. Also it has an option to run the model in the direct-only mode rather than the direct-and-diffuse mode. The direct-only mode considers that all the PAR is in the direct beam. The direct-and-diffuse mode considers the real physical properties of incoming global PAR, which are composed of direct PAR and diffuse PAR. Therefore, this model also has advantages when studying the variation and the relationships between the productivity and the global PAR and diffuse PAR.

In FLIGHT both the temporal and spatial resolution of the model are dependent on the input data. The global PAR, diffuse PAR and other ecosystem parameters have significant variations on an hourly basis. This model has an advantage when studying the pattern and trend of the vegetation productivity. Therefore, this model was selected for studying the pattern and trend due to the variation of the global and the diffuse of PAR, which is the focus of this thesis.

The FLIGHT model was developed by UK researchers (North, 1996; Barton and North, 2001; Alton et al., 2005), but none of their work was done in the UK. At first, FLIGHT was developed and validated in a dense spruce forest in Howland, ME in the

USA (North, 1996). The effects of the direct and diffuse irradiance were developed and validated in a Siberian scots pine forest in Russia, temperate forest in New England, USA and a tropical forest in Amazonia, Brazil (Alton et al., 2005; Alton and North, 2007). This, therefore, needs to be borne in mind when applying the model to vegetation productivity in the UK environment.

2.6 Concluding comments on plant productivity models

Given this abundance of models and lack of standards and protocols, the choice was made to focus on one model that was sufficiently flexible to allow investigation of all the parameters of interest.

The complexity of the real world has meant that most models have simplified either the radiation environment or the physical properties of the vegetation canopy, or both. Models intended to be applied across a range of ecosystems have had to retain many plant parameters, and so have tended to simplify the radiation environment. Others, like FLIGHT, have been developed specifically for one vegetation type (forest) so have been able to keep more detail about the radiation environment.

From table 2.6.1 and the discussion above it is clear that FLIGHT is the most appropriate model in terms of the resolution and the solar irradiance variables. Most of the models have a maximum resolution of 1km and 1 hour, but the resolutions of the FLIGHT depend on the input data. It can give even an instantaneous output if the user can give the instantaneous data. It also can give the output at a specific location.

The solar irradiance parameter input for the FLIGHT model was included in the global PAR and the diffuse fraction of PAR. It is also included in the IR (e.g. Alton et al., 2005; Alton and North, 2007), which is also believed to influence the vegetation productivity.

Table 2.6.1Vegetation productivity models and their solar irradiance handling

Year	Models	Reference	Dimension of light in the model	Resolution		Solar irradiance			
				Spatial (pixel wide)	Temporal	Global broadband	Global PAR	Diffuse PAR	Global IR
1971	Miami	(Lieth, 1975)	0D	~100 km	Yearly	-	-	-	-
1972	Montreal	(Lieth, 1975)	0D	~100 km	Yearly	-	-	-	-
1993	Century	(Parton et al., 1993)	0D	-	Monthly	-	-	-	-
1993	BIOME-BGC	(Running and Hunt, 1993)	0D	1° grid (~112 km)	Daily	Yes	Yes	-	-
1993	CASA	(Potter et al., 1993)	0D	1° grid (~112 km)	Monthly	Yes	Yes	-	-
1994	HRBM	(Esser et al., 1994)	0D	0.5° grid (~56 km)	Monthly	-	-	-	-
1995	GLO-PEM	(Prince and Goward, 1995)	0D	8 km	10 days	-	Yes	-	-
1995	TEM	(McGuire et al., 1995)	0D	0.5° grid (~56 km)	Monthly	-	Yes	-	-
1996	TURC	(Ruimy et al., 1996)	0D	1° grid (~112 km)	Monthly	-	Yes	-	-
1996	BIOME3	(Haxeltine and Prentice, 1996)	0D	0.5° grid (~56 km)	Monthly	-	Yes	-	-
1996	FLIGHT	(North, 1996; Barton and North, 2001; Alton et al., 2005; Alton and North, 2007)	3D	Depend on input data (up to a specific point)	Depend on input data (up to instantaneous)	-	Yes	Yes	Yes
2000	MOD17	(Parkinson and Greenstone, 2000)	0D	1km	8 day	-	Yes	-	-
2002	C-Fix	(Veroustraete et al., 2002)	0D	1km	Daily	Yes	-	-	-
2003	LPJ-DGVM	(Sitch et al., 2003)	0D	0.5° grid (~56 km)	Daily	-	Yes	-	-

2.7 Gaps in current research

There has been much research about PAR and vegetation productivity over the past few decades, beginning with the seminal work by McCree (1972a). Methods to measure PAR have gradually improved and more recently, methods based on data from satellite sensors have been developed, so that we now have the systems in place to map and monitor PAR (and by implication, plant productivity), over the whole globe at variable spatial and temporal resolution. However, there are still important gaps in our knowledge and uncertainties in the system, so the research in this thesis was designed to address some of these. Examples of the research questions that need answering include:

- What is the best way to monitor PAR over large areas at high temporal resolution (hourly)?
- What are the trade-offs in spatial and temporal resolution between Sun-synchronous and geostationary satellite sensors for monitoring PAR at global scale?
- In many ways, the MODIS sensor on board the NASA Terra/Aqua satellite represents the state-of-the-art in terrestrial remote sensing of vegetation, but how appropriate is the MODIS system in estimating PAR?
- How can we validate measurements of PAR from space?
- Is it possible to produce a system for monitoring and mapping PAR from space that is both scientifically rigorous but also simple enough to be used operationally?

The aim of the research described in this thesis is to investigate the spatial and temporal variability of PAR over the UK, in particular, to estimate both global PAR and the fraction of diffuse PAR at spatial and temporal scales appropriate for incorporation in a plant productivity model (FLIGHT).

The research described in subsequent chapters is an example of the 'image chain approach' proposed by Schott (1997), expressed here as the ‘PAR chain’. This envisages the Earth observation process as a series of links in a chain, with the idea that the overall process is only as strong as the weakest link. The corollary of this is that effort expended to increase the sophistication or accuracy of a single link may be wasted. What matters is that the overall chain is 'fit for purpose'. The big question addressed in this thesis is, "Is the current system for mapping and monitoring plant productivity from space, based on PAR, fit for purpose?"

With the 'PAR chain' analogy in mind, the specific objectives of this research are:

- To investigate a novel sunshine sensor, the Delta-T Devices BF3, to test whether this simple low-cost instrument would be an adequate substitute for the instruments normally used to measure the components of PAR at the ground. Such instruments provide essential validation data for satellite measurements, so they are a key link in the PAR chain. [Chapter 3]
- To test whether a sky clarity index could be used to estimate the proportion of diffuse PAR. Such indices have been used to estimate the proportion of diffuse broadband flux, but is not known whether a similar relationship exists for the PAR band. Use of such an index is the first link in converting satellite data to useful information. [Chapter 4]
- To estimate the fraction of diffuse PAR (K_{dQ}) over the whole of the UK. This parameter is important because K_{dQ} is thought to influence vegetation productivity, but it is not routinely measured anywhere in the world. Even in the UK, which has a well-established network of meteorological sites, there are no publically available data on diffuse PAR. [Chapter 4]
- To estimate the amount of global PAR (Q_t) over the whole of the UK. The amount of PAR varies greatly over time and space, and its role in plant growth is fundamental. As with diffuse PAR, this parameter is rarely measured, for example there are only two sites in the UK. [Chapter 5]
- To investigate the effect on gross primary productivity of spatio-temporal variations in the fraction of diffuse PAR (K_{dQ}) and the amount of global PAR (Q_t) using an established plant productivity model applied to data from two well-

instrumented sites in the southern UK. This final step is important as it is the final link in the PAR chain, which begins with satellite sensor measurements of spectral radiance, which are then passed through linked empirical and physical models, before being provided to the user as a validated product (GPP).

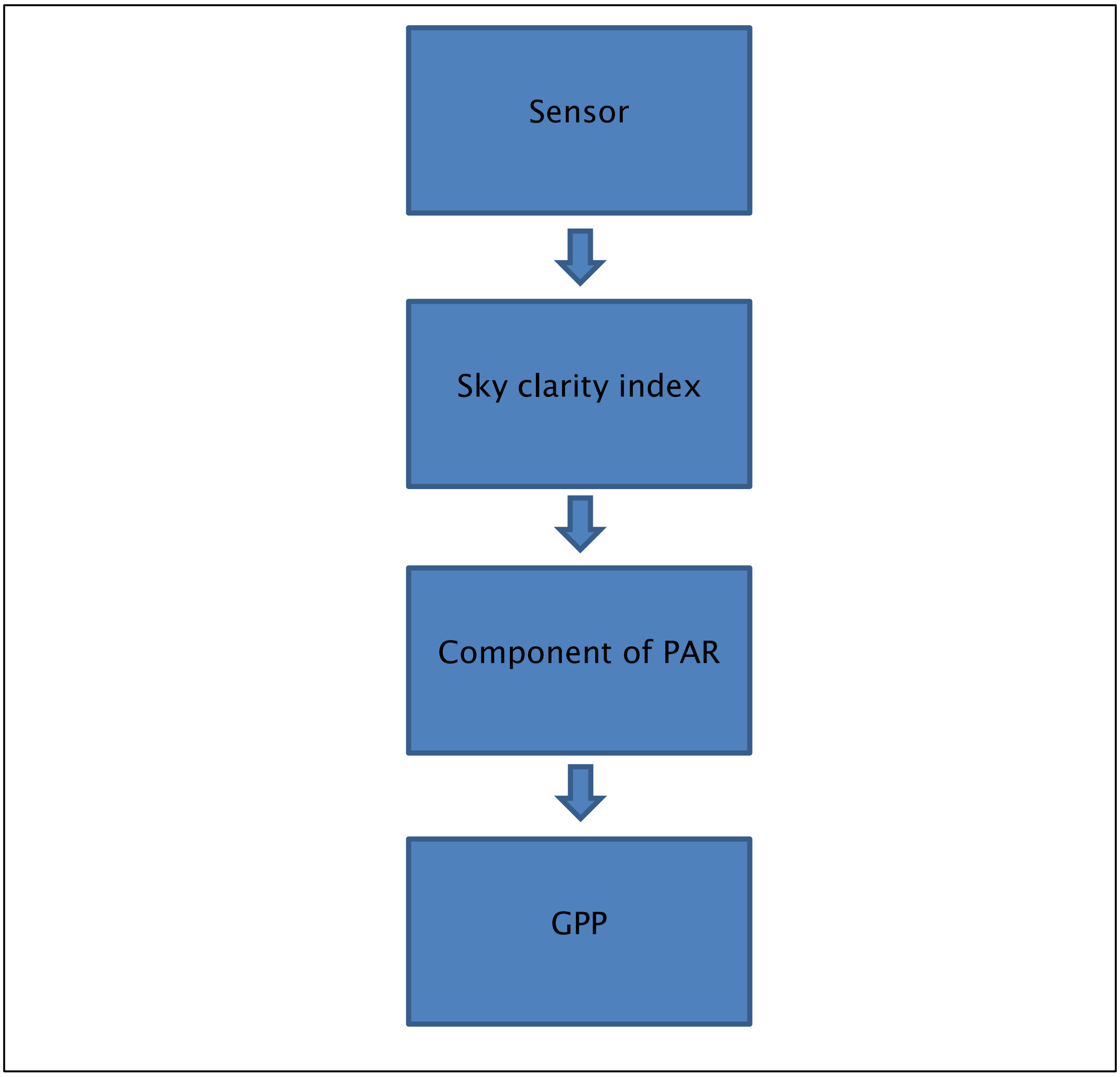

Figure 2.7.1 A simple block diagram of the 'PAR chain'

Chapter 3 Test sites and Instruments

3.1 Introduction

The previous chapter reviewed the literature on the measurement of PAR and its estimation using data from satellite sensors, and showed the importance of studying the separate components of PAR (i.e. direct vs diffuse), as well as the total amount. This chapter describes the test sites and instruments used to address the aims outlined at the end of Chapter 2.

Most of the data used in the study were collected using high quality meteorological instruments following well-established protocols, the exception being measurement of the proportion of direct-to-diffuse flux, and for that a relatively untested instrument was used: the BF3 Sunshine Sensor from Delta-T Devices, Cambridge, UK. Although this instrument has been available for several years, proper validation of its performance over a range of environmental conditions is not available. It was therefore necessary to perform some tests on the BF3 as a preliminary part of this research (Section 3.4).

The sites described in this chapter include those used for the instrument tests and those used in the main phase of the research, which involved the development of an improved method to estimate PAR using data from satellite sensors. For this two established sites in the UK were used: Wytham Woods in Oxfordshire and Alice Holt forest in Hampshire.

3.2 Instrument Test Sites

3.2.1 Chilbolton Facility for Atmospheric and Radio Research (CFARR), Hampshire, UK

The CFARR is approximately 25 km north of Southampton, on a former airfield near the village of Chilbolton. The site is operated by the Science and Technology Facilities Council (STFC), one of the UK research councils. It has wide range of high quality meteorological instruments, and CFARR staff support research across the meteorological and atmospheric sciences (www2). Although many meteorological measurements are made routinely at the CFARR, the proportion of direct-to-diffuse irradiation was not being measured when this research started, so it was necessary to install the BF3 Sunshine Sensor on site, close to the existing instruments. The instruments for this research were installed on the roof of the main building at CFARR, adjacent to a Cimel sunphotometer used in the AERONET network (www3), and with a clear view of the sky.

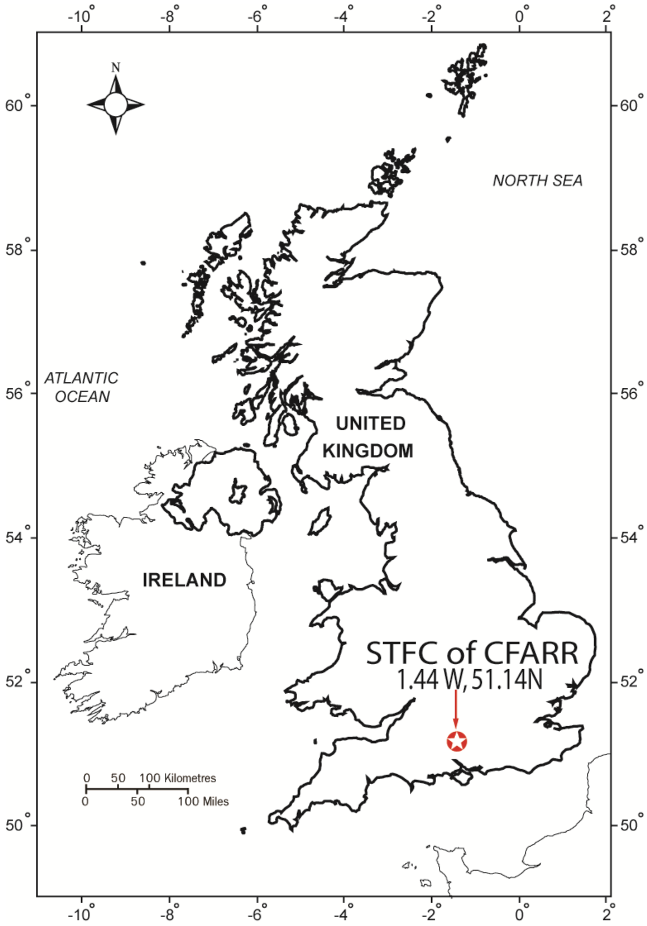

Figure 3.2.1 Position of Chilbolton, Hampshire, UK

Table 3.2.1Relevant instruments at the Chilbolton Facility for Atmospheric and Radio Research (CFARR), Hampshire, UK

Model, company (Instrument)	Measurement	Accuracy	Repeatability	Traceability
BF3, Delta-T device (Sunshine Sensor)	Global PAR, Diffuse PAR	12-15%	-	Manufacturer certify
CM21, Kipp and Zonen (Pyranometer)	Global irradiance	3%	-	High quality (WMO), Secondary standard (ISO)

3.2.2 Solar Energy Research Laboratory, Silpakorn University, Nakhon Pathom, Thailand

It was convenient to do some of the initial work at the Solar Energy Laboratory on the campus of Silpakorn University in Nakhon Pathom, Thailand (longitude 100.04 °E, latitude 13.82 °N, Figure 3.2.2). This site was used because it has an established instrument to measure meteorological data and solar radiation on the roof of Science Building 1, next to the Solar Energy Research Laboratory, and access was easily arranged as this is the author's home university. This made it possible to install an additional BF3 sensor for a period of several months, so that the instrument could be extensively tested. The roof of the laboratory is approximately 50 m above ground level, and the instruments have a clear view of the sky.

The BF3 (Serial No. BF3-34/57) was operated from 3 November 2010 to 11 January 2011, close to an existing installation of high quality meteorological instruments which included two Kipp and Zonen pyranometers (Model CM 11) and two EKO Instruments PAR sensors (Model ML-020-P). All four instruments are regularly calibrated to ensure traceability to national standards.

The CM 11 uses a temperature compensated thermopile detector to give a spectral range 305 to 2800 nm and achieves an accuracy of better than 10 W m^{-2} for solar incidence angles less than 80°. It has an hourly uncertainty of less than 3%, and a daily uncertainty of less than 2% meeting the World Meteorological Organisation (WMO) requirements of a 'Secondary Standard pyranometer' (ISO 9060) (Kipp & Zonen, 2000; McArthur, 2005). The EKO PAR sensors use a silicon photodiode and integral filters to measure PAR to an accuracy of 7.7%, with a cosine response accurate to 1.5% at 60° incidence angle (e.g. EKO Instruments, 2011). Although not certified by the WMO, the EKO PAR sensors are representative of a range of commercially available instruments commonly used to measure total PAR, and are therefore taken as the standard for this study. A Kipp and Zonen shade ring (Model CM 121) was fitted to one of the pyranometers and one of the EKO PAR sensors so as to measure diffuse solar radiation.

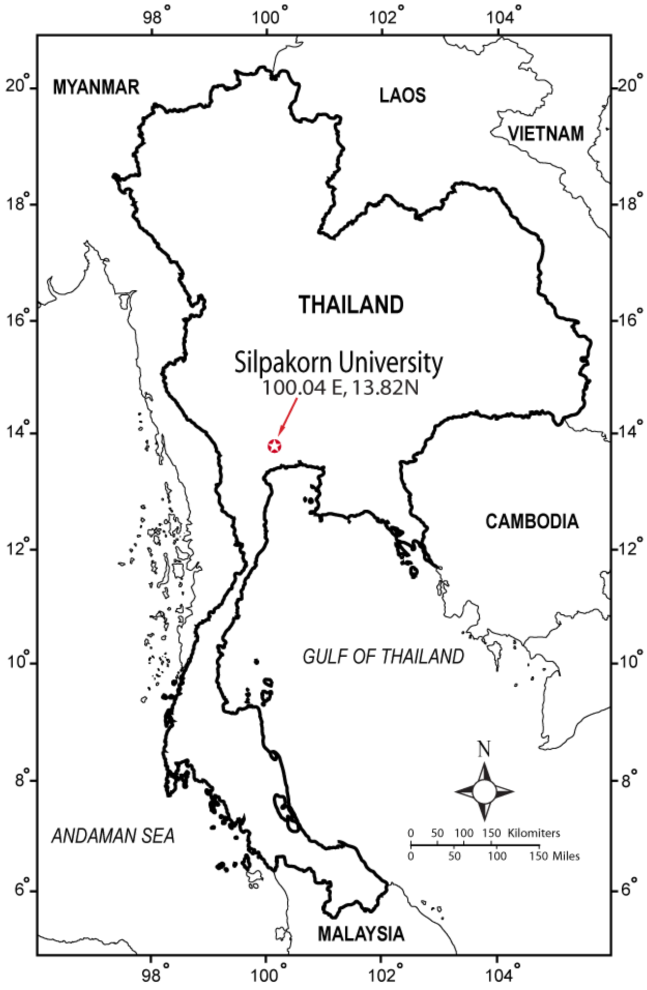

Figure 3.2.2 Position Silpakorn University, Thailand

Table 3.2.2 Relevant instruments at Silpakorn, University

Model, company (Instrument)	Measurement	Accuracy	Traceability
BF3, Delta-T device (Sunshine Sensor)	Global PAR, Diffuse PAR	12-15%	Manufacturer certify
CM11, Kipp and Zonen (Pyranometer)	Global irradiance	3%	High quality (WMO), Secondary standard (ISO)
ML-020-P, EKO (PAR sensor)	Global PAR	7%	Manufacturer certify
CM-121, Kipp and Zonen (Shadow ring)	Diffuse irradiance, Diffuse PAR	15-20 %	Widely use

3.3 Forest Test Sites

3.3.1 Wytham Woods

Wytham Woods comprise an area of ancient semi-natural woodland, plantation and grassland near the village of Wytham, Oxfordshire (longitude 0° 51´ 18˝W, latitude 51°10´45˝N). The main tree canopy is formed by pedunculate oak (*Quercus robur*), ash (*Fraxinus excelsior*), sycamore (*Acer pseudoplatanus*), beech (*Fagus sylvatica*), and a conifer plantation (Norway Spruce: *Picea abies*). The site covers approximately 2 km^2 and is surrounded by grasslands and agriculture fields. Wytham Woods are owned by Oxford University and were designated a Site of Special Scientific Interest (SSSI) in 1950, since when they have become one of the most researched areas of woodland in the world (www4).

Wytham Woods is located in a large meander of the River Thames. The woodland is situated on a hill surrounded by tributaries of the River Thames and is between 60 to 170 metres above sea level. There is a FLUXNET site situated near the northern edge of the woodland, near the top of the hill. The woodland occupies hilly terrain, surrounded by agricultural fields (crops and grass) and a few small villages. The town of Oxford is about 10km to the south-east.

The Wytham Woods FLUXNET site was installed in 2007 and is maintained by the Centre for Ecology and Hydrology (CEH, www5). It has an ultrasonic wind sensor and infrared gas analyser for GPP measurement based on the eddy covariance method. Since mid-2012 a BF5 Sunshine Sensor (the newer model of the BF3) has been installed at the Wytham Woods. There is no another PAR sensor at the site. The global broadband solar radiation at this site is measured using a pyranometer (more detail of instruments in Table 3.3.1).

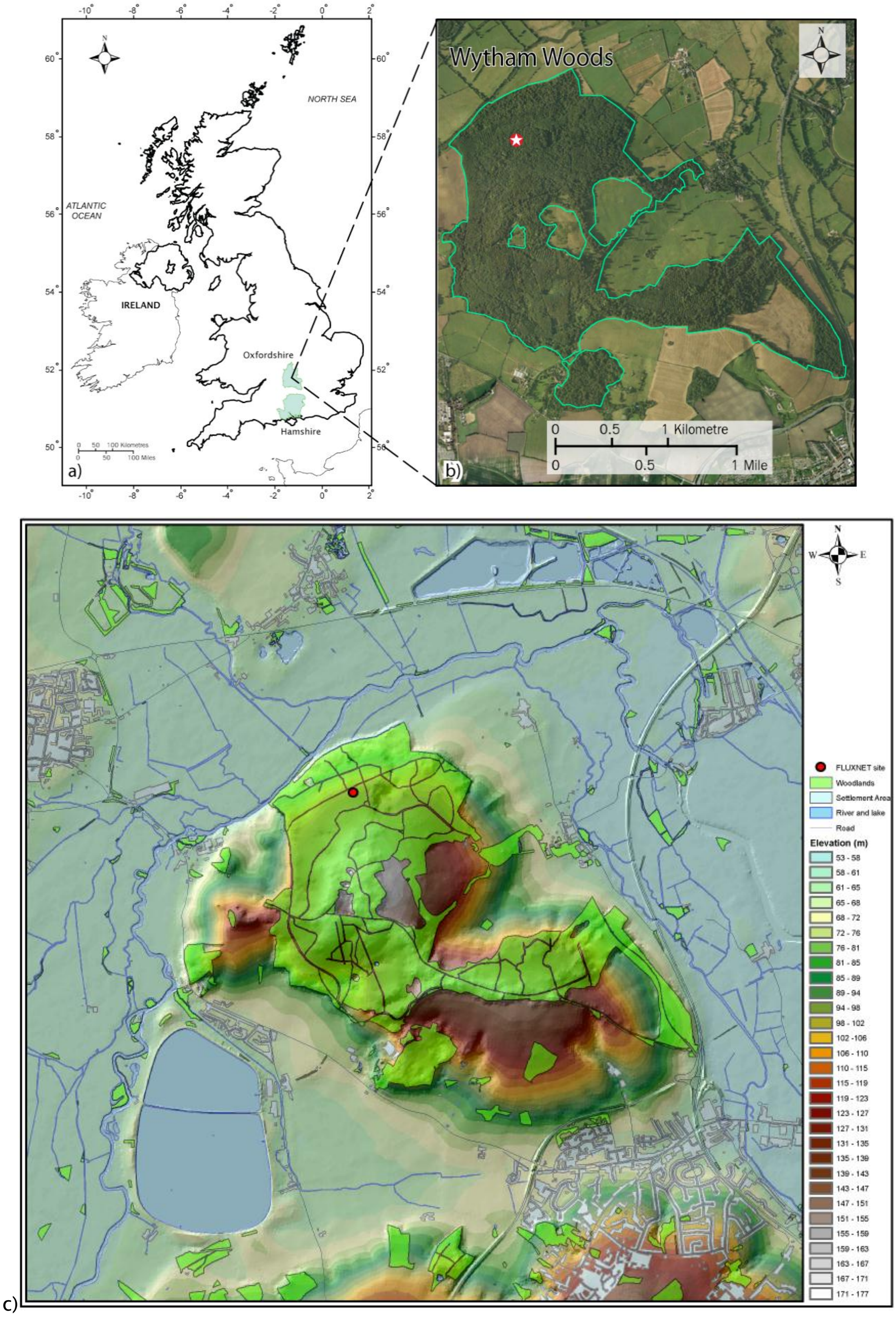

Figure 3.3.1 The Wytham Woods with a FLUXNET site (✪), a) location of area b) land cover, c) topography (applied after data from www6)

Figure 3.3.2 Example of trees and leaf density in Wytham Woods in the winter, picture taken in 8th February 2013, from approximately half-way up the flux tower (by author).

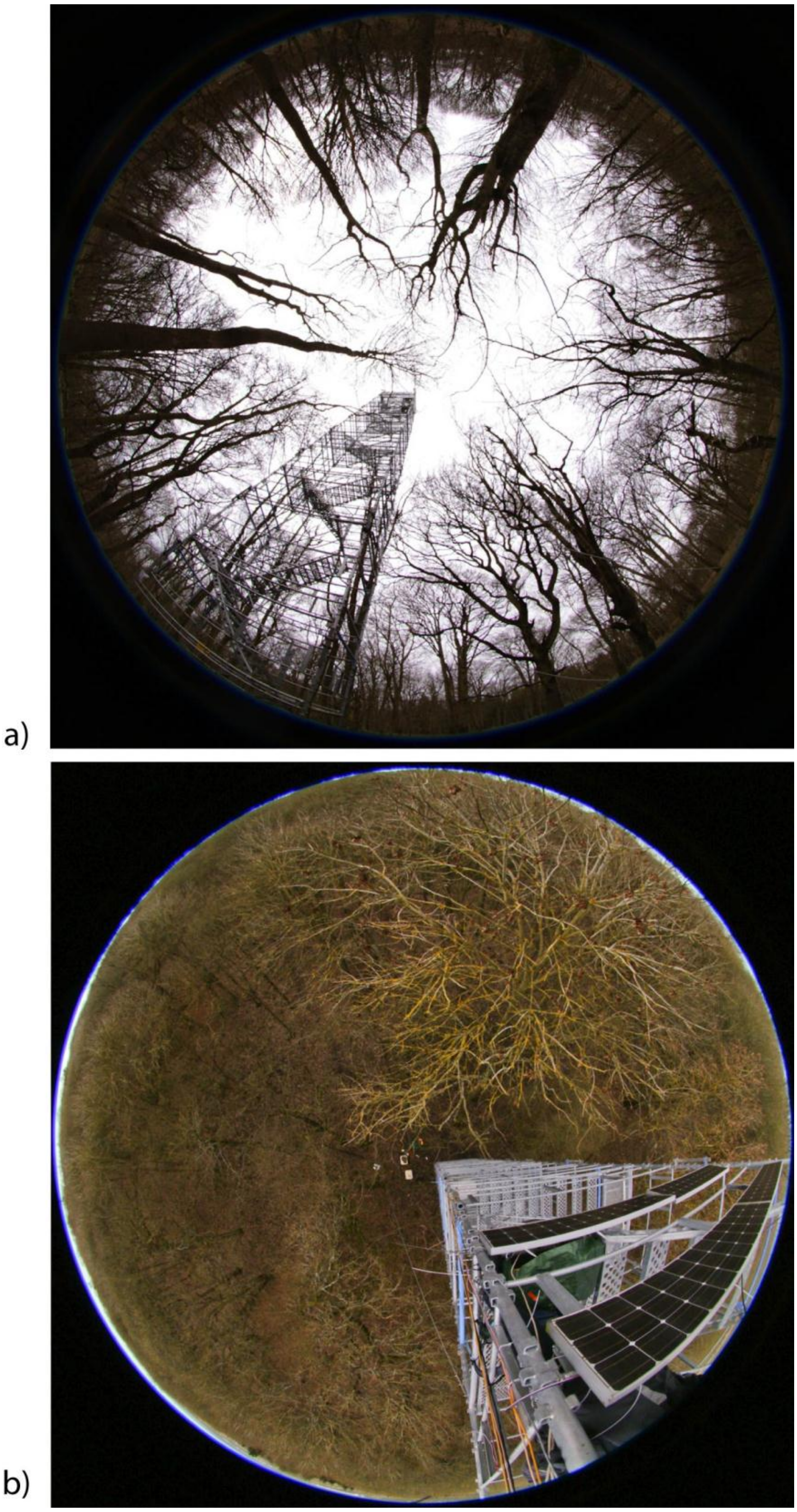

Figure 3.3.3 Example of trees and leaf density at Wytham Woods in the winter, using fish eye lenses on 8th February 2013, a) from the bottom upward, b) from the top downward (by author)

Figure 3.3.4 Example of trees and leaf density in Wytham Woods in the summer, picture taken in 11th September 2013, from approximately half-way up the flux tower (by author)

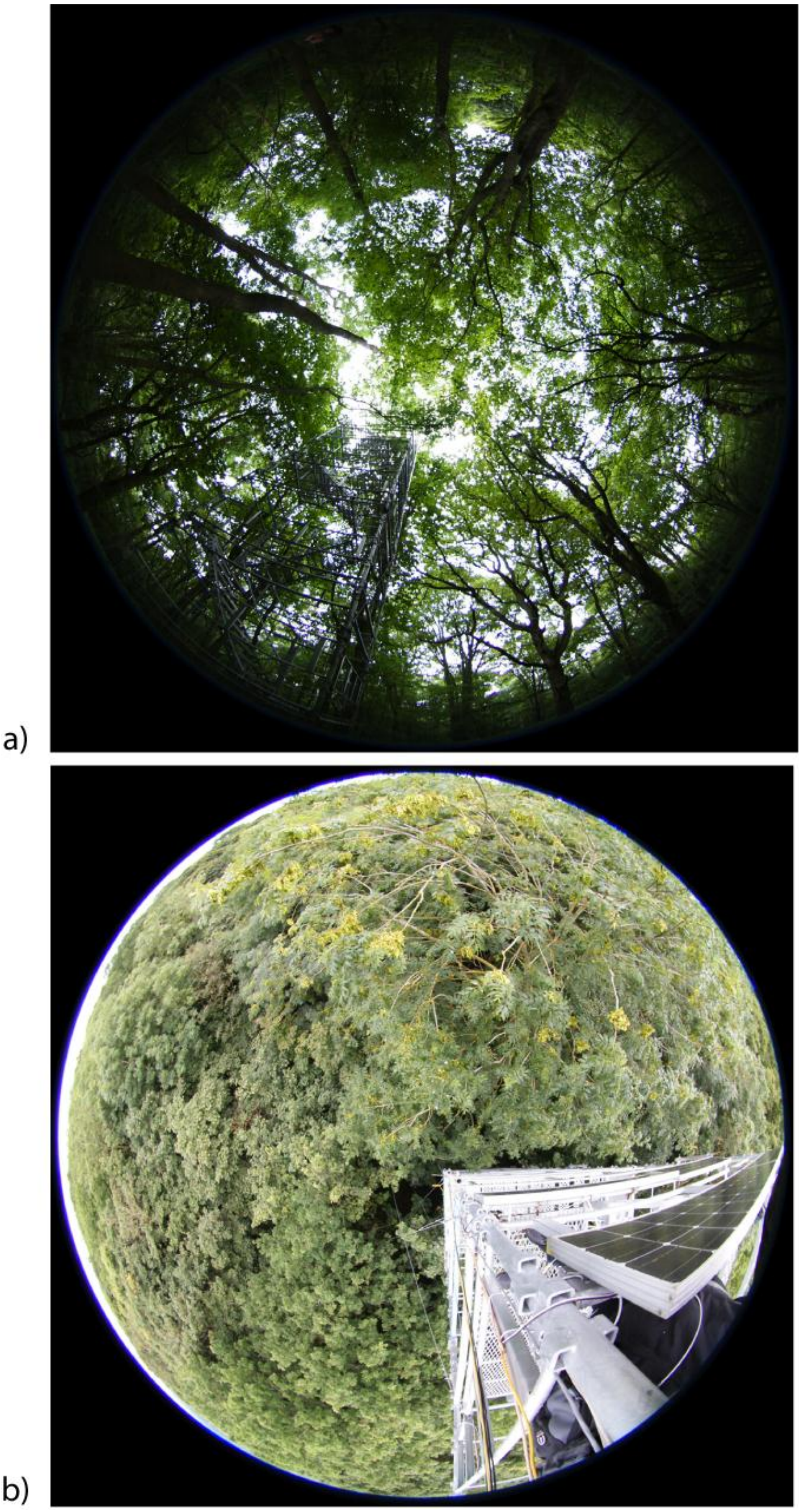

Figure 3.3.5 Example of trees and leaf density at Wytham Woods in the late summer, using fish eye lenses in 11th September 2013, a) from the bottom upward, b) from the top downward (by author)

Table 3.3.1 Relevant instruments at Wytham Woods

Model, company (Instrument)	Measurement	Accuracy	Repeatability	Traceability
CNR4, Kipp and Zonen (Pyranometer)	Global irradiance	3%	-	High quality (WMO), Secondary standard (ISO)
LI-7500A, LI-COR (Gas analyzer)	Gas component	1%	-	Manufacturer certify, Widely use
R3-100, Gill Instruments (3D anemometer)	3D wind speed and direction	1%	-	Manufacturer certify, Widely use

3.3.2 Alice Holt Forest

Alice Holt Forest is located in Hampshire (longitude 0° 51´ 18˝W, latitude 51°10´45˝N). The forest is a mixed forest with the main tree canopies being Corsican pine (*Quercus robur, Q. petraea*) and Oak (*Pinus nigra var. maritima*). It is classified as semi-natural ancient woodland. The forest covers an area approximately 8.5 km^2 and is maintained by UK Forestry Commission (www7), which has one of its main field stations at the site.

The Alice Holt forest is located in a hilly part of western Hampshire. The elevation of the forest ranges between approximately 55 to 125 metres above the average sea level. The FLUXNET site is in the south-west of the forest, at an elevation of approximately 75 metres. The area of the forest is surrounded by agricultural fields (crops, livestock and grassland) (Figure 3.3.6).

The FLUXNET site at Alice Holt began collecting data in 2004 and is maintained by the Forest Research Environmental Change Research Group, Alice Holt Lodge (www8). The site has instruments for estimation of GPP using the Eddy Covariance method (more detail of relevant instruments is in Table 3.3.2).

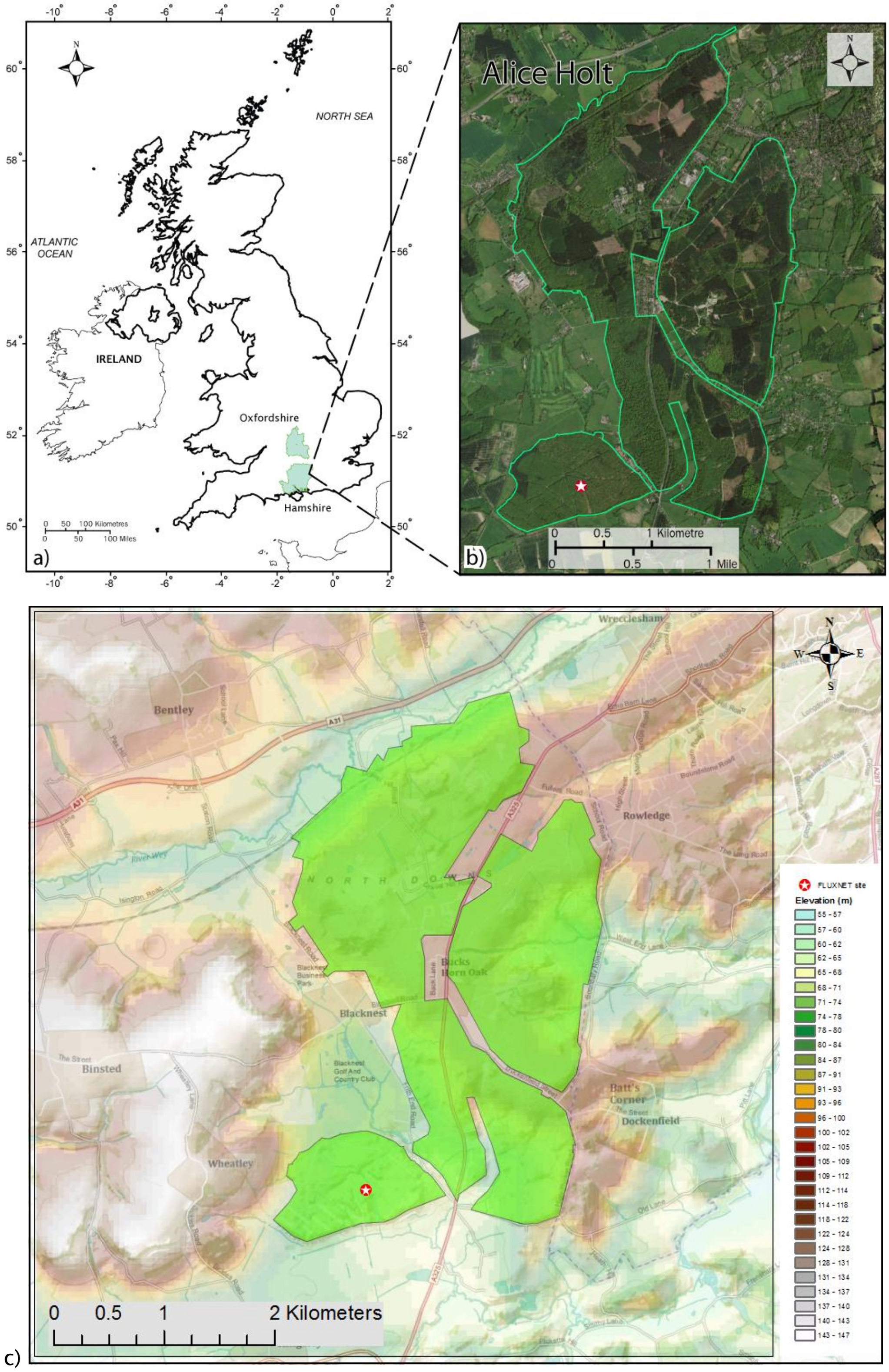

Figure 3.3.6 The Alice Holt with a FLUXNET site (✪), a) location of area b) land cover, c) topography (applied after data from www6)

Figure 3.3.7 Example of trees and leaf density in Alice Holt forest in the winter, picture taken in 11th January 2013, from approximately half-way up the flux tower (by author)

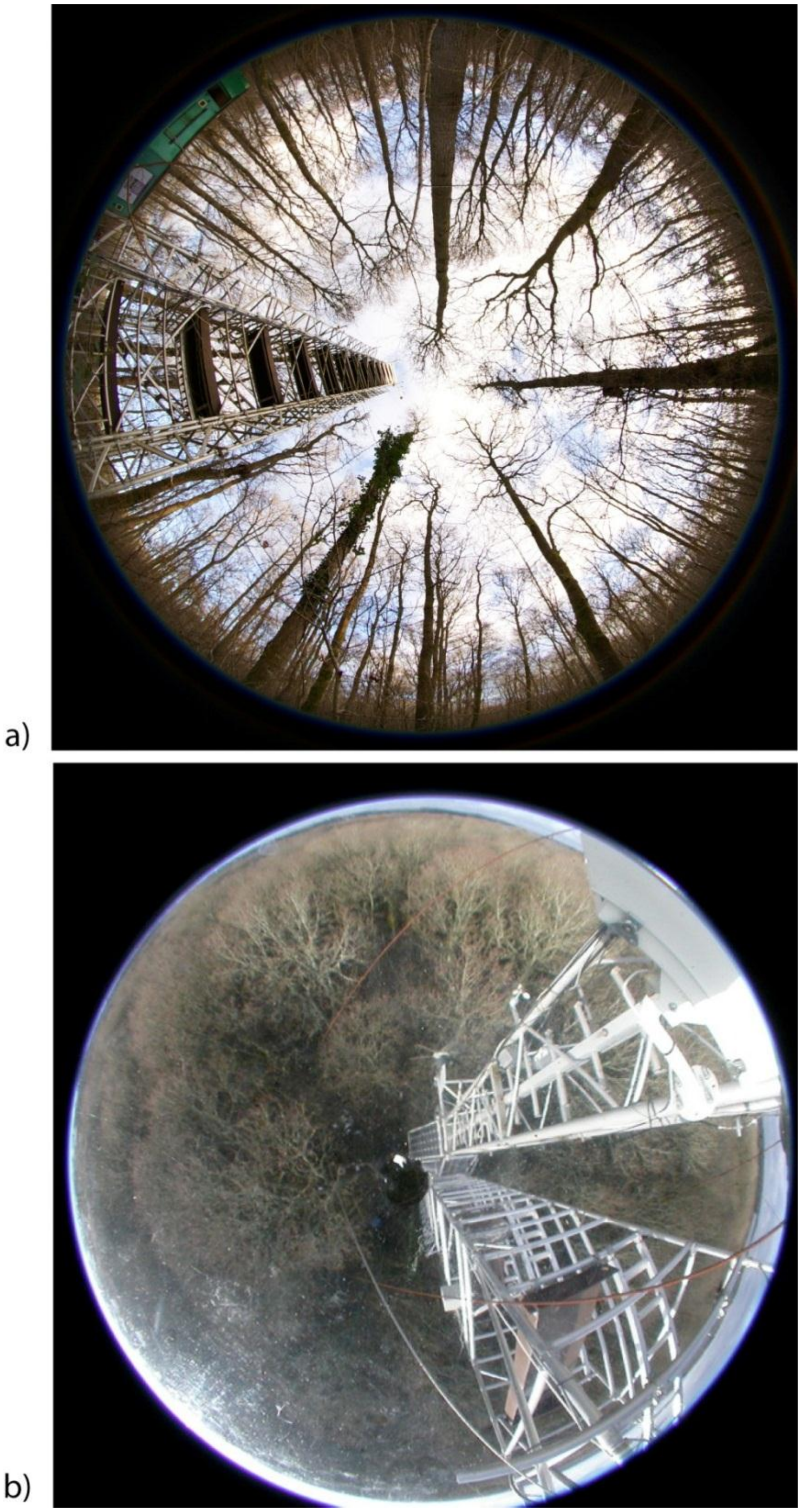

Figure 3.3.8 Example of trees and leaf density at Alice Holt forest in the winter, using fish eye lenses, 11th January 2013, a) from the bottom upward (by author), b) from the top downward (www9)

Figure 3.3.9 Example of trees and leaf density in Alice Holt forest in the summer, picture taken in 21th June 2013, from approximately half-way up the flux tower (by author)

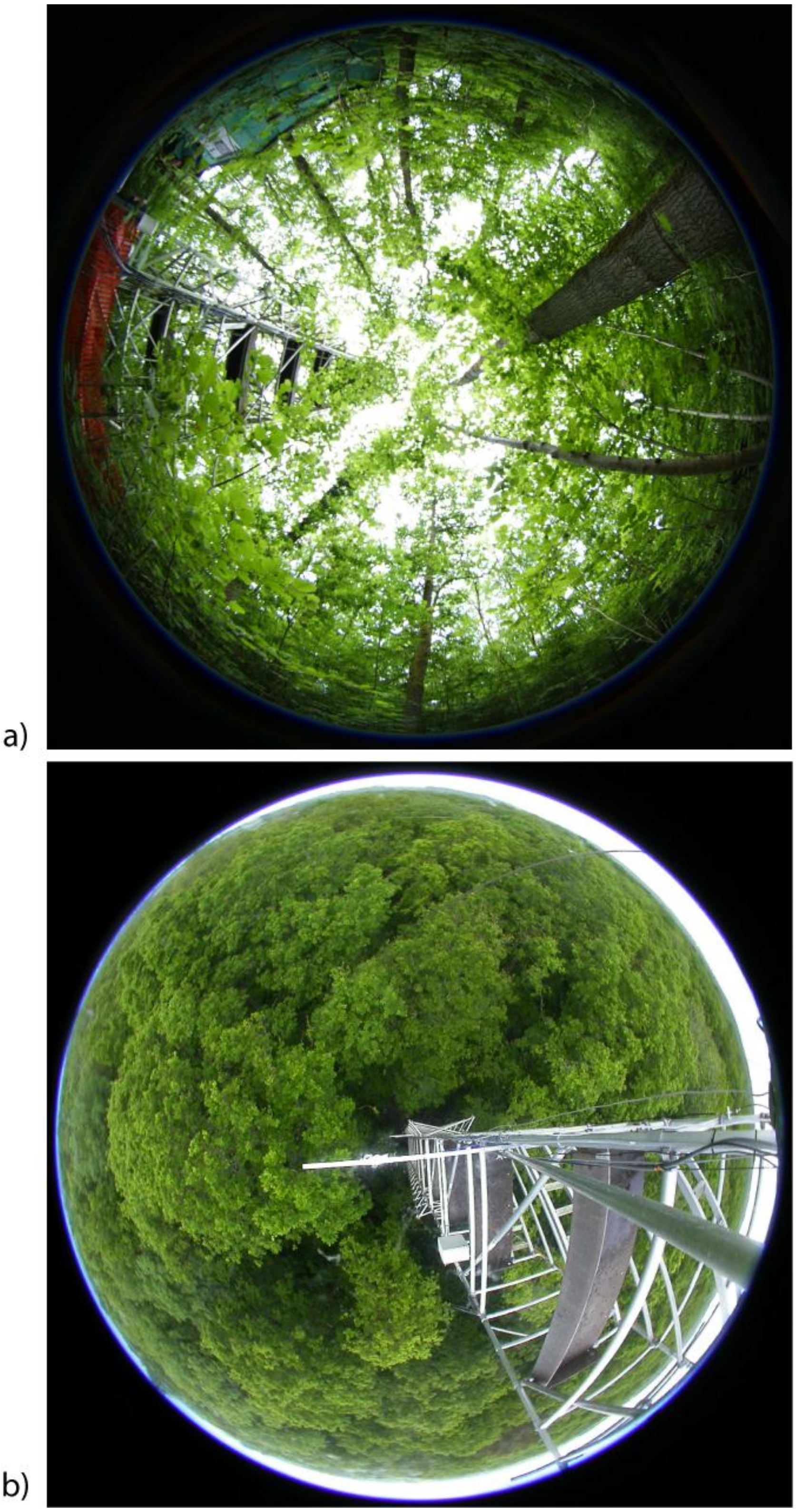

Figure 3.3.10 Example of trees and leaf density at Alice Holt forest in the summer, using fish eye lenses, 21th June 2013, a) from the bottom upward (by author), b) from the top downward (www9)

Table 3.3.2 Relevant instruments at Alice Holt

Model, company (Instrument)	Measurement	Accuracy	Repeatability	Traceability
CM2, Kipp and Zonen (Pyranometer)	Global irradiance	-	-	> 50 year old, cannot be calibrated
LI-7200, LI-COR (Gas analyzer)	Gas component	1%	-	Manufacturer certify, Widely use
R3-100, Gill Instruments (3D anemometer)	3D wind speed and direction	1%	-	Manufacturer certify, Widely use

3.4 Evaluation of the Delta-T Devices BF3 Sunshine Sensor

Conventional PAR sensors typically consist of a photosensor fitted with a filter to restrict its sensitivity to the desired range of wavelengths (Angstrom and Drummond, 1961; Biggs et al., 1971). This provides total PAR at a single point but does not allow us to separate PAR originating directly from the Sun from that contained in the diffuse flux. To determine the total PAR received by a plant canopy would require many such sensors located at different positions within the canopy. In the last decade a new method to measure PAR has been developed by Delta-T Devices Ltd. and this is now available commercially as the BFx range of instruments (current model BF5) (Delta-T Devices Ltd., 2002a, b; Wood et al., 2003). The BFx Sunshine Sensor can measure global and diffuse PAR without complicated manual adjustments and also records total sunshine hours, making it a very attractive instrument for biophysical measurements and for the validation of remotely sensed PAR from satellite sensors (e.g. Van Laake and Sanchez-Azofeifa, 2004, 2005).

The BFx Sunshine Sensor can also be programmed to measure global and diffuse irradiance (units $\mathrm{W\,m^{-2}}$) which enhances its utility as a general purpose instrument for energy measurements (Iqbal, 1983), satellite sensor validation (Perez et al., 2004; Janjai et al., 2005; Vignola et al., 2007) and the atmospheric correction of remotely sensed data (Tarpley, 1979; Janjai et al., 2009; Janjai et al., 2011). However, there are some problems with its use in this mode. First, the GaAsP photodiodes used in the BFx are only sensitive in PAR wavelengths (400 – 700 nm), and second, the nature of the BFx design means that its detectors do not have an unobscured view of the sky. Therefore, the values of global and diffuse irradiance are estimates based on incomplete data.

Wood et al. (2003) compared the accuracy of global and diffuse broadband radiation (S_t and S_d) measured by a BF3 Sunshine Sensor with that measured by a conventional thermopile-based meteorological instrument, a Kipp and Zonen CM 11, and found good agreement (R^2=0.994, for hourly averages; Wood et al., 2003) at a site near Edinburgh, Scotland. They also found that the sunshine hours recorded by the BF3 Sunshine Sensor compared well with those measured by a Campbell-Stokes Sunshine Recorder.

Validation of PAR measurements from space is a major challenge, and as will be show later, there is an urgent need for a global network of accurate PAR measurement sites (global and diffuse). The BFx Sunshine Sensor has great potential to meet this need, however, it is based on an innovative design which has not been independently tested (John Wood designed the instrument). For this reason it was decided to perform an evaluation of the BF3 before using it to undertake the main research tasks. This part of the research took place in Thailand, at the University of Silpakorn Solar Energy Research Laboratory (Section 3.2.2).

3.4.1 Method

a) PAR measurements

Data were sampled every second and 10 minute averages stored from both the BF3 and a pair of EKO PAR sensors using a Yokogawa data logger. The data from the BF3 were already in molar units ($\mu\text{mol m}^{-2}\text{ s}^{-1}$), but those from the EKO sensors needed scaling by application of a calibration factor provided by the manufacturer. The diffuse EKO PAR sensor also had an adjustment for the shade ring provided by Kipp and Zonen to convert the measured signal into diffuse PAR flux (Steven, 1977; Steven and Unsworth, 1980a; Steven and Unsworth, 1980b; Kipp & Zonen, 2012, p. 64).

b) Irradiance measurements

Most solar irradiance measurements are expressed in units of W m^{-2}. This unit is normally used in the explanation of the energy balance in the atmosphere, and is also widely used in the modelling of solar radiation (e.g. Tarpley, 1979; Gautier et al., 1980). The limited spectral sensitivity of the BF3 sensors means that there is no direct way to measure broadband irradiance. To convert the results from the BF3 Sunshine Sensor to $\mathrm{W\,m^{-2}}$ within the PAR wavelength band it is necessary to consider the integration of solar spectral irradiation (Frouin and Pinker, 1995; LI-COR Inc., undated).

$$\mathrm{PAR} = \int_{400}^{700} \mathrm{I}(\lambda)\,\mathrm{d}\lambda \ \ (\mathrm{unit\ W\,m^{-2}}) \tag{3.4.1}$$

where $\mathrm{I}(\lambda)$ is the spectral solar irradiance for units of $\mathrm{W\ m^{-2}\ nm^{-1}}$ at wavelength λ. For the units of photon flux density, it is generally defined as (e.g. Frouin and Pinker, 1995):

$$\mathrm{PAR} = \frac{1}{\mathrm{hc}}\int_{400}^{700} \lambda\mathrm{I}(\lambda)\mathrm{d}\lambda \ \ (\mathrm{unit\ quanta\ m^{-2}s^{-1}}) \tag{3.4.2}$$

where h is Planck's constant (6.63×10^{-34} J s), and c is the velocity of light, 3.00×10^{8} m s^{-1}. The traditional unit of PAR is read from the sensor in $\mathrm{\mu mol\,m^{-2}\,s^{-1}}$. The equation (3.4.2) can be written as

$$\mathrm{PAR} = (\frac{1}{6.022\times10^{17}})\frac{1}{\mathrm{hc}}\int_{400}^{700} \lambda\mathrm{I}(\lambda)\mathrm{d}\lambda \ \ (\mathrm{unit\ \mu mol\ m^{-2}s^{-1}}) \tag{3.4.3}$$

where 1 μmol is 6.022×10^{17} quanta of photon. Therefore,

$$\int_{400}^{700} \mathrm{I}(\lambda)\mathrm{d}\lambda\ (\mathrm{unit\ Wm^{-2}s^{-1}})$$

is equivalent to

$$(\frac{1}{6.022\times10^{17}})\frac{1}{\mathrm{hc}}\int_{400}^{700} \lambda\mathrm{I}(\lambda)\mathrm{d}\lambda\ (\mathrm{unit\ \mu mol\ m^{-2}s^{-1}})$$

It can be written as

$$\sum_{i} I(\lambda_i)\Delta\lambda \ \ (Wm^{-2}s^{-1}) = (\frac{1}{6.022 \times 10^{17}})\frac{1}{hc}\sum_{i} \lambda I(\lambda_i)\,\Delta\lambda \ \ (\mu mol\, m^{-2}s^{-1}) \qquad (3.4.4)$$

If the solar radiation spectrum in the wavelength between 400 and 700 nm was flat, and the photon flux density spectral response of the PAR measurement was flat, it would be perfect for the measurement of PAR (LI-COR Inc., undated). In this case we could use the mean wavelength of the photons of PAR (550 nm) for the calculation in this unit conversion. The energy of a photon can be calculated from the equation:

$$E = h\nu \qquad (3.4.5)$$

by

$$\nu = \frac{c}{\lambda} \qquad (3.4.6)$$

where h = Planck's constant (6.63×10^{-34} J s), ν = Photon frequency (Hertz),
c = Light velocity ($3.00 \times 10^{8}\ m\,s^{-1}$), λ = Photon wavelength (m).

By approximation, if the spectral distribution of solar radiation is assumed to be a flat curve between the range of 400 and 700 nm, the variables in the equation can be given as: i = 1

$$\Delta\lambda = 300\ nm \qquad (3.4.7)$$

$$\lambda_i = 550\ nm \qquad (3.4.8)$$

Therefore, the approximate conversion factor between the radiometric quantity and the photon flux density for PAR measurements using a photodiode sensor is

$$1\ Wm^{-2}\ (PAR) = 4.5976\ \mu mol\ m^{-2}s^{-1}\ (PAR) \qquad (3.4.9)$$

The BF3 Sunshine Sensor gives the results of the total molar of the photon in the PAR wavelength band. Solar irradiance measurements give the results in units of $W\,m^{-2}$. To investigate the BF3 Sunshine Sensor for the measurement of solar irradiance, this study used 550 nm for the mean wavelength of the photons in the PAR waveband. A photon of this wavelength has energy 3.6117×10^{-19} Joule (J). A mole is the quantum amount equal to the Avogadro number (N_A), 6.022×10^{23}.

Therefore a μmol of photon is equivalent to 6.022 $\times 10^{23}$ quanta. The conversion factor between Joules (J) and Watts (W) is 1 Joule per second (J s^{-1}) equals 1 W.

Therefore:

$$1\ \mu\text{mol m}^{-2}\text{s}^{-1}\ (\text{PAR}) = 0.2175\ \text{W m}^{-2}\ (\text{PAR}). \qquad (3.4.10)$$

On this basis, equation 3.4.10 provides the conversion factor between molar units and energy units within the PAR wavelength band, and this is different from the conversion factor provided by the instrument manufacturer (0.48). This discrepancy was investigated further by converting the measured data to energy intensity using both methods. Firstly, the theoretically calculated conversion factor based on the energy intensity within the PAR-band (equation 3.4.10) was used. Secondly, the BF3 was set to measure in units of $\mu\text{mol m}^{-2}\ \text{s}^{-1}$ which were then converted into W m^{-2} using the correction factor 1 $\mu\text{mol m}^{-2}\ \text{s}^{-1}$ per 0.48 W m^{-2} (Delta-T Devices Ltd., 2002a). In each case, the diffuse radiation of the BF3 Sunshine Sensor was calculated using the equations provide by the manufacturer (Delta-T Devices Ltd., 2002a)

3.4.2 Results

a) PAR

Figure 3.4.1and Figure 3.4.2 compare 10-minute averages of global and diffuse PAR measured every second by the BF3 with that measured by the EKO sensors over the period 3 November 2010 – 5 January 2011. A strong linear relationship was found (R^2 = 0.995, 0.989 respectively). There was no significant zero offset for either instrument, but the slope of the best-fit line was steeper than the 1:1 line, resulting in the BF3 recording higher values of global and diffuse PAR.

After correction using the relationship from Figure 3.4.1 and Figure 3.4.2 (the EKO was used to correct the BF3), the variation of % difference compared to measured PAR is in Figure 3.4.3. The average daily trend of global and diffuse PAR is in Figure 3.4.4. Figure 3.4.5 reveals that for much of the day the difference is fairly constant, whereas during the early morning and late afternoon the difference is greater, probably due to differences in the cosine response between the two instruments.

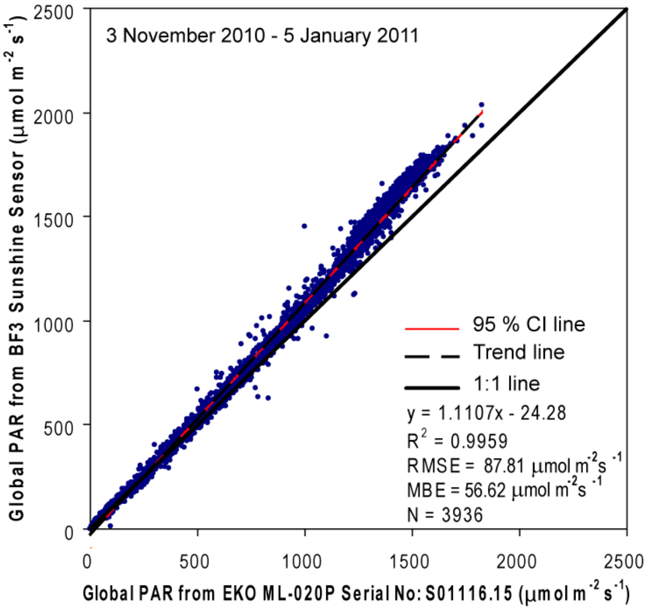

Figure 3.4.1 10-minutely comparison of global PAR between measured data from BF3 and EKO ML-020P

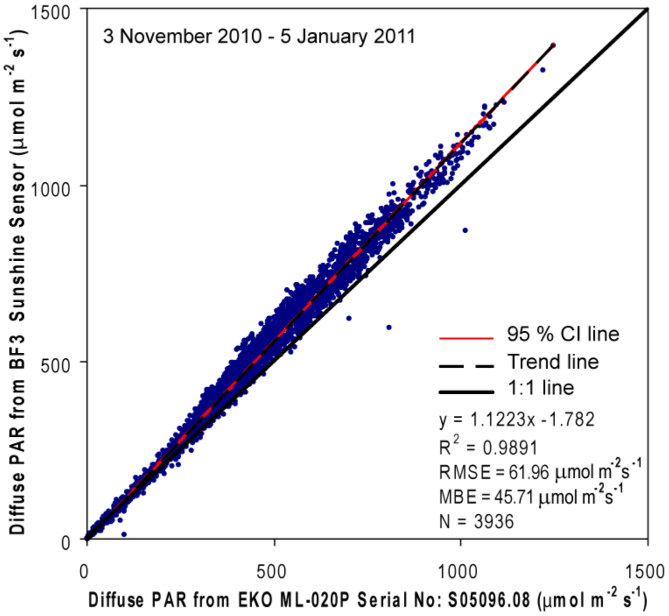

Figure 3.4.2 10-minutely comparison of diffuse PAR between measured data from BF3 and EKO ML-020P with a shade ring

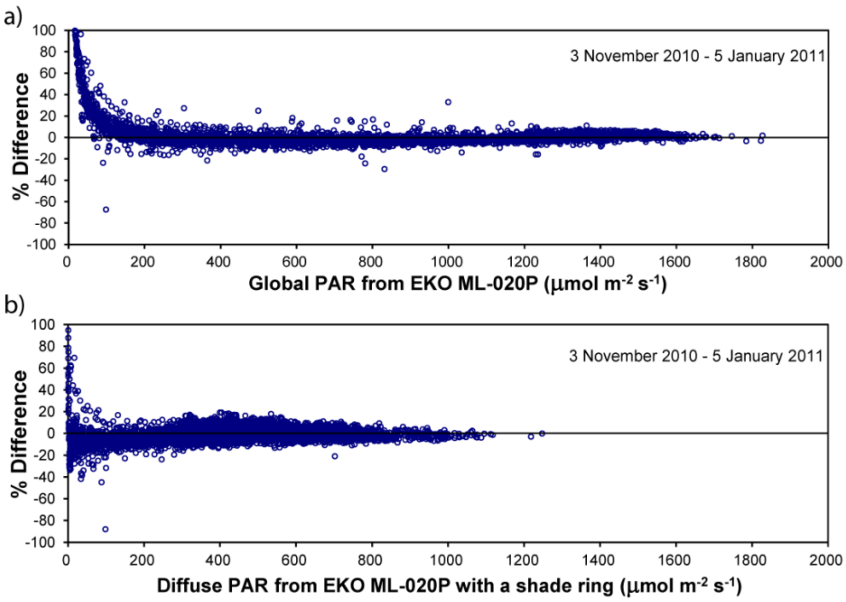

Figure 3.4.3 Percentage difference in PAR from the BF3 and EKO ML-020P a) global PAR, b) diffuse PAR, after correction

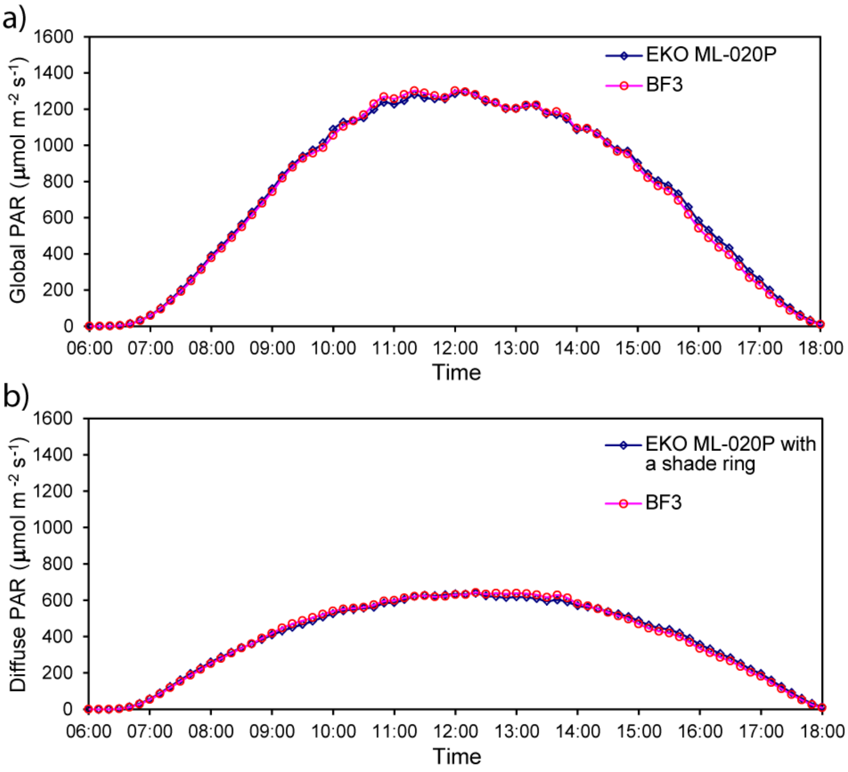

Figure 3.4.4 10-minutely average variation of a) global PAR and b) diffuse PAR form the EKO ML-020P and BF3, during 3 November 2010 – 5 January 2011, after correction

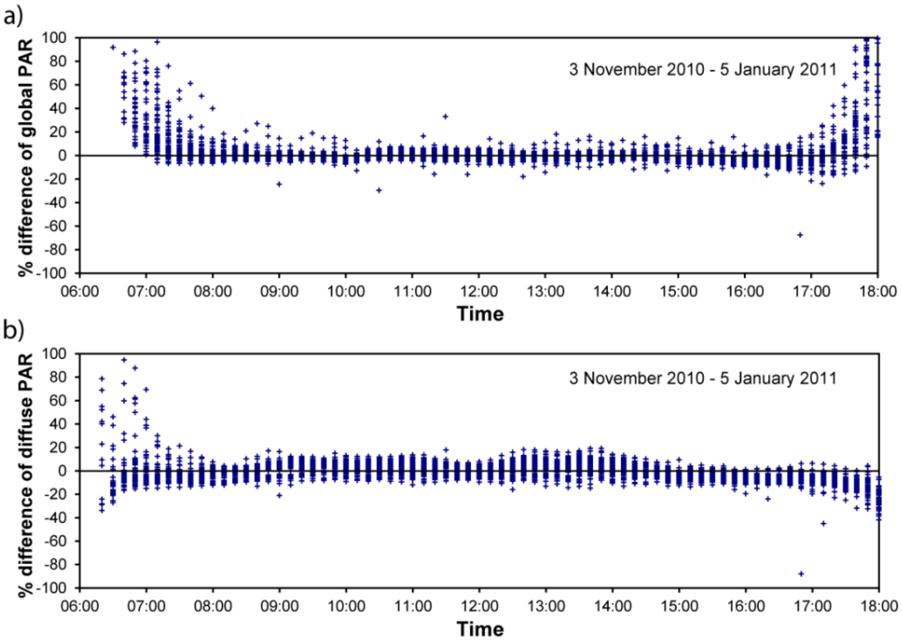

Figure 3.4.5 Percent difference in daily PAR from the BF3 and the EKO ML-020P sensor a) global PAR, b) diffuse PAR, after correction

b) Irradiance measurements

The first test for irradiance measurements used the theoretical conversion factor between PAR flux and energy intensity in equation (3.4.11). Figure 3.4.6 and Figure 3.4.7 show the results of the 10-minute averages of measurements made every second between 3 November 2010 and 5 January 2011. There is more scatter around the measurements of diffuse irradiance, but the overall relationship between both instruments is highly linear and unbiased, except perhaps at high levels of broadband irradiance (> 400 Wm^{-2}).

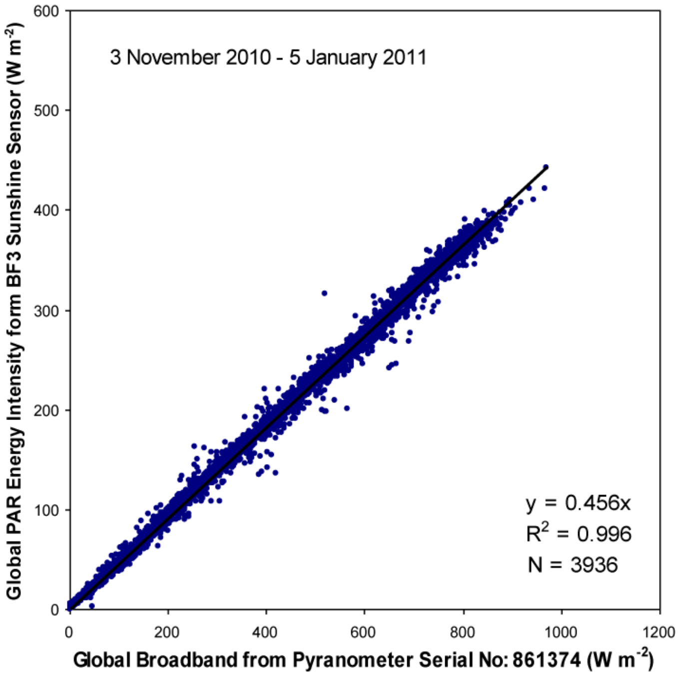

Figure 3.4.6 10-minutely relationship between global PAR energy intensity from BF3 and global broadband irradiance from Kipp and Zonen CM 11 pyranometer

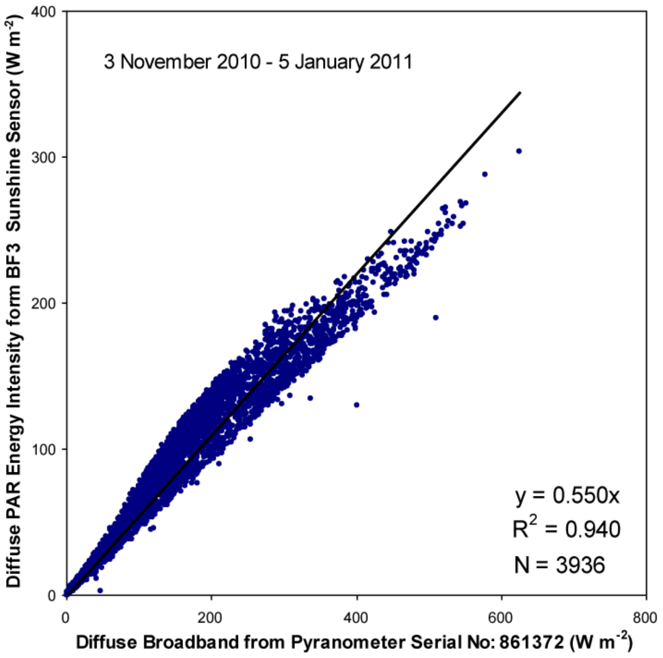

Figure 3.4.7 10-minutely relationship between diffuse PAR energy intensity from BF3 and diffuse broadband irradiance from Kipp and Zonen CM 11 pyranometer

The second test used the BF3 set to record in units of $\mu\mathrm{mol\,m^{-2}\,s^{-1}}$ and then used the conversion factor provided by the manufacturer (0.48) to convert the data into $\mathrm{W\,m^{-2}}$. The results for 10-minute averages of data collected every second are shown in Figure 3.4.8 and Figure 3.4.9 for the period 3 November 2010 – 5 January 2011. The global irradiance estimated by the BF3 was highly correlated with that measured by the CM 11 reference pyranometer (R^2 = 0.998), and the data closely followed the 1:1 line. The relationship between diffuse broadband radiation measured by the two instruments was less precise; there was significantly more scatter in the relationship, although the overall correlation was still high (R^2=0.949).

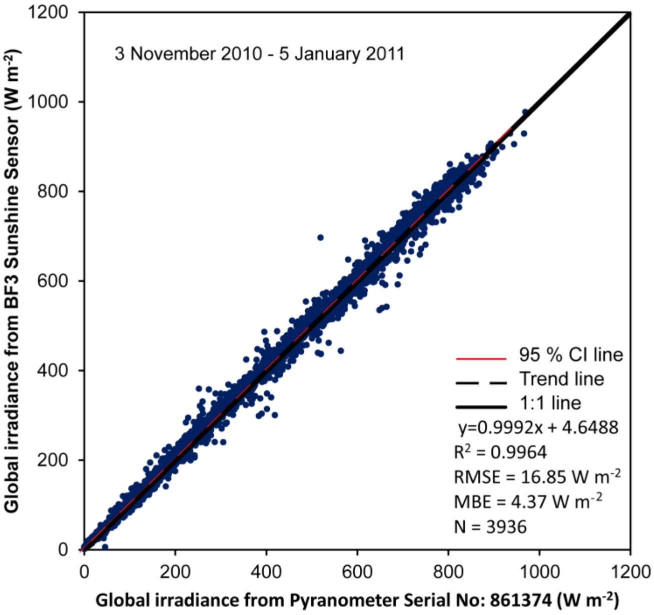

Figure 3.4.8 10-minutely comparison of global irradiance between data from BF3 and Kipp and Zonen CM11 pyranometer

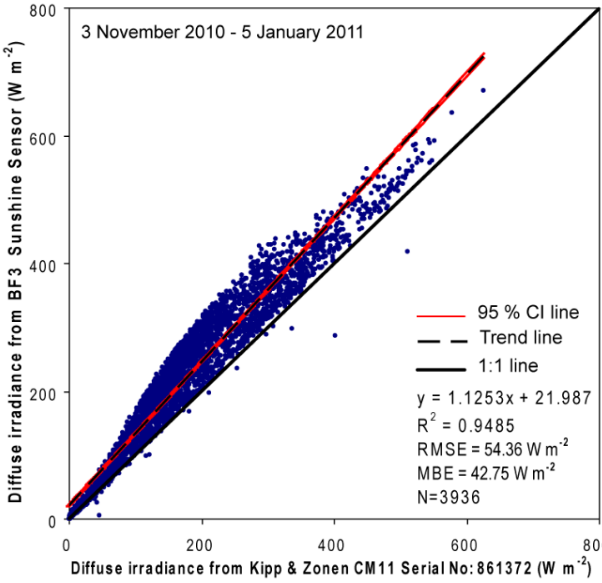

Figure 3.4.9 10-minutely comparison of diffuse broadband between BF3 and Kipp and Zonen CM11 pyranometer with a shade ring

Figure 3.4.10 confirms the close agreement between the CM 11 and the BF3, after correction using relationships in Figure 3.4.6 and Figure 3.4.7, over the whole range of global solar irradiance values, measured by the BF3 compared with that measured by the CM 11. This is also seen in the diurnal variation in comparison of the global and diffuse irradiance measured by the two instruments (Figure 3.4.11).

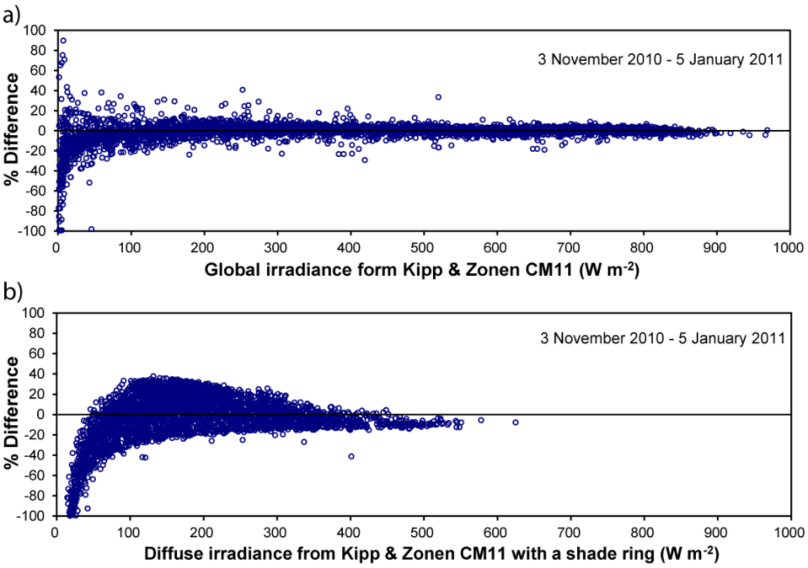

Figure 3.4.10 Percent difference between BF3 and Kipp and Zonen CM11 a) global irradiance, and b) diffuse irradiance, after correction

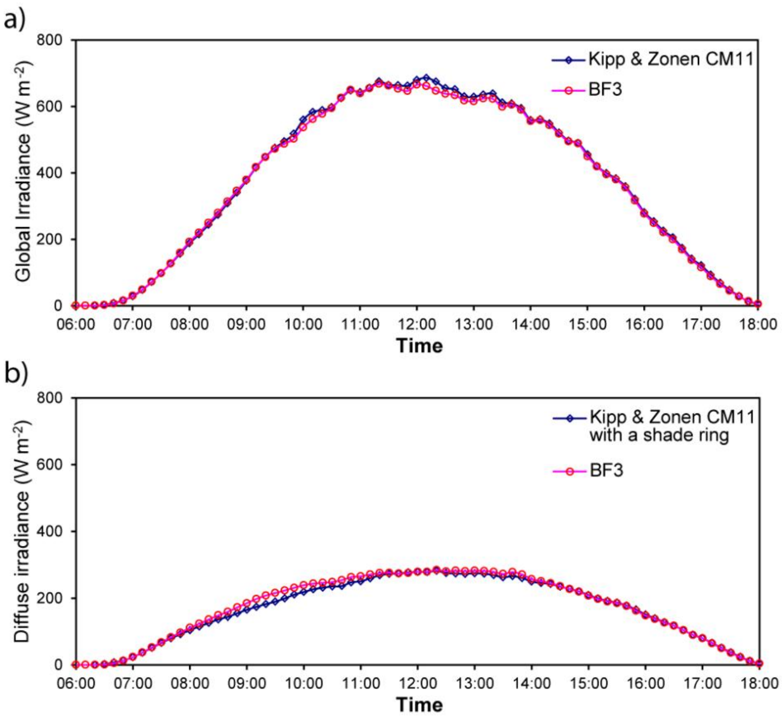

Figure 3.4.11 10-minutely average variation of a) global irradiation and b) diffuse irradiation from Kipp and Zonen CM11 pyranometer and BF3, during 3 November 2010 – 5 January 2011, after correction

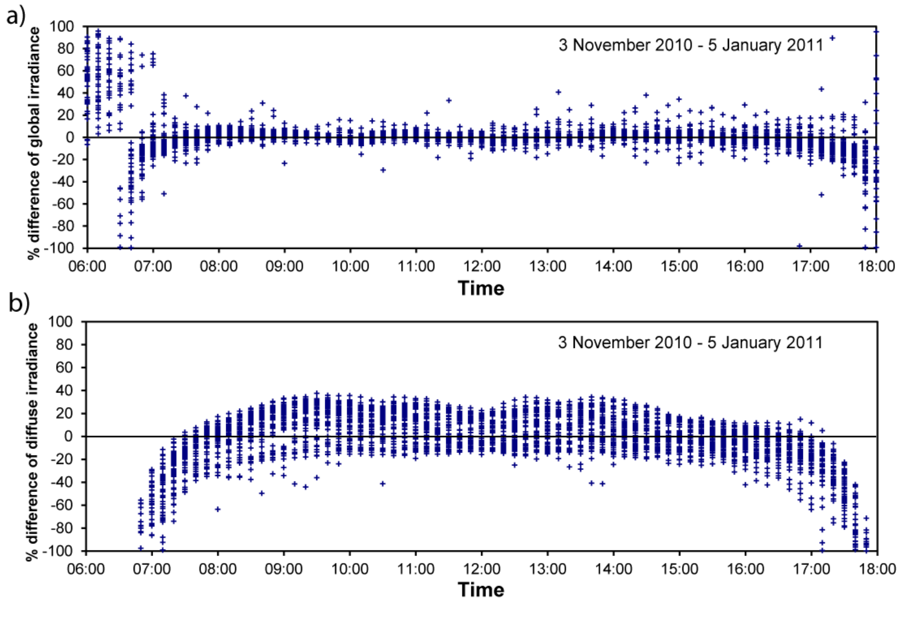

Figure 3.4.12 Percent difference between BF3 and Kipp and Zonen CM11 plotted according to time of day, a) global irradiance and b) diffuse irradiance after correction

Figure 3.4.12 shows that the relationship between the two instruments described above held for much of the day, only breaking down in the early morning (before 08:00) and late afternoon (after 16:00), presumably due to differences in their cosine correction. This figure also shows the high level of uncertainty in the 10-minute averages of diffuse irradiance.

3.5 Discussion

Only the total PAR output accuracy is certified by Delta-T Devices Ltd. (2002a). The other values, diffuse radiation and alternative output setting are calculated relative to the total PAR (Delta-T Devices Ltd., 2002a).

The semiconductor for the photodiode sensors in the BF3 Sunshine Sensor is different to that in most PAR sensors. The sensors in the BF3 Sunshine Sensor are GaAsP photodiodes while the sensors in most other types are silicon photodiodes. The spectral responses of these sensors are different, so the over-estimation and under-estimation characteristics of each sensor types vary. Using both types of sensor under the same spectral solar radiation will give a small difference in output, as shown in the comparison of the PAR measurements (Figure 3.4.1and Figure 3.4.2). The difference of the spectral responses of the BF3 Sunshine Sensors affects the measured PAR output. Ideally for PAR measuring, the spectral response of the sensors should be flat in quantum terms. In practice, the spectral response of PAR sensors is difficult to flatten. Therefore photodiode sensors cannot avoid errors from over- or under-estimation in each wavelength. Also, they cannot avoid the error in estimation from outside the range of 400 nm – 700 nm. In the laboratory, differences between PAR sensors can also be expected due to the interaction between the spectrally-selective response of the different detectors and the spectral properties of the light source used.

Furthermore, the decay of the sensitivity of each of the photodiodes in the BF3 Sunshine Sensor over time will be different. For measurements in the equatorial area the Sun follows almost the same path all year which means that some photodiodes will be in full Sun most of the time, while some will be in full shade. Therefore, we would expect the decay in sensitivity to act differentially and cause the measurement accuracy to suffer.

The variation of the percent difference in the early morning and late evening (before 07:30 and after 17:00) is higher than the variation during late morning to late afternoon (07:30 – 17:00), as shown in Figure 3.4.5 and Figure 3.4.12. The variation of the percent difference is higher when the measured PAR and irradiance is low, as shown in Figure 3.4.4 and Figure 3.4.11. These results show that the cosine response of the instruments is different at high solar zenith angles. One of the causes of the error in diffuse PAR and diffuse irradiance measurements is likely to be incorrect shade ring alignment, and the shading pattern of the BF3 might also introduce some errors (Wood et al., 2003).

In this testing, the regression equation (Figure 3.4.6) can be used to calculate back to the conversion factor 0.48 of Delta-T Devices Ltd. (2002a). The relation of global PAR energy intensity and global broadband solar irradiation from pyranometer is the global PAR energy intensity equivalent to 0.456 of global broadband solar irradiation. This means there is 0.456 W m^{-2} of PAR in every 1 W m^{-2} of broadband solar irradiance. The calculated conversion factor for the conversion of photon density into energy intensity in PAR band is 1 $\mu\text{mol m}^{-2}\text{s}^{-1}$ per 0.2175 W m^{-2}. The relation and the calculated conversion factor can be calculated back to the factor 1 $\mu\text{mol m}^{-2}\text{s}^{-1}$ per 0.48 W m^{-2} for the over-band-spectral-response of Delta-T Devices Ltd. (2002a), as equations:

From the relation in Figure 3.4.6, it can be written as an empirical equation:

$$0.456\ \text{W m}^{-2}\ (\text{PAR}) = 1\ \text{W m}^{-2}\ (\text{broadband}), \tag{3.5.1}$$

from equation (3.4.11) and (3.5.1):

$$1\ \mu\text{mol m}^{-2}\text{s}^{-1}\ (\text{PAR}) = \frac{0.2175\ \text{W m}^{-2}\ (\text{PAR})\ \times 1\ \text{W m}^{-2}\ (\text{broadband})}{0.456\ \text{W m}^{-2}\ (\text{PAR})}. \tag{3.5.2}$$

Therefore, $1\ \mu\text{mol m}^{-2}\text{s}^{-1}(\text{PAR}) \approx 0.48\ \text{Wm}^{-2}(\text{broadband})$ which corresponds to the conversion factor provided by the manufacturer (Delta-T Devices Ltd., 2002a) and suggests that the PAR energy intensity is around half that of the broadband energy. However, the relationship of diffuse irradiance in Figure 3.4.7 cannot be used to calculate back to the conversion factor 0.48 of the Delta-T Devices Ltd. (2002a).

Atmospheric components and clouds have strong effects on incident solar spectral in both the PAR and broadband regions. The measured global and diffuse PAR using the BF3 gave positively biased results in the Tropics. Over-spectral-response-range for the global irradiance in the Tropics has similar accuracy to those made in mid-latitudes, and the same conversion factor may be applied to global irradiance collected using the BF3. The measured diffuse irradiance using the BF3 gives positive bias result in the Tropics. The error in diffuse irradiance measurements is likely to be the difference of using the shading pattern of the BF3 and the shade ring of Kipp and Zonen. The data available for this study represent only two months during the winter in Thailand. They do not capture any seasonal effects affecting the accuracy and precision of the BF3 instrument.

3.6 Conclusion

This chapter has provided a description of the test sites used for the research, the instruments from which the data were collected and the international programmes from which data were also sourced. It has also reported the results of a field-based investigation of a novel sunshine sensor, the first independent evaluation of this instrument.

It is concluded that measurements of global irradiance with the Delta-T BF3 sunshine sensor are comparable with those made by the Kipp and Zonen reference instrument. Measurements of global PAR made with the BF3 and the EKO reference instrument were similar, but not directly comparable, and a scaling factor was necessary to normalise the two instruments. Measurements of diffuse PAR with the BF3 and the EKO instrument (with shade ring) showed an average difference of +0.07% once the BF3/EKO scaling factor had been applied. Total diffuse irradiance showed the most difference between the BF3 and the reference instrument. Significant bias was present if the manufacturer's recommended calibration factor was used, but this was greatly reduced if a calibration factor based on the conversion of photon density to energy intensity in the PAR band was used. However, significant differences remained between diffuse irradiance measured with the BF3 and that measured with the reference instrument (average difference +2.98%).

Although these results are based on a limited time period, and one location, they suggest that the method of measurement (shade ring vs shading pattern) has a significant effect on measurements of both diffuse PAR and diffuse irradiance.

Chapter 4 Variation of diffuse PAR fraction across the UK

4.1 Introduction

Over a period of time, the proportion of solar energy reaching the Earth's surface as diffuse flux depends upon the clearness of the sky and on the frequency and type of clouds. Cloud properties are highly variable in time and space. They are composed mostly of water vapour, so their main impact on solar energy in the PAR region is scattering, which results in an overall reduction of the direct solar flux reaching the ground in a cloud shadow. Areas at the edges of cloud shadows may receive enhanced PAR due to forward-scattering at the edges of clouds (e.g. McKee and Cox, 1974; Weinman, 1982; Coakley and Davies, 1986; Berk et al., 1998; Alados et al., 2000; Várnai, 2000; Roderick et al., 2001). Sky clearness in the PAR region is also affected by the amount and type of aerosols, as represented by the aerosol optical thickness (AOT), and by the concentration of ozone.

The proportion of diffuse flux reaching the Earth's surface is thought to have changed over the last 100 years (approximately 10% increase, between 1900 to 2000; Mercado et al., 2009), as a result of global climate change (e.g. Fröhlich, 1991; Philipona, 2002; Mercado et al., 2009) and regional anthropogenic processes (e.g. Stanhill and Cohen, 2001). A change in the proportion of PAR flux reaching the Earth's surface as diffuse flux is significant because some plant communities(for example forests) are known to utilise diffuse PAR more efficiently (e.g. Goward and Huemmrich, 1992; Barton and North, 2001; Roderick et al., 2001; Gu et al., 2002; Rocha et al., 2004; Alton et al., 2005; Alton et al., 2007a; Alton and North, 2007; Alton et al., 2007b) and therefore the significance of plant canopies as a feedback component of the climate system will be affected. However, in many global/ regional bio geochemical models the diffuse PAR is poorly represented.

Change in the productivity of plant canopies has global consequences for biodiversity, land cover and food security. Therefore, accurate estimation of diffuse PAR could potentially provide improved estimation of vegetation-climate interactions and in turn reduce the source of uncertainty in global estimates of carbon, water and energy fluxes.

The aim of this chapter is to investigate three different methods to estimate the diffuse PAR fraction (K_{dQ}) reaching the Earth's surface. These methods were selected because each has the potential to be applied over large areas and is therefore suitable for making a map of K_{dQ} over a whole country or region, over different time periods depending upon the sampling frequency of the input data. The three methods are:

- Estimation of K_{dQ} based on a sky clearness index calculated from ground-based meteorological data.
- Estimation of K_{dQ} based on cloud fraction from the International Satellite Cloud Climatology Programme (ISCCP) DX data set.
- Estimation of K_{dQ} based on cloud cover determined from data collected by sensors on the Meteosat satellite.

The ISCCP DX data set was derived from analysis of satellite-measured radiances from several geostationary and polar orbiting satellites, combined with data from the TIROS Operational Vertical Sounder (TOVS) (Schiffer and Rossow, 1983; Rossow et al., 1996; Rossow and Schiffer, 1999). Although this means it has a strong physical basis, it has the disadvantage for the present application that it has a nominal pixel size of 30 km and a temporal resolution of 3 hours. In contrast, the Meteosat sensor provides data every 30 minutes in near real-time and has a nominal pixel size of 2 km from the British Atmospheric Data Centre (BADC) (www10), making it much better suited to near real-time vegetation monitoring across a large spatial scale. Furthermore, the visible wavelength channel of the Meteosat sensor (450 – 1000 nm) is a closer match to the PAR region than the spectral band available from the ISCCP product. Cloud cover was estimated from the Meteosat data using a simple empirical method, as described below.

4.2 Data

4.2.1 Ground data

Chapter 2 described the instruments available to measure the diffuse broadband fraction (K_{dS}) and K_{dQ} at a single point, but such instruments are generally not deployed in sufficient numbers to provide regional or national scale data on diffuse PAR (Q_d). One reason for this is the need for regular manual adjustment of a shadow band or similar device, which means that such instruments cannot be deployed at automated weather stations. The impact of this is seen in the UK, where routine measurements of diffuse proportion were terminated at 11 stations when automated instruments were introduced to replace the previous manual instruments (www11). Despite having over 100 meteorological stations in total across the UK, only two stations recorded diffuse flux data during the period 2001 – 2007, at Camborne and Lerwick (Fishwick, 2007b; Fishwick, 2007a).

Ground data for this research were collected at the Chilbolton Facility for Atmospheric and Radio Research (CFARR), a research station owned and operated by the UK Science and Technology Facilities Council (STFC) (see Section 3.2.1). Of the extensive suite of instruments at CFARR, two were used in this research: (1) a Delta-T Devices BF3 Sunshine Sensor™ (Figure 4.2.1a) which was installed at the CFARR from September to November 2009, for direct measurement of diffuse PAR (Q_d), and total PAR (Q_t) specifically for this study and (2) a Kipp and Zonen CM 21 pyranometer (Figure 4.2.1 b), measuring global broadband (305-2800 nm) solar irradiance, S_t, which has been installed at the CFARR since May, 2003.

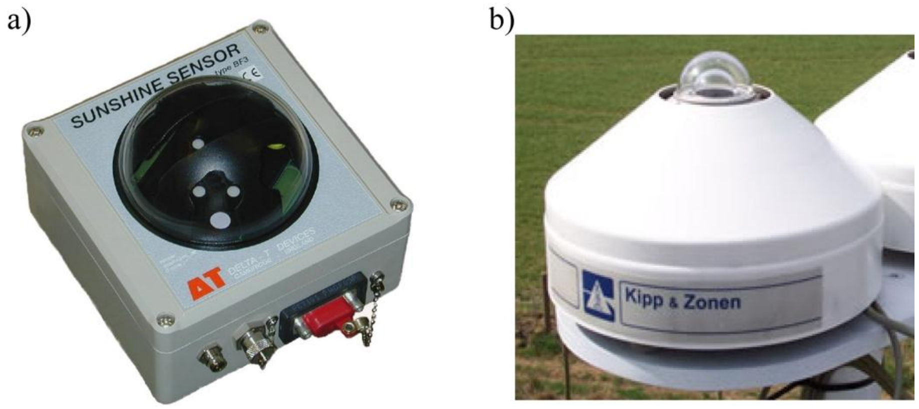

Figure 4.2.1 a) Delta-T Device Sunshine Sensor model BF3, b) Kipp and Zonen pyranometer model CM 21

Both instruments were set to measure the solar radiation falling on a horizontal plane. Data collected from the pyranometer and the BF3 Sunshine Sensor during the period September to November 2009 were used to derive and test the relationship between K_{dQ} and the amount of total broadband radiation reaching the ground, expressed as a fraction of the extraterrestrial solar radiation at the top of the Earth's atmosphere. Data from these instruments were used to calculate K_T, the sky clearness index. The CFARR site is relatively flat and the instruments had a clear view of the sky in all directions. The area around the site is mostly agricultural.

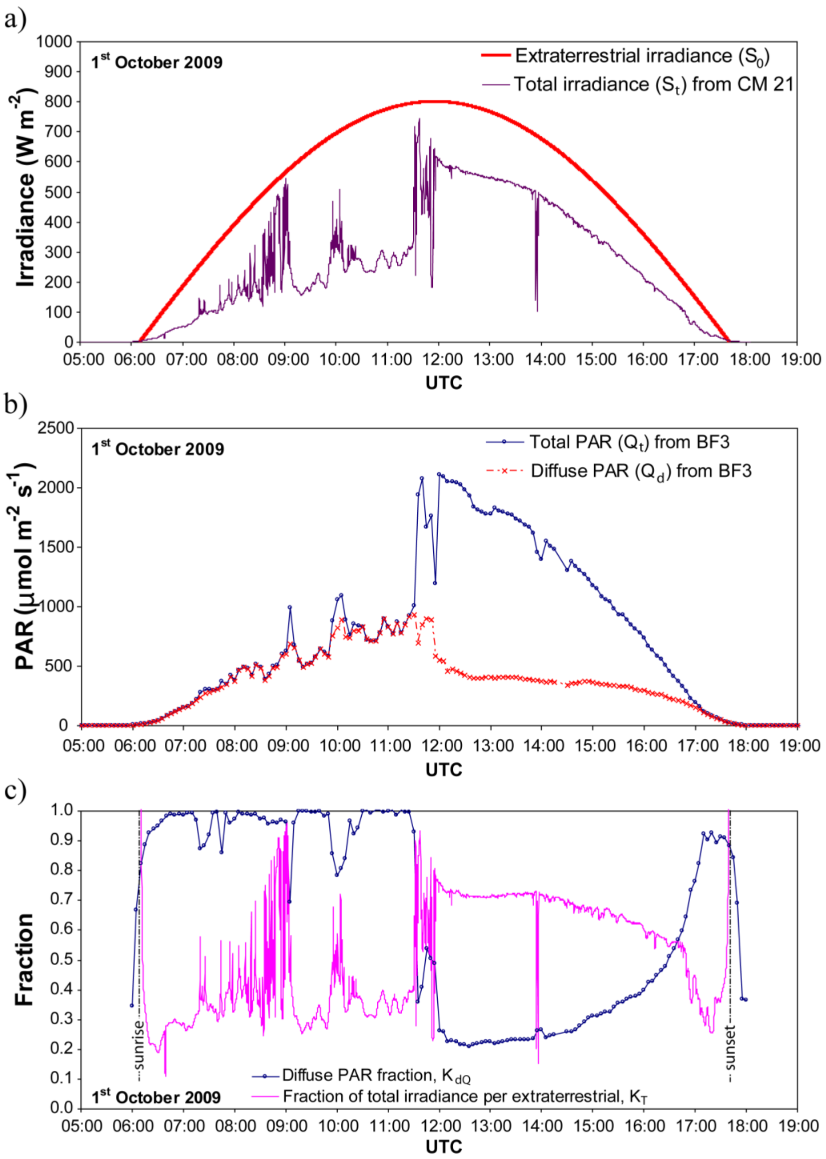

Figure 4.2.2 a) an example of variation of extraterrestrial solar radiation on the horizontal plane at the top of the Earth's atmosphere (S_0) and variation of total broadband radiation on the Earth's surface (S_t), b) an example of variation of diffuse and total PAR at CFARR, c) comparison between K_{dQ} and K_T at CFARR, 1st October 2009

The BF3 was programmed to measure Q_d and Q_t every five minutes during daylight hours. The limitation of the memory of the BF3 data logger made the frequency of the recorded data from the BF3 to be every five minutes. Measured data show the variation of Q_d and Q_t (Figure 4.2.2 b).

The broadband solar irradiance data measured at CFARR during 2003-2009 was downloaded from the BADC (www10). The CM 21 pyranometer measures instantaneous solar irradiation every ten seconds over the range of wavelength 305 nm to 2800 nm. Measured data show the variation of total irradiance at the CFARR (Figure 4.2.2b, thin purple line).

4.2.2 Extraterrestrial solar irradiance

The extraterrestrial solar radiation on a horizontal plane at the top of the atmosphere (S_0) can be calculated using equation in Iqbal (1983).

$$S_0 = I_{sc}E_0(\sin\delta \sin\phi + \cos\delta \cos\phi \cos\omega) \qquad (4.2.1)$$

I_{sc} = solar constant (1,367 W/m^2), E_0 = eccentricity correction factor (unit less), δ = declination angle (degree), ϕ =latitude angle (degree) and ω = hour angle (degree). This S_0 data was used in the method to estimate the K_{dQ} using the ground data. An example of the variation of calculated extraterrestrial solar radiation at the CFARR, every ten seconds on 1st October 2009, is shown in Figure 4.2.2a (thick red line).

4.2.3 Satellite data

a) ISCCP-DX data

ISCCP DX data were used to estimate K_{dQ} following the method developed by Butt et al. (2010) in Amazonia (described in the next section). The time stamps for each 3 hourly collection of the ISCCP DX data were 03:00, 06:00, 09:00, 12:00, 15:00, 18:00, 21:00 and 24:00 Coordinated Universal Time (UTC). Each cell of ISCCP DX covers an area of approximately 30 km × 30 km (Rossow et al., 1996; Rossow and Schiffer, 1999).

The ISCCP DX is a subset of the ISCCP D1 data. The ISCCP D1 data have a nominal spatial resolution at the ground of 280 km, and a temporal resolution of three hours (Rossow et al., 1996, p. 16). The ISCCP D1 data have 6596 grid cells around the globe (Figure 4.2.3), so the whole of the UK is covered by fewer than 10 grid cells. The ISCCP DX data has a finer spatial resolution (30 km) and the same temporal resolution (Rossow et al., 1996, p. 27).

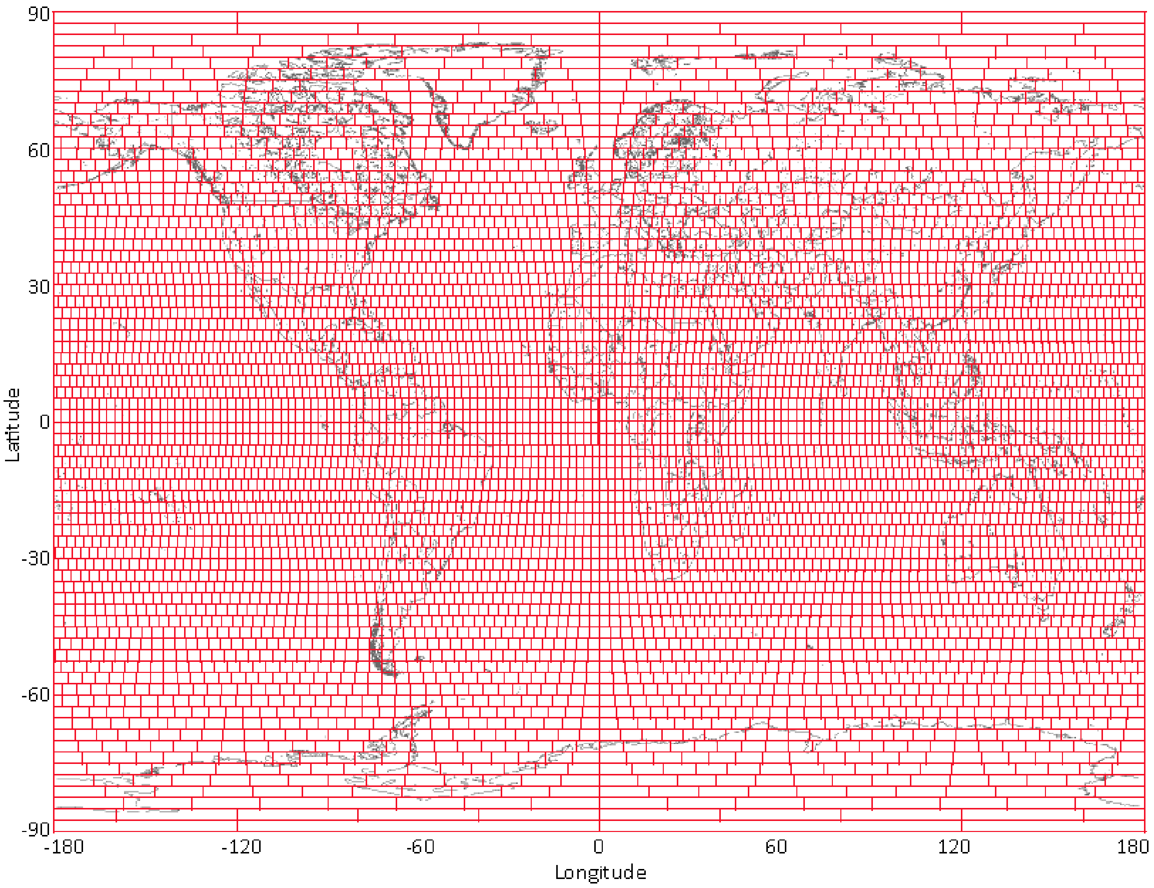

Figure 4.2.3 ISCCP D1 equal-area map grid (modified after Rossow et al., 1996)

The ISCCP DX and ISCCP D1 data over the test site in southern England is in Figure 4.2.4.

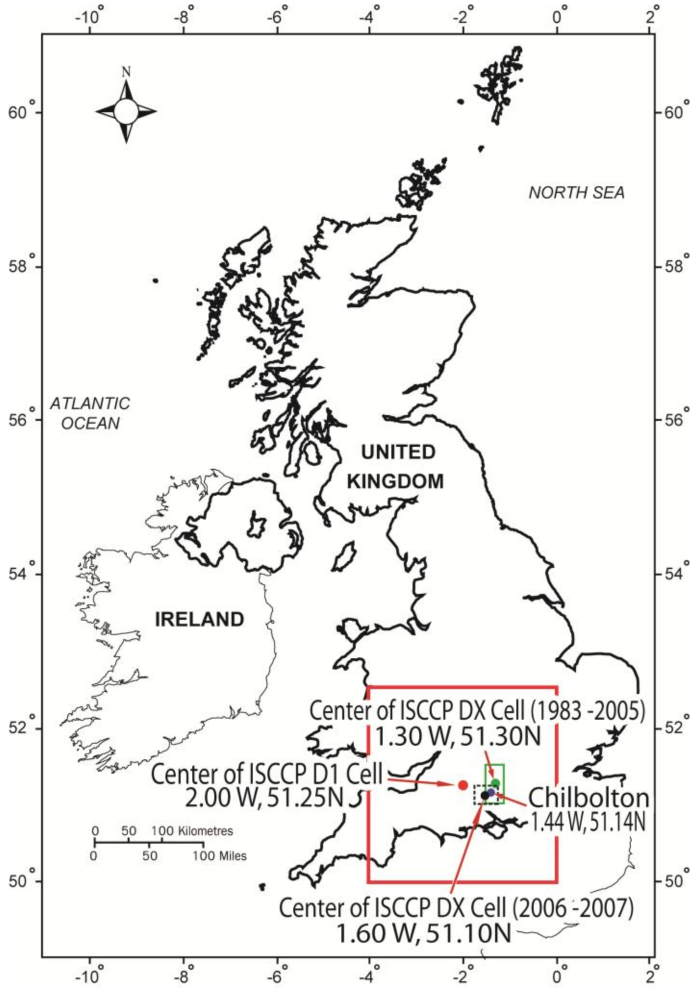

Figure 4.2.4 A ISCCP D1 equal-area map grid and ISCCP DX cells over the study site in southern of UK

b) Meteosat Satellite data

Meteosat is geostationary satellite permanently located at 0 degrees latitude and 0 degrees longitude, 35,786 km above the equator. The theoretical coverage of the sensors on Meteosat extends to 81 degree radius of latitude-longitude; approximately covering 40 % of the Earth's surface over Europe and Africa (www12). The visible band of many geostationary satellites have been widely used to represent cloud in modelling and estimation for studying solar radiation on the Earth's surface (e.g. Gautier et al., 1980; Diak and Gautier, 1983; Dedieu et al., 1987; Frouin and Pinker, 1995; Skartveit et al., 1998; Ineichen and Perez, 1999; Vignola et al., 2007; Janjai et al., 2009; Janjai et al., 2011; Janjai and Wattan, 2011).

Visible band data (450 – 1000 nm) from the Meteosat sensor were obtained from the British Atmospheric Data Center (BADC; www11) in the form of full disc 8-bit images, 5000 x 5000 pixels in size, every 30 minutes from 03:30 UTC to 20:30 UTC, over the period August 2003 – June 2006 (approximately 30,000 images) (an example is in Figure 4.2.5). The pixel size is 2.5 km at nadir. Each pixel has an 8-bit digital number (DN), i.e. grey levels in the range of 0-255.

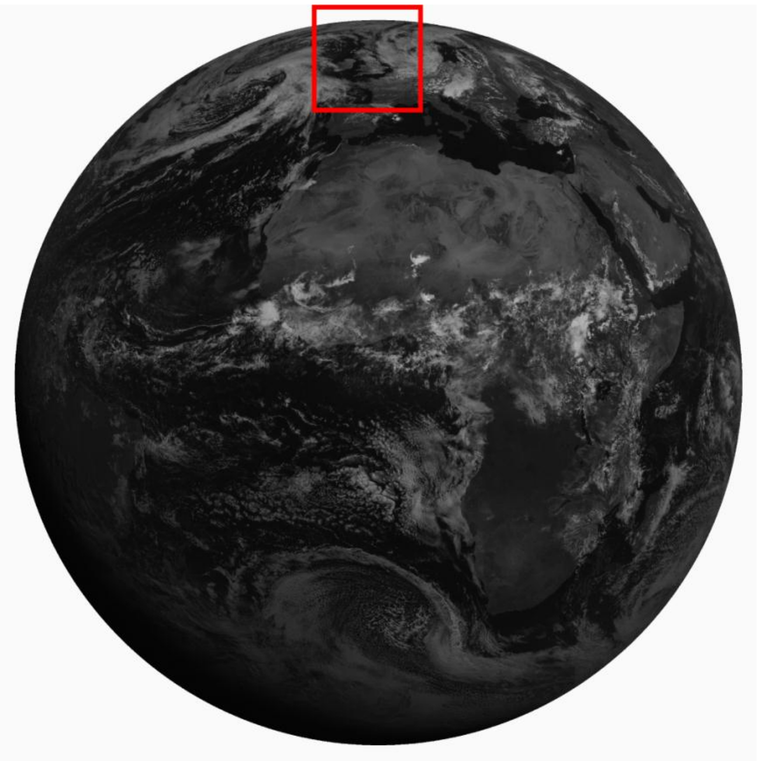

Figure 4.2.5 Full-disk satellite image (5000 × 5000 pixels), at 11:00 UTC on 25th June, 2004

The full-disk DN data were converted to a cylindrical projection. Geometry correction from the full-disk images, to become the cylindrical projection images over UK, is needed to identify the position of pixels for the interested location. The geometry correction is processed using transformation of map projection to correct the images from the full-disk of satellite projection into the cylindrical projection for a three-year time series.

Cylindrical projection images were then adjusted using Ground Control Points (GCP). In this adjustment, coast and boundary lines were used for identifying the location of the latitude and longitude position of the whole image pixels. Each image has been moved until the position of the boundary line and the coast line of the DN images is the best fit to the reference coast and boundary line.

The geocorrected DN images were then subset to extract the area over the UK, resulting in a three-year time series of images 460 × 700 pixels, with nominal pixel size 2.5 km × 2.5 km, an example of which is shown in Figure 4.2.6.

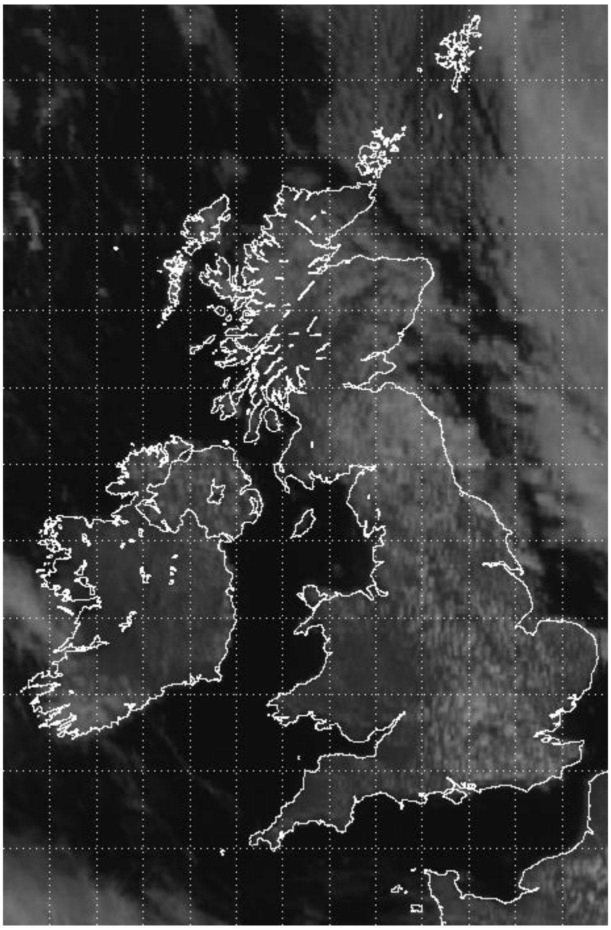

Figure 4.2.6 Subset of Meteosat data between latitude 49 °N to 61 °N, longitude 11 °W to 2 °E (460 × 700 pixels), with the coastline of the British Isles overlain (cylindrical projection), at 11:00 UTC on 25th June, 2004

4.3 Methods

4.3.1 Estimation of K_{dQ} based on a sky clearness index calculated from ground-based meteorological data

The aim of the first method was to estimate K_{dQ} from a sky clearness index calculated from the ratio between broadband extraterrestrial irradiance and broadband irradiance measured by a sensor at ground level. Chapter 2 described the development of this method by the meteorological research community. However, the emphasis of previous work has been on estimation of diffuse broadband fraction, unlike in this study in which the aim is estimation of the diffuse PAR fraction.

Figure 4.2.2 shows an example of the data collected at CFARR on 1st October 2009, a day with highly changeable weather conditions in which a wide range of cloud conditions were present. Variation of calculated extraterrestrial solar radiation on the horizontal plane at the top of atmosphere, S_0 at CFARR has been plotted to compare against variations of the measured total irradiance, S_t from the Kipp and Zonen CM 21 pyranometer every ten seconds (Figure 4.2.2a). Variations of the measured diffuse PAR (Q_d) and measured total PAR (Q_t) from the BF3 Sunshine Sensor have been plotted every five minutes (Figure 4.2.2b) over the same day.

From diurnal variation of the observed data (Figure 4.2.2 a and b) and diurnal variation of the K_{dQ} with fraction of the global broadband per extraterrestrial irradiance on the horizontal surface (K_T, clearness index) (Figure 4.2.2 c), it appears that K_{dQ} has an inverse relationship with K_T which is similar to the widely known relationship between the K_{dS} and K_T (e.g. Hay, 1993; Roderick, 1999; Jacovides et al., 2006; Boland et al., 2008). K_T and K_{dQ} were calculated and a time series of K_T every ten seconds was plotted to compare with every five minutes of K_{dQ}. An example of these data is shown in Figure 4.2.2c. When K_T increases, K_{dQ} decreases. In the same way, when K_T decreases, K_{dQ} increases. K_{dQ} fluctuated around 0.2-0.8 while K_T mostly varied between 0.2 -1.0.

From Figure 4.2.2c there are extreme values of K_{dQ} around sunset and sunrise. These are due to the calculated values of extraterrestrial solar radiation, S_0 being zero shortly before sunrise and after sunset, therefore K_T has sharp peaks at the beginning and the end of the day, at sunrise and sunset time (continuous line without circle in Figure 4.2.2c). However, both Q_d and Q_t come from measured data using BF3; the BF3 can measure Q_d and Q_t before sunrise and after sunset, probably because the effect of the twilight; therefore the graph still shows K_{dQ} before sunrise and after sunset time (continuous blue line with small circles in Figure 4.2.2c).

The measured data between 1st October – 6th November 2009, sunrise until sunset, were used to find the 3-hourly relationship between K_{dQ} and K_T. The relationship is shown in Figure 4.3.1.

The best-fit equation for this relationship follows a power law, and is defined as:

$$y = -2.2171x^2 + 0.5355x + 0.9644 \qquad (4.3.1)$$

where $y = K_{dQ}$ (unitless) and $x = K_T$ (unitless). The coefficient of determination, R^2 = 0.94. The relationship between K_{dQ} and K_T is therefore confirmed as similar to that between K_{dS} and K_T described by Jacovides et al. (2006).

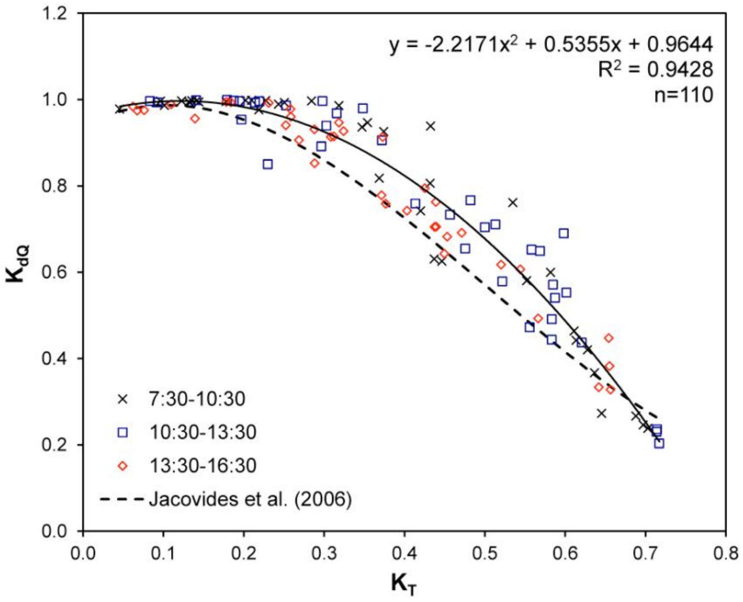

Figure 4.3.1 3-hourly relationship between K_{dQ} and K_T at CFARR, 1st October – 6th November 2009

The relationship between K_{dQ} and K_T was validated using an independent data set collected at CFARR between 10th-30th September 2009 (Root Mean Square Error (RMSE) = 0.09, Mean Bias Error (MBE) = -0.03).

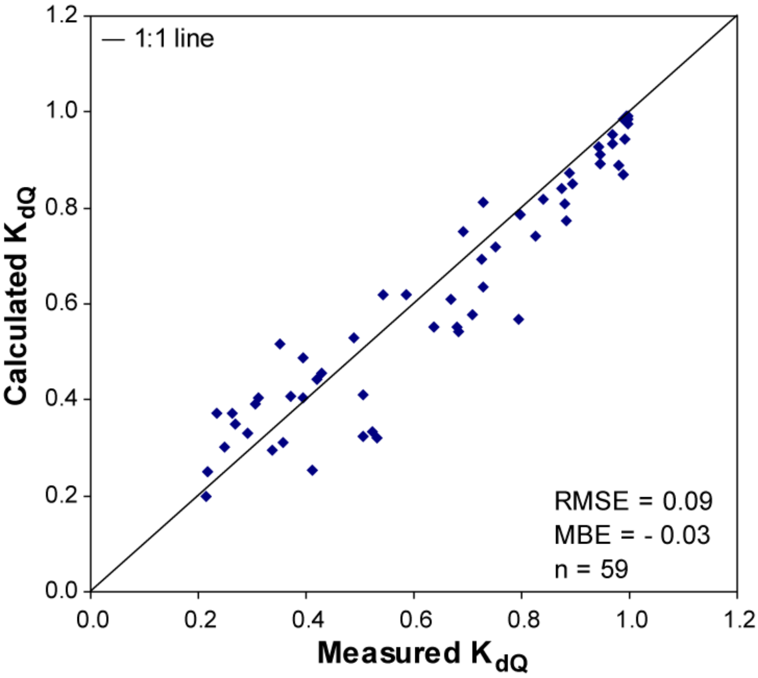

Figure 4.3.2 Comparison of 3-hourly measured and calculated K_{dQ} at the CFARR, using data collected during 10th-30th September 2009

The results of the first investigation show that it is possible to estimate K_{dQ} reaching the ground to a high level of precision, based on a simple broadband sky clearness index.

Ideally, the diffuse PAR fraction would have been derived from the measurement of Q_d and Q_t, using the equation: $K_{dQ} = Q_d/Q_t$. Unfortunately, Q_d and Q_t are not routinely measured at most of UK meteorological stations. However the strong relationship between K_{dQ} and K_T (Equation 4.3.1) suggests a way to overcome this problem. K_T was calculated as $K_T = S_t/S_0$, which only needs measurement of S_t, as S_0 can be calculated using equations in Iqbal (1983). Many meteorological stations measure S_t, therefore it is possible to calculate K_T and then K_{dQ} can be estimated using the relationship between K_{dQ} and K_T (Equation 4.3.1).

It would be possible to use this method to produce a map of K_{dQ} across the whole of the UK. Although attractive in its simplicity, this method would not address the aims of this thesis as it would require the interpolation of data between meteorological sites and this might obscure subtle effects such as the influence of land cover on the proportion of diffuse flux. For example, a large forest might affect the local climate and therefore the local diffuse PAR flux, which would not be captured by data derived from meteorological stations at distant locations, such as airfields.

The aim of this thesis requires a per-pixel estimate of K_{dQ} derived from satellite data, in which complete coverage of the study area is available. Therefore the role of the ground-based method in this thesis is twofold. First, it provides a method to extend the short period of K_{dQ} measurements made at CFARR (a few weeks) to a much longer time period (several years). Second, it provides a method to create a spatially distributed validation data set since we can be reasonably confident that the measurements made at other meteorological stations around the UK conform to the relationship shown in Figure 4.3.1.

4.3.2 Estimation of K_{dQ} based on cloud cover from the International Satellite Cloud Climatology Programme (ISCCP) DX data set

As described earlier, the ISCCP DX cloud cover data set provide a physically-based, validated global data set extending over several years, it is therefore an attractive source of data to use when estimating trends and patterns of diffuse PAR at the ground.

To find the relationship between K_{dQ} and cloud fraction from ISCCP DX data, long-term ground data are needed in order to estimate sky clearness (Equation 4.3.1). However, Q_d and Q_t were only available from CFARR for a short period, 1st October – 6th November 2009. Therefore it was necessary to develop a method to estimate K_{dQ} over the longer period desired.

Butt et al. (2010) found a relationship between K_{dS} and cloud fraction based on ISCCP DX data, at two study sites in Amazonia (in Supplementary Fig.S2 in Appendix

A of Butt et al., 2010). In this chapter, the Butt et al. (2010) method was used to test the relationship between $\mathrm{K_{dQ}}$ and cloud fraction at CFARR.

First, Equation 4.3.1 was used to estimate $\mathrm{K_{dQ}}$ at CFARR every 10 s during daylight hours between May 2003 and June 2008, and these data were averaged to produce a three-hourly data set to match the sampling time of ISCCP DX (09:00, 12:00 and 15:00). The relationship between $\mathrm{K_{dQ}}$ and cloud fraction on a daily, 5-day, 10-day and monthly basis during May 2003 – June 2008, was then analysed.

The cloud fraction from the ISCCP DX is an indication of the quantity of cloud cover over a cell of contiguous pixels. In each cell, the cloud fraction for each 3-hourly time step is divided into two types: cloudy and cloudless over the area of interest, indicated as 1 and 0 respectively. The ISCCP-DX cloud fraction is determined from satellite data in the visible, near-infrared and thermal wavebands (Rossow et al., 1996).

The cloud fraction is 1 (for cloudy) otherwise 0 (for cloudless), determined from the condition in the DXREAD Fortran software (Rossow et al., 1996, p. 32):

$$\begin{array}{l}\mathrm{If\,(\,ITHR\ >\ 3\,OR\,VTHR\ >\ 3\,OR\,NTHR\ >\ 8\,)}\\ \mathrm{then\ CLOUD} = 1\ /*\ \text{pixel is cloudy}\ */\\ \mathrm{else\ CLOUD} = 0\ /*\ \text{pixel is clear}\ */\end{array} \qquad (4.3.2)$$

where ITHR is final IR threshold result (0-5), VTHR is final VIS threshold result (0-5) and NTHR is NIR threshold result (1-13).

The relationship between the estimated $\mathrm{K_{dQ}}$ at the CFARR and cloud fraction from ISCCP DX data during May 2003 – June 2008 for daily, 5-day, 10-day and monthly periods is shown in Figure 4.3.3.

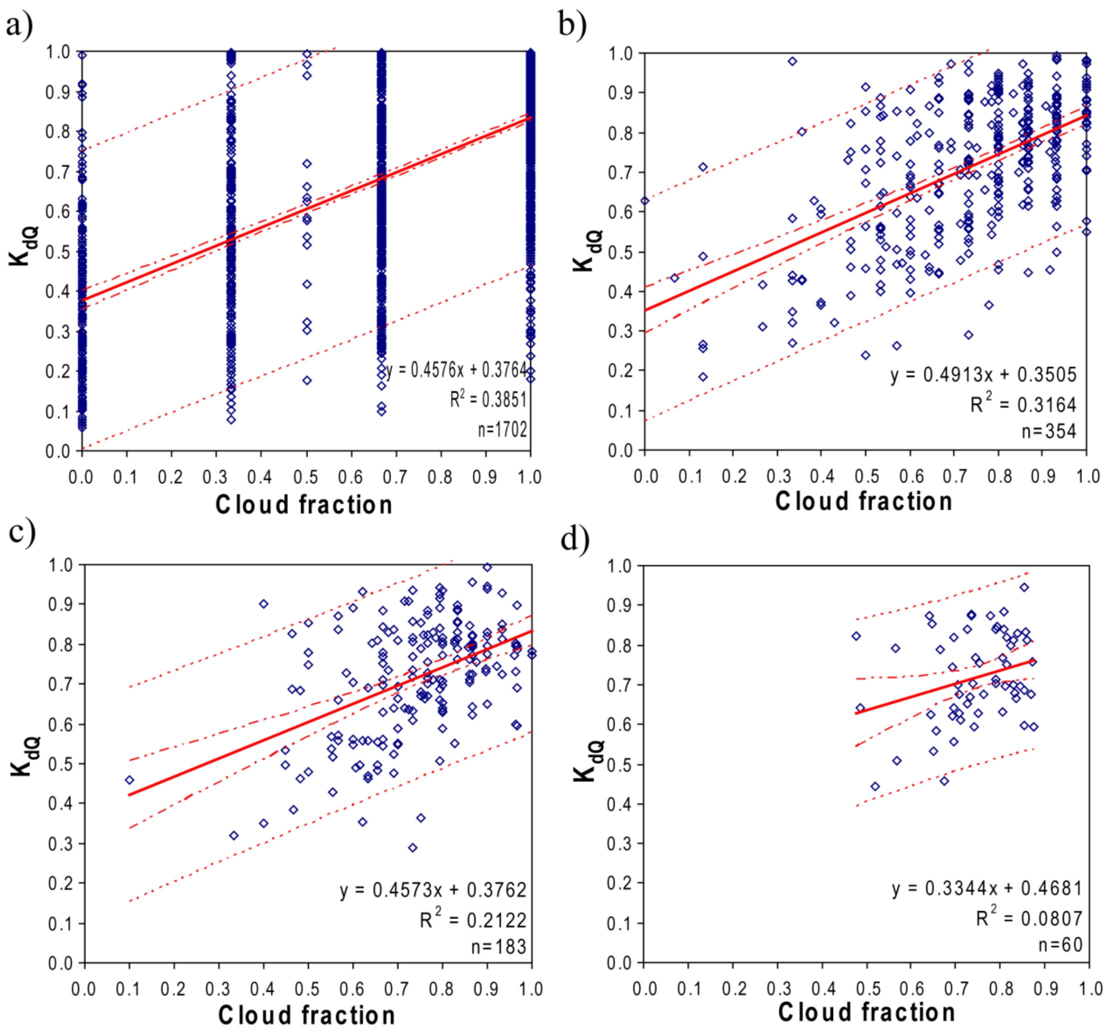

Figure 4.3.3 Relationship between estimated diffuse PAR fraction, K_{dQ}, at CFARR and cloud fraction from ISCCP DX data for a) daily, b) 5-daily, c) 10-daily and d) monthly basis (May 2003 – June 2008), ——— is trend line, -·-·-·- is 95 % confidence interval line, , ·········· is 95 % prediction interval line

Cloud fraction for the daily, 5-daily, 10-daily and monthly relationship came from 3-hourly data, and for some time periods grouping of data values was created by the way the ISCCP cloud fraction data were made available. This can be seen in the daily and 5-day data. For example, from the days that have three values of cloud fraction, the possible result for the sum in each day is 0, 1, 2 and 3; therefore the average results could only be either 0, 1/3, 2/3 or 1, as indicated by the line of dots in Figure 4.3.3a).

The results of estimating K_{dQ} from the ISCCP cloud fraction data were disappointing, with none of the relationships (daily, 5-day, 10-day, monthly) being statistically significant. The strongest relationship was found over the 5-day sampling interval, but the scatter of points was very high, meaning that the uncertainty in predicted K_{dQ} would be too large to be useful. Possible reasons for this failure of the method have been alluded to earlier, and it is thought that the large pixel size of the ISCCP DX data combined with the three-hour averaging period is the main problem. A three-hour average over a 30 km x 30 km pixel is too generalised for this type of analysis in the UK, unlike in Amazonia, where Butt et al (2010) found much better relationships between K_{dS} and cloud fraction derived from ISCCP DX.

4.3.3 Estimation of K_{dQ} based on cloud cover determined from data collected by the Meteosat instrument

Compared to ISCCP DX data, Meteosat has finer spatial resolution and better temporal resolution. The spatial resolution and temporal resolution of the ISCCP DX is approximately 30 km at 3-hourly intervals, while the nadir resolution of the Meteosat data is approximately 2.5 km every half-hour. Therefore, in terms of both spatial and temporal resolution, the Meteosat data should give a better relationship to K_{dQ} than ISCCP DX data.

To find the relationship between the K_{dQ} and Meteosat data, the Meteosat DN values were converted into an index of Estimated Cloud Cover (ECC) by dividing each DN value by the monthly maximum of DN value for that particular half-hour period, assuming that the highest visible DN values would occur when the pixel was cloud covered. It can be written as an equation:

$$\mathrm{ECC} = \mathrm{DN}/\text{monthly maximum DN} \qquad (4.3.3)$$

The ECC from available Meteosat data over the CFARR site were extracted and used to test the relationship between K_{dQ} and ECC over a daily, 5-day, 10-day and monthly basis, between August 2003 and June 2006 (Figure 4.3.4).

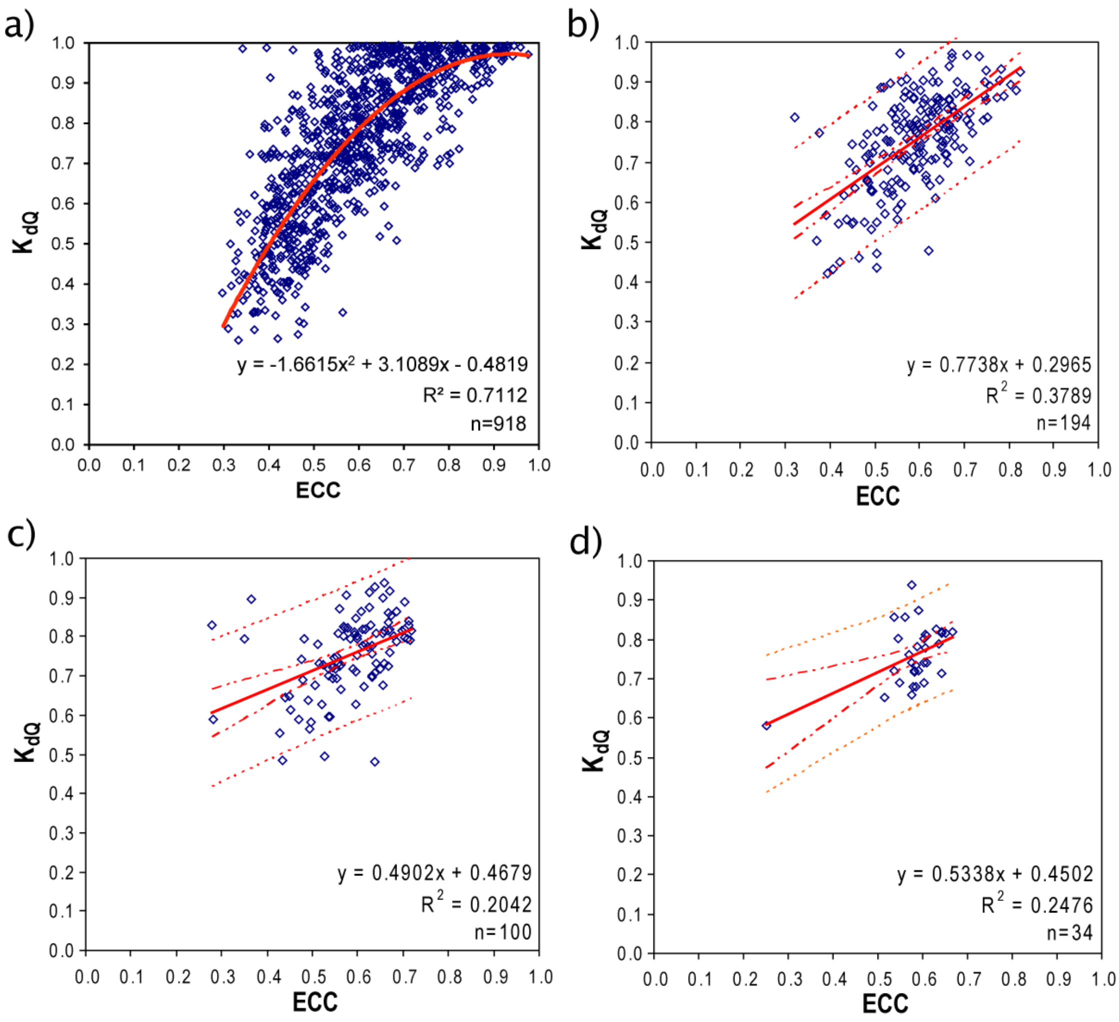

Figure 4.3.4 Relationship between estimated diffuse PAR fraction, $\mathrm{K_{dQ}}$, from ground based measurements at CFARR and the ECC from Meteosat satellite for a) daily, b) 5-day, c) 10-day and d) monthly basis (August 2003 – June 2006), —— is trend line, -·-·- is 95 % confidence interval line, ······ is 95 % prediction interval line

The clearest relationship between ECC and $\mathrm{K_{dQ}}$ was found for the daily data (Figure 4.3.4.a). A second-order polynomial was fitted to the data using least trimmed squares (LTS) regression, a method of robust linear regression that reduces the effect of outliers on the fitted relationship (e.g. Wang et al., 2008; Doornik, 2011).

$$\mathrm{K_{dQ}} = -1.6615(\mathrm{ECC})^2 + 3.1089(\mathrm{ECC}) - 0.4819 \qquad (4.3.4)$$

The R^2 value (0.711) was significant at $P < 0.001$, so despite the large amount of scatter, variation in ECC is able to explain approximately 70% of the variation in daily K_{dQ}.This confirms the hypothesis that Meteosat data is better than ISCCP DX data for estimating the proportion of diffuse PAR in the UK.

In the next section, the daily relationship between ECC derived from Meteosat data and the proportion of diffuse PAR reaching the ground is used to generate maps of K_{dQ} for the whole of the UK.

4.4 Application to mapping diffuse PAR across the UK

4.4.1 UK Diffuse PAR fraction mapping from Meteosat satellite data

The spatial pattern of K_{dQ} over the whole of the UK was calculated for all 30,000 Meteosat images, every half-hour, using the daily relationship between K_{dQ} and ECC from Figure 4.3.4a (Equation 4.3.4). These data were then used to generate the monthly average of K_{dQ} across the whole country over the period August 2003 - June 2006. The long-term monthly average was then calculated based on the predicted values of K_{dQ} across the UK during August 2003 – June 2006 (Figure 4.4.1).

The maps suggest that, on a monthly basis, at least two-thirds of the PAR reaching the ground does so as diffuse flux, for all parts of the UK and at all times of the year. The diffuse proportion is highest for the whole country in the winter months (December, January and February) as would be expected, although the K_{dQ} was lower in eastern Scotland in February. This might be caused by lying snow which could be mistaken for cloud in the calculation of maximum monthly DN from Meteosat data. A clear north-south gradient in K_{dQ} is evident in the summer months (June, July, August), with southern England receiving a much higher proportion of direct PAR than areas further north, especially Scotland and Northern Ireland.

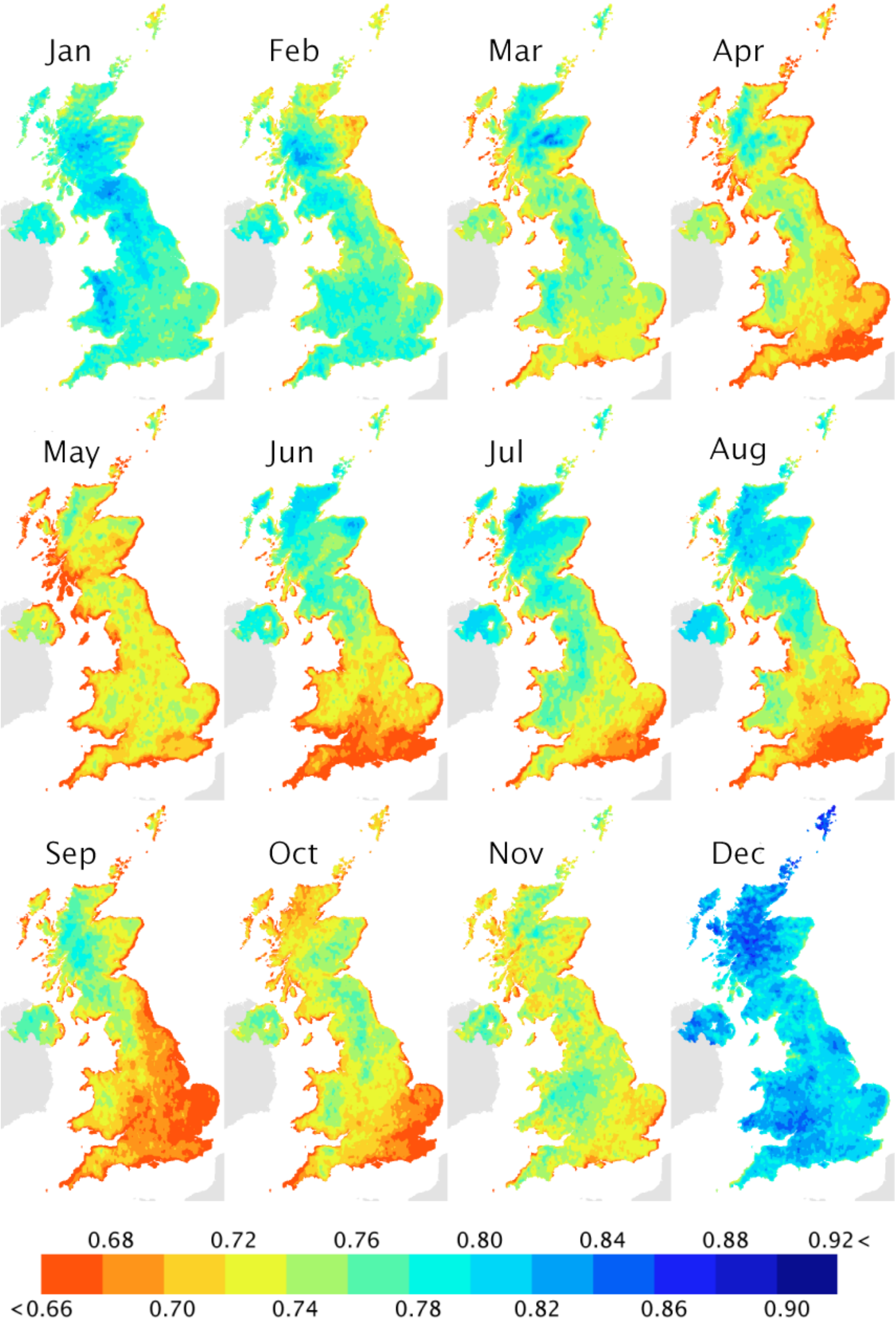

Figure 4.4.1 Monthly K_{dQ} averaged from long-term data during 2003-2006

The results show lowest values of K_{dQ} in coastal areas, especially the southern coast during the summer months. Also notable is the low K_{dQ} along the west coast of Scotland in May and along the east coast of England in September. The greatest contrast between different parts of the country appears to be during the summer months, especially August, when a much higher fraction of the PAR in Scotland is in the form of diffuse PAR, than in England.

In general, coastal regions have lower K_{dQ} than inland regions K_{dQ}, which might be due to errors in geometric correction being more obvious in these areas or it could be an accurate record of the conditions in these areas.

The maps presented in Figure 4.4.1 were derived from relationships that had a lot of scatter, but the broad trends appear plausible, considering the monthly variation of the UK weather (Prior, 2010). From the maps, it can be seen that over the period 2003-2006, K_{dQ} in the UK was highest in December and most spatially uniform in January and May. In the south of the UK, the highest K_{dQ} was in December, it then slowly decreased to a minimum during April-September and increased again after September.

In the northern UK, the maximum K_{dQ} was in December and August. From the highest K_{dQ} in December, it slowly decreased to reach the lowest in May and then slowly increased to reach a second maximum in August. It then decreased to reach a low K_{dQ} in October-November and become high again in December. The greatest contrast between different parts of the country appears to be during the summer months, especially August, when a much higher fraction of the PAR in Scotland is in the form of diffuse PAR, as opposed to the situation in England.

4.4.2 Validation of the relationship between K_{dQ} and ECC using independent data

The map shown in Figure 4.4.1 was validated in two ways. First, by direct comparison with those meteorological sites where direct measurements of diffuse proportion were made during the period studied. Second, by comparing the data measured at meteorological sites where the ground-based method could be applied (i.e. Equation 4.3.1).

a) Validation using independent measurements of K_{dQ}

The independent measurements of diffuse fraction were made at two UK meteorological stations: (i) Camborne (Latitude 50.2167 °N, Longitude 5.3167 °W) and (ii) Lerwick (Latitude 60.1333 °N, Longitude 1.1833 °W) (Figure 4.4.2). The data at both sites during 2001 to mid-2007 were made available at: (www13) by Fishwick., (2007a, b). The in-situ data comprised broadband irradiance (total and diffuse) measured using a Kipp and Zonen solarimeter fitted with a shadow band, therefore, it was necessary to assume that $K_{dQ} = K_{dS}$.

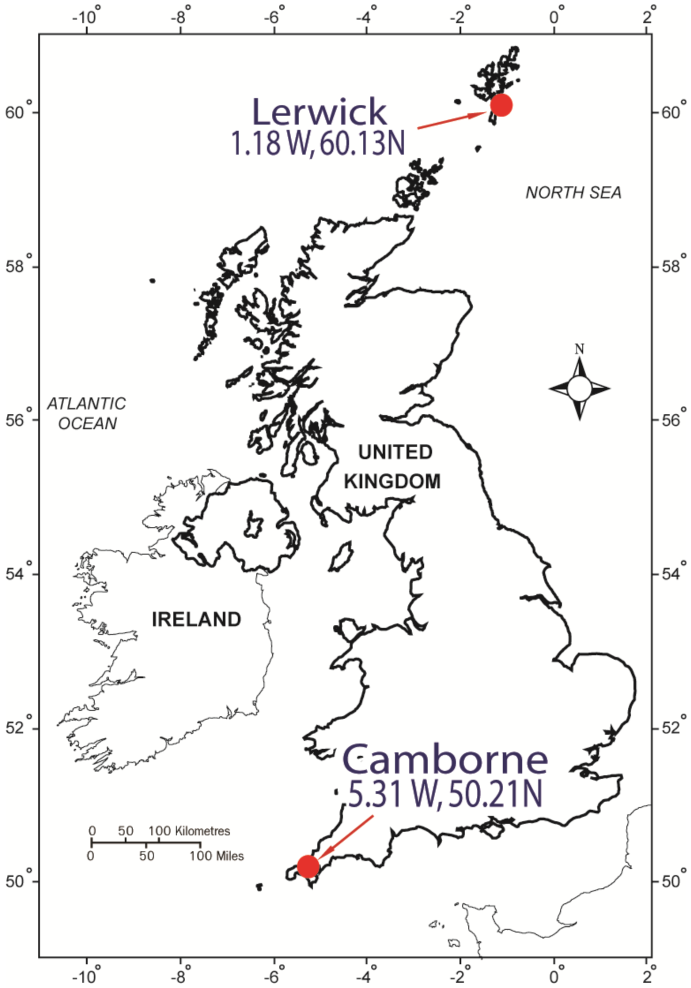

Figure 4.4.2 Position of two meteorological stations that have diffuse irradiance measurement, Camborne in Cornwall and Lerwick in the Shetland Isles

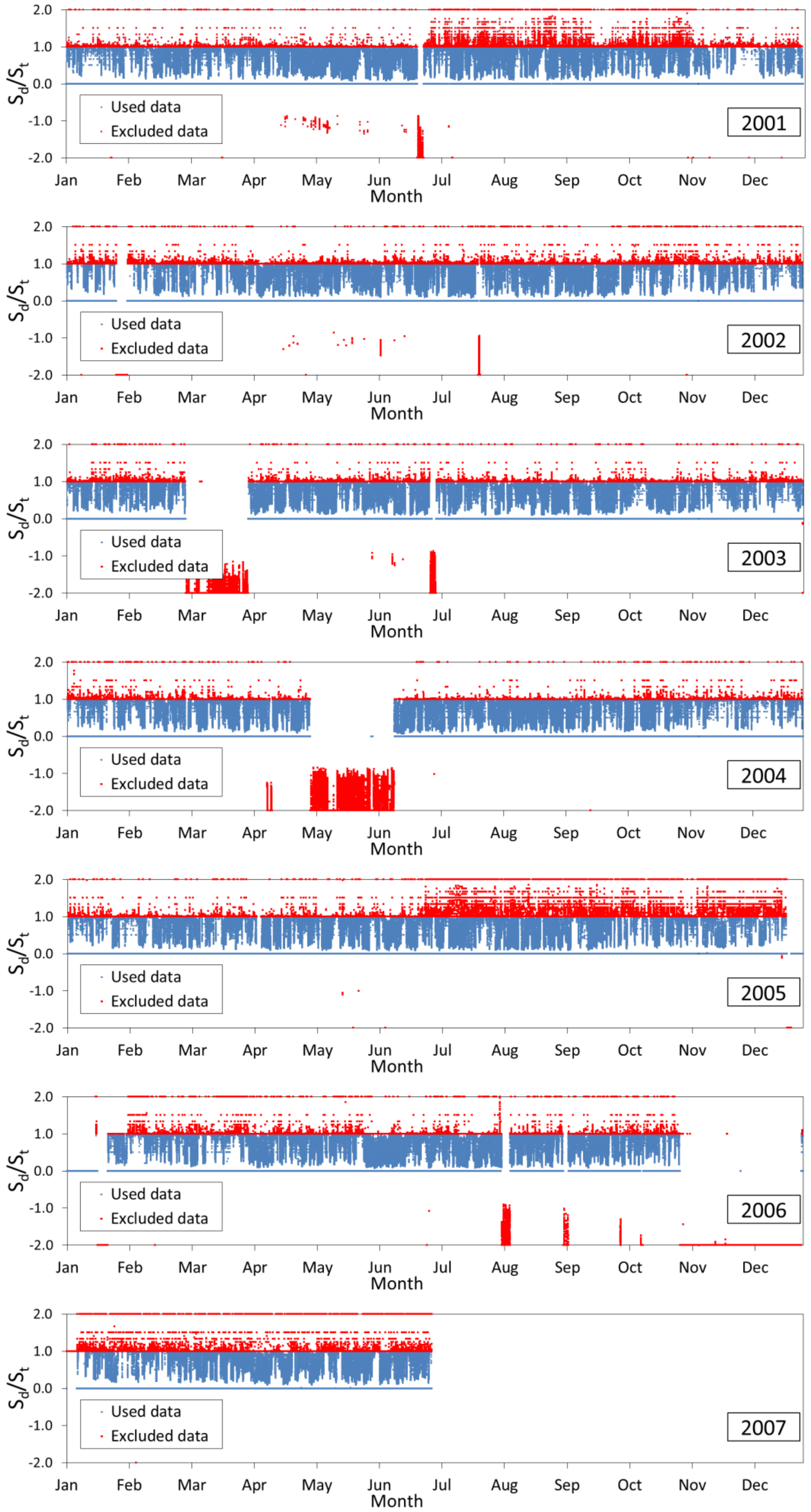

Figure 4.4.3 Used data and excluded data for the K_{dQ} validation at Camborne

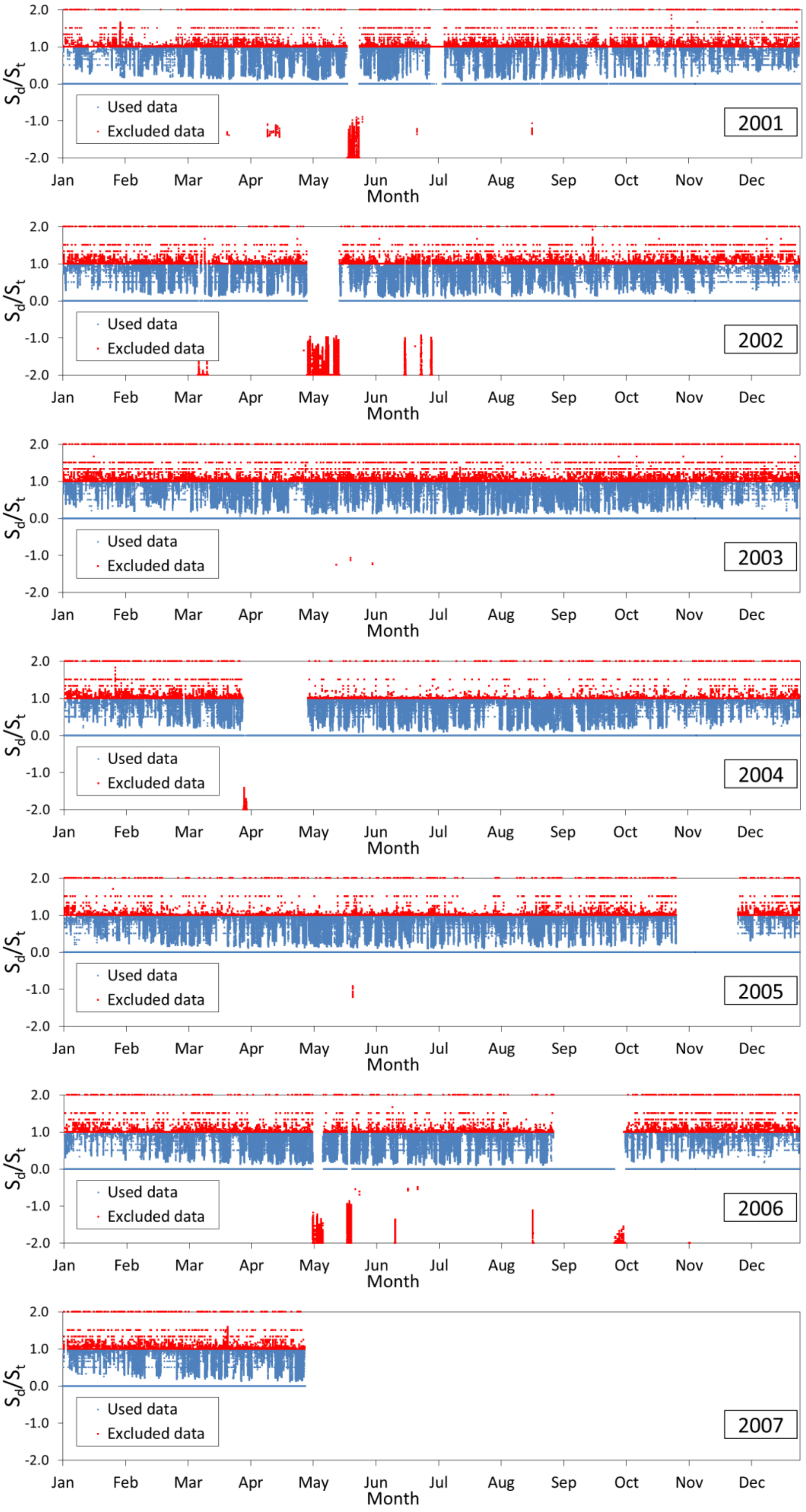

Figure 4.4.4 Used data and excluded data for the K_{dQ} validation at Lerwick

Inspection of the in-situ data revealed some values with S_d equal to or greater than S_t, which is not realistic, and suggested that the shadow band was not adjusted correctly on those occasions. Some data (n = 472,561; approximately 34% of the minutely data at Camborne and n= 610,775; approximately 44% of the minutely data at Lerwick in 2001 -2007, Figure 4.4.3 – 4.4.4) were omitted from the validation, resulting in the relationship shown in Figure 4.4.5 in which data from the two sites were estimated to within 10% RMSE.

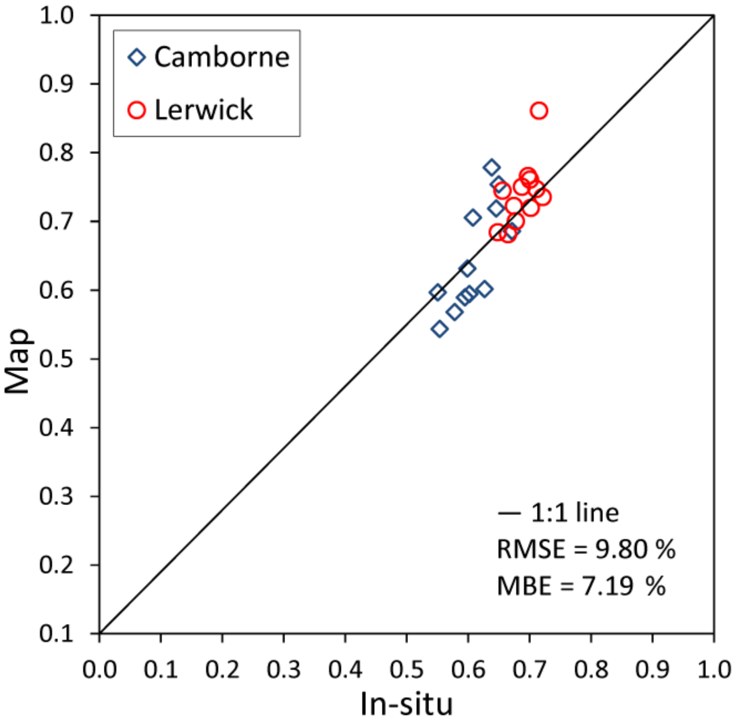

Figure 4.4.5 Validation between the map and the in-situ data at Camborne and Lerwick

To conclude, direct validation using independent ground data from two geographically separated Met Office stations, and based on the assumption that $K_{dQ} = K_{dS}$, the method had an accuracy (RMSE) of 9.80 % (MBE=7.19 %). In order to achieve this level of accuracy it was necessary to exclude those ground data in which $S_d \geq S_t$, which were assumed to be in error.

b) Validation using independent estimates of K_{dQ}

The monthly long-term average maps (Figure 4.4.1) were also validated using the measured S_t data from 98 UK meteorological stations (Figure 4.4.6). Those stations did not have available diffuse irradiance data but did have S_t data measured using CM11 Kipp and Zonen pyranometers. The S_t data from the 98 stations were used to calculate K_T using equation: $K_T = S_t/S_0$. Then, the relationship between K_{dQ} and K_T (Equation 4.3.1), was used for the in-situ K_{dQ} calculation. The validation result is shown in Figure 4.4.7.

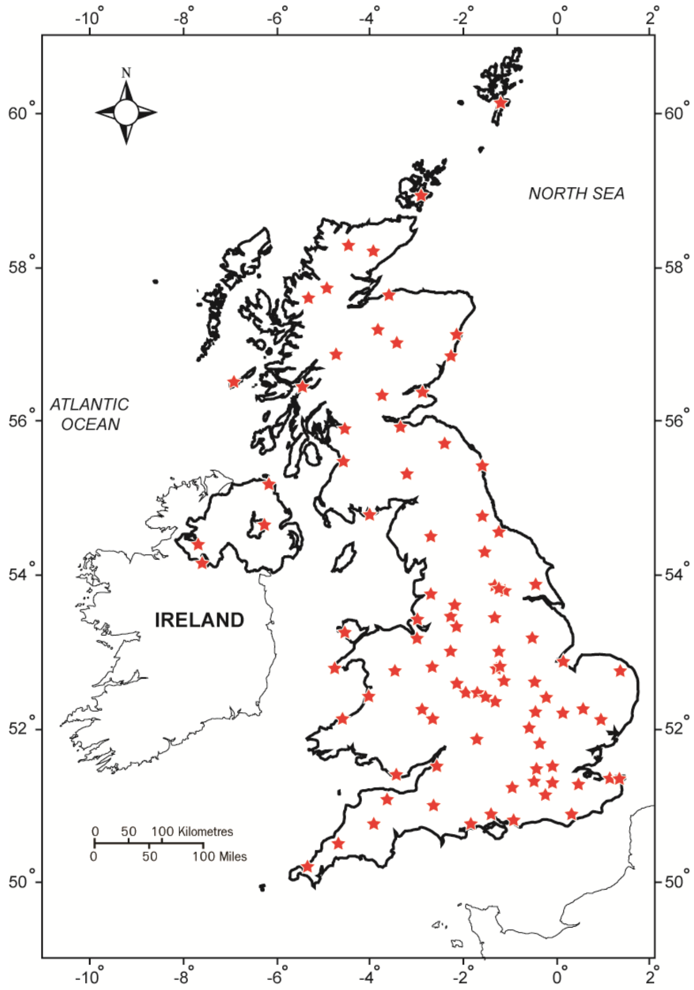

Figure 4.4.6 Positions of 98 meteorological stations (★) during 2003-2006, from which K_{dQ} was calculated based on, S_t and using the relationship between K_{dQ} and K_T (Equation 4.3.1)

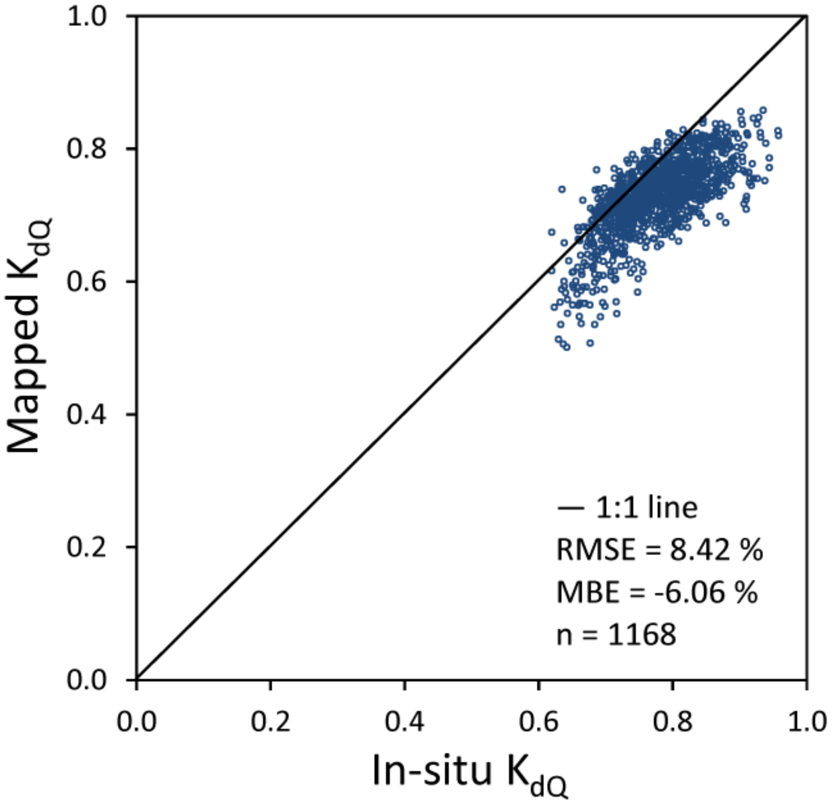

Figure 4.4.7 Validation between the map and the in-situ data. The in-situ K_{dQ} was calculated from relationship between K_{dQ} and K_T and the measured S_t data

The accuracy of the second validation method was similar to that of the first method, but the larger number of points in Figure 4.4.7 reveal a slight negative bias (i.e. mapped K_{dQ} slightly underestimated). This may be a real bias in the method (using Equation 4.3.1 estimate K_{dQ} from K_T) or it could be due the proportion of diffuse broadband flux being slightly different to the proportion of diffuse PAR flux (i.e. the assumption that $K_{dQ} = K_{dS}$ is incorrect).

4.5 Limitations of the Meteosat method and its validation

Although using Meteosat data provides advantages in terms of spatial and temporal resolution, there are a number of disadvantages of the data and the model proposed here.

- **Geo-location errors in the Meteosat data.** The geo-correction process was based on ground control points (mainly coastline features), and is subject to error. A mis-registration error as little as one pixel along the shoreline can introduce significant error into the model, so the estimated values along the coastline have high uncertainty. The problem is made worse by the oblique view angle as Meteosat is positioned over the equator and the UK is located around 52° north.

- **Snow cover.** The method used to estimate cloud cover ignores the possibility that the ground may be snow covered at certain times of the year. As the main focus of interest was vegetation during the growing season, and as the primary test sites were all located in southern England, this was not seen as a major problem as the number of days with snow on the ground would be few. However, if the method was to be applied in Scotland or northern England it would be necessary to screen the data for lying snow, perhaps using one of the other bands available on Meteosat. Snow is not just a problem for remote sensors, it also may obscure a ground-based pyranometer, affecting the measurement of S_t.

- **Changes in sensor sensitivity.** It is well known that pyranometer sensors are subject to calibration drift over time, and for this reason the manufacturers recommend regular calibration. The sensors used in this study were mostly maintained by the UK Met Office, so can be assumed to be well-calibrated, but even slight changes in sensitivity would cause large changes in K_{dQ}. The occurrence of data values where $S_d \geq S_t$, shows that the ground data were not entirely free of errors.

- **Limited validation data available.** No nationwide measurements of K_{dQ} were found, so it was necessary to substitute measurements of K_{ds}, and even so this variable was only measured at two locations in the UK, one in the south-west and one in the extreme north. It is ironic that one of the consequences of modernisation of the UK meteorological station network has been a drastic reduction in the number of stations recording the proportion of diffuse flux.

4.6 Discussion

One of the most significant current debates in ecosystem modelling is how K_{dQ} influences carbon assimilation in the vegetation. Despite its perceived importance, there are not many ground-based studies and even fewer plant growth models that take into account K_{dQ}. The lack of in-situ measurement and mapping might be the reason why K_{dQ} is omitted from most carbon accumulation models.

This chapter has described three methods of estimating the proportion of diffuse PAR. In principle, any one of them would be suitable for estimating K_{dQ} across the whole of the UK, but in practice each has limitations when applied to estimating K_{dQ} for use in plant canopy and/or climate models. The first method, based on a sky clearness index calculated from ground-based meteorological data requires spatial interpolation between measurement sites, which means that any feedback between local vegetation and the overlying atmosphere may not be revealed. In the second method, the spatial resolution of the ISCCP DX data was not fine enough to be applied to the landscape of southern England, and in any case the source data are no longer being produced. The third method, an empirical approach based on Meteosat data, was simple enough to be applied to a large number of images (> 30,000), and produced plausible results. However, the lack of high quality validation data meant that it was questionable whether it was worth devoting more effort to refining the method. Even if a perfect method had been devised it would have been impossible to validate it. In that context, the decision was made to accept the results from the third method as the best available high spatial resolution maps of monthly average K_{dQ} across the UK.

The hypothesis that diffuse fraction could be estimated using satellite data still faces problems about the accuracy of the validation. Uncertainty at each stage of the process is the main problem in predicting K_{dQ}. The K_{dQ} is a derived fraction based on other measurements, Q_d and Q_t. Therefore, to measure K_{dQ} accurately, it is necessary to measure Q_d and Q_t accurately in the first place. However, Q_d and Q_t

are not routinely measured, even in the UK, because it is a complicated procedure and needs manual intervention (see Section 1.4).

The invention of the Delta-T BFx series of Sunshine Sensors for automatic Q_d and Q_t measurement is to be welcomed, but these are not yet widely used and have not been validated over a range of conditions (Chapter 3). Accessibility to the data is also a limitation. Therefore, it is difficult to gather a long period of data to be the input to a vegetation model for studying the effect of variations in K_{dQ} on carbon accumulation.

There are no long-term data series from PAR sensors and BF3 sensors, however, there are long-term S_t data from CM 21 Kipp and Zonen pyranometers. This study shows that K_{dQ} can be calculated from broadband irradiance measured using these standard meteorological instruments. Section 4.3.1 showed that measured S_t from the CM 21, calculated S_0 and the relationship between the K_{dQ} and K_T, can be used to calculate K_{dQ}. However, long-term data from CM 21 sensors alone are not sufficient. It is also necessary to have some sites at which K_{dQ} is also measured, so that the relationship between K_T and K_{dQ} can be established.

The fact that K_{dQ} can be estimated from remote sensing data, as shown in Section 4.4.1, supports the hypothesis that the diffuse fraction of solar irradiance can be estimated using satellite data, as suggested by Butt et al. (2010). However the accuracy of the prediction for the UK using the satellite data is not high, for both ISCCP and Meteosat data. Despite this, the maps produced in this chapter are still useful as a guide to the spatial and temporal variation of the K_{dQ} in the UK.

Turning to the second method, based on ISCCP data, there is limited value in developing further this approach. Although the cloud fraction estimates are based on physical processes and quality controlled, the data set is no longer disseminated so it is not useful for future environment monitoring. Also the spatial resolution is much coarser compared to other remote sensing data. There are other sources of satellite data, such as the Meteosat Second Generation (MSG) and Meteosat Third Generation (MTG), that are up-to-date, have better resolution and are useful for future work.

A recent publication by Furlan et al. (2012) has included investigation of the factors involved in the estimation of K_{dS} using the relationship between K_{dS} and K_T. Furlan et al., (2012) included parameters such as cloudiness, cloud type, air temperature, relative humidity, atmospheric pressure and air pollution. The strength of the relationship in term of R^2 ($R^2 = 0.93$) is not better than the result in Section 4.3.1 ($R^2 = 0.94$), and the accuracy in term of RMSE (RMSE = 0.085) is not much different (RMSE = 0.09), but the idea of controlling for the influence of other factors is interesting. This is one way in which the method described in the chapter could be developed further.

Another recent publication (Bortolini et al., 2013) studied the relationship between K_{dS} and K_T in Europe. They used multi-location models for the annual, summer and winter scenarios to find the relationship between the K_{dS} and the K_T using third degree polynomial equations. Bortolini et al. (2013) used the broadband irradiance data from 44 Europe weather stations. Applying the same method to the UK data set might help to improve the in-situ estimation.

The study in this chapter is different from most other studies, in terms of wavelength band. This study focused on K_{dQ} which is the PAR wavelength band, using the relationship between the K_{dQ} and K_T. Most other studies focus on K_{dS} which is the broadband irradiance (~ 305 - 2800 nm), using the relationship between K_{dS} and K_T (e.g. Liu and Jordan, 1960; Orgill and Hollands, 1977; Erbs et al., 1982; Spitters et al., 1986; Stuhlmann et al., 1990; Gonzalez and Calbo, 1999; Muneer, 2004; Muneer, 2006; Boland et al., 2008; Ridley et al., 2010; Furlan et al., 2012; Bortolini et al., 2013).

Although, the relationship between K_{dQ} and K_T looks like the same as the relationship between K_{dS} and K_T, it is known that PAR and broadband irradiance are different. Therefore, there is no certainty that a method which improves the relationship in the broadband region will give the same result in the PAR band.

The K_{dQ} maps might be improved further for vegetation mapping if the relationship between K_{dQ} and the satellite data could be further improved, for example, by including the same parameters as Furlan et al. (2012) which might enhance the accuracy of the K_{dQ} prediction. The accurate K_{dQ} mapping using satellite data then might be useful for the vegetation model to predict and study the carbon accumulation over a wide area.

The estimation methods for K_{dQ} in this chapter are an essential step towards later chapters in the thesis. Two of the methods described in this chapter will be used later: (i) ground estimation using the relationship between K_{dQ} and K_T in Section 4.3.1 and (ii) satellite estimation from the Meteosat data in Section 4.3.3.

The estimation of K_{dQ} using the relationship with K_T (ground method) will be used in Chapter 6 for the studying the effects of K_{dQ} in the selected vegetation model. The estimation using the relationship between K_{dQ} and K_T was selected to be used in Chapter 6 because it has a good relationship and good accuracy in testing (as shown in Section 4.3.1).

K_{dQ} estimation using satellite data will not be used in the vegetation productivity model because the accuracy of the satellite prediction was not sufficiently high. To prevent the errors from the mapping propagating through the vegetation productivity model, the relationship between K_{dQ} and K_t was therefore selected for use in Chapter 6.

However, in terms of the pattern and trend of the solar irradiance, the K_{dQ} estimation using satellite data is useful for further application. The estimation of K_{dQ} using satellite data is useful for diffuse PAR (Q_d) mapping in the next chapter. Considering the accuracy, resolution and accessibility of the data, the estimation of K_{dQ} using Meteosat data is better for use in Q_d mapping, rather than using the ISCCP DX data.

It is essential to clarify that the K_{dQ} in this chapter is not the quantity Q_d. K_{dQ} is the fraction between Q_d and Q_t. To understand the spatial variation of the irradiance due to cloud, both K_{dQ} and Q_d are necessary because they are different things, explaining the variation in a different way. The K_{dQ} maps explain the <u>fraction</u> while the Q_d maps explain the physical <u>quantity</u> of irradiance. The variation is also different, the monthly average K_{dQ} has not much variation and not much difference, but Q_d has high variation on a monthly basis. Mapping of Q_d is covered in the next chapter.

4.7 Conclusion

This chapter has investigated three different ways to estimate the proportion of diffuse PAR flux (K_{dQ}) reaching the ground:

- Estimation of K_{dQ} based on a sky clearness index calculated from ground-based meteorological data.

- Estimation of K_{dQ} based on cloud fraction from the International Satellite Cloud Climatology Programme (ISCCP) DX data set.

- Estimation of K_{dQ} based on cloud cover determined from data collected by the Meteosat instrument.

One of the main challenges faced was the lack of high quality validation data, even for the UK, a small country with a well-established programme of meteorological measurements. In the past, the proportion of diffuse flux, whether broadband or PAR, has not been a priority measurement, although that is now changing as it is realised that climate change involves changes in cloudiness and sky clarity as well as the overall amount of solar radiation. Physically-based vegetation productivity models require data on the proportion of diffuse flux because vegetation canopies are three-dimensional and diffuse flux penetrates further into them.

The research described in this chapter produced good results using two of the three methods. The use of data from ground-based meteorological instruments confirmed that the well-established relationship between sky clearness and the proportion of broadband diffuse flux was also true for the PAR region. This was an important result in its own right, but it also provided a means to generate credible validation data for the other two methods. Of these, use of data from the Meteosat sensor was the most successful in the UK context.

Meteosat satellite images from August 2003 to June 2006 (approximately 30,000 images) were used to map the monthly K_{dQ}, over the whole of the UK. The monthly K_{dQ} map was validated using two sets of independent data:

- Using data from two meteorological sites and based on the assumption that $K_{dQ} = K_{dS}$. The validation result showed that K_{dQ} could be estimated to an accuracy of 9.80 % RMSE (MBE = 7.19 %).

- Using data from 98 meteorological sites to calculate K_{dQ} from K_T gave nationwide monthly estimates of K_{dQ} to an accuracy of 8.42 % RMSE (MBE = - 6.06 %).

Despite several weaknesses and limitations of the method, it has been possible to produce and validate a series of maps showing monthly average K_{dQ} across the whole of the UK. This is the first time such a product has been produced with this level of spatial detail. These maps of K_{dQ} are important because carbon emission and accumulation is happening on a global scale, not just in the UK. If K_{dQ} influences carbon accumulation in vegetation, it will influence the entire global biosphere.

Chapter 5 Estimation of PAR amount over the UK and extension to SEVIRI data

5.1 Introduction

The previous chapter developed and tested a simple method to estimate the fraction of diffuse PAR (K_{dQ}) reaching the ground, based on data from the Meteosat Visible and Infrared Imager (MVIRI). This chapter builds on that work by replacing MVIRI with the Meteosat Spinning Enhanced Visible and Infrared Imager (SEVIRI), a sensor with finer spatial resolution from the Meteosat Second Generation satellite (MSG). Table 5.1.1 compares the two sensors. The nominal area sensed by each SEVIRI pixel at the latitude of the UK is around a sixth that of MVIRI (approx. 5 km^2 compared with 30 km^2), making it much better suited to the spatially complex landscape of Europe.

Table 5.1.1 Difference between data from MVIRI sensor in Meteosat and SEVIRI sensor in MSG from British Atmospheric Data Centre (BADC)

	Meteosat	Meteosat Second Generation (MSG)
Nadir spatial resolution from satellite	2.5 km (from 35,756 km, using MVIRI)	1 km (from 35,800 km, using SEVIRI)
Spatial resolution over UK (based on satellite sensor)	5.44 km (at 55 °N)	2.18 km (at 55 °N)
Spatial resolution over UK (based on data from BADC)	5.44 km	~ 1 km
Spatial resolution manipulated to use	~ 2.5 km	~ 1 km
Temporal Resolution (achieved from BADC)	An instantaneous image at every 30 minutes	An instantaneous image at every 1 hour
Number of used Images	34,508	29,168
Spectral response	450 – 1000 nm	400 – 1100 nm
Period of data from BADC used in thesis	August 2003 - June 2006 (~ 3 years long)	March 2005 – March 2012 (~ 7 years long)
Position of satellite	0 degree	0 degree
Projection form BADC	Satellite full disk	Stereographic
Covered area from BADC	Europe and Africa	UK

The main aim of this chapter is to develop and test a method to estimate the amount of PAR reaching the Earth's surface, so as to produce maps of global PAR over different timescales for the whole of the UK. SEVIRI data will be used for this task, as a combination of hourly observations and fine spatial resolution is required. Other sensors, such as MODIS, offer even finer spatial resolution but they are limited to two images per day, at most. This is a problem in an area such as the UK as cloud cover is an important control on PAR reaching the ground, and this varies markedly during a day.

Taken together, these two research tasks aim to produce the first detailed maps of incident hourly PAR (global and diffuse) for every month of the growing season in the UK. Such maps will be useful for local and regional scale plant productivity models as well as being of practical use in agriculture and environmental management.

Like the previous chapter, the approach combines freely available satellite data with pre-existing meteorological data. The method involves empirical modelling and a simplified representation of the physical interactions in the atmosphere, appropriate for the intended purpose of the data, which relates to the use of these data in regional and national scale plant productivity models (Chapter 6).

5.2 Data sources

5.2.1 Satellite data

The SEVIRI instrument on board the Meteosat Second Generation (MSG) satellite has a High Resolution Visible (HRV) channel which provides measurements of reflected solar irradiance in the satellite spectral band (400-1100 nm) every 15 minutes from pixels with a nominal sub-satellite sampling distance of 1 km. The MSG satellite is positioned over the equator, giving SEVIRI HRV an instantaneous field-of-view 2-3 km at the latitude of the UK.

Data from the whole hemisphere are resampled during pre-processing and provided as 1 km pixels in a stereographic map projection. For this chapter the area covering the UK was selected and re-projected to a cylindrical projection for ease of overlay with other geographical data sets (Figure 5.2.1). SEVIRI HRV data covering the period March 2005 – March 2012 were used in this chapter (approximately 29,000 images)

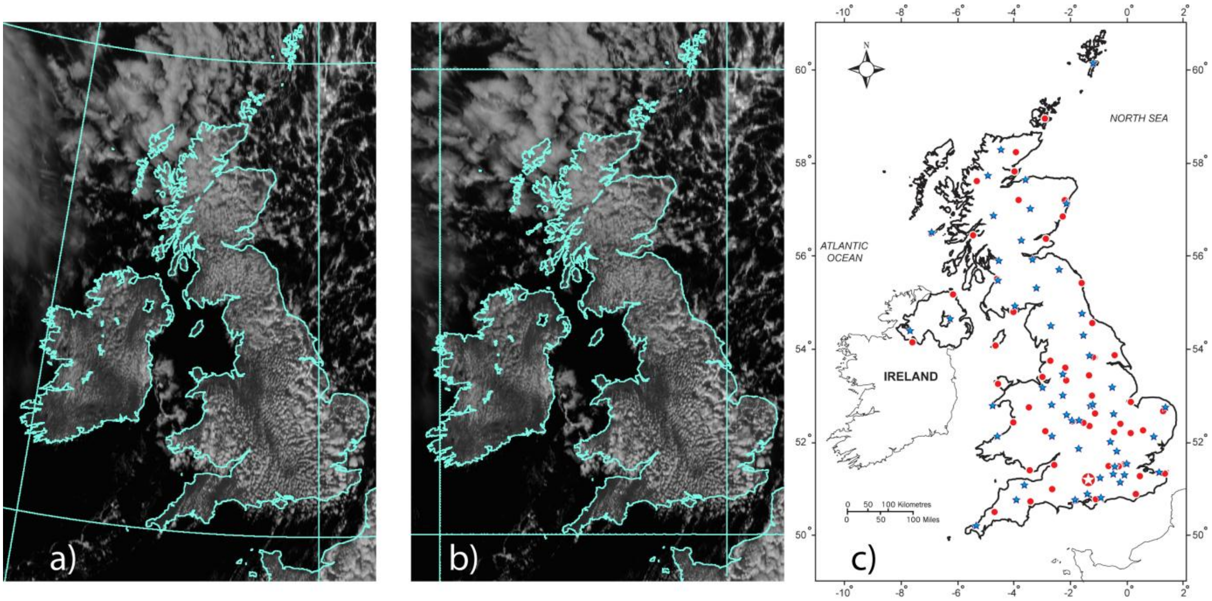

Figure 5.2.1 The SEVIRI subset a), transformed to cylindrical map projection b) and the distribution of pyranometer sites c) used for generating the model (★) and for validation (●). The location of the Chilbolton Facility for Atmospheric and Radio Research is shown in c) (✪)

Data from the Earth Probe Total Ozone Mapping spectrometer (EP/TOMS) (McPeter et al., 1998, www14) and the Ozone Measurement Instrument (OMI) (www15) were acquired for the same period as the MSG data to provide information on the amount of ozone in the upper atmosphere as this would affect the absorption in the PAR region.

5.2.2 Ground data

Ground data were needed to develop and test the method, but the lack of a UK-wide PAR network meant that this was not straightforward. A method was developed that took advantage of the well-established network of Met Office meteorological stations across the UK, and also used the relationship between global broadband irradiance (S_t) and global PAR (Q_t), as follows.

A Li-Cor Biosciences LI-190SA quantum sensor was installed for 12 months specifically for this chapter at the STFC Chilbolton Facility for Atmospheric and Radio Research (CFARR) (latitude 51.14° N, longitude 1.44° W) in close proximity to a Kipp and Zonen CM21 pyranometer from the UK network of pyranometers (Figure 5.2.1c). This provided data to establish the relationship between S_t and Q_t in the UK under a range of solar zenith angles and weather conditions (especially cloud type and amount).

This relationship could then be used to estimate Q_t from S_t, which is measured at many of the UK Met Office meteorological stations using CM11 Kipp and Zonen pyranometers. For this chapter, a total of 108 pyranometer stations, each having at least 6,000 hours of recorded data between March 2005 and March 2012 were selected and randomly assigned to two equal sized groups, one for model development, one for validation (Figure 5.2.1c).

A more direct validation was also possible using data from UK FLUXNET sites (www16), eight of which measured broadband irradiance data that can be converted to PAR at hourly resolution corresponding to the period of MSG data used in this chapter (Figure 5.2.2). These data were used as an independent test of the accuracy of estimated PAR.

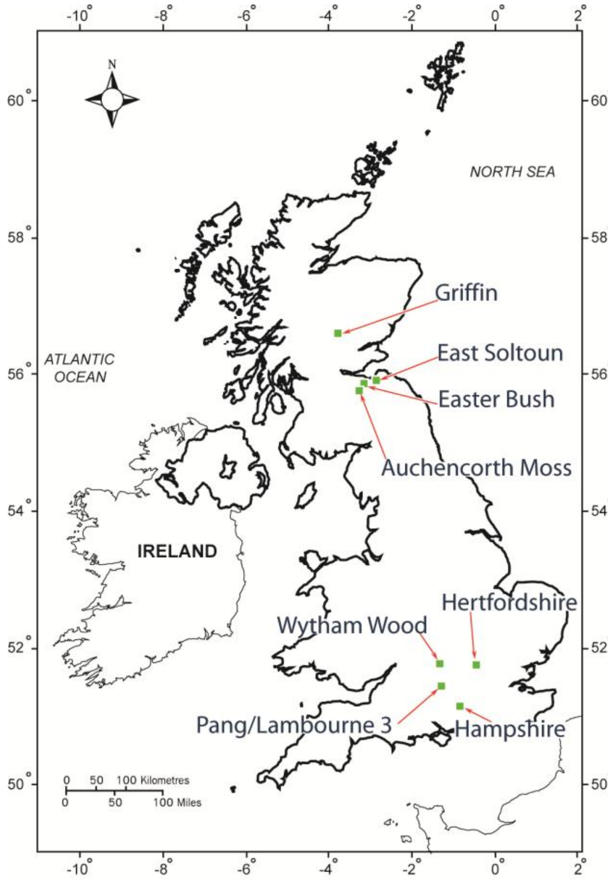

Figure 5.2.2 Location of the FLUXNET sites used in this chapter

Table 5.2.1Type of land cover at FLUXNET sites

Site	**Land cover**
Griffin	Forest
East Saltoun	Crops
Easter Bush	Grassland
Auchencorth Moss	Grassland
Wytham Wood	Forest
Hertfordshire	Crops
Pang/Lambourne	Forest
Hampshire	Forest

5.3 Modelling

A model was devised to map global PAR (Q_t) in the UK using existing satellite data and meteorological data. This model considered the spectral radiative transfer in the atmosphere. Transmittance in the atmosphere was considered separately in two bands: satellite band (as measured by SEVIRI) and the PAR band. Reflection from clouds was used to estimate the transmittance in the PAR band from the MSG data.

5.3.1 Principles of the model

The Transmittance of PAR through the atmosphere (T_Q) can be represented as the amount of PAR reaching the ground surface (Q_t), as a proportion of that at the top of the atmosphere (TOA) (Q_0). The effect of water vapour in the atmosphere upon transmittance in the PAR region is negligible (Iqbal, 1983; Asrar, 1989), so it is assumed the main atmospheric influences on the amount of PAR received at the ground surface are the amount and type of cloud, molecular scattering and absorption due to ozone. Therefore the combined transmittance of the atmosphere in the PAR region can be represented as:

$$T_Q = T_{Q,c} T_{Q,r} T_{Q,oz} \tag{5.3.1}$$

where $T_{Q,c}$, $T_{Q,r}$ and $T_{Q,oz}$ are the transmittance of PAR due respectively to cloud, molecular scattering and ozone. Therefore,

$$Q_t = Q_0 T_{Q,c} T_{Q,r} T_{Q,oz} \tag{5.3.2}$$

where Q_t is the global PAR at the Earth's surface ($\mu\mathrm{mol\,m^{-2}\,s^{-1}}$) and Q_0 is the extraterrestrial PAR at TOA ($\mu\mathrm{mol\,m^{-2}\,s^{-1}}$).

For the simplicity of the model, the transmittance due to aerosol was not included. It is also assumed that the aerosols in the UK will not effect the accuracy of the model, due to the main effect in the model coming from abundant cloud in the UK.

5.3.2 Extraterrestrial PAR

The extraterrestrial PAR, Q_0, can be calculated using the spectral solar irradiance at the top of the atmosphere, $I_{ex}(\lambda)$, and the following equations:

$$Q_0 = \left(\frac{1}{6.022 \times 10^{17}}\right)\frac{1}{hc}\int_{400}^{700} \lambda \, I_{ex}(\lambda)\, d\lambda \tag{5.3.3}$$

Where

$$I_{ex}(\lambda) = E_0 \cos\theta_z \, \dot{I}_{0n}(\lambda) \tag{5.3.4}$$

$$E_0 = r / r_0 \tag{5.3.5}$$

and

$$\cos\theta_z = \sin\delta \sin\phi + \cos\delta \cos\phi \cos\omega \tag{5.3.6}$$

Where 6.022 × 10^{17} is the number of photons in a μmol. The term $\left(\frac{1}{6.022 \times 10^{17}}\right)\frac{1}{hc}$ is required to convert from power intensity ($W\,m^{-2}$) to photosynthetic photon flux density (PPFD) ($\mu mol\, m^{-2}\, s^{-1}$). The term $\dot{I}_{0n}(\lambda)$ is solar spectral irradiance ($Wm^{-2}nm^{-1}$) averaged over a limited bandwidth and was based on data from Iqbal (1983).

5.3.3 Effect of molecular scattering on PAR Transmittance

The local airmass (m_a) was calculated from the following equation:

$$m_a = m_r (P_{local} / P_{standard}) \tag{5.3.7}$$

In which

$$m_r = 1/\{\cos\theta_z + [0.15(93.885 - \theta_z)^{-1.253}]\} \tag{5.3.8}$$

and

$$P_{local} = P_{standard} \exp(-0.0001184 \cdot Z) \tag{5.3.9}$$

The transmittance of PAR due to molecular (Rayleigh) scattering could therefore be calculated as:

$$T_{Q,r} = \frac{(\frac{1}{6.022 \times 10^{17}}) \frac{1}{hc} \int_{400}^{700} T_{\lambda,r} I_{ex}(\lambda) d\lambda}{Q_0} \tag{5.3.10}$$

Where

$$T_{\lambda,r} = \exp(-k_{\lambda,r}\ m_a) \tag{5.3.11}$$

and

$$k_{\lambda,r} = 0.008735\ \lambda^{-4.08} \tag{5.3.12}$$

5.3.4 Effect of ozone absorption on PAR Transmittance

Ozone in the upper atmosphere absorbs in the region between 375-650 nm (Chappuis bands; Chappuis, 1880; Brion et al., 1998), which overlaps with the PAR region. Transmittance due to ozone was calculated from the following equations:

$$T_{Q,oz} = \frac{(\frac{1}{6.022 \times 10^{17}}) \frac{1}{hc} \int_{400}^{700} T_{\lambda,oz}\ I_{ex}(\lambda) d\lambda}{Q_0} \tag{5.3.13}$$

and

$$T_{\lambda,oz} = \exp(-k_{\lambda,oz}\ \ell\ m_r) \tag{5.3.14}$$

where the $K_{\lambda,oz}$ for each wavelength was based on data in Iqbal (1983).

5.3.5 Atmospheric transmittance due to cloud

The transmittance due to cloud ($T_{Q,c}$) was derived from the reflectance of cloud ($R_{Q,c}$), assuming no absorption within cloud:

$$T_{Q,c} = 1 - R_{Q,c} \tag{5.3.15}$$

therefore

$$R_{Q,c} = 1 - [T_Q / (T_{Q,r} T_{Q,oz})] \tag{5.3.16}$$

and

$$R_{Q,c} = 1 - [(Q_t / Q_0) / (T_{Q,r}\ T_{Q,oz})] \tag{5.3.17}$$

where $T_{Q,r}$ is the Transmittance due to Rayleigh scatter and $T_{Q,oz}$ is the Transmittance due to ozone (both unitless).

Data from the 54 ground stations were transformed from S_t to Q_t using the relationship established at the field site (Section 5.4.1) and used in equation (5.3.17) to provide estimates of the reflectance of cloud. A relationship was then established between $R_{Q,c}$ and an index of cloud reflectance from the SEVIRI data, calculated as:

$$R_{sat,c} = (DN - DN_{min}) / (DN_{max} - DN_{min}) \tag{5.3.18}$$

Where $R_{sat,c}$ is the reflection due to cloud in satellite band, DN is the digital number from the satellite data, DN_{min} is the minimum of the digital number and DN_{max} is the maximum of the digital number. The DN_{min} at each pixel was selected from the minimum satellite data at monthly noon. The DN and DN_{max} at different positions and times have different incident zenith angle (solar zenith angle, θ_z) so the data were split into groups based on θ_z (Figure 5.3.1).

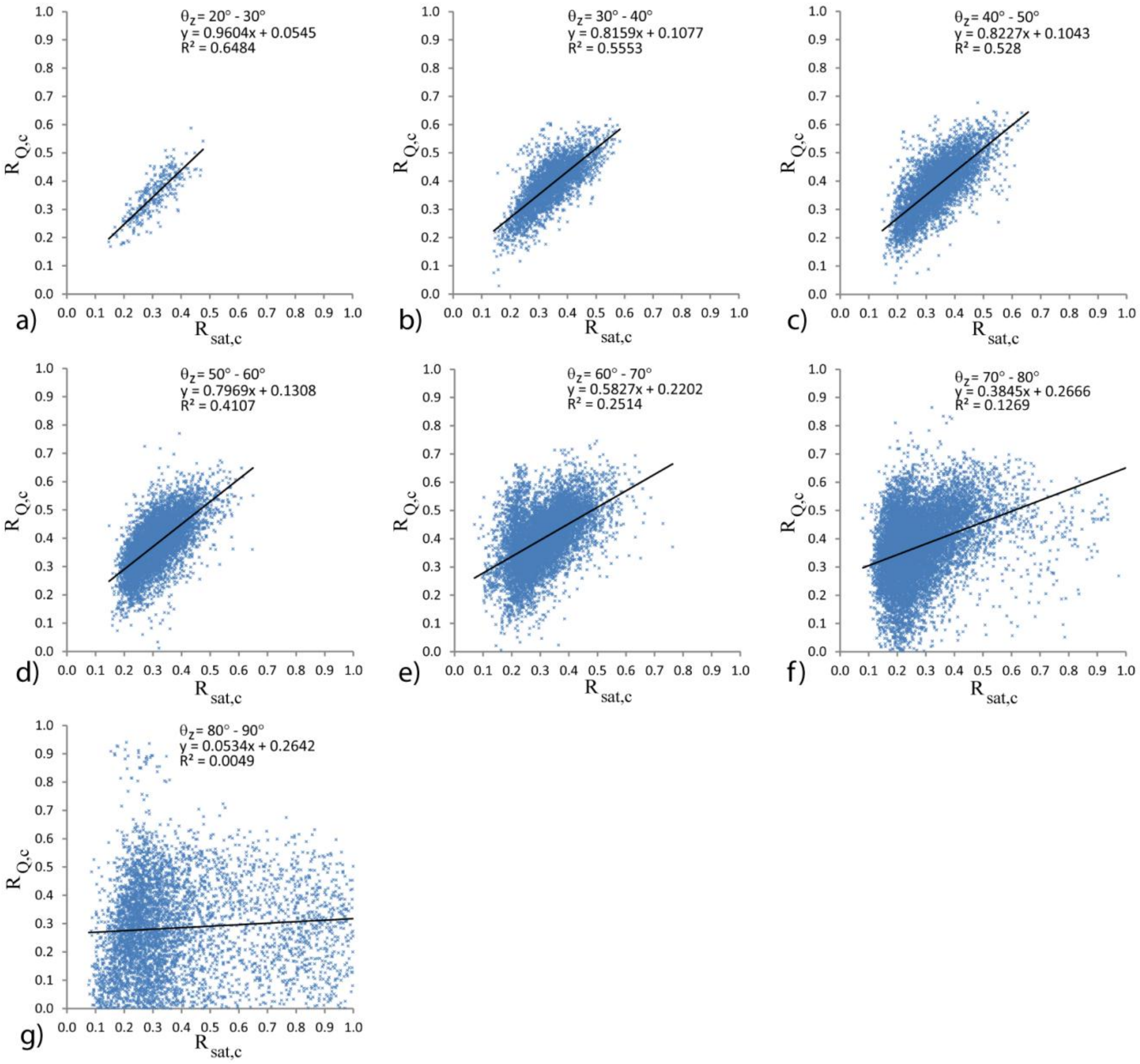

Figure 5.3.1 Relationship between $R_{Q,c}$ and $R_{sat,c}$ using data from 54 stations, every 10 degree period of θ_z; a) 20°-30°, b) 30°-40°, c) 40°-50°, d) 50°-60°, e) 60°-70°, f) 70°-80° and g) 80°-90°

5.4 Results

5.4.1 Relationship between in-situ global PAR (Q_t) and in-situ global irradiance (S_t)

A review of the literature suggested that PAR in PPFD units (μmol m^{-2} s^{-1}) is typically double that of solar irradiance measured in energy units (W m^{-2}), but also that this conversion factor could be sensitive to atmospheric conditions (Table 5.4.1).

Data from the PAR sensor and pyranometer co-located at CFARR between April 2011 and February 2012 are shown in Figure 3. The strong linear relationship (R^2 = 0.99) showed no evidence of variability over time or with atmospheric conditions, so the conversion factor 1.9455 μmol m^{-2} s^{-1} = 1 W m^{-2} was used for the in-situ Q_t calculation for the rest of this Chapter. The in-situ estimated Q_t was then used to validate the modelling using satellite data.

The relationship can be written as a simple equation:

$$y = 1.9455x \tag{5.4.1}$$

where $y = Q_t$ (in unit $\mu mol\ m^{-2}\ s^{-1}$) and $x = S_t$ (in unit $W\ m^{-2}$).

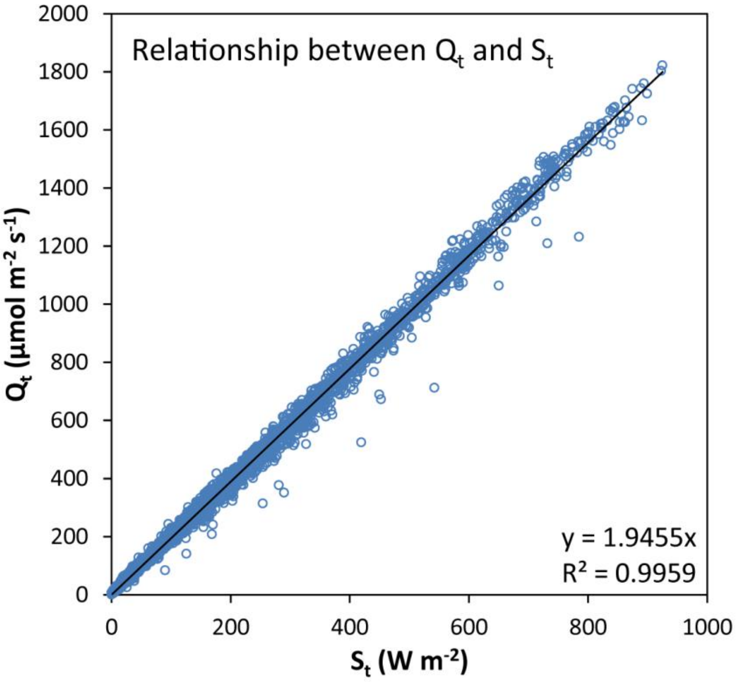

Figure 5.4.1 Relationship between measured global PAR (Q_t) and measured global irradiance (S_t)

Table 5.4.1 Summary of conversion factors reported in the literature to convert from solar irradiance ($\mathrm{W\ m^{-2}}$) to photosynthetic photon flux density ($\mu\mathrm{mol\ m^{-2}s^{-1}}$)

Publications	Locations	Latitude, Longitude	Period (years)	S_t sensor (model)	S_t λ band (nm)	S_t unit	Q_t sosor (model)	Q_t unit	Slope	Intercept	Testing
(Britton and Dodd, 1976)	Texas, USA	30°35´N 96°21´W	Apr 1973 - May 1974 (1)	Lambda pyranometer (LI-200 SR)	300 - 2000	$\mathrm{MJ\ m^{-2}\ d^{-1}}$	Lambda quantum sensor (LI-190 SR)	$\mathrm{E\ m^{-2}\ d^{-1}}$	2.0671 - 2.6199	0.0000	0.9776 - 0.9992 (R^2)
(Gonzalez and Calbo, 2002)	Girona, Spain	41°58´N 2°49´E	May 1998 - Mar 2000 (1.9)	Kipp and Zonen (CM11)	305 - 2800	J	LI-COR (LI-190SA)	μE	1.9900	0.0000	0.050 μE/J (RMSD)
(Howell et al., 1983)	California, USA	36°20´N 120°20´W	Jul 1980 - Jun 1981 (1)	Eppley (PSP)	285 - 2800	$\mathrm{J\ m^{-2}\ s^{-1}}$	LI-COR (LI-190S)	$\mu\mathrm{E\ m^{-2}\ s^{-1}}$	1.803 - 2.993	-4.753 - 4.033	0.8348 - 0.9994 (R^2)
(Jacovides et al., 2003)	Athalassa, Cyprus	35°15´N 33°40´W	Jan 1998 - Dec 1999 (2)	Kipp and Zonen (CM11)	305 - 2800	$\mathrm{MJ\ m^{-2}\ d^{-1}}$	LI-COR (LI-190SA)	$\mathrm{MJ\ m^{-2}d^{-1}}$	0.454 - 0.501	-0.406 - 0.442	0.997 - 0.992 (R^2)
(Li et al., 2010)	Tibetan Plateau	35°15´N 93°5´E	Sep 1993 - Dec 1998 (5.3)	EKO (MS-42)	280 - 3000	$\mathrm{MJ\ m^{-2}\ d^{-1}}$	Radiometer (TBQ-4-1)	$\mathrm{MJ\ m^{-2}d^{-1}}$	0.43 - 0.49	0.0000	0.954 - 0.998 (R^2)
(Udo and Aro, 1999)	Ilorin, Nigeria	8°32´N 4°34´E	Sep 1992 - Aug 1993 (1)	Eppley (PSP)	285 - 2800	MJ	LI-COR (LI-190SA)	$\mathrm{E\ m^{-2}}$	1.92 - 2.31	0.0000	0.022 - 0.077 (Morsdorf et al.)
(Wood et al., 2003)	Edinburgh, UK	55°55´N 3°13´W	Feb 2001 - Jul 2001 (0.5)	Kipp and Zonen (CM11)	305 - 2800	$\mathrm{W\ m^{-2}}$	Delta-T Sunshine Sensor (BF3)	$\mu\mathrm{mol\ m^{-2}s^{-1}}$	2.08	0.0000	0.992 - 0.994 (R^2)
This work	Chilbolton, UK	51°8´N 1°26´W	Apr 2011 - Feb 2012 (0.75)	Kipp and Zonen (CM21)	305 - 2800	$\mathrm{W\ m^{-2}}$	LI-COR (LI-190SA)	$\mu\mathrm{mol\ m^{-2}s^{-1}}$	1.9455	0.0000	0.9959 (R^2)

5.4.2 Validation of the model

The model from section 5.2 was validated with surface data, before it was used for the mapping. The model was validated using independent data from meteorology stations and FLUXNET sites in UK.

a) Comparison with data from Met Office sites

This was achieved by comparing the Q_t calculated using the model with that measured at each of the 54 pyranometer sites at the meteorological stations that had not been used to generate the model (Figure 5.4.2). The surface PAR was estimated based on the conversion factor between Q_t and S_t derived in Section 5.4.1. Figure 5.4.2 shows a good correspondence to the surface data (R^2=0.97, MBE = 2.42 $\mu\text{mol m}^{-2}\text{ s}^{-1}$).

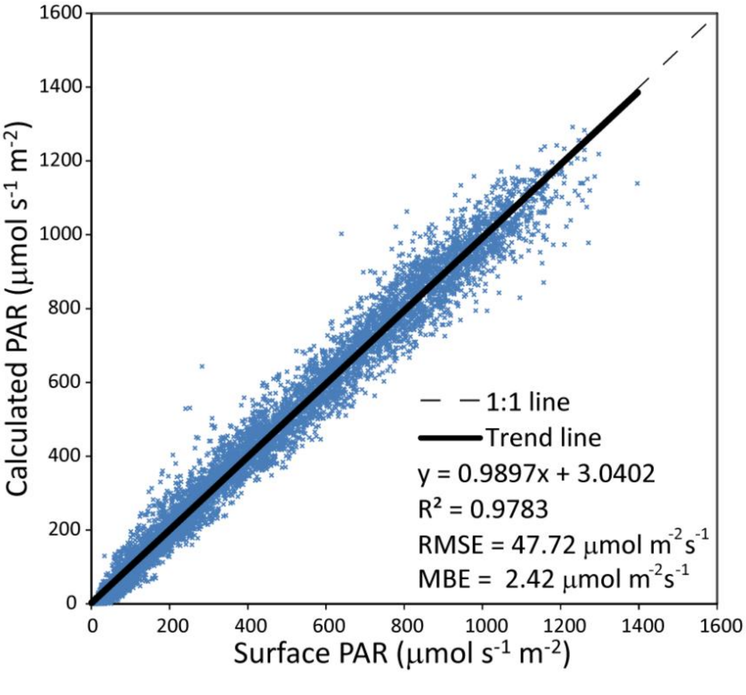

Figure 5.4.2 Comparison between calculated Q_t using the model and that measured Q_t at 54 independent sites for hourly averages

The monthly Q_t also showed a good correspondence to the measured Q_t at the surface at the meteorological stations (R^2 = 0.98, MBE = -0.01 $\mathrm{mol\,m^{-2}\,s^{-1}}$) (Figure 5.4.4). The monthly Q_t in each month was summed from the hourly average in each month.

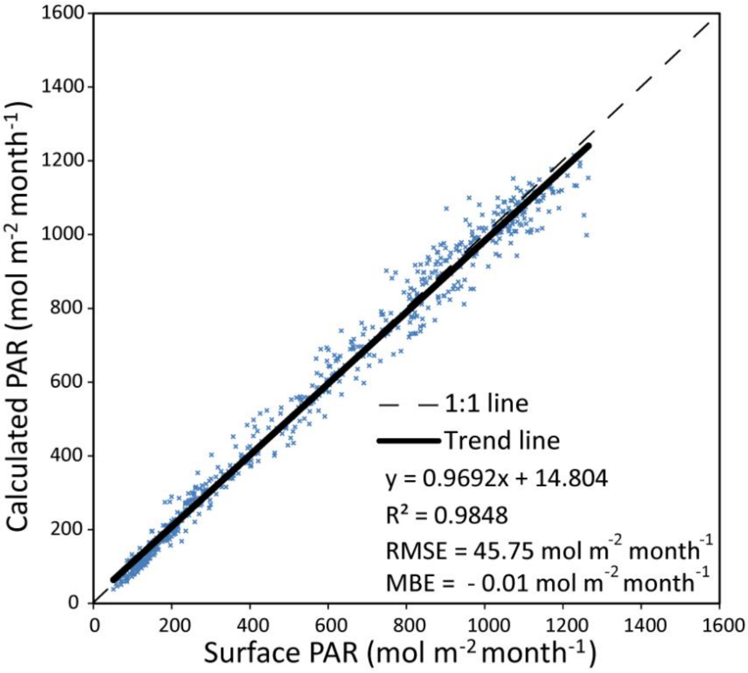

Figure 5.4.3 Comparison between calculated Q_t using the model and that measured Q_t at 54 independent sites for monthly basis

The yearly averages also showed a good correspondence ($R^2 = 0.71$, MBE = -0.04 $\mathrm{kmol\ m^{-2}\ s^{-1}}$) (Figure 5.4.5).

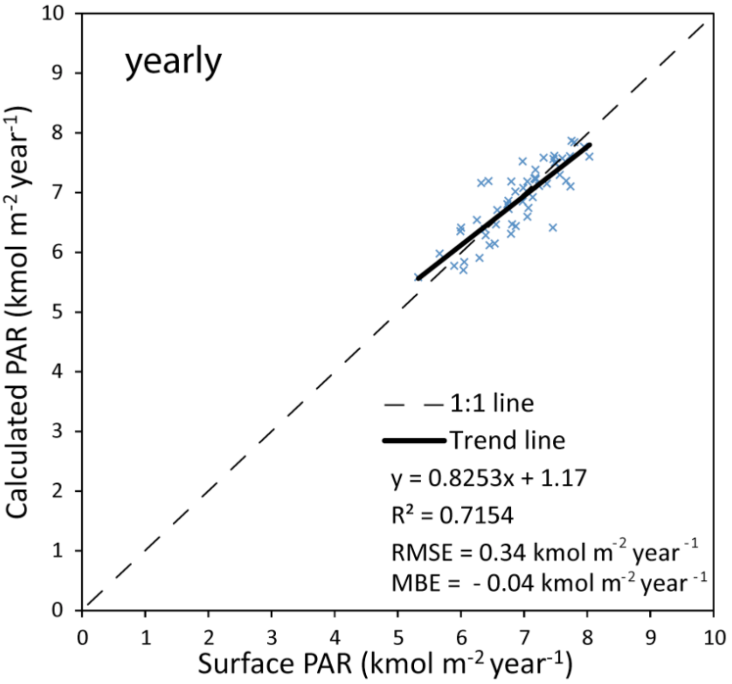

Figure 5.4.4 Comparison between calculated Q_t using the model and that measured Q_t at 54 independent sites for yearly basis

b) Comparison with FLUXNET data

Figure 5.4.5 shows the eight FLUXNET sites used in this work. The nature of the UK landscape means that small areas centred on the flux towers contains multiple land cover types (example of 2 km x 2 km areas are in Figure 5.4.5). Even within the relatively uniform forest sites there are clearings, tracks and compartments with trees of different age or species. These spatial variations will have affected the SEVIRI data acquired from a single pixel and will therefore introduce uncertainty into a direct comparison with data from the tower-mounted instruments.

The comparison is between hourly averages of PAR from the eight FLUXNET sites and the values estimated by the model in the map over the FLUXNET sites. The most accurate estimates of hourly average PAR, as measured by the RMSE, was from three of the forest sites: Griffin, Pang/Lambourne and Wytham Woods, (35-44

$\mu mol\ m^{-2}\ s^{-1}$). The least accurate estimate of hourly average PAR was from the Hertfordshire agricultural crop site (87 $\mu mol\ m^{-2}\ s^{-1}$).

Table 5.4.2 Comparison result between mapped data and the data from FLUXNET

site	Latitude (°N)	Longitude (°W)	RMSE (μmol $m^{-2}s^{-1}$)	MBE (μmol $m^{-2}s^{-1}$)
Griffin	56.61	3.80	44.35	12.09
East Saltoun	55.91	2.86	51.38	6.16
Easter Bush	55.87	3.21	48.20	21.37
Auchencorth Moss	55.79	3.24	69.34	41.30
Wytham Wood	51.45	1.27	35.45	11.41
Hertfordshire	51.78	0.48	86.80	-13.95
Pang/Lambourne 3	51.15	0.86	42.37	20.56
Hampshire	51.78	1.34	58.45	5.88

More information about the response of the individual sites can be gained by looking at the annual pattern of average hourly PAR (Figure 5.4.6). The data from Griffin forest show good correspondence during the summer months but during the autumn and spring months the estimated PAR was larger than that measured from the tower, possibly due to the larger θ_z at those times of the year. The results from two other sites are worthy of comment. Firstly, average hourly PAR at midday at Auchencorth Moss was overestimated during eleven months of the year (MBE = 41 $\mu mol\ m^{-2}\ s^{-1}$). As Figure 5.4.5 shows, this grassland site was embedded within a matrix of very different land cover types: moorland to the north-west and a large peat bog to the east. It is likely that the SEVIRI data were affected by these local variations in spectral reflectance during the year. Secondly, the Hertfordshire agricultural crop site is seen to not only have low overall accuracy but also some missing data from the flux tower and successive months during which PAR is under-estimated and then over-estimated, suggesting the spatial-temporal complexity of the surrounding land cover may not be the only factor affecting data from this site.

Griffin (Forestry-Commission) 44.35 [12.09]
lat 56.60722, long -3.798056

East Saltoun (crops) 51.38 [6.16]
lat 55.90694, long -2.858611

Easter Bush (grassland) 48.20 [21.37]
lat 55.866, long -3.205778

Auchencorth Moss (grassland) 69.34 [41.30]
lat 55.79167, long -3.238889

Wytham Wood (Forestry-Commission) 35.45 [11.41]
lat 51.772, long -1.3385

Hertfordshire (crops) 86.80 [-13.95]
lat 51.7838, long -0.47608

Pang/Lambourne (Forestry-Commission) 42.37 [20.56]
lat 51.45, long -1.266667

Hampshire (Forestry-Commission) 58.45 [5.88]
lat 51.15353, long -0.8583

Figure 5.4.5 FLUXNET sites used in the work showing site name (land cover), RMSE (μmol m^{-2} s^{-1}), MBE (μmol m^{-2} s^{-1}) and latitude and longitude (decimal degrees). The area covered in each image is approximately 2 km x 2 km.

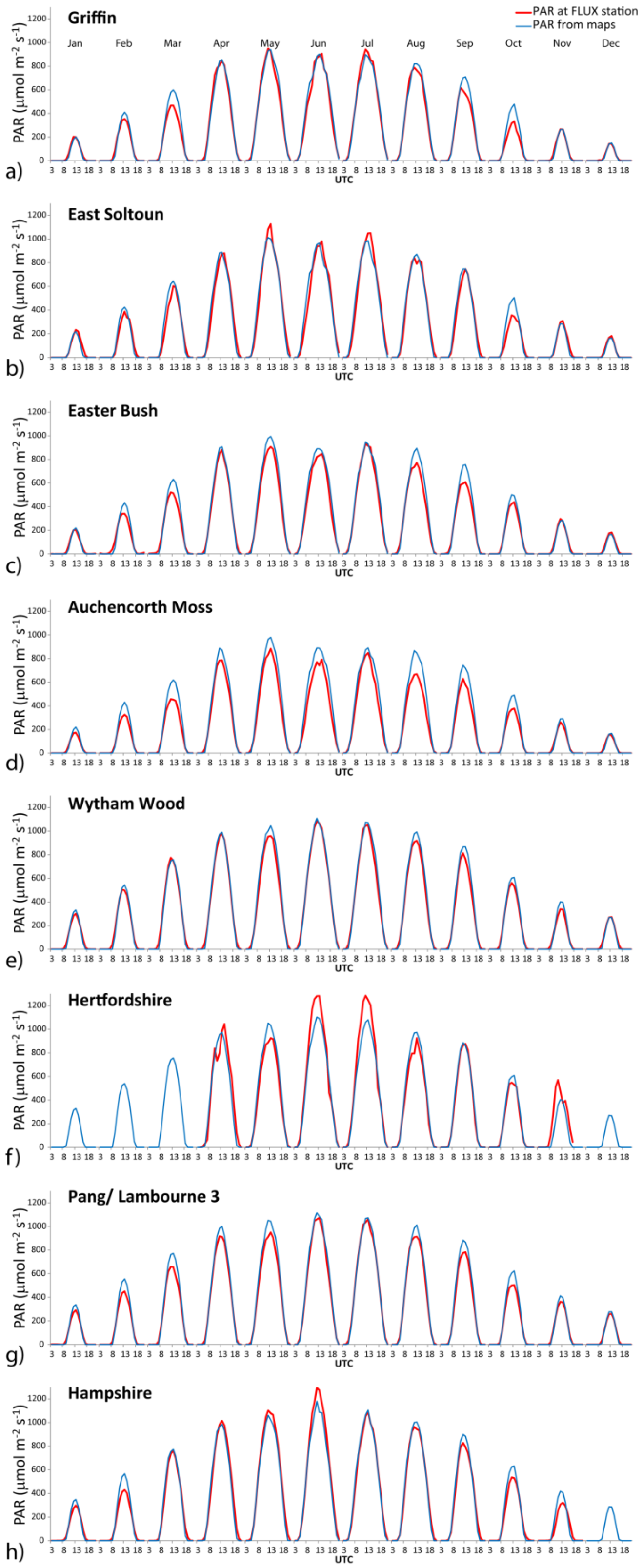

Figure 5.4.6 Average hourly PAR for each month of the year, comparing data measured at eight FLUXNET sites (red line) with modelled results (blue line).

The effect of temporal and spatial variation in the area surrounding each of the eight FLUXNET sites was averaged out by pooling the data from all of the sites (Figure 5.4.7). Moderate values of PAR were slightly overestimated by the model, but otherwise hourly average PAR estimated by the model was very similar to that measured at the FLUXNET tower. The largest anomalies came from the Hertfordshire agricultural crop site, and the data also show the over-estimation of hourly average PAR at Auchencorth Moss.

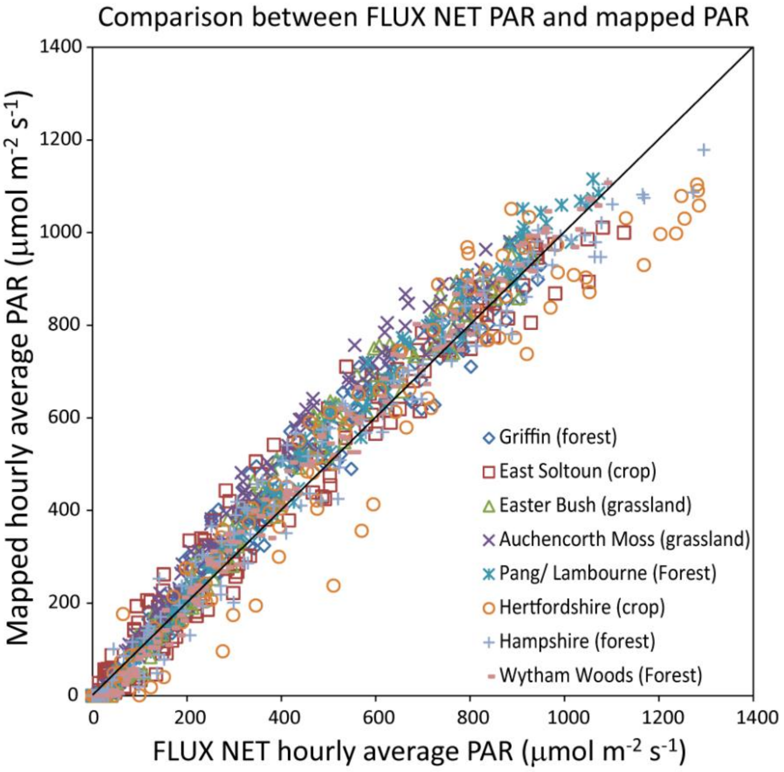

Figure 5.4.7 Comparison between PAR measured at eight FLUXNET sites and PAR estimated by the model

5.5 Application to mapping

5.5.1 Global PAR (Q_t) across the UK

The model was used to produce maps of PAR over the whole of the UK in different time periods.

a) Hourly PAR

Figure 5.5.1 shows an example of PAR averaged over each hour for all seasons, from sunset to sunrise. This map was needed in order to accumulate monthly and yearly totals of PAR but it is also interesting in its own right, especially the period March to September (the growing season) (Figure 5.5.2).

Figure 5.5.2 shows the north-south gradation in PAR throughout the growing season, upon which is superimposed the diurnal gradient (higher Q_t in the east during the morning hours, higher Q_t in the west in the afternoon).

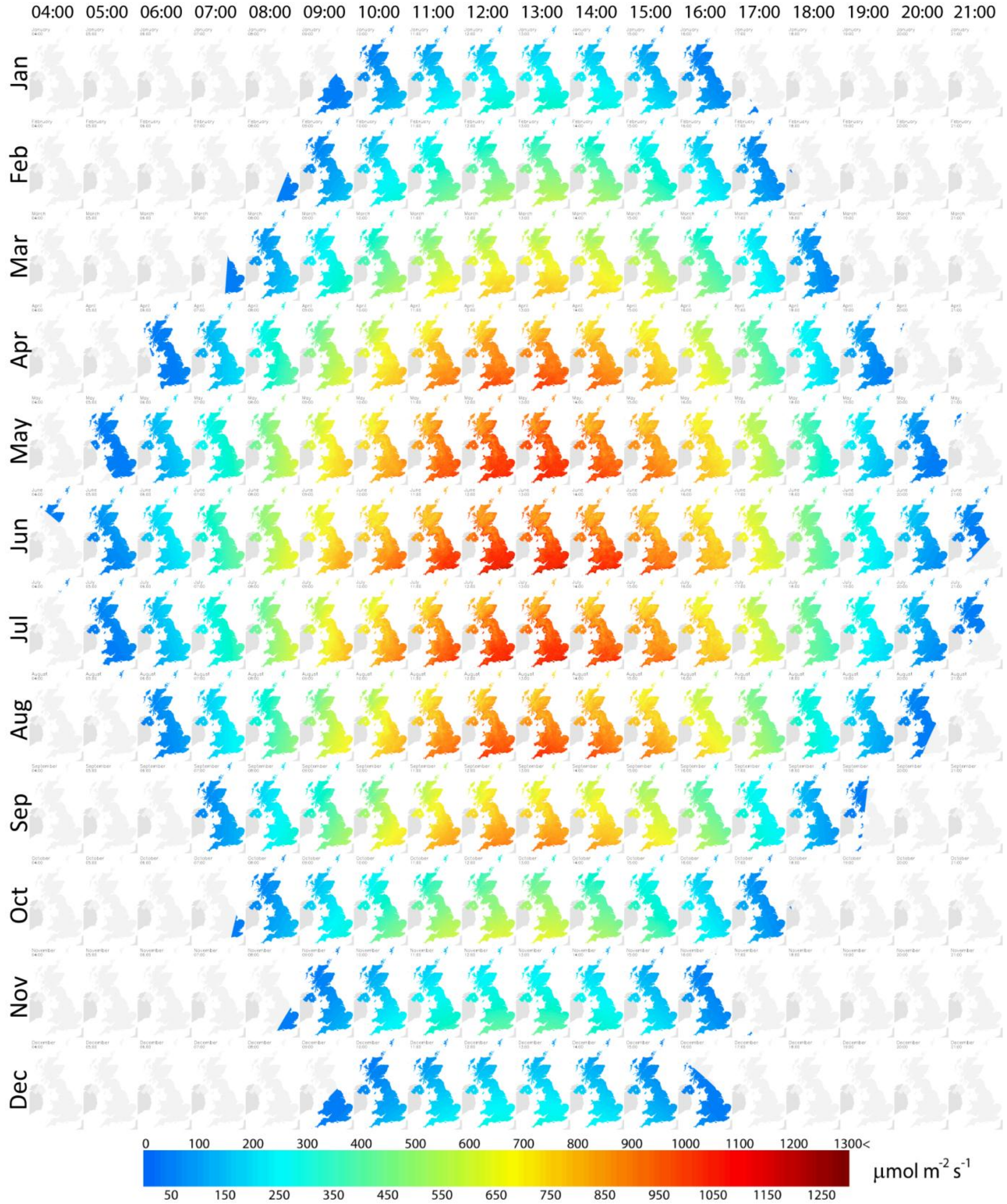

Figure 5.5.1 Averaged hourly global PAR (Q_t) for each month, all θ_z (0°-90°) over the whole of the UK

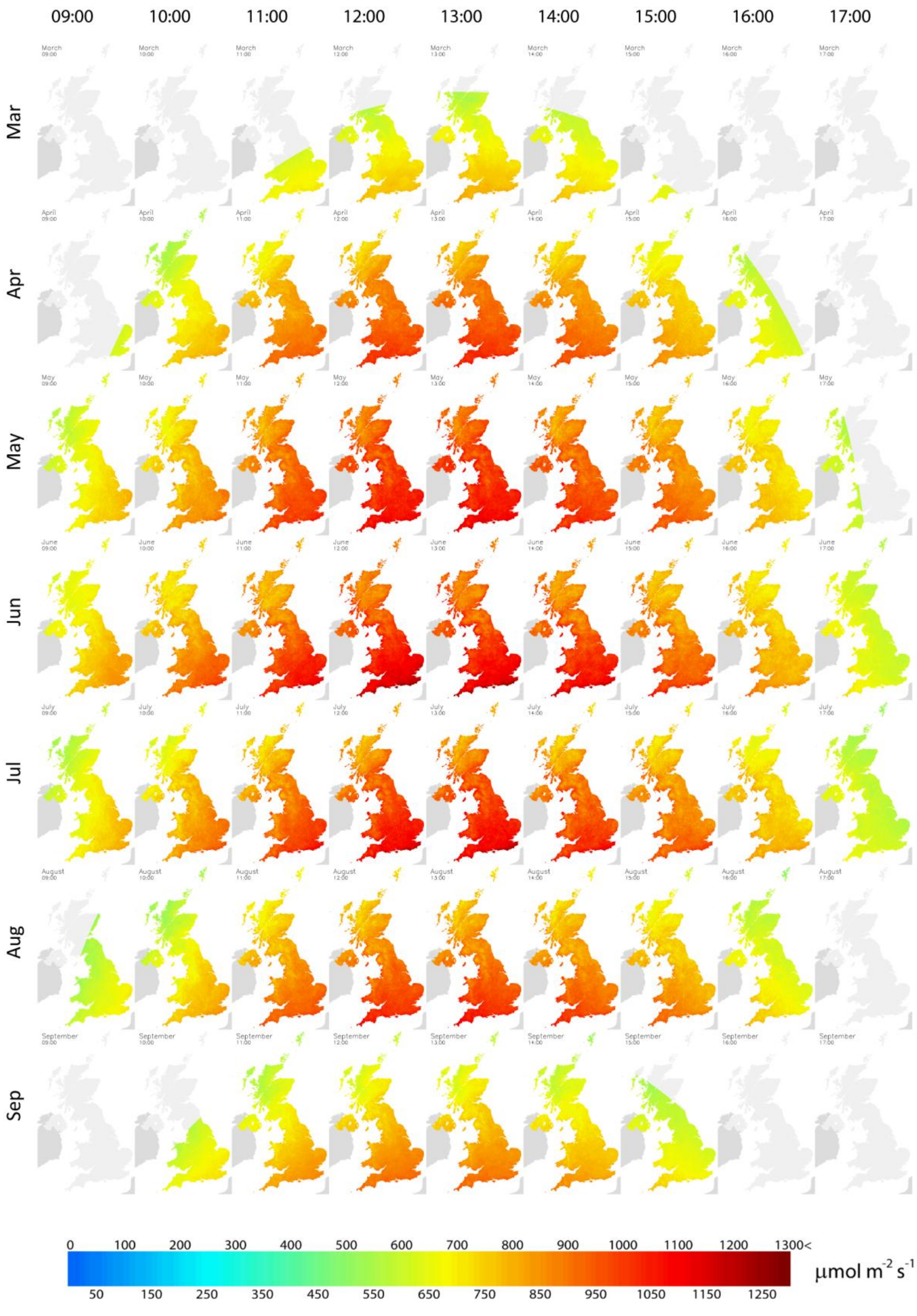

Figure 5.5.2 Averaged hourly global PAR (Q_t) map for each month of the growing season (March – September), mapped over the whole of the UK

b) Monthly PAR

Monthly Q_t across the UK was created by summing the hourly PAR from the model (Figure 5.5.3). The map shows an order of magnitude difference between monthly Q_t in the middle of winter compared with mid-summer.

Day length, together with the influence of θ_z and Sun Earth geometry are the main factors controlling monthly Q_t in the UK. Day length in the winter of the UK is almost one-third of that in summer (London, England shortest day is 7 hours 49 minutes on 21st December, longest day is 16 hours 38 minutes on 21st June). The combination of a much shorter day and lower hourly Q_t accounts for why Q_t in winter can be ten times less than Q_t in summer.

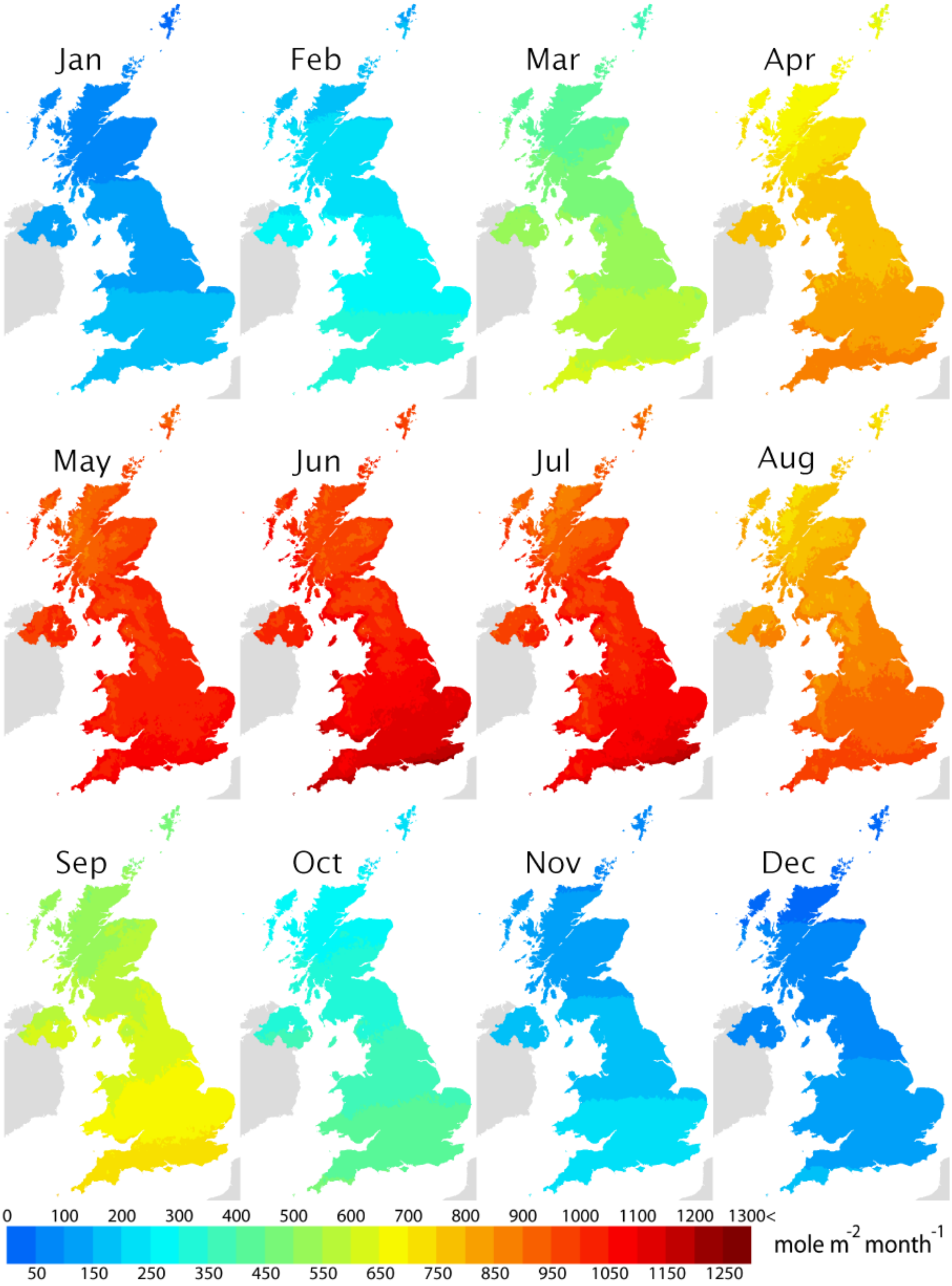

Figure 5.5.3 Monthly global PAR (Q_t) map of the UK

c) Annual PAR

The mean annual of Q_t (Figure 5.5.4) was calculated by summing the monthly averaged Q_t over the period 2005-2012. The annual range is from around 5 $\mathrm{kmol\ m^{-2}\ year^{-1}}$ in the North of Scotland to around 8 $\mathrm{kmol\ m^{-2}\ year^{-1}}$ along the south coast of England.

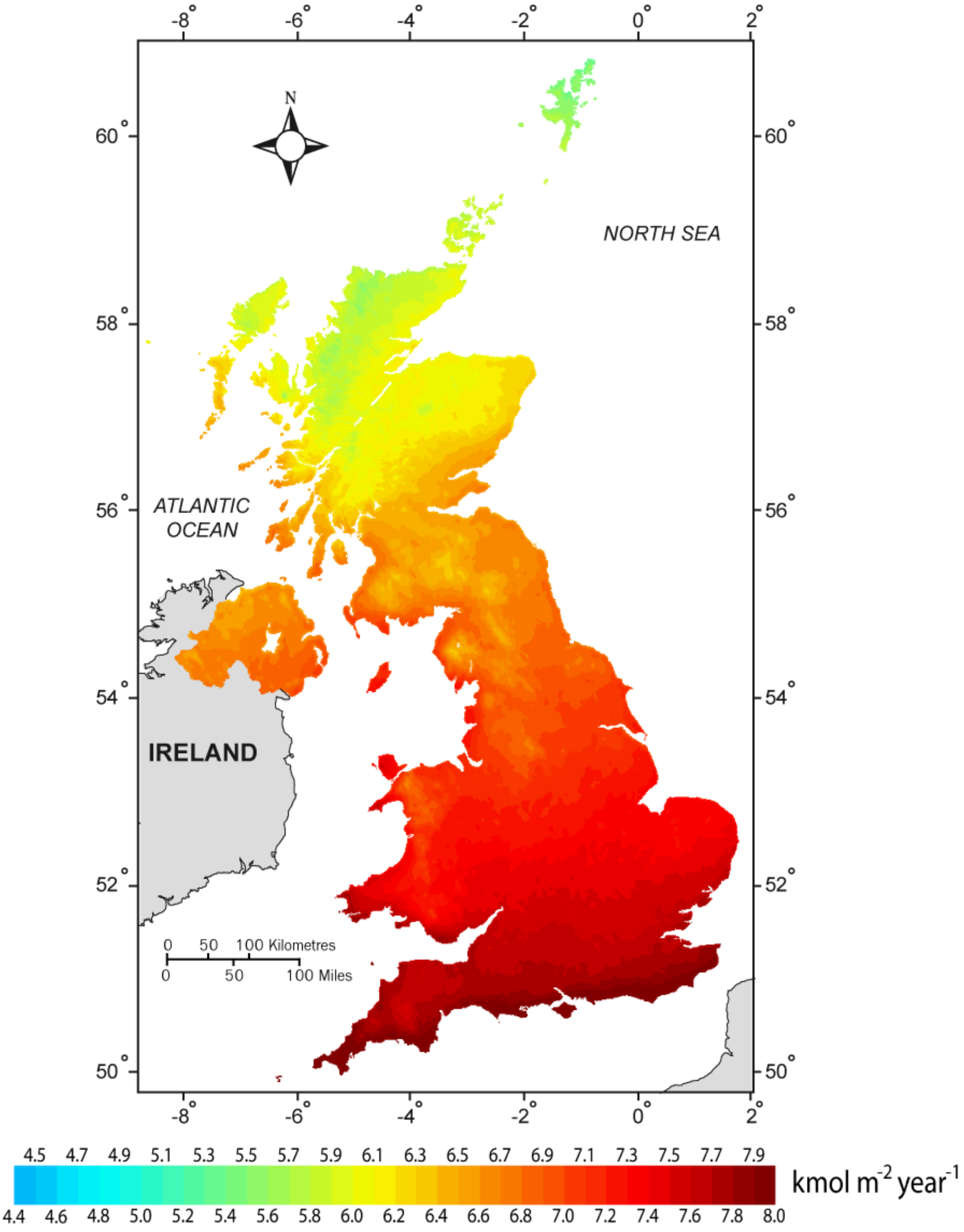

Figure 5.5.4 Mean annual global PAR (Q_t) of the UK

5.5.2 Diffuse PAR (Q_d) across the UK

Having produced maps of the amount of PAR over the UK at different time intervals, these can be combined with the method presented in the previous chapter to create maps of the amount of diffuse PAR (Q_d). To do this, monthly Q_d was estimated using the equation $Q_d = Q_t \times K_{dQ}$, where Q_t was derived from the results presented in Section 5.5.1. The method for estimating monthly K_{dQ} was based on that described in Chapter 4, modified to use data from the SEVIRI sensor, rather than MVIRI.

a) Diffuse PAR fraction (K_{dQ}) using MSG data

The MSG data used for estimating K_{dQ} covered the same period as the data used for the Q_t mapping, March 2005-March 2012. The purpose of repeating the K_{dQ} mapping with the SEVIRI data is twofold: first, the higher spatial resolution is necessary to capture the fine scale features; and second, the SEVIRI sensor represents the current generation of geostationary satellite sensors. The monthly K_{dQ} from the MSG data is shown in Figure 5.5.5.

The monthly K_{dQ} maps from the MSG data (Figure 5.5.5) has better spatial detail than the K_{dQ} from the MFG data (Figure 4.4.1, p95). The better spatial accuracy made the K_{dQ} from the MSG can be mapped without red-edge problem, which used to be in the K_{dQ} maps from MFG data. The different time period of the MSG (March 2005 – March 2012) and MFG (August 2003 – June 2006) made monthly average K_{dQ} maps from MSG data has slightly different from the K_{dQ} maps from MFG data (comparison between Figure 5.5.5 and Figure 4.4.1).

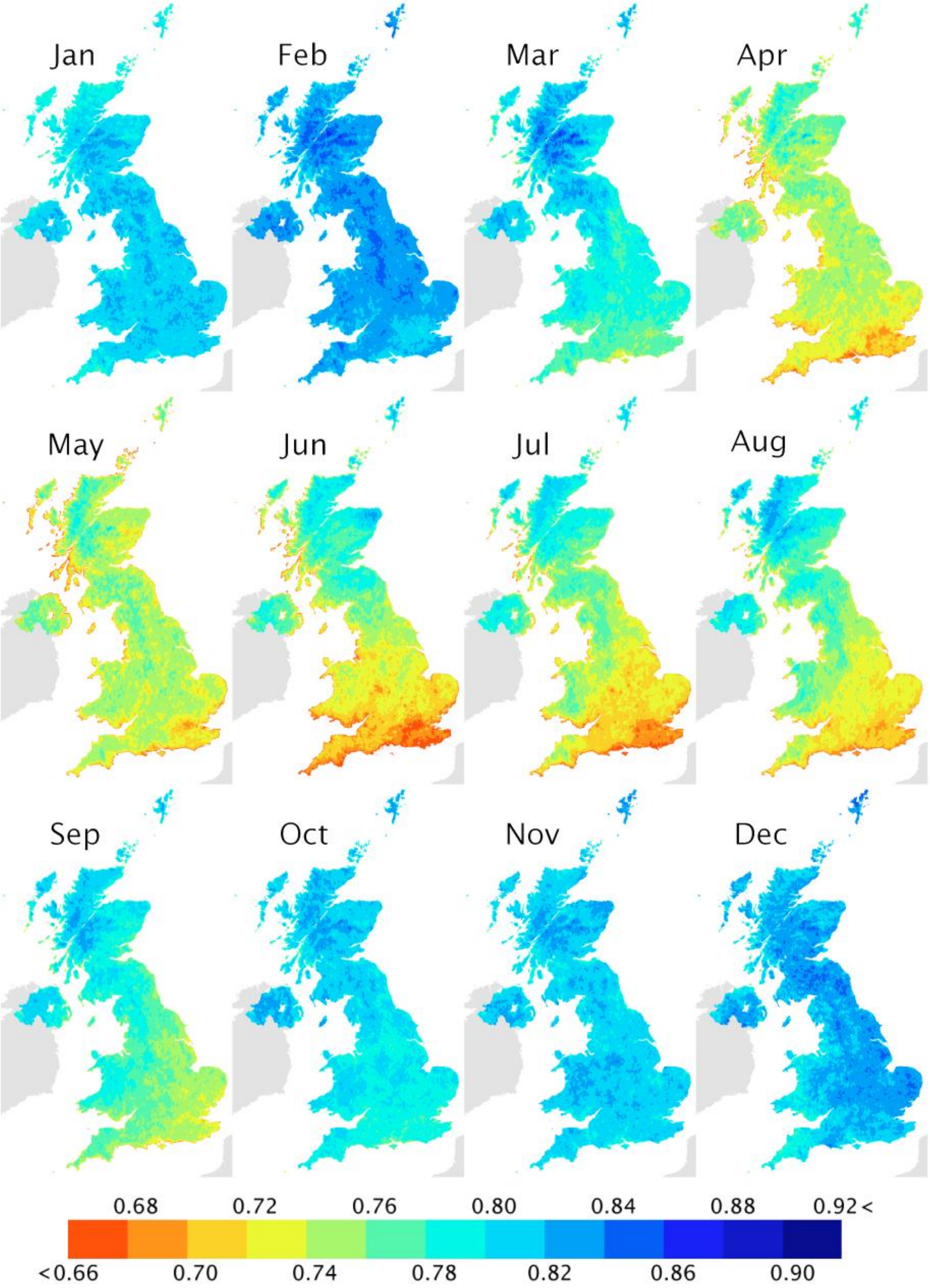

Figure 5.5.5 Monthly diffuse PAR fraction (K_{dQ}) map using MSG data

b) Diffuse PAR (Q_d) map

The maps of Q_d and K_{dQ} are different as they each represent unique physical interactions which vary in different ways:

- Q_d is a quantity representing a directional property of PAR, while K_{dQ} is a fraction, Q_d/Q_t. Q_d has the same physical units as Q_t, but K_{dQ} is unitless.
- Q_d is highest at midday (solar noon), and low in the morning and evening, but K_{dQ} is the inverse.

Finally the monthly Q_d has been summed to shows the spatial variation of the yearly Q_d in the UK (Figure 5.5.6).

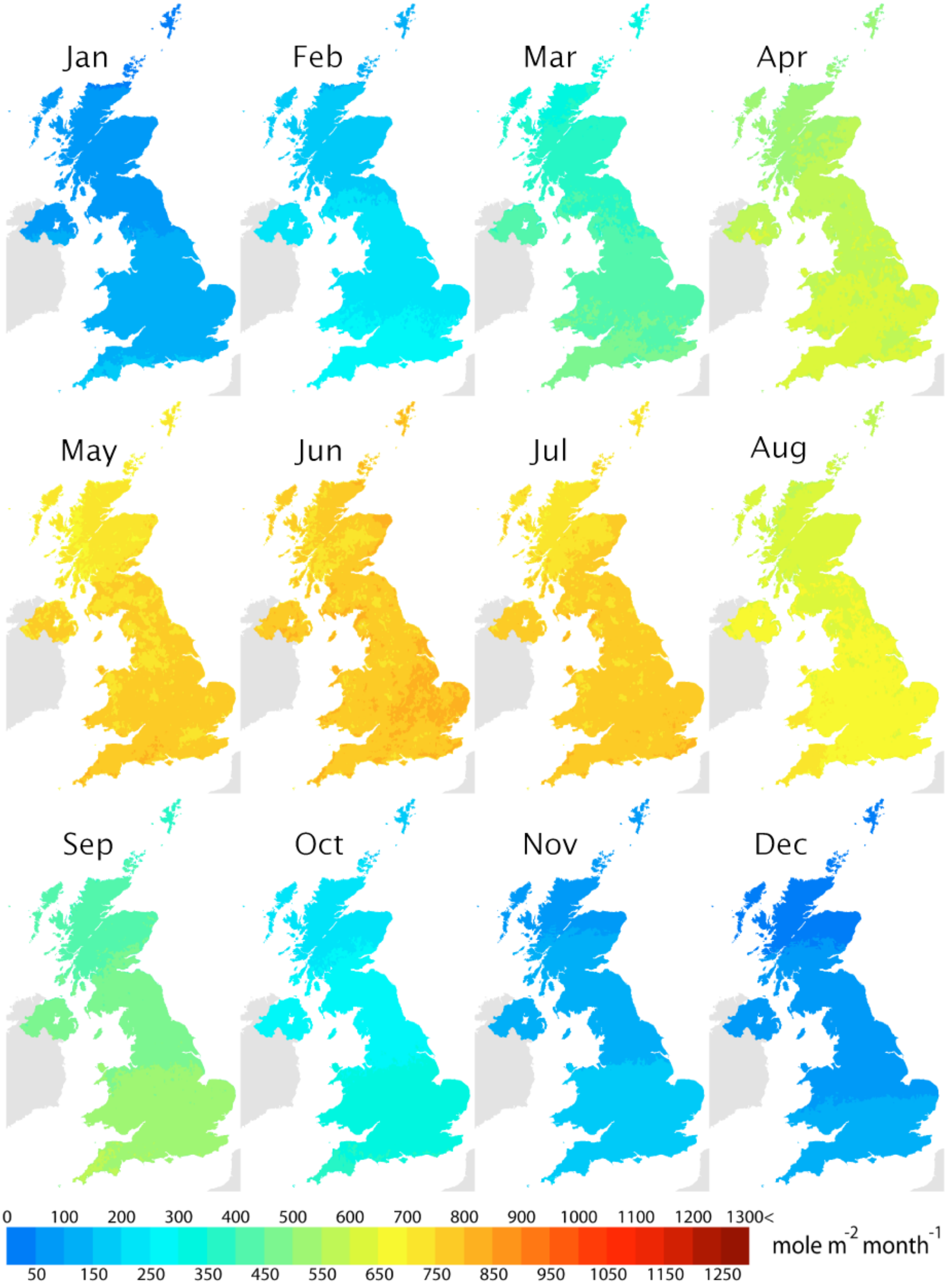

Figure 5.5.6 Monthly diffuse PAR (Q_d) maps based on MSG data

The monthly map of the Q_d and the monthly map of K_{dQ} showed obvious different variation. Both temporal and spatial variation between the Q_d and K_{dQ} is different.

- **The temporal variation**: the monthly Q_d is highest in the summer period, inversely, K_{dQ} is highest in the winter. Monthly Q_d in the UK varies between 0 – 1300 mole m^{-2} month^{-1}, while monthly K_{dQ} varies between 0.66 – 0.92.
- **The spatial variation**: within each month, Q_d does not differ much across the whole country. In contrast, K_{dQ} has more spatial variation.

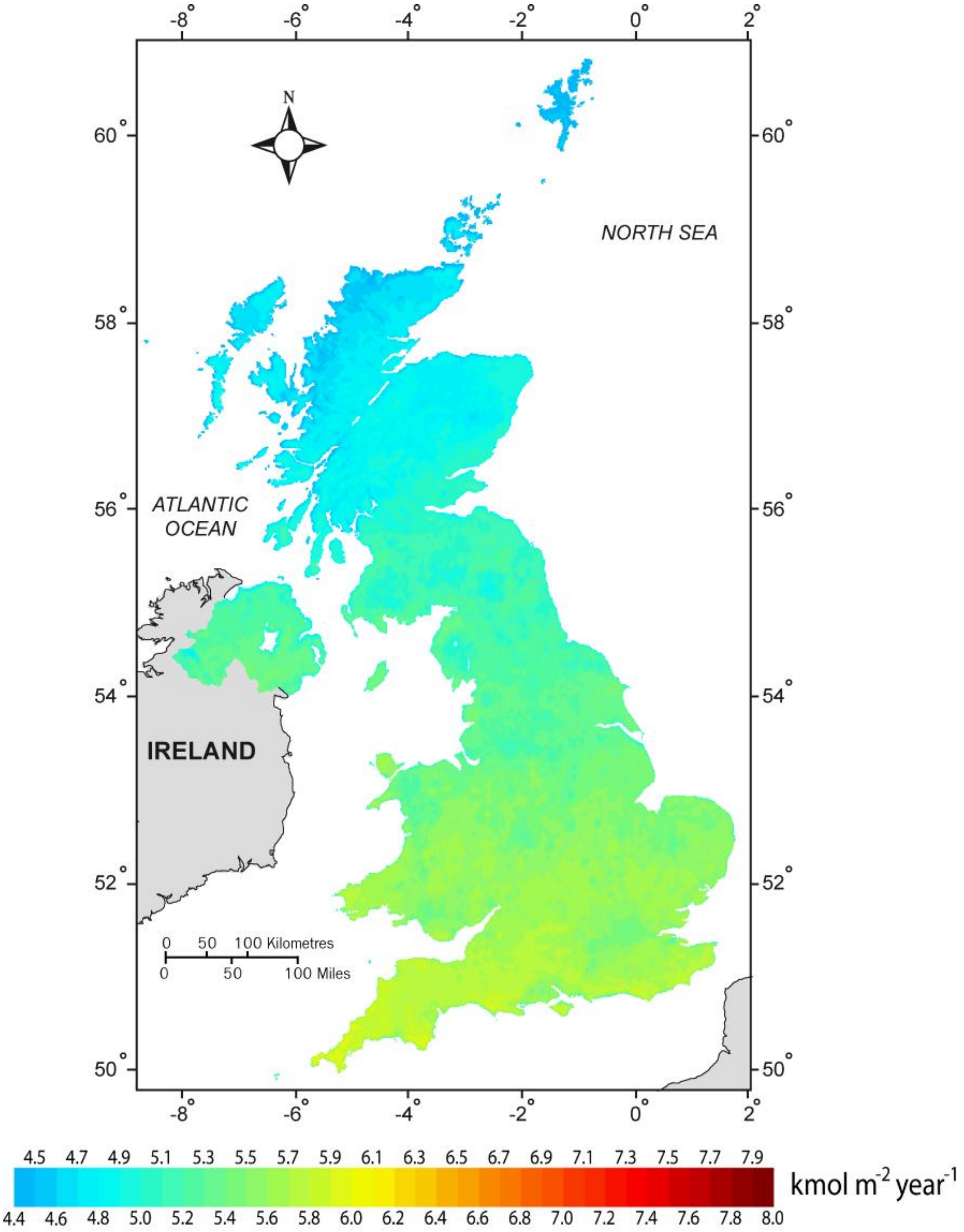

Figure 5.5.7 Yearly diffuse PAR (Q_d) map

The spatial patterns and variations of the annual Q_d follow the spatial variations of the annual Q_t, with the quantity lower around two-third of the annual Q_t (Figure 5.5.7). The annual range of the Q_d is from around 4.4 $\mathrm{kmol\,m^{-2}\,year^{-1}}$ in the North of Scotland to around 6.0 $\mathrm{kmol\,m^{-2}\,year^{-1}}$ along the South of England.

5.6 Discussion

PAR is a key input variable in most of the ecosystem gross primary productivity (GPP) models. However, at present there are no standardised products available that provide regular high spatial and temporal resolution observations of PAR. Therefore, most of the remote sensing based regional/global estimates of primary productivity rely on coarse scale interpolated data. For example, the MODIS GPP product (MOD17GPP) uses a PAR data at 1° x 1° spatial resolution (Running et al., 2000). The poor representation of PAR in those models is identified as one of the main source of uncertainty in the model prediction of GPP (McCallum et al., 2009). The method proposed in this chapter provides the potential opportunity to generate PAR at 1 km spatial resolution at a regional to global scale which is at a comparable spatial resolution to other model inputs, thus it would help to reduce uncertainty of global carbon estimation.

This study has described a method by which the amount of $\mathrm{Q_t}$ and $\mathrm{Q_d}$ may be estimated at a time interval suitable for use in process-based vegetation productivity models. The method achieves high temporal resolution by the use of data from a geostationary satellite sensor, something which in the past would have meant sacrificing spatial resolution and cartographic accuracy when used at the latitude of the UK. The advent of sensors such as SEVIRI on MSG means that ‘hypertemporal’ multispectral sensing is now possible for such areas, complementing the less frequent but more detailed measurements from sensors such as MODIS and AVHRR.

Liang et al. (2006) published a method for estimation of incident photosynthetically active radiation from Moderate Resolution Imaging Spectrometer (MODIS) data, with spatial resolution 1 km. The method described by Liang et al. (2006) is for daily PAR estimation but the limitations of MODIS sampling meant that it had to be based on two observations (one observation in the morning and one observation in the afternoon) sampled within an eight-day window (approximately 90 images a year). The method described in this chapter has the potential to capture better temporal detail of PAR.

The method as described here could be improved in several ways. Absorption by aerosols was not included in the method due to lack of data at suitable spatial resolution, something which is being addressed in a related study (Wilson et al, 2012). The aerosol amount in the sky over the UK has reduced over the last 50 years due to anti-pollution measures (e.g. Freney et al., 1975; DEFRA, 2012). However, yearly averages of aerosol optical thickness (AOT) at CFARR are still around 0.26 at 500 nm (www17). Incorporation of AOT into the PAR model will most likely improve its accuracy across the whole country, but especially over urban areas.

Aerosols are not the main factors causing attenuation of PAR in the UK. Weather in the UK is dominated by the passage of fronts so dense cloud controls PAR much more than aerosol amount. Also, the country has little biomass burning, the factories and vehicles have strict CO_2-emission controls, there is no desert, and the UK is an island, so absolute levels of aerosols are generally low. However, for future research, including the AOT into PAR modelling and mapping is desirable because this will increase the physical basis of the model.

In the model there is no coefficient for the transmittance of water vapour and the uniform mixed gases. The reason for this is that the effect of water vapour and uniform mixed gases is negligible in the PAR wavelength band (e.g. Iqbal, 1983, pp. 130 - 131; Asrar, 1989, p. 338). In the future, including transmittance due to water vapour and due to aerosols in the model will probably increase its accuracy.

The empirical basis of the model means that although it worked well over the UK, it is unlikely to be extendable to other areas in its present form. However, the method is based on meteorological and satellite data that are widely available, and it is readily adapted to data from different satellite sensors for example. Ironically, one of the main limitations of the method is that it relies on the presence in every pixel of bright cloud on at least a few occasions during the observation period, in order to establish the value of $\mathrm{DN}_{\mathrm{max}}$. This is not a problem in the UK but it would be for some parts of the world, such as desert areas.

In summary, the previous chapters have presented a method to estimate incident PAR (global and diffuse) at high temporal resolution and fine spatial detail across the UK. The aim was to produce a method that was sufficiently accurate for the task intended (as an input to plant productivity modelling), but not so demanding in input data or computation to make it unworkable in practice. This aim has been achieved, and the method has been validated as far as that is possible, given the lack of independent data on global/diffuse PAR in the UK. In the next chapter the maps of global and diffuse PAR produced by the method will be used in conjunction with a state-of-the-art plant productivity model to assess the significance of temporal and spatial variations in the amount and distribution of PAR across the UK.

Chapter 6 Application of the satellite estimated PAR within the FLIGHT model

6.1 Introduction

Photosynthetically active radiation (PAR) is an important factor controlling plant photosynthesis, which in turn affects carbon sequestration. Most plant productivity models use coarse resolution PAR, either in time (e.g. 8-day window from MODIS) or over space (e.g. 1°×1.25° from TOMS PAR, 2.5°×2.5° from ISCCP PAR; Wang et al, 2010). This means there is uncertainty in estimating carbon flux at time scales and over spatial extents that are needed for ecosystem survey and management. Furthermore, diffuse PAR is an important component of solar radiation, but most models do not account for it (Lieth, 1975; Parton et al., 1993; Potter et al., 1993; Running and Hunt, 1993; Esser et al., 1994; McGuire et al., 1995; Prince and Goward, 1995; Haxeltine and Prentice, 1996; Ruimy et al., 1996; Parkinson and Greenstone, 2000; Veroustraete et al., 2002; Sitch et al., 2003) (see more detail in Section 2.6 and 2.7 of Chapter 2). It is unclear from the literature whether this omission is a significant source of uncertainty in plant productivity models. The aims of this chapter are (i) to evaluate the potential of the satellite-derived finer spatial resolution PAR in estimating primary productivity, (ii) to evaluate the effect of direct and diffuse PAR in a productivity model.

A number of plant productivity models have been developed over the last three decades, but only a few have the capability to separate direct and diffuse PAR to drive the photosynthesis process and hence the resulting plant productivity. The Forest Light (FLIGHT) model was selected for study because it has an option to use the diffuse PAR fraction (fDIF) (more information on FLIGHT is in Section 2.6 of Chapter 2).

The Forest Light model (FLIGHT) is a 3-dimensional (3D) model of light interaction in a forest, based on Monte Carlo methods, and has been developed specifically for forest scenes (North, 1996). In the FLIGHT model, the forest is represented as a 3D arrangement of trees, leaves, branches etc., the properties of each (size, shape, orientation etc.) being represented by parameters. Solar and sky irradiance in

FLIGHT is represented as a function of angular variables (zenith and azimuth) in 3D. The essential solar radiation variables for FLIGHT determine the parameters related to PAR: global PAR (on a horizontal plane), direct PAR (on a horizontal plane) and fDIF, the diffuse fraction.

The original FLIGHT model was modified to include photosynthetic rate calculation by Barton and North (2001). Then, it was expanded to a full photosynthesis model by Alton et al. (2005). The input files for FLIGHT are composed of those describing the overstory and understory vegetation, and others for soil and solar radiation parameters. The model considers the path of individual photons of the light through the forest canopy, which is represented by the aggregated characteristics of individual leaves. A 3D model was essential for this research as it enabled the geometric distribution of sky radiance to interact with the canopy architecture. There are several 3D models available and they have been compared in the RAMI benchmarking exercise (www18). FLIGHT was also selected because of its ability to estimate GPP, which is rare for any vegetation canopy reflectance model and because it can accept the diffuse fraction of PAR as an input.

6.1.1 Principles of light interaction in FLIGHT

The Monte Carlo method is used to calculate random light direction, transmittance and absorption of photons in the PAR wavelength band in the FLIGHT model. North (1996) summarised the Monte Carlo algorithm in FLIGHT as:

1. A photon is initialized above the canopy from the direction of the solar disc, with known intensity as the input data.
2. The photon moves to the next position on any part of a tree in the forest (depending on random light trajectory). The new direction and the intensity is changed, the path of the photon is known from the simulation.
3. Calculate new position of the photon on any tree in the forest (depending on random light trajectory).
4. Simulate the new scattering direction after collision.
5. Calculate the intensity of the photons in the solid angle at the point that a collision occurs.

6. If the photon leaves the canopy, accumulate the intensity in the direction of that solid angle, otherwise repeat the process from step 2 until the number of photons drops below some threshold.
7. Repeat from step 1 for other photons.

The accumulated photons in the solid angle for each direction is the intensity scattered in that direction. From the intensity in each direction, the reflection, absorption and transmittance are calculated. Figure 6.1.1 summarises the processes involved in the FLIGHT simulation model.

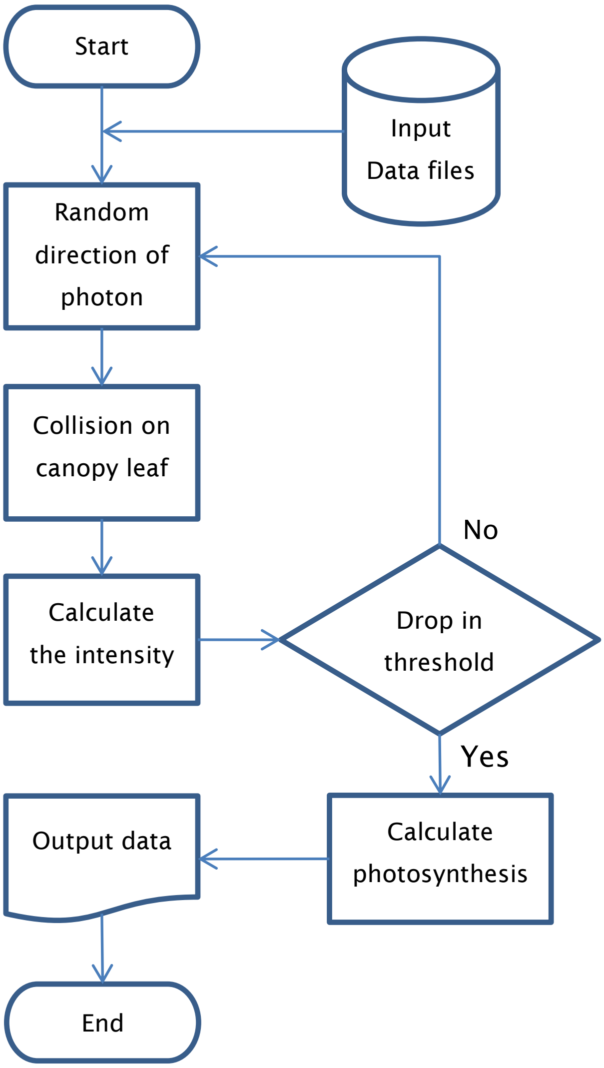

Figure 6.1.1 Summarised FLIGHT flowchart

6.1.2 Advantages of the FLIGHT model

FLIGHT can use difference sources for the input data, both from in-situ and remote measurements. In practice, most forests will not have all the measured data to input to FLIGHT, therefore remotely sensed data are an ideal alternative data source.

The FLIGHT model has many input parameters to represent the vegetation canopy in as much detail as possible, making it one of the most accurate models of vegetation-light interaction and in turn forest productivity (North, 1996; Barton and North, 2001; Alton et al., 2005; Alton and North, 2007). However, in the calculation of GPP, FLIGHT does not include wind direction and wind velocity components. Therefore the output from FLIGHT is the canopy productivity at a given point, disregarding horizontal fluxes.

6.1.3 Definition of input parameters

The parameters and coefficients used in the FLIGHT simulation were either generated from previous studies (Chapter 4 and 5) or from standard vegetation characteristics of the canopy determined during site visits. There are more than 40 input variables in FLIGHT needed to generate GPP. In this study the key variables and the sources of data used are in Table 6.1.1.

Table 6.1.1 Key variables and actual numbers used in the FLIGHT

Key variables used in FLIGHT	**Actual number used**
PAR ($\mu\text{mol m}^{-2}\text{s}^{-1}$)	Calculated from the global broadband irradiance and from the developed model (Chapter 5)
fDIF (Diffuse PAR fraction)	Calculated from the developed equation (Chapter 4)
IR ($\text{Infrared}, \mu\text{mol m}^{-2}\ \text{s}^{-1}$)	Calculated from the global broadband irradiance and the calculated PAR
Photosynthetic rate coefficient	200.0 $\mu\text{mol PAR m}^{-2}\ \text{s}^{-1}$
Maximum photosynthetic rate ($\mu\text{mol C m}^{-2}\text{s}^{-1}$)	Estimated the maximum value from the FLUXNET data
Mode of operation: Forwards ('f'), image ('i'), solid-object image ('s'), reverse ('r')	Reverse ('r'), represented by 'r' to enable using the fDIF
Dimension of simulation: '3' means 3D, '1' means 1D	3D, represented by '3'
Solar zenith and solar azimuth (degree)	Calculated using Sun-Earth geometry equations, depending on position and time
Total LAI (one side leaf area index)	Monthly averaged after MODIS data
Foliage composition: (1) fraction of green leaves in foliage by area, (2) fraction of senescent/shoot material in foliage (3) fraction of bark in foliage	1.0, 0.0, 0.0
Leaf angle distribution (LAD), between normal to leaf and vertical, expressed as fraction lying within 10° bins (0-10, 10-20, 20-30…80-90)	0.125, 0.045, 0.074, 0.100, 0.123, 0.143, 0.158, 0.168, 0.174
Soil roughness index (0-1), Lambertian soil has soil roughness = 0, the 60° slope has soil roughness =1	Lambertian, represented by '0'
Aerosol optical thickness at 555 nm (A negative value means direct only)	Monthly averaged after AOT from AERONET sunphotometer at CFARR
Leaf size (radius, approximating leaf as circular disc, unit metre)	0.1 m
Fraction of ground cover by vegetation	0.5
Crown shape: 'e' for ellipsoid, 'c' for cones, 'f' for field data	Ellipsoid, represented by 'e'
Crown radius and centre to top distance (metre)	10.0, 10.0
Min and Max height to first branch (metre)	1.0, 9.0

Infrared (IR) irradiance is a solar irradiance parameter used in FLIGHT that is not included in most other models. The IR value used in this study was determined from the energy left after subtracting the PAR energy from the measured broadband energy.

The hourly average aerosol optical thickness (AOT) at 555 nm was estimated using the AOT measured by a sunphotometer of the aerosol robotic network (AERONET, www19) at the STFC Chilbolton Observatory in Hampshire. The LAI data for the FLIGHT input in this study was the average of the MODIS LAI product (MOD15A2) in each month, during 2005-2010.

a) Influence of PAR on the vegetation productivity in FLIGHT

The main input solar irradiance data for the FLIGHT model is the PAR, the molar quantity of photons in PPFD units (μmol m^{-2} s^{-1}). The variation of the vegetation productivity in FLIGHT strongly depends on the variation of PAR, as it is one of the key inputs for photosynthesis. However, the rate of photosynthesis saturates at higher levels of PAR.

The global PAR (Q_t) is widely used as the main parameter in many general vegetation productivity models. The influence of the diffuse PAR (Q_d) in terms of the diffuse PAR fraction ($fDIF$) is not yet properly understood. Not many long-term measurements of Q_d and $fDIF$ are available, and very few models include $fDIF$ as an input parameter.

b) Influence of diffuse PAR fraction on the vegetation productivity in FLIGHT

Considering the same intensity, Q_t, the vegetation productivity under Q_d is thought to be higher than vegetation productivity under direct radiation alone (e.g. Gu et al., 1999; Gu et al., 2002; Alton et al., 2005; Alton et al., 2007a; Alton and North, 2007; Alton et al., 2007b). Accurate determination of Q_d in terms of the $fDIF$ for

FLIGHT is therefore an important parameter which could influence the accuracy of the model output.

The influence of fDIF on productivity also depends on the Q_t intensity. Higher fDIF can enhance the vegetation productivity for the same amount Q_t but if the Q_t is reduced then fDIF cannot enhance the productivity (Alton et al., 2007). These interactions between fDIF and Q_t needed to be represented in the model in order to provide a realistic estimation of the vegetation productivity.

In the FLIGHT model, fDIF is estimated as the fraction of the Q_d in Q_t. FLIGHT has an option to use or not use fDIF. By using fDIF, the vegetation productivity output from FLIGHT is higher than the case without fDIF. Alton et al. (2005) found the Light use efficiency (LUE) increased up to 10% for the canopy when fDIF was increased from 25% to 75%, using ground data. These findings support the use of fDIF in FLIGHT for better representation of the natural environment that has a significant proportion of diffuse irradiance.

In practice, a larger fDIF for the same amount of Q_t gives more chance of the canopy leaves to receive more PAR because it scatters the Q_d over many different directions. Therefore canopy leaves below other leaves can become exposed to Q_d. The increase of Q_d on those leaves enhances their photosynthesis.

LUE has been reported to increase > 50% under diffuse sky conditions (Choudhury, 2001; Gu et al., 2002; Alton et al., 2007b). However, the relationship between PAR, photosynthesis rate and GPP is complicated (e.g. Gaastra, 1963; Hubbard et al., 1999; Gu et al., 2002). Too much direct PAR (approximately >1500 $\mu\text{mol m}^2\ \text{s}^{-1}$) can cause photosynthesis to reduce due to the direct effects of the high energy on the leaf photosystem (e.g. Powles, 1984; Long et al., 1994). A high level of direct PAR that has been diffused by cloud and other atmospheric components is more tolerable as the load on individual leaves is less.

In this study, the fDIF was calculated using the relationship (Equation 4.3.1) between the fDIF and the fraction of the global broadband irradiance per extraterrestrial irradiance ($K_T = S_d/S_t$), using equations from previous study in Chapter 4. The diffuse PAR fraction was calculated based on Butt et al. (2010) and given the symbol K_{dQ}. In the current Chapter, the diffuse PAR fraction is fDIF based on the nomenclature of the variables in FLIGHT. Therefore, $\mathrm{fDIF} = \mathrm{K_{dQ}}$, which has the same definition as in Chapter 4.

6.2 Using FLIGHT with the PAR from maps of hourly average per month

There are two study sites in this work: (i) Alice Holt and (ii) Wytham Woods. Both are mature mixed forests, mainly oak and conifer. The forests are situated in Hampshire and Oxfordshire respectively and are described in Chapter 3.

The FLIGHT model was manipulated to use the data from the generated PAR maps in Section 5.5.1 of Chapter 5. This was done in order to calibrate the FLIGHT simulation using the ground FLUXNET GPP data.

6.2.1 Method

The FLIGHT model requires more than 40 parameters (model parameterization is in North, 1996; Alton et al., 2005), many of which are not routinely observed at the study sites. For some parameters an approximate value based on literature was used. For example, parameters for the 3D structure of the tree were based on approximation from field visits, LAI was taken from MODIS data, and the IR parameter was derived from the broadband irradiance data. There were also no fDIF measurement at the sites, so it needed to be derived by using the equations from the broadband data.

The derived equation for calculating IR in unit of $\mathrm{\mu mol\ m^2\ s^{-1}}$ for FLIGHT input was:

$$\mathrm{IR\ [\mu mol\ m^{-2}\ s^{-1}] = 2.02366\ [\mu mol\ s^{-1}/W] \times S_t\ [W\ m^{-2}\ ]} \qquad (6.2.1)$$

The equation for calculating fDIF was (from Section 4.3.1 of Chapter 4):

$$\mathrm{fDIF} = \mathrm{K_{dQ}} = -2.2171\,\mathrm{K_T}^2 + 0.5355\,\mathrm{K_T} + 0.9644 \qquad (6.2.2)$$

The result of a FLIGHT simulation using these data is shown in Figure 6.2.2.

Figure 6.2.1 summarises some of the key variables used with the FLIGHT model, computed as the average of hour in each month during the period 2005-2010, and plotted over a year. The LAI values were obtained from MODIS product MOD15A2 (Collection 5), and the summer values in particular are lower than would have been expected from a mixed forest site in southern England. However, the trend in LAI is as expected and the absolute LAI values are similar at both sites.

The monthly averaged aerosol optical thickness (AOT) measured at the AERONET site in north Hampshire ranged from 0.16 to 0.37.

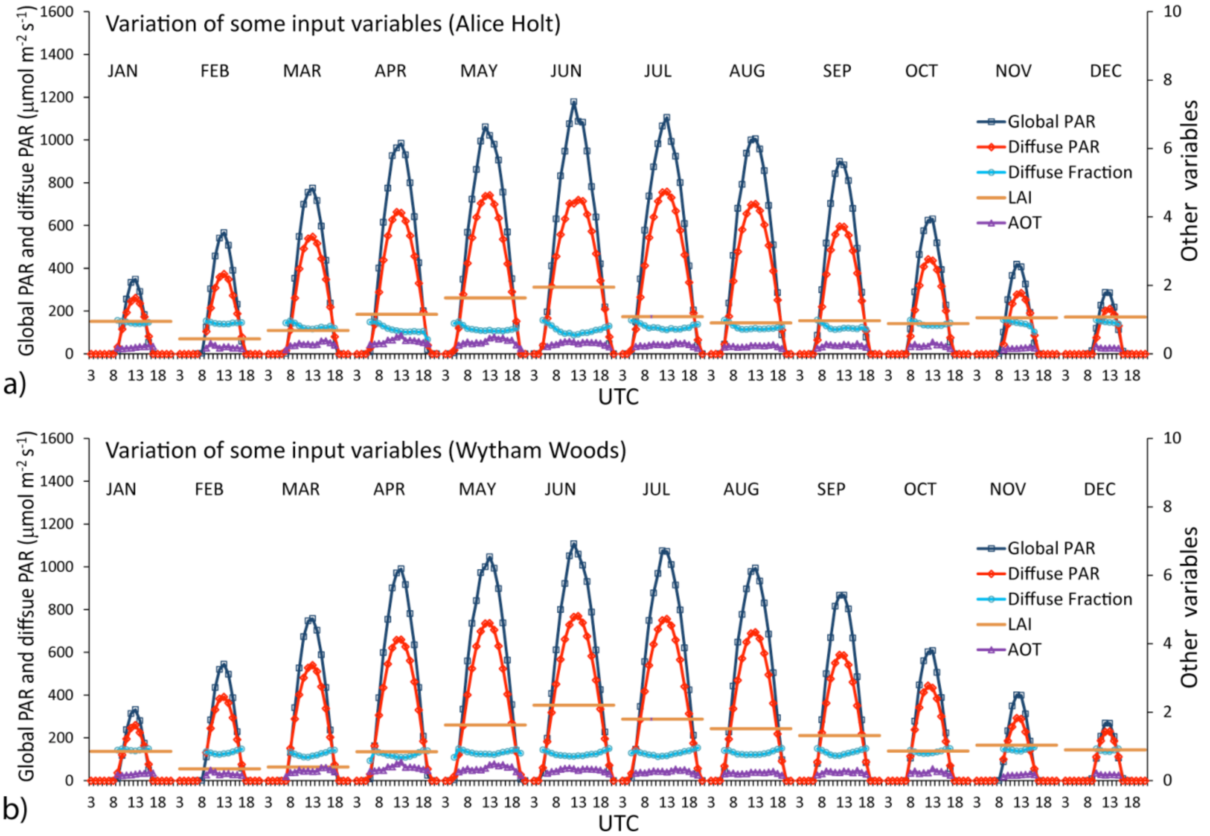

Figure 6.2.1 Variation of some input variable for FLIGHT at a) Alice Holt and b) Wytham Woods (this study focus on the hourly average in each month therefore the x-axis is hour of the day; each curve represent the average diurnal variation in that month)

The use of LAI data from MOD15A2 was a possible source of error, as the relatively large pixel size of MODIS would have included areas of understorey, canopy gaps and possibly even non-forest land cover. However, this was the best available long-term data set for the sites.

A more fundamental issue concerned the comparison between GPP estimated using FLIGHT and GPP measured using sensors on the FLUXNET towers. The FLUXNET GPP uses the eddy covariance method with the measured wind 3D component and gas concentration data, derived from an ultrasonic anemometer and infrared gas analyzer, respectively. FLIGHT simulates GPP from the parameters without considering wind strength and direction. For this reason, the GPP product from FLIGHT simulation and FLUXNET data can be different. FLUXNET GPP data come from the mixed canopy in the real situation. It was therefore necessary to adjust the FLIGHT GPP output to match the diurnal variation of the FLUXNET GPP.

In the light of the necessary scaling of the GPP data, the apparent error in the MODIS data was treated in the same way, and a single correction factor was derived to deal with both issues. Although a more accurate physically-based correction would have been preferred, this was not an option in the time available and, in any case, would have needed data sets that were not available. It was still possible to use the FLIGHT model to investigate the effect of changes in fDIF on GPP, which was the main aim of the research.

6.2.2 Intercalibration of FLIGHT GPP and FLUXNET GPP

Firstly, hourly GPP simulated using FLIGHT was compared with hourly GPP from FLUXNET measured data (Figure 6.2.2 and 6.3.3). At both sites the FLUXNET GPP has more variation than the FLIGHT GPP (Figure 6.2.2), being lower in the winter and spring season and higher in the summer. The FLIGHT underestimate of GPP in the summer period is consistent with the LAI values being lower than those measured by FLUXNET.

Scatter plots of the data at both sites (Figure 6.2.3) show similar relationships between GPP estimated by FLIGHT and that measured by FLUXNET, however, the relationship at Alice Holt forest is much weaker than that at Wytham Woods. This again points to site-specific factors affecting the results. It may be significant that the pyranometer at Alice Holt forest is very old and its calibration is in question (Table 3.3.2).

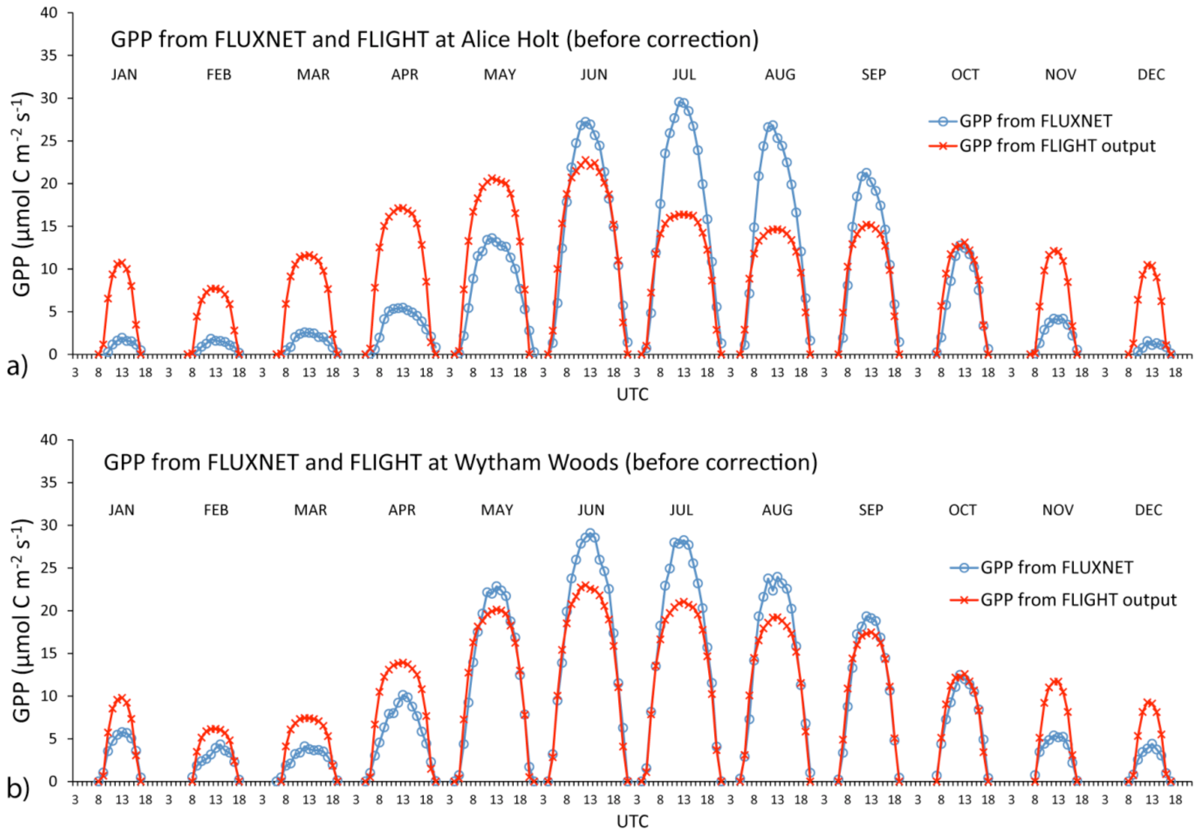

Figure 6.2.2 Comparison of the variation of the hourly GPP between the predicted GPP using FLIGHT and measured GPP using FLUXNET at a) Alice Holt and b) Wytham Woods, by using PAR data from maps

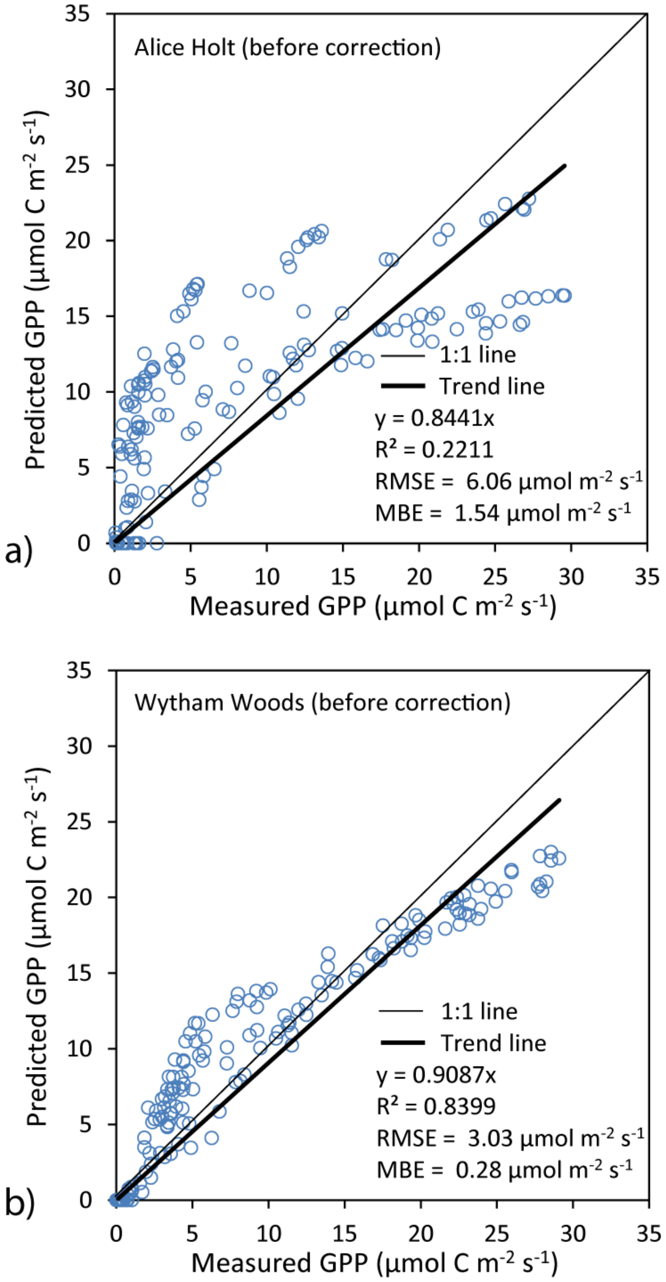

Figure 6.2.3 Comparison between hourly average per month of the predicted GPP using FLIGHT before correction and measured GPP using FLUXNET at a) Alice Holt and b) Wytham Woods, by using PAR data from maps

Additional insight into the patterns of GPP at the two sites is provided by looking at the monthly trends of GPP at midday, which we would expect to be the time with the most accurate data (least shadow, highest irradiance). Figure 6.2.4 shows that the FLIGHT midday GPP tracks the seasonal pattern of FLUXNET GPP at both sites, but at Alice Holt the spring increase in GPP occurred around one month before a similar increase was shown by the FLUXNET GPP. The data from Wytham Wood showed a much closer match for the spring green-up, and a similar pattern in the summer months. This was further evidence that site-specific factors at Alice Holt forest were affecting the data, and that for a more suitable site (e.g. Wytham Woods), a simple correction factor could be used to standardise the two data sets.

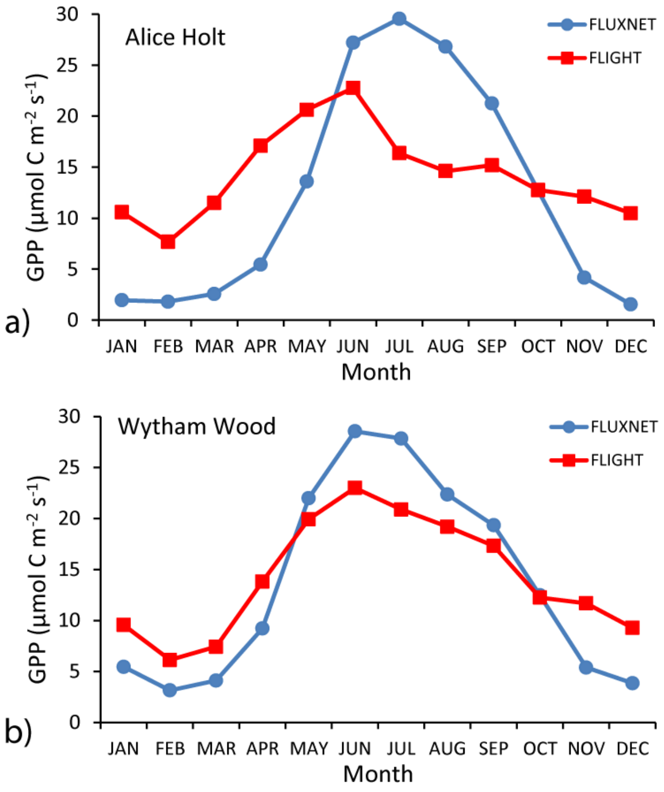

Figure 6.2.4 Variation of the midday GPP from FLIGHT and the midday GPP measured using FLUXNET at a) Alice Holt and b) Wytham Woods

Site-specific correction factors were calculated for each month from midday data. The correction factors were calculated by dividing the midday FLUXNET GPP by midday FLIGHT GPP in each month, as equation:

$$\text{Monthly correction factor} = \frac{\text{Midday FLUXNET GPP each month}}{\text{Midday FLIGHT GPP each month}} \tag{6.2.3}$$

Then the monthly correction factor was used to multiply the FLIGHT GPP product at every hour of day. To see the variation pattern, the graph of FLIGHT GPP and FLUXNET GPP at both sites is plotted (Figure 6.2.5).

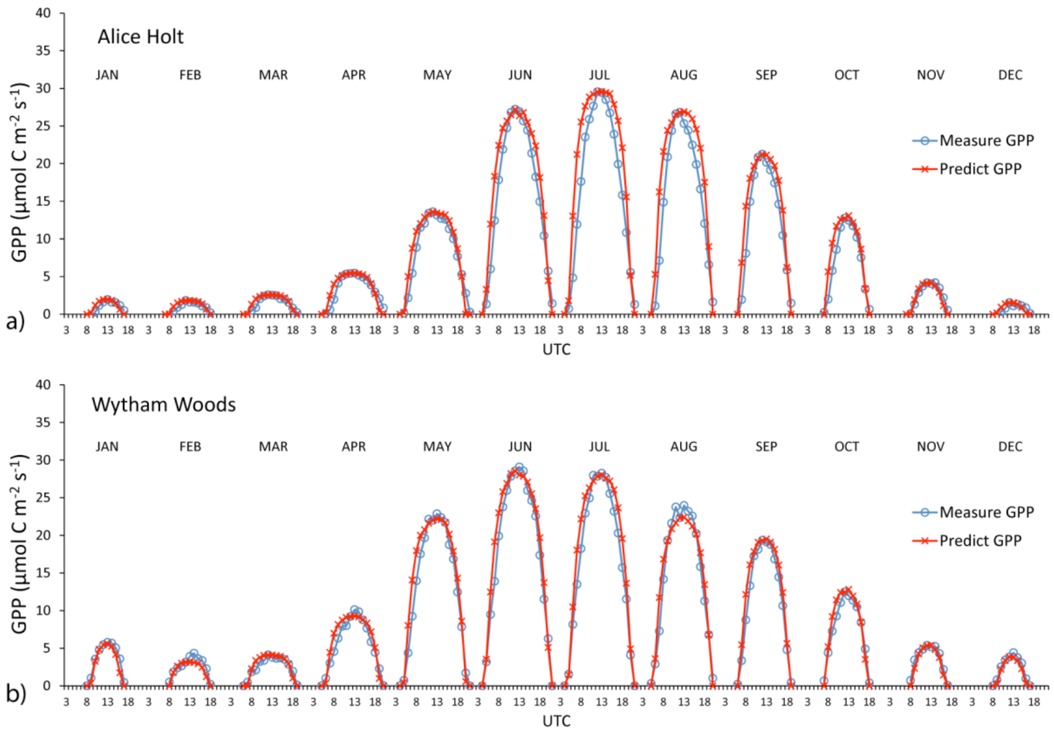

Figure 6.2.5 Comparison of the variation of the hourly GPP after correction between the predicted GPP using FLIGHT and measured GPP using FLUXNET at a) Alice Holt and b) Wytham Woods, by using the PAR data from maps

As expected, the two sets of measurements now match more closely, both as annual series (Figure 6.2.5) and as scatter plots (Figure 6.2.6). The remaining mismatch and scatter is due to the GPP data including measurements from all daylight hours, not just midday.

This empirical correction enabled the apparent error in LAI and uncertainty in GPP to be corrected, and made it possible to use the FLIGHT model to investigate the effect of changing input parameters, specifically fDIF. Figure 6.2.7 shows the simulated GPP from FLIGHT for two illumination regimes: (i) the direct and diffuse and (ii) direct only case, assuming that the total amount of the Q_t remained the same at the specific time but varying the proportion of the direct and diffuse.

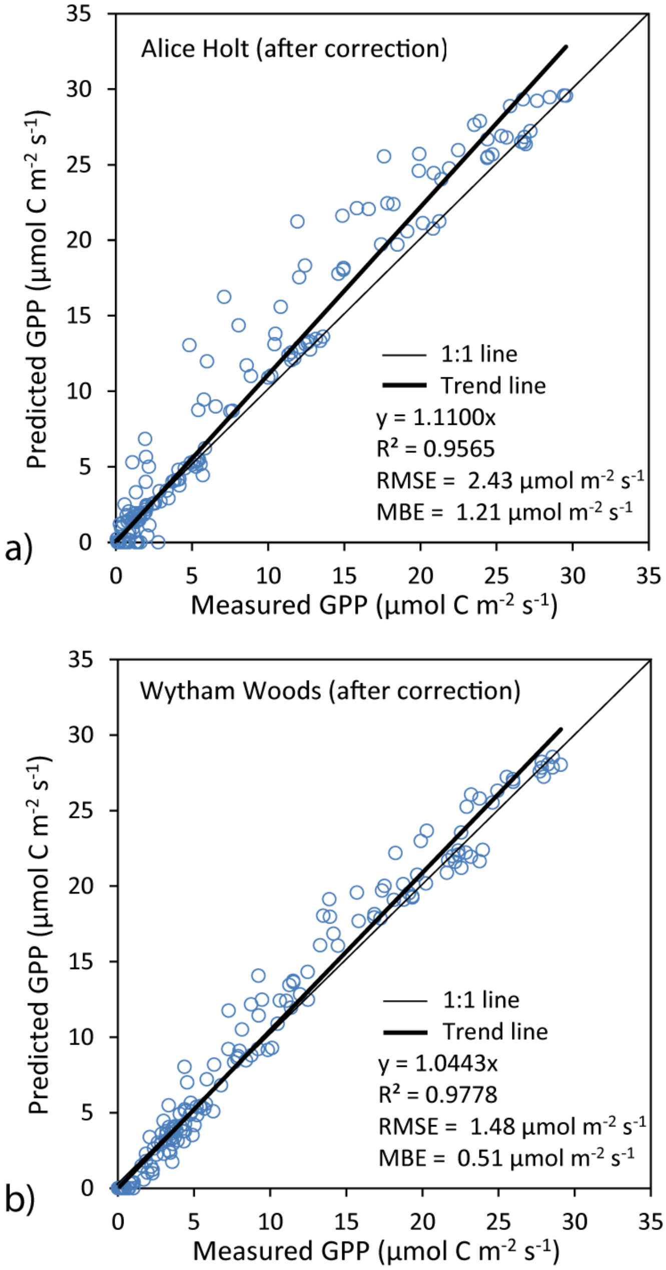

Figure 6.2.6 Comparison of the hourly average GPP between the predicted GPP using FLIGHT after correction and measured GPP using FLUXNET at a) Alice Holt and b) Wytham Woods, by using the PAR data from maps

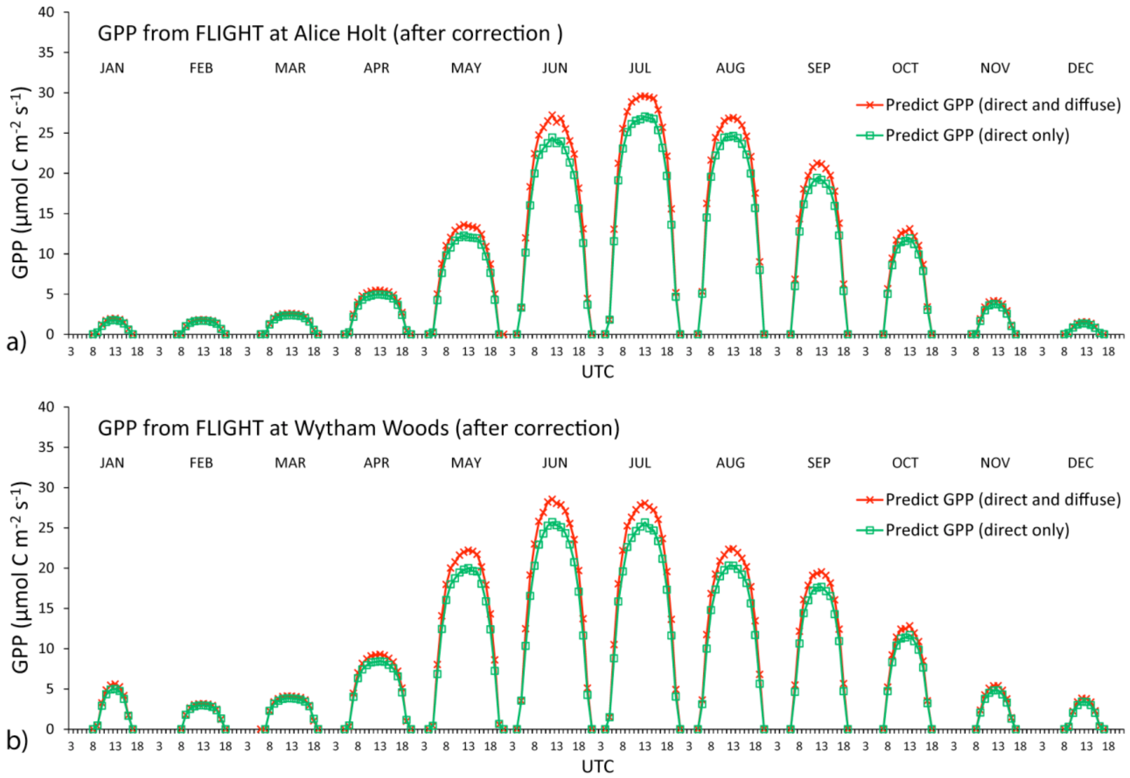

Figure 6.2.7 Variation of the predicted GPP from FLIGHT after correction base on the midday measured data at a) Alice Holt and b) Wytham Woods, by using the PAR data from maps

From Figure 6.2.7 the predicted GPP values can be divided into two groups:

- **Peak averaged GPP** $> \mathbf{10\ \mu mol\ C\ m^{-2}\ s^{-1}}$; composed of the six months of the growing season, between May – October.

- **Peak averaged GPP** $\leq \mathbf{10\ \mu mol\ C\ m^{-2}\ s^{-1}}$; composed of the six months of winter and autumn, between November – April, the dormant period.

Predicted GPP increased in every month of the year, which is more easily seen in Figure 6.2.8 which expresses the data as a percentage change. The average increase of GPP was 12.0 % and 12.4% for Alice Holt and Wytham Woods, respectively. This is consistent with the observations by Gu et al. (1999, 2002) and the modelled results from Alton et al. (2005, 2007) that vegetation productivity increases under diffuse sky conditions.

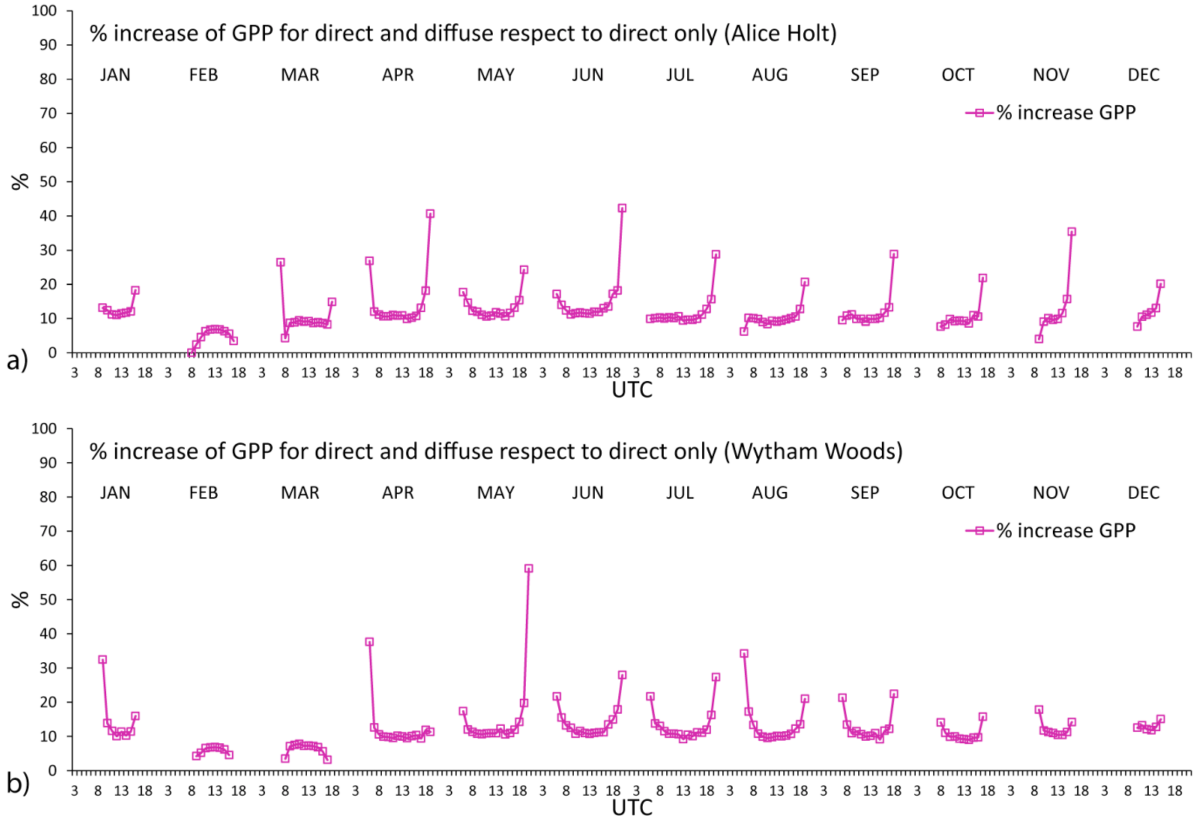

Figure 6.2.8 % increase of the GPP for direct and diffuse case respect to direct only at a) Alice Holt and b) Wytham woods

Variation of the GPP on PAR for the cases ‘direct and diffuse’ and ‘direct only’ of the FLIGHT using the PAR data from map were plotted (Figure 6.2.9).

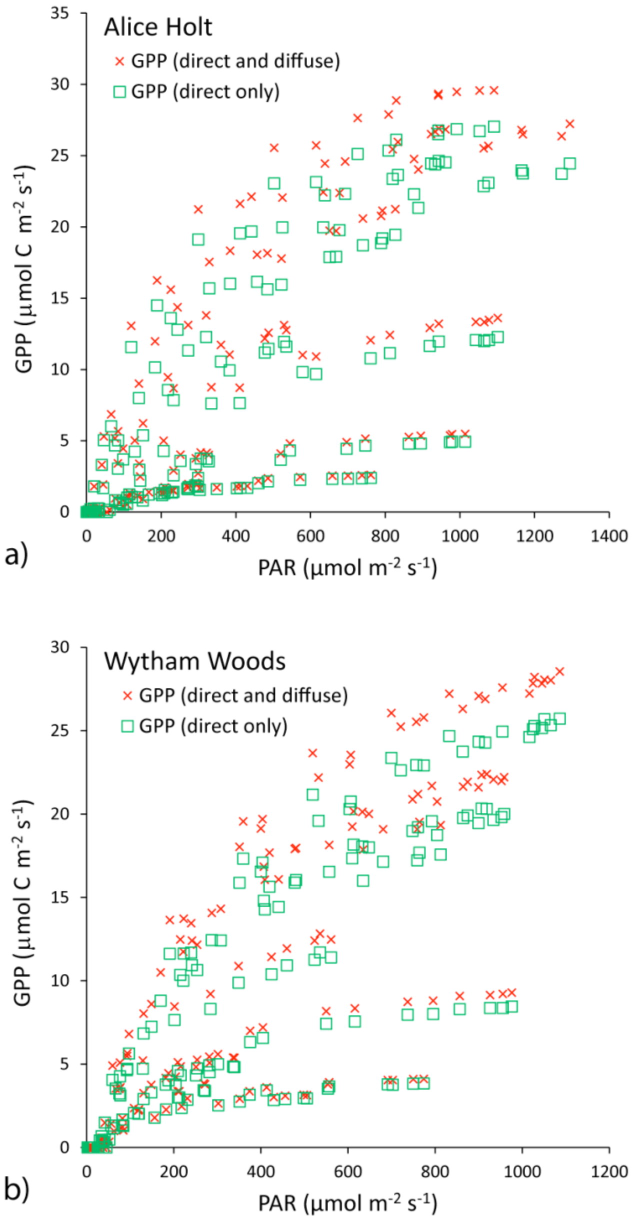

Figure 6.2.9 Relationship between PAR and the GPP from the prediction at a) Alice Holt and b) Wytham Woods, by using the PAR data from maps

6.3 Using FLIGHT with the instantaneous PAR from MSG

The previous section described how the FLIGHT model could be driven by averaged monthly data. In this section, MSG data were used to estimate hourly PAR which was then used as an input to the FLIGHT simulation. The model developed in Chapter 5 was used to estimate instantaneous PAR data for every hour on selected days. After that, the estimated instantaneous PAR at the two forest sites was used in the FLIGHT simulation. This was done in order to study the variation of GPP on PAR under different sky conditions, at high temporal resolution.

6.3.1 Method

Data were selected from days that have a high value of PAR, based on the measured data at the site and the appearance of cloud in the MSG images. The data were selected from June and July as these were considered to be the two months of highest PAR and GPP.

Possible MSG scenes were screened visually to identify days that had similar cloud conditions all day long. The selected days for the cloudy (high fDIF) and cloudless (low fDIF) for Alice Holt and Wytham Woods are shown in Table 6.3.1.

Table 6.3.1 Selected cloudy days and cloudless days

	Cloudy day (representing high fDIF)	Cloudless day (representing low fDIF)
Alice Holt	10th June 2010	16th June 2010
Wytham Woods	26th July 2007	27th July 2007

PAR was mapped over the whole UK at every daytime hour for the selected days, using the MSG data to determine the transmittance coefficient due to cloud. Other transmittance coefficients were calculated at the same time on the selected days using the model presented in Chapter 5. PAR data from the map over the FLUXNET sites, Alice Holt and Wytham Woods, were used as input data into the FLIGHT simulation.

Using FLIGHT with the instantaneous PAR data gave the GPP output at every hour on the selected days. The relationship between the hourly GPP from FLIGHT and the hourly PAR from maps was plotted to show the variation of the GPP with PAR, for the cloudy and cloudless case. The in-situ GPP and in-situ PAR from FLUXNET at the sites were also plotted to show the variation at the same site on the selected days (Figure 6.3.2).

6.3.2 Result

PAR at every hour from the maps on the selected days showed the spatial variation and the hourly variation over the UK (Figure 6.3.1). The maps show lower PAR beneath the cloud and the higher PAR in the exposed areas. From the modelling and mapping, it is clear that the variation of PAR at the surface depended on clouds.

The temporal variation shows a consistent pattern from the early morning to late evening. The variation in the spatial and temporal variation was also influenced by the extraterrestrial PAR, which was lowest in the morning, highest at midday and decreased again in the evening.

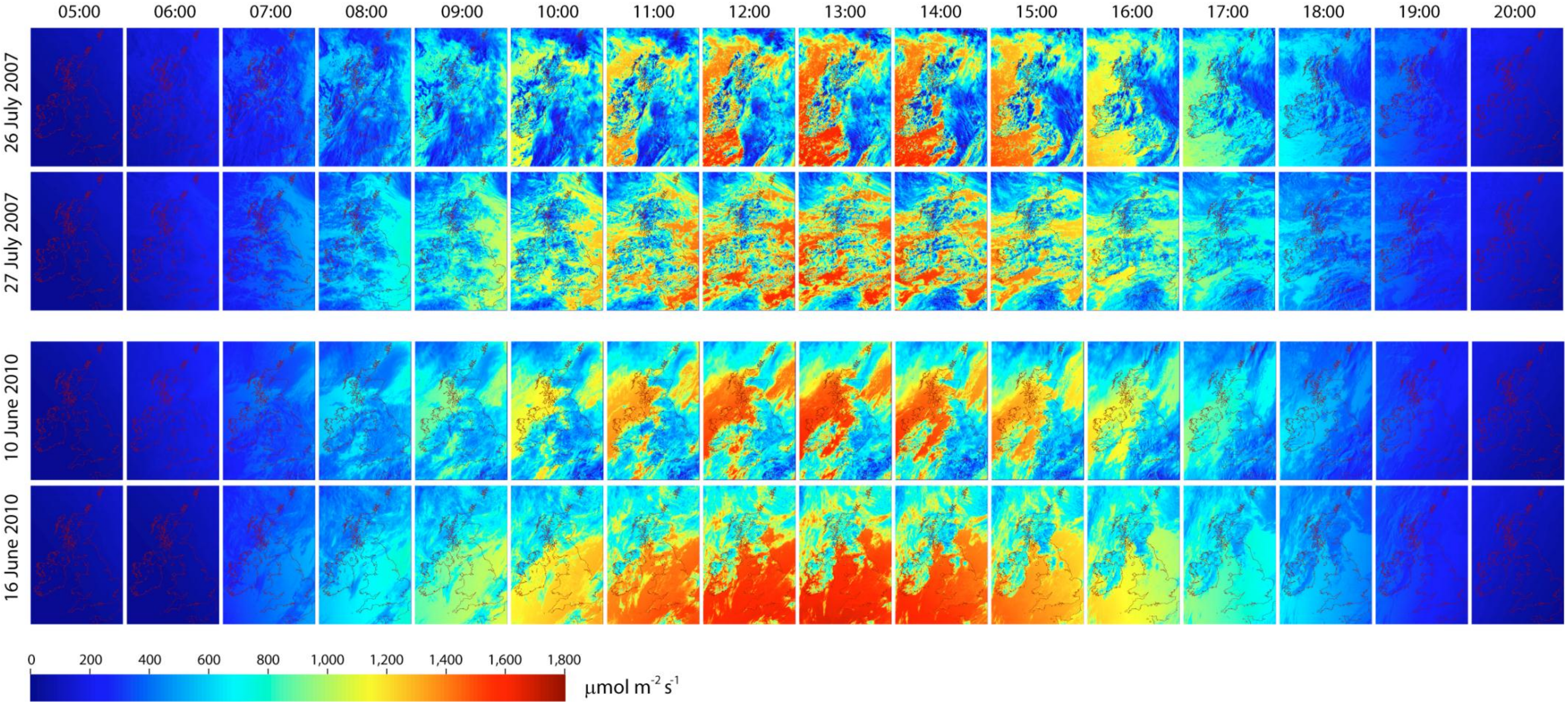

Figure 6.3.1 Hourly PAR map over the UK using instantaneous MSG data in the selected days

The relationship between GPP from FLIGHT and PAR from the maps are different from those the relationship between GPP and PAR from the FLUXNET (Figure 6.3.2).

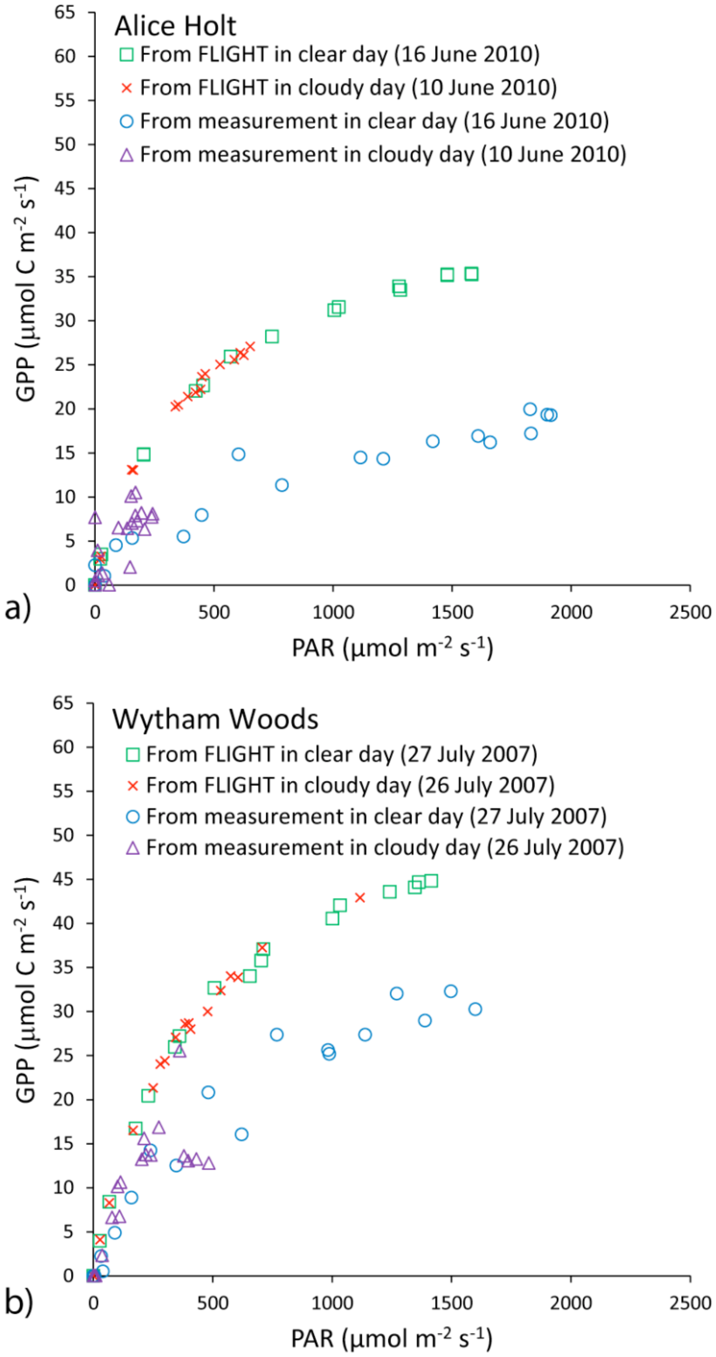

Figure 6.3.2 Variations of GPP on PAR from the prediction and from the measured data at a) Alice Holt and b) Wytham Woods

The clear days (Figure 6.3.2a, b) have the maximum PAR from modeling at ~ 1500-1600 $\mu\mathrm{mol\,m^{-2}\,s^{-1}}$. The difference between GPP from FLIGHT and that from FLUXNET increases with increasing PAR. GPP from FLIGHT on the selected days reached an upper limit at ~ 30 – 35 $\mu\mathrm{mol\,C\,m^{-2}\,s^{-1}}$.

The variation on the cloudy day (Figure 6.3.2a, b) had a maximum PAR from the modeling up to ~1000 $\mu\mathrm{mol\,m^{-2}\,s^{-1}}$. The variation of the GPP from FLIGHT increased with PAR on the same course as the clear day, but with a lower upper limit.

The difference between the measured GPP and the estimated PAR from FLUXNET might be explained by several reasons:

- **Time mismatch**: The time for each satellite image in the instantaneous PAR modeling is different with the time and period of the in-situ measured data. The MSG data are instantaneous snapshots at a specific time, while the available data from the FLUXNET is the average hourly data.

- **Small forest size**: The forest size at both Alice Holt and Wytham Woods is very small (< 10 km^2), but the FLIGHT model was derived from very big forests (North, 1996; Barton and North, 2001; Alton et al., 2005; Alton et al., 2007a; Alton et al., 2007b): (i) spruce forest in Howland, ME in USA (ii) Amazonia in Brazil and (iii) Siberian scots pine forest in Russia. Therefore FLIGHT may not be directly applicable to vegetation productivity at Alice Holt and Wytham Woods.

- **Wind problems**: The GPP from the surroundings area might contaminate the GPP of the forest. At an average wind speed of ~ 5 m/s an air parcel can be blown from more than 10 km within an hour. Furthermore, the surrounding areas of both forests have mixed rural land cover. Therefore, the different GPP rate could have been due to horizontal transport into the forests by wind. The FLIGHT simulation did not have any parameter to manage those problems. Therefore it is difficult to claim that the measured GPP from FLUXNET is only the pure GPP from the forest canopy.

6.4 Discussions and conclusions

6.4.1 Effect of diffuse PAR on productivity by using FLIGHT model

The effect of diffuse PAR fraction (fDIF) on productivity, based on FLIGHT simulation is clear. A vegetation canopy under 'direct and diffuse' illumination has an increase in GPP around 12.0 % compared to one under direct illumination. Importantly, the increased productivity due to fDIF is with the same Q_t, so it is the geometric distribution of PAR that is important, not just the amount.

However, the effect of the increase of fDIF due to cloudy conditions for both FLIGHT simulation and FLUXNET data did not enhance the productivity (Figure 6.3.2). The higher fDIF under cloudy sky has lower productivity, for both FLIGHT simulation and FLUXNET data. This might be because, in nature, cloud increases the fDIF but decreases the Q_t at the same time. Therefore the GPP cannot increase due to the decrease in Q_t.

Q_t has a stronger effect than fDIF on the GPP. It is also mentioned in the case of short wave (broadband) irradiance (SW, S_t), in Alton et al. (2007, p785):

> *'Although the fraction of diffuse sky radiance increases with cloudiness, the LUE enhancement we infer under diffuse sunlight is insufficient to increase NEE when SW is reduced.'*

Therefore, we cannot conclude that an increase in fDIF alone is sufficient to increase the GPP. It needs to be considered together with other parameters especially global irradiance, such as Q_t, S_t, and SW.

6.4.2 Using mapped PAR in FLIGHT

The calculated Q_t (Chapter 5) can be used in the vegetation productivity model. This study uses the estimated Q_t in the FLIGHT model. By applying appropriate correction factors, the FLIGHT simulation can give accurate prediction. Therefore, it might be a possible to map GPP on an hourly basis using the hourly Q_t maps with a model such as FLIGHT in the future.

The advantage of the FLIGHT model is that the user can input the data from different sources. The input data can come from measured data or from remotely sensed data. It is possible to use the FLIGHT model for mapping the hourly GPP. It will be challenging to use FLIGHT simulation for monitoring and mapping GPP over a larger area, on an hourly basis. However, it depends on the input remote sensing data (PAR, fDIF etc.) which have to be available at a similar time interval.

Using FLIGHT still has a lot of problems, especially choosing the input parameters. Some parameters cannot be measured exactly without a lot of effort, such as the 3D tree parameters to represent the tree in the forest. Even though there are FLUXNET sites to measure the GPP for the validation, the methods used are different. Unfortunately, the FLUXNET sits were not designed to measure all the input parameters for FLIGHT, making full validation of the FLIGHT model impossible.

Using FLIGHT in the UK has a few limitations:

- The FLIGHT model was designed for forests (North, 1996), however it is only possible to simulate a single vegetation type at one time. In general, a forest is composed of different types of trees, of different sizes, and it is difficult to represent mixed forest in FLIGHT. The shape of the trees in FLIGHT might not represent real trees that have a variety of shapes. This made the FLIGHT simulation less accurate than that based on FLUXNET data (see Section 6.2 and 6.3).

- There is no wind parameter in FLIGHT, therefore the GPP predictions from FLIGHT may not match with the eddy covariance measurements which takes into account the wind speed and velocity. This makes it quite challenging both to calibrate and validate FLIGHT GPP output.

The forests and woodlands in the UK are patches among grassland and agriculture fields. Less than 20% of the area of the UK is covered by forests or woodland (Forestry-Commission, 2009). Furthermore, most of the forests and woodlands in the UK are impure with roads and human habitation. Therefore, it is not possible to compare directly between FLUXNET measured GPP and simulated GPP from FLIGHT. This study demonstrated that a simple empirical method can be used to correct the mismatch. The accuracy of the FLIGHT GPP is improved after correction and can explain the patterns of the hourly average for diurnal variation in each month compared to the FLUXNET data.

However, the instantaneous PAR modelling and mapping (Section 6.3), and using the result as input to FLIGHT for GPP prediction, did not give the anticipated output. The reason might be the different sampling time and period between the data from the satellite and the measured data from the surface. The SEVIRI sensor on MSG takes a snapshot of satellite image at the instantaneous time, however, the ground data are the average from an hour before the stamped time.

Chapter 7 Conclusion

This research has addressed an important scientific challenge: measuring the components of incident photosynthetically active radiation from space and using those data in plant productivity model, and has investigated each step in a possible methodology to achieve this. The underlying thesis is that understanding the assumptions and limitations of each step is necessary if we are to make intelligent use of such data in global plant productivity models - the 'PAR chain' idea.

- The first part of the research investigated a novel sunshine sensor, the Delta-T Instruments BF3, to test whether this simple low-cost instrument was an adequate substitute for the instruments normally used to measure the components of PAR. It was concluded that the BF3 was highly suitable for this task. There was some evidence that the method of obscuring the Sun (shadow band *vs*. patterned dome) affected the data, but the discrepancy was not great, and the need for regular manual adjustment of a shadow band is a major weakness removed by the design of the BF3.

- Having established the suitability of the BF3 to measure the components of PAR, the research went on to test whether a sky clarity index could be used to estimate the proportion of diffuse PAR. Such indices have long been used to estimate the proportion of diffuse broadband flux, and this is the basis to many satellite-based methods to estimate irradiance at the ground. The research presented here showed that a similar relationship was also found in the PAR region, and this finding underpinned the main body of the research in Chapters 4, 5 and 6.

- Chapter 4 described three methods to estimate the fraction of diffuse PAR (K_{dQ}) over the whole of the UK. The first used ground-based meteorological data, while the others used satellite sensor data. Although the ground-based method was successful, it was argued that its role should be to validate estimates from a spaceborne sensor. It is inevitable that there will never be enough PAR instruments, and they will never be in the right places, so a per-pixel method based on satellite sensor data is preferable. Only in that way can we study things like the feedback between land cover types and CO_2 flux for example.

- Of the two satellite-based methods, that using data from the ISCCP was largely unsuccessful, however, the method based on data from Meteosat produced daily estimates of diffuse PAR fraction based on estimated cloud cover which were statistically significant (R^2 =0.71, $p<0.001$). Maps were generated using this method showing, for the first time, the monthly averages of daily PAR diffuse fraction over the whole of the UK (Figure 5.5.1). The research described in Chapter 4 was a pilot study based on Meteosat data from 2003-2006, and acted as a proof-of-concept for the main study, reported in Chapter 5, which used better quality data from the Meteosat Second Generation satellite.

- The overall amount of PAR (Q_t) is not widely measured in the UK, despite its importance in plant productivity. Chapter 5 described a method to estimate Q_t using data from a geostationary satellite sensor, the Spinning Enhanced Visible and Infrared Imager (SEVIRI) on Meteosat Second Generation (MSG). In an environment such as the UK, the amount and type of cloud has a huge influence on the components of PAR at the ground. The difficulties with cloud effects are their unpredictable characteristics: elevation, position, size and light interaction. Furthermore, the solar zenith angle and the direction of the irradiance complicates any procedure for the estimation of PAR. To address the problem of clouds and evaluate the pattern and trend of PAR irradiance from satellite data, it was necessary to use an enormous amount of satellite data. Although a physical-based model would have been more satisfying, the generalisation of cloud effects was a necessary step in creating a workable method to estimate PAR at the ground.

- The research described in Chapter 5 built upon the previous work and extended it through use of a simplified radiative transfer model to estimate the amount of PAR across the whole of the UK. The method developed in Chapter 4 to estimate the fraction of diffuse PAR was applied to the new data set from 2005-2012. The resulting maps of global and diffuse PAR over the whole of the UK were validated using the limited ground data available, and these represent the first attempts to record this information over the whole country. It is estimated that global PAR was accurate to RMSE = 47.72 $\mu\mathrm{mol\,m^{-2}\,s^{-1}}$ and diffuse PAR fraction to RMSE = 8.42%.

- Having developed and tested methods to estimate both the amount of PAR and the fraction of diffuse PAR reaching the Earth's surface, the research then incorporated these data into a forest productivity model, FLIGHT. This was a challenging task for several reasons. First, gathering in situ $\mathrm{Q_d}$ data for modelling and validation was difficult. If all the data had been accurate, the $\mathrm{Q_d}$ mapping might have been easily done by using equation: $\mathrm{Q_d} = \mathrm{Q_t} \times \mathrm{K_{dQ}}$, where $\mathrm{K_{dQ}}$ is the diffuse PAR fraction. Unfortunately, $\mathrm{Q_d}$ is not widely measured. Furthermore, some of the other data required were either not available or were ill-defined or uncertain. For example, although it was possible to estimate $\mathrm{Q_d}$ from diffuse broadband irradiance ($\mathrm{S_d}$), there is still some error. Furthermore, there are errors in the ground data, even in a well-instrumented country such as the UK, due to the complicated adjustment of the shade ring or similar shade object. Also, a small percentage of error of the sensor sensitivity can affect the accuracy of measurement under low light conditions.

The research leaves important questions unanswered regarding the suitability of FLIGHT for application across the whole range of vegetation types in the UK, and about the empirical adjustments used, so the final map presented in Figure 5.5.1 should be treated with caution. Much greater confidence can be placed in the maps showing the components of PAR (Chapters 4 and 5), which show for the first time the spatio-temporal patterns of global and diffuse PAR across the whole of the UK.

7.1 Despite these concerns, the overall approach shows how it would be possible to implement a national system to monitor and measure the components of PAR using data from a geostationary satellite.

Returning to the gaps in current knowledge identified at the end of Chapter 2, the following observations may be made:

7.1.1 What is the best way to monitor PAR over large areas at high temporal resolution (hourly)?

Two contrasting approaches have been prevalent in remote sensing: large-area frequent monitoring using a coarse spatial resolution sensor on a geostationary platform, or less frequent observation using a higher spatial resolution sensor from a platform in Sun synchronous orbit. The research presented in Chapters 4, 5 and 6 has shown that broadband visible/near IR sensors on geostationary satellites are well-suited to this task, and that they have advantages over satellites in low Earth orbit such as Terra for this task. In recent years the distinction between these two approaches has become blurred due to:

- Improvement in the spatial resolution, and to a lesser extent, multispectral capability of sensors in geostationary orbit, e.g. MSG SEVERI replacing the first generation Meteosat

- The development of constellations of satellites in Sun-synchronous orbit, e.g. the DMC satellites.

If the aim is to produce a global map of relative PAR, averaged over a month or a growing season, then a vegetation index integrated over time may suffice. However, if the aim is to provide data for a process model, then finer temporal resolution is required. The first conclusion of this research is that even the best Sun-synchronous satellite system currently available (MODIS on the NASA Terra/Aqua satellites) cannot provide such data, and that a geostationary platform is preferable. Not only does the geostationary platform provide frequent temporal sampling, but it also allows measurement of the Earth’s surface over the full range of solar geometries, unlike the Sun-synchronous orbit.

7.1.2 How can we validate measurements of PAR from space?

Clearly, it is important that we have some way of checking the accuracy of our estimates of incident PAR measured from space, a process known as validation. However, that is not easy to achieve. First there is the problem that PAR is not routinely measured at many locations worldwide, and the diffuse fraction is hardly ever measured. This is partly because there are no simple and cost-effective ways to measure the diffuse component, but also because its importance has been overlooked in the past. The research presented here has confirmed the suggestions made in the literature that high levels of diffuse PAR can play a significant role in plant productivity, increasing levels of GPP in forests by over 10%.

In practice, PAR is often estimated using a correction factor applied to broadband irradiance data measured with a pyranometer. The research presented here has confirmed that this is a viable method to estimate global PAR, but it does not help us estimate the diffuse PAR. For this, the Delta-T Devices BFx Sunshine Sensor has been shown to offer a convenient, relatively low-cost solution.

Bibliography

Alados, I., Olmo, F. J., Foyo-Morono, I., & Alados-Arboledas, L. (2000). Estimation of photosynthetically active radiation under cloudy conditions. *Agricultural and Forest Meteorology, 102*, 39-50.

Alton, P. B., Ellis, R., Los, S. O., & North, P. R. (2007a). Improved global simulations of gross primary product based on a separate and explicit treatment of diffuse and direct sunlight. *Journal of Geophysical Research, 112*, D07203. doi: 10:1029/2006JD008022

Alton, P. B., & North, P. (2007). Interpreting shallow, vertical nitrogen profiles in tree crowns: A three-dimensional, radiative-transfer simulation accounting for diffuse sunlight. *Agricultural and Forest Meteorology, 145*, 110-124.

Alton, P. B., North, P., Kaduk, J., & Los, S. (2005). Radiative transfer modeling of direct and diffuse sunlight in a Siberian pine forest. *Journal of Geophysical Research, 110*, D23209. doi: 10.1029/2005JD006060

Alton, P. B., North, P. R., & Los, S. O. (2007b). The impact of diffuse sunlight on canopy light-use efficiency, gross photosynthetic product and net ecosystem exchange in three forest biomes. *Global Change Biology, 13*, 776-787.

Angstrom, A. K., & Drummond, A. J. (1961). Basic concepts concerning cutoff glass filters used in radiation measurements. *Journal of Meteorology, 18*, 360-367.

Asrar, G. (1989). *Theory and applications of optical remote sensing*: John Wiley & Sons.

Badescu, V. (2008). *Modeling solar radiation at the earth's surface*. Heidelberg: Springer.

Barton, C. V. M., & North, P. R. J. (2001). Remote sensing of canopy light use efficiency using the photochemical reflectance index: Model and sensitivity analysis. *Remote Sensing of Environment, 78*(3), 264-273. doi: http://dx.doi.org/10.1016/S0034-4257(01)00224-3

Batlles, F. J., Olmo, F. J., & Alados-Arboledas, L. (1995). On shadowband correction methods for diffuse irradiance measurements. *Solar Energy, 54*(2), 105-114. doi: http://dx.doi.org/10.1016/0038-092X(94)00115-T

Bentham. (2010, 5 November 2010). Calibration Standards Retrieved 11 December, 2010, from http://www.bentham.co.uk/calibration_standards.htm

Berk, A., S., B. L., Anderson, G. P., Acharya, P. K., Robertson, D. C., Chetwynd, J. H., & Adler-Golden, S. M. (1998). MODTRAN Cloud and Multiple Scattering Upgrade with Application to AVIRIS. *Remote Sensing of Environment, 65*, 367-375.

Biggs, W. W., Edison, A. R., Eastin, J. D., Brown, K. W., Maranville, J. W., & Clegg, M. D. (1971). Photosynthesis light sensor and meter. *Ecology, 52*, 125-131.

Bird, R. E. (1984). A simple, solar spectral model for direct-normal and diffuse horizontal irradiance. *Solar Energy, 32*(4), 461-471.

Bird, R. E., & Riordan, C. (1986). Simple solar spectral model for direct and diffuse irradiance on horizontal and tilted planes at the earth's surface for cloudless atmospheres. *Journal of Climate and Applied Meteorology, 25*(1), 87-97.

Blackwell, M. (1954). Five years' continuous recording of total and diffuse solar radiation at Kew Observatory. *Met. Pap*(895).

Boland, J., Ridley, B., & Brown, B. (2008). Models of diffuse solar radiation. *Renewable Energy, 33*, 575-584.

Boland, J., Scott, L., & Luther, M. (2001). Modelling the diffuse fraction of global solar radiation on a horizontal surface. *Environmetrics, 12*, 103-116.

Bortolini, M., Gamberi, M., Graziani, A., Manzini, R., & Mora, C. (2013). Multi-location model for the estimation of the horizontal daily diffuse fraction of solar radiation in Europe. *Energy conversion and management, 67*(0), 208-216. doi: http://dx.doi.org/10.1016/j.enconman.2012.11.008

Brion, J., Chakir, A., Charbonnier, J., Daumont, D., Parisse, C., & Malicet, J. (1998). Absorption spectra measurements for the ozone molecule in the 350–830 nm region. *Journal of Atmospheric Chemistry, 30*(2), 291-299.

Britton, C. M., & Dodd, J. D. (1976). Relationships of photosynthetically active radiation and shortwave irradiance *Agricultural Meteorology 17* 1-7.

Butt, N., New, M., Malhi, Y., da Costa, A. C. L., Oliveira, P., & Silva-Espejo, J. E. (2010). Diffuse radiation and cloud fraction relationships in two contrasting Amazonian rainforest sites. *Agricultural and Forest Meteorology, 150*(3), 361-368. doi: DOI 10.1016/j.agrformet.2009.12.004

Campbell Scientific (Canada) Crop. (2001). PAR LITE Sensor for photosynthetic photon flux Retrieved 11 December, 2010, from http://www.campbellsci.ca/Catalogue/PAR_Lite_Br.pdf

CFARR. Visible and IR Broadband Radiometers Retrieved 14 September, 2010, from http://www.chilbolton.rl.ac.uk/broad.htm

Chappuis, J. (1880). *C.R. Acad. Sci. Paris 91*, 985.

Chen, L., Gao, Y., Yang, L., Liu, Q., Gu, X., & Tian, G. (2008). MODIS-derived daily PAR simulation from cloud-free images and its validation. *Solar Energy, 82*(6), 528-534.

Choi, K. Y., & Milton, E. J. (2011). *Airborne hyperspectral skydome: the new dimension of hyperspectral sensing*. Paper presented at the In, Annual Conference of the Remote Sensing and Photogrammetry Society: Earth Observation in a Changing World (RSPSoc 2011), Bournemouth, GB, 13 - 15 Sep 2011.

Choudhury, B. J. (2001). Estimating gross photosynthesis using satellite and ancillary data: Approach and preliminary results. *Remote Sensing of Environment, 75*(1), 1-21.

Coakley, J. A., & Davies, R. (1986). The Effect of Cloud Sides on Reflected Solar Radiation as Deduced from Satellite Observations. *Journal of the Atmospheric Sciences, 43*(10), 1025-1035. doi: 10.1175/1520-0469(1986)043<1025:teocso>2.0.co;2

Dedieu, G., Deschamps, P. Y., & Kerr, Y. H. (1987). Satellite Estimation of solar irradiance at the surface of the earth and of surface albedo using a physical model applied to Meteosat data. *Journal of Climate and Applied Meteorology, 26*, 79–87.

Delta-T Devices Ltd. (2002a). *Technical Manual for the Sunshine Sensor Type BF3*. Cambridge: Delta-T Devices Ltd.

Delta-T Devices Ltd. (2002b). *User Manual for the Sunshine Sensor Type BF3*. Cambridge: Delta-T Devices Ltd.

Diak, G. R., & Gautier, C. (1983). Improvements to a Simple Physical Model for Estimating Insolution from GOES Data. *American Meteorological Society, 22*, 505-508.

Doornik, J. A. (2011). Robust Estimation Using Least Trimmed Squares.

Drummond, A. (1956). On the measurement of sky radiation. *Theoretical and applied climatology, 7*(3), 413-436.

Dunagan, S. E., Johnson, R., Zavaleta, J., Russell, P. B., Schmid, B., Flynn, C., Redemann, J., Shinozuka, Y., Livingston, J., & Segal-Rosenhaimer, M. (2013). Spectrometer for Sky-Scanning Sun-Tracking Atmospheric Research (4STAR): Instrument Technology. *Remote Sensing, 5*(8), 3872-3895.

Eck, T. F., & Dye, D. G. (1991). Satellite estimation of incident photosynthetically active radiation using ultraviolet reflectance. *Remote Sensing of Environment, 38*(2), 135-146.

EKO. (2010). Small Sensors Retrieved 11 December, 2010, from http://www.eko-usa.com/products/am/pyranometer/index.html

EKO Instruments. (2011). Small sensors ML-020 series Retrieved 28 October, 2011, from http://www.eko-usa.com/products/am/pyranometer/index.html

Erbs, D. G., Klein, S. A., & Duffie, J. A. (1982). Estimation of the diffuse radiation fraction for hourly, daily and monthly-average global radiation. *Solar Energy, 28*(4), 293-302. doi: http://dx.doi.org/10.1016/0038-092X(82)90302-4

Esser, G., Hoffstadt, J., Mack, F., & Wittenberg, U. (1994). High resolution biosphere model (HRBM) - Documentation model version 3.00.00. In G. Esser (Ed.), *Mitteilungen aus dem Institute fur Pflanzenokolgie det Justus-Liebig-Universitat Giessen* (Vol. 2). Giessen, Germany.

Federer, C., & Tanner, C. (1966). Sensors for measuring light available for photosynthesis. *Ecology*, 654-657.

Fishwick, P. (2007a). Basic measurements of radiation at station Camborne (2001 - 2007).

Fishwick, P. (2007b). Basic measurements of radiation at station Lerwick (2001 - 2007).

Forestry-Commission. (2009). Forestry Facts & Figures 2009: A summary of statistics about woodland and forestry. Edinburgh. *Economics & Statistics, Forestry Commission, 23*.

Fritz, S., Krishna Rao, P., & Weinstein, M. (1964). Satellite Measurements of Reflected Solar Energy and the Energy Received at the Ground. *Journal of Atmospheric Sciences, 21*, 141-151.

Fröhlich, C. (1991). History of solar radiometry and the world radiometric reference. *Metrologia, 28*(3), 111.

Frouin, R., & Gautier, C. (1990). *Variability of photosynthetically available and total solar irradiance at the surface during FIFE- A satellite description.* Proceeding of the Symposium on FIFE- First ISLSCP Field Experiment, Anaheim, CA.

Frouin, R., & Pinker, R. T. (1995). Estimating Photosynthetically Active Radiation (PAR) at the Earth's Surface from Satellite Observations. *Remote Sensing of Environment, 38*, 98-107.

Furlan, C., de Oliveira, A. P., Soares, J., Codato, G., & Escobedo, J. F. (2012). The role of clouds in improving the regression model for hourly values of diffuse solar radiation. *Applied Energy, 92*(0), 240-254. doi: http://dx.doi.org/10.1016/j.apenergy.2011.10.032

Gaastra, P. (1963). Climatic control of photosynthesis and respiration. *Environmental control of plant growth*, 113-140.

Gautier, C., Diak, G., & Masse, S. (1980). A simple physical model to estimate incident solar radiation at the surface from GOES satellite data. *Journal of Applied Meteorology, 36*, 1005-1012.

Gonzalez, J.-A., & Calbo, J. (1999). INFLUENCE OF THE GLOBAL RADIATION VARIAGILITY ON THE HOURLY DIFFUSE FRACTION CORRELATIONS. *Solar Energy, 65*, 119-131.

Gonzalez, J. A., & Calbo, J. (2002). Modelled and measured ratio of PAR to global radiation under cloudless skies. *Agricultural and Forest Meteorology, 110*, 319-325.

Goward, S. N., & Huemmrich, K. F. (1992). Vegetation canopy PAR absorptance and the normalized difference vegetation index: An assessment using the SAIL model. *Remote Sensing of Environment, 39*(2), 119-140. doi: http://dx.doi.org/10.1016/0034-4257(92)90131-3

Grifoni, D., Carreras, G., Zipoli, G., Sabatini, F., Dalla Marta, A., & Orlandini, S. (2008). Row orientation effect on UV-B, UV-A and PAR solar irradiation components in vineyards at Tuscany, Italy. *International Journal of Biometeorology, 52*(8), 755-763.

Gu, L., Baldocch, D., Verma, A. B., Black, T. A., Vesala, T., Falge, E. M., & Dowty, P. R. (2002). Advantages of diffuse radiation for terrestrial ecosystem productivity. *Journal of Geophysical Research, 107*, ACL 2 - 1-23. doi: D6,10.1029/2001JD001242.

Gu, L., Fuentes, J. D., Shugart, H. H., Staebler, R. M., & Black, T. A. (1999). Responses of net ecosystem exchanges of carbon dioxide to changes in cloudiness: Results from two North American deciduous forests. *Journal of Geophysical Research, 104*, 31421-31434.

Gueymard, C. (1989). An atmospheric transmittance model for the calculation of the clear sky beam, diffuse and global photosynthetically active radiation. *Agricultural and Forest Meteorology, 45*(3), 215-229.

Halpern, P. (1984). Ground level solar energy estimates using geostationary operational environmental satellite measurements and realistic model atmospheres. *Remote Sensing of Environment, 15*(1), 47-61. doi: http://dx.doi.org/10.1016/0034-4257(84)90051-8

Hanson, K. J. (1971). Studies of cloud and satellite parameterization of solar irradiance at the earth's surface: National Oceanic and Atmospheric Administration, Miami, Fla.(USA). Atlantic Oceanographic and Meteorological Labs.

Hanson, K. J. (1976). A new estimate of solar irradiance at the Earth's surface on zonal and global scales. *Journal of Geophysical Research, 81*(24), 4435-4443.

Haxeltine, A., & Prentice, I. C. (1996). BIOME3: An equilibrium terrestrial biosphere model based on ecophysiological constraints, resource availability, and competition among plant functional types. *Global biogeochemical cycles, 10*(4), 693-709.

Hay, J. E. (1993). Calculating solar radiation for horizontal surfaces—II. Empirically based approaches. *Renewable Energy, 3*(4–5), 365-372. doi: http://dx.doi.org/10.1016/0960-1481(93)90103-N

Hay, J. E., & Hanson, J. K. (1978). A satellite-based methology for determining solar irradiation at the ocean surface during GATE. *Bulletin of the American Meteorological Society, 59*, 1549.

Howell, T. A., Meek, D. W., & Hatfield, J. L. (1983). Relationship of photosynthetically active radiation to shortwave radiation in the San Joaquin Valley. *Agricultural Meteorology, 28*, 157-175.

Hubbard, R. M., Bond, B. J., & Ryan, M. G. (1999). Evidence that hydraulic conductance limits photosynthesis in old Pinus ponderosa trees. *Tree physiology, 19*(3), 165-172.

Ineichen, P., & Perez, R. (1999). Derivation of Cloud Index from Geostationary Satellites and Application to the Production of Solar Irradiance and Daylight Illuminance. *Theoretical and applied Climatology, 64*, 119-130.

Iqbal, M. (1983). *An Introduction to Solar Radiation*. New York: Academic Pres.

Jacovides, C. P., Boland, J., Asimakopoulos, D. N., & Kaltsounides, N. A. (2010). Comparing diffuse radiation models with one predictor for partitioning incident PAR radiation into its diffuse component in the eastern Mediterranean basin. *Renewable Energy, 35*, 1820-1827.

Jacovides, C. P., Timbios, F., Asimakopoulos, D. N., & Steven, M. D. (1997). Urban aerosol and clear skies spectra for global and diffuse photosynthetically active radiation. *Agricultural and Forest Meteorology, 87*, 91-104.

Jacovides, C. P., Tymvios, F. S., Asimakopoulos, D. N., Theofilou, K. M., & Pashiardes, S. (2003). Global photosynthetically active radiation and its relationship with global solar radiation in the Eastern Mediterranean basin. *Theoretical and Applied Climatology, 74*, 227-233.

Jacovides, C. P., Tymvios, F. S., Assimakopoulos, V. D., & Kaltsounides, N. A. (2006). Comparative study of various correlations in estimating hourly diffuse fraction of global. *Renewable Energy, 31*, 2492-2504.

Jacovides, C. P., Tymvios, F. S., Assimakopoulos, V. D., & Kaltsounides, N. A. (2007). The dependence of global and diffuse PAR radiation components on sky conditions at Athens, Greece. *Argricultural and Forest Meteorology, 143*, 277-287.

Janjai, S., Laksanaboonsong, J., Nunez, M., & Thongsathitya, A. (2005). Development of a method generating operational solar radiation maps from satellite data for a tropical environment. *Solar Energy, 78*, 739–751.

Janjai, S., Pankeaw, P., & Laksanaboonsong, J. (2009). A model for calculating hourly global solar radiation from satellite data in the tropics. *Applied Energy, 86*, 1450-1457.

Janjai, S., Pankeaw, P., Laksanaboonsong, J., & Kitichantaropas, P. (2011). Estimation of solar radiation over Cambodia from long-term satellite data. *Renewable Energy, 36*, 1214-1220.

Janjai, S., & Wattan, R. (2011). Development of a model for the estimation of photosynthetically active radiation from geostationary satellite data in a tropical environment. *Remote Sensing of Environment, 115*, 1680-1693.

Justus, C. G. (1984). *Atmospheric and surface short-wave energy balance from combined satellite and ground-based data.* Proceeding of the Proceedings of the Conference on Satellite Meteorology and Remote Sensing Applications, Clearwater Beach, Florida.

King, D. M., Radke, L. F., & Hobbs, P. V. (1990). Determination of the spectral absorption of solar radiation by marine stratocumulus clouds from airborne measurements within clouds. *Journal of the Atmospheric Sciences, 47*(7), 894-907.

Kipp & Zonen. (2000). *CM 11 pyranometer/CM 14 albedometer instruction manual*. Delft: Kipp & Zonen B.V.

Kipp & Zonen. (2010). PQS 1 Retrieved 11 December, 2010, from http://www.kippzonen.com/?product/184292/PQS+1.aspx

Kipp & Zonen. (2012). *Product Catalogue*. Delft: Kipp & Zonen B.V.

Lacis, A. A., & Hansen, J. (1974). A parameterization for the absorption of solar radiation in the earth's atmosphere. *Journal of the Atmospheric Sciences, 31*(1), 118-133.

Lahoz, W., & Peuch, V.-h. (2012). MONITORING AIR QUALITY FROM SPACE.

Lavagnini, A., & Jibril, Z. (1991). Monthly maps of daily diffuse solar irradiance for Italy. *Renewable Energy, 1*(5–6), 779-789. doi: http://dx.doi.org/10.1016/0960-1481(91)90027-M

LI-COR Inc. (2010). Calibration of LI-COR Radiation Sensors Retrieved 11 December, 2010, from http://www.licor.com/env/Products/Sensors/rad.jsp

LI-COR Inc. (undated). *Radiation Measurement Instruments*. Nebraska: LI-COR Inc. .

Li, R., Zhao, L., Ding, Y., Wang, S., Ji, G., Xiau, Y., Liu, G., & Sun, L. (2010). Monthly ratios of PAR to global solar radiation measured at northern Tibetan Plateau, China. *Solar Energy, 84*, 964-973.

Liang, S., Zheng, T., Liu, R., Fang, H., Tsay, S. C., & Running, S. (2006). Estimation of incident Photosynthetically Active Radiation from MODIS Data. *Journal of Geophysical Research, 111*, 1-13.

Lieth, H. (1975). Modeling the primary productivity of the world. In H. Lieth & R. H. Whittaker (Eds.), *Primary productivity of the biosphere* (Vol. 14, pp. 237-263). New York: Springer-Verlag.

Liou, K. N. (2002). *An Introduction to Atmospheric Radiation* (2 ed.). California: Academic Press.

Liu, B. Y. H., & Jordan, R. C. (1960). The interrelationship and characteristic distribution of direct, diffuse and total solar radiation. *Solar Energy, 4*(3), 1-19.

Liu, R., Liang, S., He, H., Liu, J., & Zheng, T. (2008). Mapping incident photosynthetically active radiation from MODIS dataf over China. *Remote Sensing of Environment, 112*, 998.

Long, S., Humphries, S., & Falkowski, P. G. (1994). Photoinhibition of photosynthesis in nature. *Annual Review of Plant Biology, 45*(1), 633-662.

Martins, F. R., Pereira, E. B., Silva, S. A. B., Abreu, S. L., & Colle, S. (2008). Solar energy scenarios in Brazil, Part one: Resource assessment. *Energy Policy, 36*(8), 2853-2864. doi: http://dx.doi.org/10.1016/j.enpol.2008.02.014

McArthur, L. J. B. (2005). *World climate research programme baseline surface radiation network (BSRN) operation manual version 2.1*. Ontorio: Environment Canada.

McCree, K. J. (1972a). The action spectrum, absorptance and quantum yield of photosynthesis in crop plants. *Agricultural and Forest Meteorology, 9*, 191-216.

McCree, K. J. (1972b). Test of current definitions of photosynthetically active radiation against leaf photosynthesis data. *Agricultural Meteorology, 10*, 443-453.

McGuire, A. D., Melillo, J. M., Kicklighter, D. W., & Joyce, L. A. (1995). Equilibrium responses of soil carbon to climate change: empirical and process-based estimates. *Journal of Biogeography*, 785-796.

McKee, T. B., & Cox, S. K. (1974). Scattering of Visible Radiation by Finite Clouds. *Journal of the Atmospheric Sciences, 31*, 1885-1892.

McPherson, H. (1969). Photocell-filter combinations for measuring photosynthetically active radiation. *Agricultural Meteorology, 6*(5), 347-356.

Mercado, L. M., Bellouin, N., Sitch, S., Boucher, O., Huntingford, C., Wild, M., & Cox, P. M. (2009). Impact of changes in diffuse radiation on the global land carbon sink. *Nature, 458*(7241), 1014-1017.

Meyer, R., Torres-Buron, J., Marquardt, G., Schwandt, M., Geuder, N., Hoyer-Klick, C., Lorenz, E., Hammer, A., & Beyer, H. G. (2008). *Combining solar irradiance measurements and various satellite-derived products to a site-specific best estimate.*

Morsdorf, F., Kötz, B., Meier, E., Itten, K. I., & Allgöwer, B. (2006). Estimation of LAI and fractional cover from small footprint airborne laser scanning data based on gap fraction. *Remote Sensing of Environment, 104*(1), 50-61. doi: 10.1016/j.rse.2006.04.019

Möser, W., & Rachke, E. (1984). Incident solar radiation over Europe estimated from METEOSAT data. *Journal of Climate and Applied Meteorology, 23*, 166-170.

Möser, W., & Raschke, E. (1983). Mapping of global radiation and cloudiness from Meteosat image data-Theory and ground truth comparisons. *Meteorologische Rundschau, 36*, 33-41.

Mõttus, M., Ross, J., & Sulev, M. (2001). Experimental study of ratio of PAR to direct intrgral solar radiation under cloudless conditions. *Agricultural and Forest Meteorology, 109*, 161-170.

Muneer, T. (2004). *Solar radiation and daylight models*: Routledge.

Muneer, T. (2006). *Solar radiation and daylight models* (2 ed.). Oxford: Elsevier Butterworth-Heinemann.

Nasahara, K. N. (2009). Simple Algorithm for Estimation of Photosynthetically Active Radiation (PAR) Using Satellite Data. *SOLA, 5*(0), 37-40.

National Aeronautics and Space Administration. (2011, 29 September 2011). A Lambertian reflector Retrieved 3 October, 2011, from http://landsat.gsfc.nasa.gov/images/lambertian.html

Nimira, J. (1980). Comparison of estimated and observed values for solar radiation at the surface of the African continent.

Norman, J., Tanner, C., & Thurtell, G. (1969). Photosynthetic light sensor for measurements in plant canopies. *Agronomy Journal, 61*(6), 840-843.

North, P. R. J. (1996). Three-Dimensional Forest Light Interaction Model Using a Monte Carlo Method. *IEEE Transactions on Geoscience and Remote Sensing, 34*(4), 946-956.

Oliveira, A. P., Escobedo, J. F., Machado, A. J., & Soares, J. (2002). Correlation models of diffuse solar-radiation applied to the city of São Paulo, Brazil. *Applied Energy, 71*(1), 59-73. doi: http://dx.doi.org/10.1016/S0306-2619(01)00040-X

Optronic Laboratories. (2009). Products Retrieved 11 December, 2010, from http://www.olinet.com/products.php?_act=manageListProduct&DO=viewListProduct

Orgill, J., & Hollands, K. (1977). Correlation equation for hourly diffuse radiation on a horizontal surface. *Solar Energy, 19*(4), 357-359.

Pankaew, P., Milton, E. J., & Dawson, T. P. (2011). *Estimating the proportion of diffuse photosynthetically active radiation from satellite measured cloud fraction: a test under humid temperate conditions.* Proceeding of the Annual Conference of the Remote Sensing and Photogrammetry Society: Earth Observation in a Changing World (RSPSoc 2011), Bournemouth, GB, 13 - 15 September 2011.

Parkinson, C. L., & Greenstone, R. (2000). *EOS data products handbook* (Vol. 2).

Parton, W., Scurlock, J., Ojima, D., Gilmanov, T., Scholes, R., Schimel, D., Kirchner, T., Menaut, J., Seastedt, T., & Moya, E. G. (1993). Observations and modeling of biomass and soil organic matter dynamics for the grassland biome worldwide. *Global biogeochemical cycles, 7*(4), 785-809.

Perez, R., Ineichen, P., Kmiecik, M., Moore, K., Renne, D., & George, R. (2004). Producing satellite-derived irradiances in complex arid terrain. *Solar Energy, 77*(4), 367–371. doi: http://dx.doi.org/10.1016/j.solener.2003.12.016

Philipona, R. (2002). Underestimation of solar global and diffuse radiation measured at Earth's surface. *Journal of Geophysical Research: Atmospheres (1984–2012), 107*(D22), ACL 15-11-ACL 15-18.

Pinker, R. T., & Ewing, J. A. (1985). Modelling surface solar radiation: model formular and validation. *Journal of Climate and Applied Meteorology, 24*(5), 389-401.

Pinker, R. T., & Laszlo, I. (1992). Modeling surface solar irradiance for satellite application on a global scale. *Journal of Applied Meteorology, 31*, 194-211.

Potter, C. S., Randerson, J. T., Field, C. B., Matson, P. A., Vitousek, P. M., Mooney, H. A., & Klooster, S. A. (1993). Terrestrial ecosystem production: a process model based on global satellite and surface data. *Global biogeochemical cycles, 7*(4), 811-841.

Powles, S. B. (1984). Photoinhibition of photosynthesis induced by visible light. *Annual Review of Plant Physiology, 35*(1), 15-44.

Prathumsit, J., & Janjai, S. (2012). Correlation models for the estimation of diffuse fraction of global illuminance from satellite data. *Procedia Engineering, 32*(0), 414-420. doi: http://dx.doi.org/10.1016/j.proeng.2012.01.1287

Prince, S. D., & Goward, S. N. (1995). Global primary production: a remote sensing approach. *Journal of Biogeography*, 815-835.

Prior, J. (2010). *The met office book of the British weather*. Devon: David and Charles.

Ridley, B., Boland, J., & Lauret, P. (2010). Modelling of diffuse solar fraction with multiple predictors. *Renewable Energy, 35*(2), 478-483. doi: http://dx.doi.org/10.1016/j.renene.2009.07.018

Rocha, A. V., Su, H., Vogel, C. S., Schmid, H. P., & Curtis, P. S. (2004). Photosynthetic and water use efficiency responses to diffuse radiation by an aspen-dominated northern hardwood forest. *Society of American Foresters, 50*, 793-801.

Roderick, M. L. (1999). Estimating the diffuse component from daily and monthly measurements of global radiation. *Agricultural and Forest Meteorology, 95*, 169-185.

Roderick, M. L., Farquhar, G. D., Berry, S. L., & Noble, I. R. (2001). On the direct effect of clouds and atmospheric particles on the productivity and structure of vegetation. *Oecologia, 129*, 21-30.

Rossow, W. B., & Schiffer, R. A. (1999). Advances in understanding clouds from ISCCP. *Bulletin of the American Meteorological Society, 80*, 2261 – 2288. doi: 10.1175/15200477(1999)080<2261:AIUCFI> 2.0.CO;2

Rossow, W. B., Walker, A. W., Beuschel, D. E., & Roiter, M. D. (1996). *International Satellite Cloud Climatology Project (ISCCP) documentation of new cloud datasets* (Vol. WMO/TD 737). Geneva: World Meteorological Organization.

Ruimy, A., Dedieu, G., & Saugier, B. (1996). TURC: A diagnostic model of continental gross primary productivity and net primary productivity. *Global biogeochemical cycles, 10*(2), 269-285.

Running, S. W., & Hunt, E. R. (1993). Generalization of a forest ecosystem process model for other biomes, BIOME-BGC, and an application for global-scale models. *Scaling physiological processes: Leaf to globe*, 141-158.

Schiffer, R. A., & Rossow, W. B. (1983). The international satellite cloud climatology (ISCCP): the first project of the world climate research programme. *Bulletin of the American Meteorological Society, 64*(7).

Schiller, K. (2006). Derivation of photosynthetically available radiation from METEOSAT data in the German bight with neural nets. *Ocean Dynamics, 56*, 79-85.

Schott, J. R. (1997). *Remote sensing: the image chain approach*: Oxford: Oxford University Press.

Shaltout, M., & Hassen, A. (1990). Solar energy distribution over Egypt using cloudiness from Meteosat photos. *Solar Energy, 45*(6), 345-351.

Sitch, S., Smith, B., Prentice, I. C., Arneth, A., Bondeau, A., Cramer, W., Kaplan, J. O., Levis, S., Lucht, W., & Sykes, M. (2003). Evaluation of ecosystem dynamics, plant geography and terrestrial carbon cycling in the LPJ dynamic global vegetation model. *Global Change Biology, 9*(2), 161-185.

Skartveit, A., Olseth, J. A., & Tuft, M. E. (1998). An hourly diffuse fraction model with correction for variability and surface albedo. *Solar Energy, 63*(3), 173-183. doi: http://dx.doi.org/10.1016/S0038-092X(98)00067-X

Sorapipatana, C., & Exell, R. H. (1988). An operational system for mapping global solar radiation from GMS satellite data. *ASEAN Journal on Science and Technology for Development, 56*(2), 79-100.

Spitters, C., Toussaint, H., & Goudriaan, J. (1986). Separating the diffuse and direct component of global radiation and its implications for modeling canopy photosynthesis Part I. Components of incoming radiation. *Agricultural and Forest Meteorology, 38*(1), 217-229.

Stanhill, G., & Cohen, S. (2001). Global dimming: a review of the evidence for a widespread and significant reduction in global radiation with discussion of its probable causes and possible agricultural consequences. *Agricultural and Forest Meteorology, 107*(4), 255-278.

Steven, M., & Unsworth, M. H. (1980a). The angular distribution and interception of diffuse solar radiation below overcast skies. *Quarterly Journal of the Royal Meteorological Society, 106*(447), 57-61.

Steven, M. D. (1977). Standard distribution of clear sky radiance. *Quarterly Journal of the Royal Meteorological Society, 103*, 457-465.

Steven, M. D., & Unsworth, M. H. (1980b). Shade-ring corrections for pyranometer measurements of diffuse solar radiation from cloudless skies. *Quarterly Journal of the Royal Meteorological Society, 106*, 865-872.

Stuhlmann, R., Rieland, M., & Raschke, E. (1990). An improvement of the IGMK model to derive total and diffuse solar radiation at the surface from satellite data. *Journal of Applied Meteorology, 29*(7), 586-603.

Szeicz, G. (1974). Solar Radiation for plant growth. *Journal of Applied Ecology, 11*, 617-636.

Szeicz, G., Monteith, J., & Dos Santos, J. (1964). Tube solarimeter to measure radiation among plants. *Journal of Applied Ecology*, 169-174.

Tarpley, J. D. (1979). Estimating incident solar radiation at the surface from geostationary satellite data. *Journal of Applied Meteorology, 18*, 1172-1181.

Udo, S. O., & Aro, T. O. (1999). Global PAR related to global solar radiation for central Nigeria. *Agricultural and Forest Meteorology, 97*, 21-31.

Van Laake, P. E., & Sanchez-Azofeifa, G. A. (2004). Simplified atmospheric radiative transfer modelling for estimating incident PAR using MODIS atmosphere products. *Remote Sensing of Environment, 91*, 98– 113.

Van Laake, P. E., & Sanchez-Azofeifa, G. A. (2005). Mapping PAR using MODIS atmosphere products. *Remote Sensing of Environment, 94*, 554– 563.

Várnai, T. (2000). Influence of three-dimensional radiative effects on the spatial distribution of shortwave cloud reflection. *Journal of the Atmospheric Sciences, 57*(2), 216-229.

Vermote, E. F., Tanré, D., Deuze, J. L., Herman, M., & Morcette, J. J. (1997a). Second simulation of the satellite signal in the solar spectrum, 6S: An overview. *Geoscience and Remote Sensing, IEEE Transactions on, 35*(3), 675-686.

Vermote, E. F., Tanré, D., Deuzé, J. L., Herman, M., & Morcrette, J. J. (1995). *Second Simulation of the Satellite Signal in the Solar Spectrum (6S), User Guide Version 1*.

Vermote, E. F., Tanré, D., Deuzé, J. L., Herman, M., & Morcrette, J. J. (1997b). *Second Simulation of the Satellite Signal in the Solar Spectrum (6S), User Guide Version 2*.

Veroustraete, F., Sabbe, H., & Eerens, H. (2002). Estimation of carbon mass fluxes over Europe using the C-Fix model and Euroflux data. *Remote Sensing of Environment, 83*(3), 376-399.

Vignola, F., Harlan, P., Perez, R., & Kmiecik, M. (2007). Analysis of satellite derived beam and global solar radiation data. *Solar Energy, 81*, 768-772.

Wang, D., Liang, S., Liu, R., & Zheng, T. (2010). Estimation of daily-integrated PAR from sparse satellite observations: comparison of temporal scaling methods. *International Journal of Remote Sensing, 31*(6), 1661-1677.

Wang, J., Zamar, R., Marazzi, A., Yohai, V., Salibian-Barrera, M., Maronna, R., Zivot, E., Rocke, D., Martin, D., & Konis, K. (2008). Robust: insightful Robust library. http://cran.r-project.org/web/packages/robust/.

Weinman, J. (1982). Solar reflection from a regular array of horizontally finite clouds. *Applied Optics, 21*(16), 2940-2944.

Wood, J., Muneer, T., & Kubie, J. (2003). Evaluation of a New Photodiode Sensor for Measuring Global and Diffuse Irradiance, and Sunshine Duration. *Journal of Solar Energy Engineering, 125*, 43-48. doi: 10.1115/1.1531149.

Woodward, F. (1983). Instruments for the measurement of photosynthetically active radiation and red, far-red and blue light. *Journal of Applied Ecology*, 103-115.

Zheng, T., Liang, S., & Wang, K. (2008). Estimation of incident photosynthetically active radiation from GOES visible imagery. *Journal of Applied Meteorology and Climatology, 47*(3), 853-868.

(www1)http://earthobservatory.nasa.gov/GlobalMaps/?eocn=topnav&eoci=globalmaps
(www2)http://www.stfc.ac.uk/Chilbolton/default.aspx
(www3)http://aeronet.gsfc.nasa.gov
(www4)http://www.wytham.ox.ac.uk
(www5)http://www.ceh.ac.uk
(www6)http://digimap.edina.ac.uk
(www7)http://www.forestry.gov.uk/aliceholt
(www8)http://fluxnet.ornl.gov/site/778

(www9)http://pen.agbi.tsukuba.ac.jp

(www10)http://badc.nerc.ac.uk

(www11)http://badc.nerc.ac.uk/data/ukmo-midas/RO_Table.html

(www12)http://www.eumetsat.int

(www13)http://doi.pangaea.de

(www14)http://daac.gsfc.nasa.gov

(www15)http://ozoneaq.gsfc.nasa.gov

(www16)http://gaia.agraria.unitus.it

(www17)http://aeronet.gsfc.nasa.gov/cgi-bin/bamgomas_interactive

(www18)http://rami-benchmark.jrc.ec.europa.eu

(www19)http://aeronet.gsfc.nasa.gov